

DISS. ETH NO. 23905

Entropic Lattice Boltzmann Method for Two-Phase Flows

A thesis submitted to attain the degree of
DOCTOR OF SCIENCES of ETH ZURICH

(Dr. sc. ETH Zurich)

presented by

Ali Mazloomi Moqaddam
MSc in Mechanical Engineering,
Sharif University of Technology

born on 08.07.1988
citizen of Iran

accepted on the recommendation of

Prof. Dr. Ilya V. Karlin, examiner
Dr. Shyam S. Chikatamarla, co-examiner
Prof. Dr. Dimos Poulikakos, co-examiner
Prof. Dr. David Quéré, co-examiner

2016

To my parents

Abstract

Numerical simulation of multiphase flows often represents a challenging task for classical Computational Fluid Dynamics (CFD) schemes based on the macroscopic description of the fluid state leading to the Navier-Stokes equations. The reason lays in the fact that these flows are often driven by phenomena originating at meso- or micro-scales which need to be modeled into macroscopic equations. Unlike conventional CFD methods, the lattice Boltzmann method (LBM) is based on microscopic models and mesoscopic kinetic equations in which dynamics is evolved by the movement of fictitious clusters of particles on a fixed lattice. Due to this kinetic nature, the LBM has been found to be particularly useful in applications involving interfacial dynamics and complex boundaries, e.g. multiphase or multicomponent flows. However, despite of many attempts to model multiphase flows using LBM, the current approaches are still unable to address complex dynamical effects in an efficient and a quantitative fashion.

In this dissertation, firstly, a thermodynamically consistent lattice Boltzmann model that enables complex simulations of dynamics two-phase flows is proposed. The key innovation is the application of the entropic lattice Boltzmann stabilization mechanism to effectively control and stabilize the numerical artifacts that might arise at the interface of a liquid-vapor system. The former together with a polynomial regularization of known equation of states bring about a substantial increase in the operating range of multiphase simulations and thus allowing us to carry out simulations of

two-phase problems at high Weber and Reynolds numbers with sufficiently large liquid-vapor density ratio.

Secondly, thermodynamic consistency of the models is verified by simulating the liquid-vapor coexistence curve, Laplace's law, speed of sound measurements and density profile across the liquid-vapor interface.

The proposed model, is applied to study the problem of binary droplet collisions. Using an extensive numerical simulation, it is shown that the proposed approach is capable of accurately capturing the dynamics and complexities of droplet collision. Comparison with theoretical predictions of the boundaries between different types of the collision outcomes are made and good agreement found. Moreover, the evolution of the shape of stable lamella film is successfully simulated and an excellent comparison between simulation and experiments was shown.

Furthermore, our proposed entropic lattice Boltzmann method (ELBM) for multiphase flows, is extensively employed towards simulation of dynamic vapor-liquid-solid interface problems or droplet wall interaction problems. A wide range of applications from capillary filling to liquid drop impact onto both flat and particularly macrot textured surfaces are studied in detail. We begin by comparing ELBM results with large number of theoretical and experimental findings, which clearly demonstrate the promising potential of the proposed methodology for simulation of complex dynamic phenomena of multiphase flows. Next we investigate numerically, the textured superhydrophobic surfaces that are capable of reducing the contact time of an impacting liquid drop. Using numerical simulations it is first demonstrated that the ELBM can accurately predict the dynamics of a liquid drop impacting a macrot textured surface. Also, from the simulation results obtained for the existing macrot textured surfaces, we shed light on the physics involved in contact time reduction, by uncovering the role of hydrodynamics and interfacial dynamics both of which play a crucial role in droplet wall interactions. This information is further utilized in analyzing the performance of existing surfaces in terms of parameter range and also in designing of novel surface textures that can employ various modes of droplet rebound.

Lastly, the accomplishments of this study are summarized and future directions of research and short coming of the present model are discussed.

Zusammenfassung

Numerische Simulationen von Mehrphasenströmungen sind häufig eine herausfordernde Aufgabe für die klassischen Berechnungsmethoden der Strömungsmechanik (CFD) welche durch eine makroskopischen Zustandsbeschreibung von Fluiden auf die Navier-Stokes Gleichungen führen. Der Grund dafür ist, dass diese Strömungen oft von Phänomenen im mesoskopischen und mikroskopischen Bereich angetrieben werden. Diese Phänomene müssen dann allerdings in makroskopischen Gleichungen beschrieben werden. Im Gegensatz zu den konventionellen CFD Methoden beruht die Lattice-Boltzmann Methode (LBM) auf mikroskopischen Modellen und mesoskopischen kinetischen Gleichungen in welchen die Dynamik sich aus der Bewegung von fiktiven Gruppierungen von Partikeln auf einem festen Gitter entwickelt. Aufgrund dieser kinetischen Natur hat sich herausgestellt, dass die LBM insbesondere in Anwendungen der Grenzflächendynamiken und komplexen Grenzflächen, sprich Mehrphasen oder Mehrkomponentenströmung, sich als nützlich erwiesen hat. Doch trotz vieler Versuche Mehrphasenströmungen mit der LBM zu modellieren sind die derzeitigen Ansätze immer noch nicht in der Lage komplexe dynamische Effekte effizient und quantitativ anzugehen.

In dieser Dissertation wird zuerst ein thermodynamisch konsistentes Lattice-Boltzmann Modell vorgestellt welches komplexe Simulationen von dynamischen Zweiphasenströmungen ermöglicht. Die wichtigste Neueinführung ist die Einbindung des entropischen Lattice-Boltzmann Stabilisieru-

ngsmechanismus um effektiv numerische Artefakte zu kontrollieren und zu stabilisieren, welche möglicherweise an den Grenzflächen eines Flüssigkeit-Gas-Systems auftreten. Dies zusammen mit einer polynomialen Darstellung von bekannten Zustandsgleichungen bringt eine beträchtliche Erweiterung des Einsatzbereichs. Dadurch werden Simulationen von Zweiphasenproblemen bei hoher Weber und Reynoldszahl mit ausreichend grossem Dichteverhältnis zwischen Flüssigkeit und Gas durchführbar.

Zweitens wird durch Simulationen der Flüssigkeit-Gas-Koexistenzkurve, der Laplace-Gleichung, der Messung der Schallgeschwindigkeit und des Dichteprofiles entlang der Flüssigkeit-Gas Grenzfläche die thermodynamische Bestimmtheit des Modells nachgewiesen.

Das vorgestellte Modell wird angewandt um das Problem der binären Tropfenkollision zu untersuchen. Mithilfe einer umfassenden numerischen Simulation wird gezeigt, dass der vorgestellte Ansatz die Dynamik und Komplexität von Tropfenkollisionen genau einfängt. Vergleiche mit theoretischen Vorhersagen der Bereichsgrenzen zwischen verschiedenen Arten von Kollisionsergebnissen wurden gemacht und eine gute Übereinstimmung wurde gefunden. Des Weiteren wird die Entwicklung der Form eines stabilen lamellaren Films erfolgreich simuliert und die Übereinstimmung zwischen Simulation und Experiment ist exzellent.

Zusätzlich wird unsere vorgestellte entropische Lattice-Boltzmann Methode (ELBM) für Mehrphasenströmungen ausgiebig in Simulationen von dynamischen Gas-Flüssigkeit-Fest Grenzflächenproblemen und Tropfen-Wand Interaktionsproblemen zum Einsatz gebracht. Eine grosse Anwendungsvielfalt von Kapillarfüllung zu Tropfenaufschlag auf sowohl flacher wie auch spezifisch makrotexturierten Oberflächen werden ausführlich untersucht. Wir beginnen indem wir die Ergebnisse der ELBM mit vielen theoretischen und experimentellen Ergebnissen vergleichen. Dies zeigt klar das vielversprechende Potential der vorgestellten Methodik für Simulationen von komplexen Phänomenen der Mehrphasenströmungen. Daraufhin untersuchen wir numerisch texturierte superhydrophobische Oberflächen die imstande sind die Kontaktzeit eines aufprallenden Flüssigkeitstropfen zu verringern.

Durch numerische Simulationen wird erst gezeigt, dass die ELBM die Dynamik des Aufpralls eines Tropfens auf einer makrotexturierten Oberfläche genau vorhersagen kann. Mit Hilfe der Simulationsergebnisse einer existierenden makrotexturierten Oberfläche erläutern wir die Physik die hinter der Kontaktzeitreduktion liegt indem wir die Rolle der Hydrodynamik und Grenzflächendynamik darlegen, welche beide eine bedeutende Rolle in Tropfen-Wand-Interaktionen spielen. Diese Information wird dann weiter benutzt um die Leistungsfähigkeit existierender Oberflächen in Bezug auf Parameterbereiche zu analysieren und auch im Design von neuartigen Oberflächentexturen die verschiedene Moden des Zurückspringens von Tropfen erlauben.

Zuletzt werden die Leistungen dieser Arbeit zusammengefasst und zukünftige Richtungen dieser Forschung sowie Nachteile des aktuellen Modells präsentiert.

Acknowledgments

The present work could not have been accomplished without the help of many people. First and foremost, I would like to express my sincere appreciation and thanks to my advisor Prof. Ilya V. Karlin for continuous support of my Ph.D, for his motivation and immense knowledge. You have taught me the way of thinking and how a physicist tackles a scientific problem.

I would especially like to thank Dr. Shyam Chikatamarla for his invaluable help and constructive discussions during all steps of this work. For me he has been a mentor, a colleague and a friend. Thank you.

I want to thank Prof. David Quéré and Prof. Dimos Poulikakos for serving on my thesis committee and for their insightful comments on the problems of droplet wall interactions and contact time reduction. Also, their valuable feedbacks on my thesis are gratefully acknowledged.

My special thanks go to our collaborators Prof. Dimos Poulikakos and his team: Dr. Thomas Schutzius, Dr. Carlo Antonini and Gustav Graeber; Prof David Quéré and his coworkers: Prof. Christophe Clanet, Dr. Anaïs Gauthier and Pierre Chantelot; and Prof. Jan Carmeliet and his coworkers: Dr. Dominique Derome, Dr. René Rossi and Marcelo Parada; who provided us substantial information in the experimental contribution of this work. The collaboration with them was always joyful and productive.

ACKNOWLEDGMENTS

I wish also to thank all my colleagues in the Aerothermochemistry and Combustion Systems Laboratory (LAV) and particularly the head of the LAV, Prof. Konstantinos Boulouchos for giving me this opportunity to work in such a pleasant environment.

The Financial support of ETH research under the Grant No.ETH35-12-2 is gratefully acknowledged.

My thanks are extended to my fellow group members, Fabian Bösch, Nicolo Frapolli, Benedikt Dorschner, and my friends, Mahdi Kooshkbaghi, Mohsen Maleh Mir, Mahdi Asgari, Hadi Daneshmand, Reza Niroomand and all those friends of mine in Zürich.

Finally I have to thank my family members. I am deeply indebted to my father Mohammad, my mother Taiebe, my brother Reza and my sisters Malihe and Zohre for their never ending love, support and prayers through my long journey of study. They have done so much for me during my life and words can not express the gratitude I have.

Above all, praise and thanks to the *God*.

اللَّهُمَّ عَجِّلْ لِي لِقَاءَكَ الْفَرَجِ
على مظلومی مقدم
زورینج
آبان خزار و سید و نو و پنج جری شمسی

Contents

Abstract	iii
Zusammenfassung	vii
Acknowledgments	xi
Contents	xiii
List of Tables	1
List of Figures	2
1 Introduction	15
1.1 Motivation	15
1.2 Computational approaches in two-phase flow simulations . .	16
1.2.1 Macroscopic approaches	17
1.2.2 Microscopic and mesoscopic approaches	20
1.3 Multiphase LB models	22
1.3.1 Color-Fluid model	22
1.3.2 Interparticle-Potential model	23
1.3.3 Free-Energy model	23
1.3.4 Mean-Field theory model	24
1.4 Scope of research	24
1.5 Outline of the thesis	25

2	Entropic Lattice Boltzmann method for multiphase flows	29
2.1	Boltzmann equation	29
2.2	Lattice Boltzmann equation	31
2.3	Entropic Lattice Boltzmann equation	32
2.4	Two-phase fluids	34
2.4.1	Thermodynamics	34
2.4.2	Equilibrium in the presence of the interface	36
2.4.3	Korteweg's stress	38
2.5	ELBM for non-ideal fluids	38
2.5.1	An entropic pressure free energy approach	39
2.5.2	An entropic forcing free energy approach	43
2.6	Wall boundary conditions	49
2.7	Summary and Conclusions	50
3	Binary droplet collisions	51
3.1	Introduction	51
3.1.1	Validation of the model	52
3.2	Results and Discussions	56
3.2.1	Simulation setup for droplet collision	56
3.2.2	Various regimes of droplet collision	58
3.2.3	Lamella stabilization	60
3.2.4	Energy dissipation at maximum radial deformation	65
3.2.5	Satellite droplets and instabilities	66
3.2.6	Flow visualization and entropy estimate	72
3.3	Summary and Conclusions	73
4	Fluid-solid interface problems on flat surfaces	77
4.1	Introduction	77
4.2	Validation of the model	79
4.2.1	Young-Laplace equation	79
4.2.2	Motion of liquid column in a channel due to wettability gradient	80
4.3	Drop impact on a flat surface	82

4.3.1	Drop impact on a flat superhydrophobic surface . . .	83
4.3.2	Drop impact on a flat wettable surface	84
4.3.3	Universal flow in the lamella	85
4.4	Summary and Conclusions	89
5	Capillary driven flows	91
5.1	Introduction	91
5.2	Results and discussion	94
5.2.1	Capillary rise in circular cylinders	94
5.2.2	Wicking in twisted yarns	96
5.3	Summary and Conclusions	98
6	Tumbling rebound of high viscous drops from sublimating slopes	101
6.1	Introduction	101
6.2	Results and discussion	105
6.2.1	Normal axisymmetric impacts	105
6.2.2	Oblique nonaxisymmetric impacts	105
6.2.3	Vorticity generation and evolution	109
6.3	Summary and Conclusions	111
7	Drops bouncing off macrotextures: pancake bouncing	113
7.1	Introduction	114
7.2	Results and discussion	117
7.2.1	Geometry and simulation parameters	117
7.2.2	Comparison with experiment	118
7.2.3	Textures with perfect coating	120
7.2.4	Imperfect coating	124
7.2.5	Energy budget	126
7.2.6	Impact on a tilted texture	130
7.3	Summary and Conclusions	131
8	Drops bouncing off macrotextures: discovery of new surfaces	133

CONTENTS

8.1	Introduction	134
8.2	Results and discussions	136
8.2.1	Validation with experimental data	136
8.2.2	Egg-carton surface	138
8.2.3	Ring bouncing	144
8.3	Summary and Conclusions	153
9	Conclusions and future work	155
9.1	Summary of results	156
9.2	Directions for future work	160
A	Chapman-Enskog expansion of the LBM	165
B	Evaluation of derivatives	171
	Bibliography	173

List of Tables

2.1	The coefficients of the polynomial equation of state (2.55). . . .	47
3.1	The coefficients of the polynomial equation of state (2.55) at $T/T_c = 0.7268$	57
3.2	Comparison of energy dissipation of a droplet at maximum radial deformation for two different kinematic viscosities.	67
3.3	Computational cost for simulation of binary droplet collision at $Re = 75$, on 2304 CPUs.	74
3.4	Computational cost for simulation of binary droplet collision at $Re = 368$, on 2304 CPUs.	75
7.1	Reduced kinetic and surface energy for the spherical drop	127

List of Figures

2.1	The Polynomial (2.55) together with P-R (2.54) equation of state at $T/T_c = 0.7268$	46
3.1	Coexistence curve for the proposed equation of state. Symbol: ELBM simulation; Line: Maxwell's equal area rule	53
3.2	Laplace law for various values of kinematic viscosity (ν) and surface tension coefficient κ in two dimensions. With the increasing κ , the surface tension σ increases independent of the viscosity. The liquid and vapor densities are $\rho_l = 7.82$, $\rho_v = 0.071$, respectively.	53
3.3	Speed of sound as implied by the equation of state (line) and observed in the present simulation (symbol).	54
3.4	Liquid-Vapor density profile for a flat interface obtained by the free energy function (line) and simulation (symbol) for three different density ratios (10, 25 and 125).	54
3.5	Simulation results (symbol) for deformation of a droplet in simple shear flow together with theoretical results of Taylor Eq. (3.2) (line).	56
3.6	Schematic representation of the binary droplet collision.	57
3.7	Numerical simulations of three types of droplet collisional regimes (Coalescence +, Reflexive separation \blacktriangle , Stretching separation \circ) together with theoretical prediction (solid line) [1]	58

3.8	Sequence of coalescence observed for binary collision of equal sized droplet at $We = 32.8$, $Re = 210.8$ and $\chi = 0.08$. (a) Experiment of Qian and Law [2] and (b) present simulations. . .	59
3.9	Reflexive separation regime as observed during near head on collisions at $We = 37.2$, $Re = 228.8$ and $\chi = 0.01$. (a) Experiment of Qian and Law [2]; (b) Simulation	59
3.10	Snapshots of the collisional outcome of two highly viscous drops for experiment (left) [3] and present simulations (right) at $We = 92.5$, $Re = 35.65$ and $\chi = 0.6$	61
3.11	Simulation of stretching separation regime (right) compared to experiments (left) [3] at $We = 45.0$, $Re = 43.6$ and $\chi = 0.8$. . .	62
3.12	Time evolution of maximum radial expansion of a merged droplet as measured by present ELBM simulations (solid line) together with experiments (square) [4] at $We = 269$, $Re = 154$ and $We = 357$, $Re = 178$	63
3.13	Simulation of lamella stabilization at different stages ($We = 269$ and $Re = 154$). The lamella film expands from $t^* = 2.83$ to $t^* = 6.02$ before contracting from $t^* = 7.8$ to $t^* = 11.7$	63
3.14	Dimensionless thickness of the lamella at the symmetry center, $h_{lam}^* = h/D_0$, versus the non-dimensional time, $t^* = tU_0/D_0$. Open symbol: ELBM simulations for two different impact conditions, $We = 269$, $Re = 154$ and $We = 357$, $Re = 178$; Line: Analytical estimate of Ref. [5] (Eq. 3.4).	64
3.15	Snapshots of the two colliding droplets for various Weber numbers and impact parameters together with velocity magnitude (color).	68
3.16	Stream lines and velocity magnitude for the state corresponding to time $t^* = 7.1$ of the figure 3.15(c) show the presence of strong rotational motion in the side arms.	69
3.17	“End-pinching” mechanism observed during near head on collisions. This leads to formation of an odd number of satellite droplets.	70

LIST OF FIGURES

3.18	The distribution of local density, relaxation parameter α as well as mass flux observed inside a merged droplet for one of the snapshots in Fig. 3.17(a) (just before the ligament disconnects). See text for further discussion.	72
4.1	Equilibrium contact angle for a liquid drop confined inside the channel as function of the adhesion parameter κ_w (2.59). A comparison between the contact angles derived from Eq. (4.1) (circle) and the simulation results (cross). Line: A fit of numerical results. The surface tension is $\sigma = 0.353$, the liquid density is $\rho_l = 7.82$ and the vapor density is $\rho_v = 0.071$. The channel dimension is 300×70 lattice nodes.	79
4.2	Schematic representation of the confined liquid column (red) in a rectangular channel. Liquid column of length L_1 moves along the channel under a wettability step imposed on the bottom ($z = 0$) and on the top ($z = H$) walls. The dynamic contact angles are θ^+ and θ^-	81
4.3	History of the centroid velocity U of the liquid column; Line: Analytical (4.3); Symbol: Simulation. Inset: Center-of-mass position X ; Line: Analytical (4.2); Symbol: Simulation. The height of the channel $H = 60$ and the dynamic contact angles are $\theta^+ = 69.2^\circ$ and $\theta^- = 63.15^\circ$. Time and space are given in lattice units.	81
4.4	The reduced maximum diameter of the spreading drop as a function of the Weber number. Circle: ELBM simulation; Square: Experimental data [6]. Solid line corresponds to the scaling law (4.6).	83
4.5	Snapshots of a drop impacting on a wettable surface; Left: Experiment [7]; Right: Simulation. $Re = 764$ and $We = 31.5$	84
4.6	Evolution of droplet diameter on a hydrophilic surface. Line: ELBM simulation; Symbol: Experiment [7].	85
4.7	Snapshots of lamella stabilization simulation on a superhydrophobic surface at $We = 85$ and $Re = 60$	85

4.8	Drop impact on a hydrophilic surface. Non-dimensional thickness of the lamella at the symmetry center, $h_c^* = h_c/D_0$, versus the non-dimensional time, $t^* = tU_0/D_0$ is shown. Open symbol: ELBM simulation at various impact conditions; Full circle: Experiment [8]; Line: Analytical estimate of Ref. [5], Eq. (4.7).	86
4.9	Drop impact on a superhydrophobic surface. Non-dimensional thickness of the lamella at the symmetry center, $h_c^* = h_c/D_0$, versus the non-dimensional time, $t^* = tU_0/D_0$ is shown. Open symbol: ELBM simulation at various impact conditions; Line: Analytical estimate of Ref. [5], Eq. (4.7).	87
4.10	Drop impact onto a superhydrophobic surface. Thickness of the lamella as a function of the impact Weber number. Full circle: ELBM simulation result for the thickness of the lamella at the symmetry axis, at the time instant $t^* = 1$: $h_{c1}^* = h_c^*(1)$; Dashed lines: Fitting curve of the numerical results to guide the eye. Asymptotic values for h_{c1}^* for $We > 40$: $h_{c1}^* = 0.2571$ (ELBM); $h_{c1}^* = 0.2496$ (Ref. [5]). Open circle: ELBM simulation result for the minimal thickness of the lamella h_m^* .	88
5.1	Schematic representation of the geometry used in simulation of capillary rise in a tube. The h_0 is the length of the part of the capillary tube dipped into liquid, h is the meniscus height and \dot{h} implies the meniscus velocity. The R and γ_d are the tube radius and the dynamic contact angle, respectively.	92
5.2	Different snapshots of three dimensional simulation of capillary rise with no gravity ($g^* = 0$). The tube radius and static contact angle are $R^* = R/h^+ = 670$ and $\gamma_s = 36^\circ$, respectively.	93
5.3	Comparison of results obtained from simulations (square symbol) with those predicted by Eq. (5.1) (solid line). (a) Evolution of the meniscus height for tubes with different radii at zero gravity ($g^* = 0$). (b) The height of liquid column as a function of time for different gravitational forces in a tube with radius $R^* = R/h^+ = 287$.	95

LIST OF FIGURES

5.4	(a) The setup used for simulation of wicking in a twisted yarn. (b) The front view as well as the cross-sectional view of the yarn containing 32 twisted fibers.	96
5.5	Selected snapshots from simulations showing the transport of liquid through a twisted yarn. The static contact angle is $\gamma_s = 5^\circ$. To visualize the water through the fibers, we made the yarn structure transparent.	97
5.6	Simulation results for the evolution of wicking through the twisted yarn given in Fig. 5.4 for two different wettabilities. The h^* is determined as the maximum location of the wicking height through the fibers in each time step.	98
6.1	Experimental observations for drop impact onto a tilted carbon dioxide sublimating surface [9]: (a) schematic and image sequence of (b) water and (c) glycerol drop impacts. The impact condition are $\alpha = 55^\circ$, $We = \rho V^2 D_0 / \sigma = 86$ and $Oh = \mu / \sqrt{\rho \sigma D_0} = 2.7 \times 10^{-3}$ for water and $\alpha = 60^\circ$, $We = 121$ and $Oh = 3.2$ for glycerol. The nondimensional rebound time is $t_{reb} / \tau = 2.2$ for water and $t_{reb} / \tau = 1.2$ for glycerol. Also indicated are the normal V_N and tangential V_T components of impact velocity as well as the substrate tilt angle α	103
6.2	Nondimensional rebound time t_{reb} / τ as a function of the Ohnesorge number Oh for simulations (open symbols) and experiments [9] (solid symbols). Selected snapshots show the results for simulation of low viscous ($Oh = 0.025$) and high viscous drops ($Oh = 3.2$) impacting on a horizontal surface.	104
6.3	Ratio $k = V_{slide} / V_T$ as a function of Oh . The symbols denote the experimental data [9] for impacts on the sublimating substrate: Solid square, water; Upward triangle, water-glycerol mixture 40:60; Downward triangle, water-glycerol mixture 15:85; Diamond, water-glycerol mixture 7:93; Solid circle, glycerol; and Open square, water drop impact on a superhydrophobic surface (SHS) (data from [10]).	106

6.4	(a) Nondimensional rebound time t_{reb}/τ as a function of the tangential velocity V_T : both experimental data [9] and numerical results for water and glycerol are included. The legend reports values of Oh . (b) Angular velocity ω of highly viscous glycerol drop scales linearly with $2V_T/D_0$. Closed symbols show the results of experiments [9] and open symbols simulations. The fitting line is $\omega = 0.13(2V_T/D_0)$	107
6.5	Values of the drop tilting angle at the moment of rebound Ω_{reb} as a function of the tangential component of velocity V_T for a highly viscous glycerol drop ($Oh = 3.2$). Open symbols: Simulation, closed symbols: Experiment [9].	109
6.6	Evolution of simulated drop impacting on a sublimating slope: (a) a drop in the low-viscosity regime ($Oh = 0.1$, $We = 121$, and $\alpha = 60^\circ$) and (b) a drop in the high-viscosity regime ($Oh = 3.2$, $We = 121$, and $\alpha = 60^\circ$). The rebound time in the simulation was identified through matching the experimentally observed orientation of the drop at the rebound with the corresponding simulated image.	110
6.7	History of the average angular velocity ω of highly viscous liquid drop with $Oh = 3.2$, $We = 121$, and $\alpha = 60^\circ$ during tumbling (simulation). Propagation of the dominant angular velocity component of $\vec{\omega}_{loc}$ inside the drop is shown in the insets (a-f), at different stages of tumbling: stages a-c show the initial rise of the angular velocity shortly after the impact and stages d-f show rotation of the drop acting essentially as a solid. The drop rebounds (stage f) at $t/\tau = 1.15$. A shading or color increase corresponds to the increase of the clockwise rotation.	111

6.8	History of the average angular velocity ω of a low-viscosity liquid drop with $Oh = 0.1, We = 121$, and slope $\alpha = 60^\circ$ (simulation). Propagation of the dominant angular velocity component of $\vec{\omega}_{loc}$ inside the drop is shown in the insets (a–f), at different stages of drop impact. The drop rebounds (stage f) at $t/\tau = 2.1$. A shading or color increase corresponds to the increase of the clockwise rotation.	112
7.1	Simulation setup. The texture is represented a surface decorated with a lattice of tapered posts. The posts are represented by right conical frustums with the base diameters b and B ; w is the center-to-center spacing and h is the height of the posts.	116
7.2	Contact time on a flat super-hydrophobic surface with the contact angle of 161° as a function of Weber number. Dashed line: $t_{contact}^* = 2.5$, Ref. [11]; Open symbols: ELBM simulations, solid symbols: Experiment [12].	119
7.3	Comparison of simulation (bottom) and experiment [13] (top) for the pancake bouncing of a drop impinging on, (a) the tapered posts at $We = 14.1$, (b) the straight square posts at $We = 7.9$	120
7.4	Comparison of simulation (symbol) and experiment [13] (line) of characteristic times $t_\uparrow, t_{max}, t_{contact}$, and pancake quality, $Q = d_{jump}/d_{max}$, with We for a drop impinging on, (a) tapered posts, (b) square posts. The blue, red, pink and green colors show the $t_\uparrow, t_{max}, t_{contact}$ and Q , respectively	121
7.5	Snapshots of the rebound from tapered posts at (a) $We = 40$, (b) $We = 50$, (c) $We = 80$, (d) $We = 120$. Density of the texture $\Lambda_{exp} = 7.25$. Invading liquid hits the base of the texture at $We \geq 50$. Perfect coating is assumed for both the posts and the base plate (contact angle is set to $\theta = 165^\circ$). After hitting the base, penetrated liquid experiences a quick lateral extension, detaches from the base, returns to the top of the posts and demonstrates pancake rebound.	122

7.6	Contact time t_{contact} (squares) and pancake quality Q (circles) of a drop impinging on perfectly coated tapered posts with the density of texture $\Lambda_{\text{exp}} = 7.25$, for a range $6 \leq We \leq 150$	123
7.7	Dependence of the contact time on the density of the texture $\Lambda = R_0/w$ at $We = 30$. DoT of the experiment [13] is marked with a square, $\Lambda_{\text{exp}} = 7.25$	123
7.8	Contact time for a perfectly (squares) and imperfectly (diamonds) coated texture as a function of Weber number.	124
7.9	Snapshots of impact on imperfectly coated texture at (a) $We = 40$, (b) $We = 50$, (c) $We = 80$, (d) $We = 120$. Contact angle at the base plate and 10% above it set to $\theta_{\text{bottom}} = 140^\circ$, and for the rest of the texture the contact angle is $\theta = 165^\circ$. For $We \geq 50$, the penetrated liquid reaches the base at t_{mpl}	125
7.10	Top panel: History of various components of the energy balance. Circle: Normalized kinetic energy \tilde{K} ; Downward triangle: Normalized surface energy \tilde{S} ; Upward triangle: Normalized dissipated energy $\tilde{\Xi}$. Squares: Normalized energy balance $\tilde{K} + \tilde{S} + \tilde{\Xi}$. Diamond: Normalized center-of-mass kinetic energy \tilde{K}_{cm} . Bottom panel: Reduced center-of-mass velocity of the drop U_{cm}/U_0 . Impact on a perfectly coated SHT $\theta = 165^\circ$ for low and high Weber numbers.	128
7.11	Snapshots of an impact on tapered posts tilted at 30° ; $We = 31.2$. The drop rebounds at $t_{\text{contact}} = 3.6$ [ms] which is in excellent agreement with the experiment [13]. Snapshots correspond to Figure 1d of Ref. [13].	130
7.12	Contact time of a liquid drop impinging on tapered surface under a tilt angle of $\theta = 30^\circ$ for a large range of We ($6 \leq We \leq 150$). Our simulations show that significant reduction in contact time occurs for $We \geq 25$	130

LIST OF FIGURES

8.1 Drop impact on super-hydrophobic flat surface designed by adding periodic macrotextures. (a) Simulation setup where parameter λ is the center to center distance between ridges. (b) Comparison between simulations: open square, and experiment of Ref. [14]: solid square. The dimensionless contact time, t_{contact}/τ , is measured by varying the landing location of the drop, x/λ , along the periodic macrotextures. All the experimental and simulations results shown in this plot are for $We = 26.6$ 137

8.2 Contact time of a drop impacting on a superhydrophobic surface with (circles) and without (upward triangles) macrotexture as a function of impact velocity V . Open symbols are the results obtained from numerical simulations and closed symbols are the experimental observations of Ref. [12]. 138

8.3 The effect of macrotexture on drop impact dynamics and contact time. (a) The drop impacts directly on the ridge with an impact velocity $V = 1$ m/s and then it takes a butterfly shape at $t = 6.1$ ms before taking off at $t_c = 7.6$ ms, a time significantly shorter than that on a surface without macrotexture. (b) A slower impact case with an impact velocity $V = 0.5$ m/s where the drop is deformed less and it first acquires a square-like shape including two subunit of liquid and then it leaves the surface at $t_c = 10.6$ ms. The simulation results (blue images) are compared with those experimentally observed in Ref. [12](black images). 139

8.4 Left: Visualization of the egg-carton macro-texture used in the simulation. Right: egg-carton macro-texture created by group of Prof. Poulikakos, LTNT-ETHZ. (no superhydrophobic coating applied). The egg carton surface image in the experiment was provided by Gustav Graeber (LTNT-ETHZ group). 140

8.5	Selected snapshots of simulation results for a liquid drop impacting on the egg-carton surface. (a) At lower impact velocity with $V = 0.52$ m/s, the drop exhibits conventional bouncing (spreading, retracting and then leaving substrate). (b) At larger impact velocity with $V = 1.1$ m/s, the drop bounces off the surface as a pancake shape resulting a fourfold reduction in contact time compared with that on a flat surface.	141
8.6	Distribution of the pressure inside the drop impacting on egg-carton surface. The impact velocity of the drop is $V = 1.1$ m/s. The red and dark blue colors are corresponding to the zones with very high and low pressures, respectively. The pressure is visualized on the middle plane of the computational domain and to see the pressure field inside the valleys, the egg-carton surface is not shown.	142
8.7	Simulation results for the variation of contact time with impact velocity for a drop impacting on a flat (triangle) and the egg-carton surface (circle). For egg-carton surface, at low impact velocities ($V < 0.7$ m/s), the drop exhibits conventional bouncing with the same contact time of flat surfaces. While, at larger impact velocities ($V > 0.7$ m/s), the drop bounces as a pancake resulting a factor four reduction in contact time compared to conventional drop impact on flat surfaces.	142
8.8	Experimental results for impact dynamics of water droplets: (a) Conventional rebound on a flat surface at $V = 0.75$ m/s; (b) Conventional rebound on the egg carton surface at $V = 0.6$ m/s; (c) Pancake rebound at $V = 0.8$ m/s; all images have the same scale bar and are synchronized in time with (a) if not otherwise stated. The drop diameter in experiment was 2.2 mm. The experimental images were provided by Gustav Graeber (group of Prof. Poulidakos, LTNT ETHZ).	144
8.9	Ring bouncing simulation setup. A water drop with diameter of 2.6 mm is impacted on a spherical defect of diameter 0.4 mm. .	145

LIST OF FIGURES

8.10 Selected snapshots of a drop impinging on a spherical defect. Each image shows the interface profile for middle plane of the computational domain. The drop impact velocity is 1.28 m/s. 146

8.11 Visualization of velocity field inside the drop during impact on the macrot textured spherical defect. The drop impact velocity is 1.28 m/s. 146

8.12 Different snapshots obtained by numerical simulations showing front and top view of a liquid drop with diameter of 2.6 mm impacting on a spherical defect of diameter 0.4 mm. 147

8.13 Selected snapshots obtained by experiments showing a water drop of diameter 3.2 mm impacting on a superhydrophobic surface textured by a bead of diameter 0.4 mm. The experimental images were prepared by Pierre Chantelot (group of Prof. Quéré, Interfaces & Co., ESPCI). 148

8.14 Evolution of the radius of the outer and the inner rim during the impact. R_{out} is the maximum radial expansion of the outer rim. The R_{in1} and R_{in2} are measured when the drop breaks from the center and generates an inner rim. The R_{in1} and R_{in2} stand for the minimum and maximum radial expansion of the inner rim. The impact velocity of the drop is 1.28 m/s. 148

8.15 The inner rim radius, R , as a function of time for different impact velocities. The R is measured from the moment when the spreading film is ruptured, $t_{rupture}$, till the moment when it collides with the outer rim. Open symbols are simulations and solid symbols are experiments. The dash lines are computed by Taylor-Culick law ($R = \sqrt{2\sigma/(\rho_l h_l)}(t - t_{rupture})$). The experimental data were provided by Pierre Chantelot (group of Prof. Quéré, Interfaces & Co., ESPCI). 149

8.16 Variation of contact time with impact velocity for a drop impacting on a flat surface (triangles) and spherical defect (circles) of diameter 0.4 mm. Open symbol: simulations, Solid symbol: experiments. The experimental data were provided by Pierre Chantelot (group of Prof. Quéré, Interfaces & Co., ESPCI). 149

8.17	Variation of contact time with distance x (the distance between drop center to spherical defect center along the symmetry axis) for water drops impacting on spherical defect. Open symbol: simulations, Solid symbol: experiments. For all measurements, the impact velocity of the drop is fixed to 1.28 m/s. The experimental data were provided by Pierre Chantelot (group of Prof. Quéré, Interfaces & Co., ESPCI).	150
8.18	Contact time versus drop radius for a flat surface with (circles) and without (triangles) spherical defect. Results for flat surface are fitted by the gray dashed line computed by the equation $t_{\text{contact}} = 2.55\sqrt{\rho R_0^3/\sigma}$ as found in Ref. [11] and data for flat surface with defect fitted by the equation $t_{\text{contact}} = (2.55\sqrt{\rho R_0^3/\sigma})/2$ (red dashed line) as found in this research. Open symbol: simulations, Solid symbol: experiments. The experimental data were provided by Pierre Chantelot (group of Prof. Quéré, Interfaces & Co., ESPCI).	150
8.19	Contact time versus impact velocity for a drop impacting a cylindrical defect of different radii. The height of texture is kept constant and equal to diameter of spherical defect (0.4 mm) while the diameter is varied ($d=0.8, 1.5$ and 2 mm). For all simulations and experiments the droplet diameter is fixed to 2.6 mm. Open symbol: simulations, Solid symbol: experiments. The experimental data were provided by Pierre Chantelot (group of Prof. Quéré, Interfaces & Co., ESPCI).	151
9.1	Comparison between simulation (bottom) and experiment [15] (top) for a compound droplet in shear flow (Janus droplet) at orientation angle $\varphi = 0^\circ$ (c1), $\varphi = 58^\circ$ (c2) and $\varphi = 145^\circ$ (c3). .	160
9.2	Different snapshots for simulation of droplet splashing on a thin liquid film.	163

Chapter 1

Introduction

1.1 Motivation

The physics and dynamics of two-phase flow have grown into a major scientific topic with crucial fundamental issues as well as many practical and industrial applications. Fields of interests ranging from drop impact phenomena involved in the study of rain on soils or foliages [16], self-cleaning surfaces [17], anti-icing applications [18], ink-jet printing [19], combustion chambers [20] and transport of liquids in textiles [21]. The dynamics of liquid-liquid or liquid-solid interfaces is rich and complex with many mathematical and technical issues that need to be resolved to account for specific role of these interfaces (a surface in three dimensions and a line in two dimensions) separating two domains with different physical properties. Further complications arise when the solid phase (walls) also starts influencing the behavior of liquid-gas interface. Therefore, due to the complex nature of multiphase flows, theoretical solutions are generally limited to relatively simple cases. Meanwhile, the experimental approaches for multiphase flows are very expensive and are yet unable to provide in-depth information of the flow field, stresses and strains close to the interfaces for such a complex flows. Nevertheless, numerical simulations provide a great degree of freedom in the choice of initial and boundary conditions as well as provide substantial information on the flow field, stress, and fluxes of both the fluid phases. Hence, it is reasonable to say that numerical simulations, when combined with theoretical analysis and experimental studies can be powerful tools in studying the underlying physics of multiphase flows and can provide valuable insights into the role of hydrodynamics in these complex phenomenon.

From the perspective of numerical methods for simulation of interfacial problems; conventional CFD methods are based on macroscopic equations, while molecular dynamics simulations seek to model the microscopic behavior of individual molecules. The lattice Boltzmann method takes a mesoscopic approach that could be imagined to lie in between the micro and macro worlds. Based on the kinetic lattice Boltzmann equation, particle interactions are directly implemented, while the movement of those particles is confined to a discrete lattice. This makes the LBM very useful in modeling interfacial dynamics and multiphase flows, while avoiding the enormous computational complexity of a direct molecular dynamic simulation.

Therefore, it is not surprising that LB methods have been used by many authors (see [22–28] and references therein) to simulate multiphase fluids. However, lattice Boltzmann multiphase models still suffer from substantial drawbacks such as restriction on the kinematic viscosity, interface thickness, low density ratio between the liquid and vapor phases, and others. In spite of a number of refinements (see review, e.g., [26–28] and references therein), existing LB formulations for multiphase or multicomponent flows are still unable to address complex dynamical effects, such as droplet collisions, wetting and spreading phenomena in a quantitative fashion. Among these approaches the free energy model proposed by Swift et al. [23] takes the advantage of having thermodynamic consistency. However, this approach severely suffers from numerical instability and hence its application was restricted to simulation of stationary droplets suspended in the vapor or quasi-dynamical droplets with slow motion and low liquid-vapor density ratio.

Hence, to overcome the aforementioned problems of existing multiphase LB models and subsequently to simulate realistic multiphase flow problems, further developments in the context of lattice Boltzmann method are much needed. In this research, we aim to propose a novel two-phase model built upon the thermodynamically consistent free-energy lattice Boltzmann approach for two-phase flow simulations free of above limitations.

1.2 Computational approaches in two-phase flow simulations

Computational fluid dynamics or CFD is a branch of fluid dynamics that uses numerical analysis and algorithm to solve the governing equations for transport phenomena in discrete space and time. The equations to be solved, and the manner in which they are discretized, can vary greatly depending

on the problem of interest. Over the last 50 years, the solution of the Navier-Stokes (N-S) equations using finite volume and finite difference approaches has dominated the fluid flow modeling community. However, in the past two decades, alternative approaches have arisen and are beginning to take hold due to their ability to capture more complex flow dynamics.

1.2.1 Macroscopic approaches

The Navier-Stokes equations are a macroscopic perspective of fluid flow and govern the motion of fluids and can be seen as Newton's second law of motion for fluids. In the Navier-Stokes world, one directly deals with the variations in fluid observables i.e. density, velocity, pressure etc. and predicts the state of the fluid in terms of these observables. Discretizing the equations in space and time and solving them numerically yields the flow properties at each node of the grid. As CFD techniques have evolved and their utility in both research and industry have been proven, there has been considerable interest in modeling more diverse and more complex flow fields. Highly accurate and efficient schemes are now capable of solving a multitude of problems, but some regimes, such as turbulent flows and multiphase flows, are still the subject of intense research. Flows which occur when multiple phases are present, provide a particularly interesting complication as the phase separation process is a consequence of long-range molecular interactions. Given that no consideration is given in the macroscopic N-S equations to molecular behavior, the simulation of multiple phases needs to be modeled explicitly with these approaches.

Simulation of the phase separation using macroscopic N-S solvers is artificially done by tracking the location of interface between phases. These models fall into two categories: the front tracking method and front capturing method. In the following, we will briefly review these methods.

1.2.1.1 Front tracking methods

Front tracking methods directly track the location of the interface between two phases [29, 30]. Such methods produce very accurate description of the interface, since the interface is explicitly traced using an unstructured moving mesh that is transported in a Lagrangian fashion. While enjoying the benefit of a purely Lagrangian transport, this method requires frequent mesh rearrangements that could affect the conservation of the liquid volume. Moreover, the parallelization of such a method is very challenging. The main limitation of this approach is the lack of automatic topology modification. Any interface merging or break-up events have to be handled manually,

which can be a complex procedure, especially for three-dimensional simulations. Since topology changes are extremely frequent in atomization and transport through porous media, front tracking method seem unadapted for these applications. Although the surface tension effects can be accurately described due to the ready availability of the interface shape and location, several challenges are faced during interface breakup and merging [31].

1.2.1.2 Front capturing methods

Front-capturing methods first track the movement of fluid and then capture or establish the location of the two-phase interface. In these methods, the two fluids are modeled as a single continuum with discontinuous properties at the interface. The fluid flow equations for both fluids are solved in the same Eulerian mesh. The interface capturing methods generally produce less accurate representation of the interface than the interface tracking approaches. In spite of that, the interface capturing methods enjoy various advantages: in contrast with the front tracking methods, they are relatively convenient to implement and efficient to compute, since there is no need to constantly update the mesh and they are capable of handling topological transitions naturally. The most commonly used front capturing methods are Volume-of-Fluid method [32] and Level-set method [33]. A brief review of these methods will be presented in following.

Volume-of-Fluid Method: In volume-of-fluid (VOF) method, the volume fraction of fluid in each cell is used to track the movement of the liquid. Therefore, VOF relies on a liquid volume fraction scalar to represent the interface. This method ensures discrete mass conservation. However, since the VOF scalar is discontinuous across the interface, a specific geometric advection scheme is required, which puts constraints on both the accuracy of the method and the time step. Additionally, accessing the interface quantities such as the interface normals or curvature can prove challenging.

In volume tracking methods interfaces are "tracked" by evolving fluid volume forward in time with solution of an advection equation. Interface geometry must be inferred based on local volume data and the assumption of the particular algorithm, before interfaces can be reconstructed. The reconstructed interface is then used to compute the volume fluxes necessary to integrate the volume evolution equations. The VOF's use, reliability and effectiveness are widespread: the method has been known for several decades, has gone through a continuous process of improvement and is used by many commercially available software programs. Moreover, the volume conservation is good and no special provision is necessary to perform reconnection

or breakup of the interface as the change of topology is implicit in the algorithm. The VOF method is easy to extend to 3D of space and simple to implement. Applications of the VOF model include stratified flows or the steady or transient tracking of any liquid-gas interface. However, apart from that the interface geometry reconstruction is challenging, the VOF method involves massive calculations and data burden, which leads to important CPU time [34].

Level-Set Method: The level set method aims at representing the interface implicitly by an iso-level of a smooth function (signed distance function). This smooth function is preserved with a re-initialization process. Simple scalar transport schemes can be used to transport this function and, therefore, highly accurate methods are available. Moreover, parallelization is straightforward and highly efficient and the smoothness of the level set function makes the interface normals and curvature readily available.

To model the two-phase flow using level set method two sets of equations are required. The first set is comprised of the single fluid N-S equations, which are employed to determine the momentum. The second set is a transient scalar advection equation which tracks the level set function. The level set function equals zero at the interface, a negative value for locations inside one phase, and a positive value for locations inside another phase. The location of the interface is determined by interpolating between the level set function values. In the level set method, the interface is much easier to determine compared to VOF method. However, due to no inherent conservation property of the level set function, the level set methods are typically plagued by mass conservation issues which is a sever drawback. Recently, a simple modification to the level set method in order to reduce the mass conservation errors while retaining the simplicity of the original method was proposed in [35]. By replacing the usual signed distance function of the classical level set approach by a hyperbolic tangent profile that is transported and re-initialized using conservation equation, it was demonstrated in Ref. [35] that the mass conservation errors could be reduced by an order of magnitude in comparison with the results obtained with a signed distance function. There are further improvements by several groups for enhancing accuracy and robustness of the scheme. However due to numerical implementation, the level set function needs to be re-initialized at every time step to ensure conservation of the scalar. Much effort goes into computation of normals and curvature of the interface together with accurate transport of the level set function. In general, the level set method were designed for multiphase problems in multiple space dimensions in which the topology of

the evolving interface changes during the course of events, and problems in which sharp corners and cusps are present [36].

1.2.2 Microscopic and mesoscopic approaches

Using conventional fluid dynamics and thermodynamics, a description of the macroscopic transport of a system is available. However, they do not provide any information to describe the molecular behaviors that cause the macroscopic effects. Kinetic theory, on the other hand, uses the knowledge that fluids are composed of a large number molecules to describe why flows behave the way they do [37]. Each molecule is treated as a particle with a position and a velocity. All of the particles are then allowed to flow through the domain and collide with other particles, obeying the classical mechanics. This process of streaming and collision, when averaged over the very large number of molecules in a system, gives a fluid with macroscopic properties of density, velocity, temperature and etc.

Microscopic Molecular Dynamics : Molecular dynamics (MD) approaches are the simplest and the most accurate representation of fluid flow in which the Newtonian motion of all the particles composing the system, are tracked in time. Interactions among the particles are implemented via prescribing the inter-particle force potential functions. Using MD-type approaches, very detailed information about the state of a system can be obtained. However, MD is time consuming and computationally expensive because the time step size used in the analysis is small and the number of atoms or molecules required for a statistically steady ensemble is extremely large. Consequently, only very small systems with limited number of molecules are capable of being modeled with current computational resources. Therefore, it is impractical to apply MD for macro-scale problems [38].

Mesoscopic Lattice Boltzmann Method: In order to simulate fluid flow on higher scales, one has to coarsen over the real particles. In such a modeling scheme, pseudo-particles, a pack of real particles, are considered where the pseudo-particles can be placed either on a fixed lattice or off-lattice. Dissipative particle dynamics and Direct Simulation Monte Carlo (DSMC) are off-lattice pseudo-particle methods in which pseudo-particles move continuously in space. Lattice Boltzmann Method is one of the on-lattice pseudo-particle approach in which dynamics is evolved by movements of fictitious clusters of particles on a fixed lattice which do not follow Newtonian dynamics as in MD and thus are computationally more affordable. In LBM,

the collective behavior of particles is represented by a single-particle probability distribution function. Therefore, instead of tracing the movement of particles, the evolution of the density distribution function, which depends on position and velocity, is traced. The velocity is discretized such that, in one time step, the density distribution functions or populations move to the neighboring lattice sites to which their associated velocity points. This movement is called streaming. After streaming steps, collisions occur at lattice sites and change the density distribution function. The integration of the probability distribution function in velocity space readily provides macroscopic variables such as: density, velocity and temperature (a detailed review on LBM will be presented in chapter 2). The LBM appears to be very promising because it is easy to code, to implement and to parallelize. In addition, being a “particle method,” the LBM can easily include interfacial phenomena [39].

However, despite the many advantages and simplicity, one of the limitations of the standard LBM is the inability to attain low viscosity because of numerical instabilities. Hence, large Reynolds numbers in the standard LBM simulation can be achieved only by extensive grid refinement. Recent theoretical development of the entropic lattice Boltzmann method [40–43] alleviate this obstacle by restoring the second law of thermodynamics (Boltzmann’s H theorem). This entropy requirement renders the method nonlinearly stable numerically and extends the range of applicability of LBM into new fields which could not be targeted due to stability issues of the standard lattice Boltzmann method.

One of the most interesting applications and active area of research for LBM are multiphase flows. On a phenomenological level, it is possible to include the effect of phase separation and interface dynamics into the LBM framework. Indeed, since LBM deals with particle distribution functions, no explicit equation for tracking interface is required and, in turn, interfaces are constructed naturally by incorporating intermolecular forces. Therefore, the key step in developing the LBM multiphase model is to correctly incorporate the particle interactions into the evolution of probability distribution functions so that macroscopically correct multiphase flow behavior can be obtained. To date, many of the existing LB multiphase models cannot be applied for simulation of dynamical problems with large density ratio between liquid and vapor or large viscosity ratio. In other words, existing LBM approaches for multiphase flows often fail in terms of robustness and stability when they are applied to simulate real industrial problems (large Weber and Reynolds number). This restriction encourages us to introduce a new multiphase model equipped by entropic lattice Boltzmann approach free of limitations of current multiphase LB approaches.

This research is mainly concentrated on two-phase systems with one component and problems related to it. First, using a literature review on the existing multiphase LBM models, we state problems associated with multiphase simulations in the LBM and then we continue by introducing our entropic lattice Boltzmann method for multiphase flows in chapter 2.

1.3 Multiphase LB models

Different approaches on how to treat multi-phase flows in the framework of lattice Boltzmann method have been proposed in the literature. The four main lattice Boltzmann based approaches for analyzing two-phase flows are: color-fluid model [22, 44], interparticle-potential model [24, 45], free-energy model [23] and mean-field theory model [25]. A brief review on these approaches are now given.

1.3.1 Color-Fluid model

One of the first models for two-phase simulations implemented for the LBM, was inherited from the lattice gas automata color model [22, 44]. The model utilizes two distribution functions representing the red and blue fluids. Each of the distribution functions is run by the usual Lattice Boltzmann implementation. Then, at every time step the interface between two fluids is calculated. The surface tension is applied to the fluids as the external force. The original method allows one to obtain sharp interfaces but it is computationally demanding due to calculation of the interface location and surface tension terms at every time step. Also, it was shown by [46] that due to appearance of large value of the spurious currents around interface, the model becomes unstable for large fluid density ratios. Recently the original color fluid model was modified in [47] by adjusting the two-phase flow operator in order to recover the single-phase Navier-Stokes equations. Moreover, based upon the appropriate continuum physics, it was demonstrated in [48] that using an algorithm for inserting an interface between the immiscible phases of a multicomponent lattice Boltzmann fluid, the spurious velocities around interfaces can be reduced significantly in contrast with original model. However, these modifications allow one to use this approach to model larger density ratios between phases for stationary cases (droplet do not move a significant distance) only and still it can not be used to address the complex dynamical effect of multiphase phenomena.

1.3.2 Interparticle-Potential model

The interparticle-potential model proposed by Shan and Chen [24, 45] relies on a microscopic picture of multi-phase flows, where an additional forcing term based on the nearest neighbor interaction mimics the intermolecular interaction. This force guarantees phase separation and introduces surface tension effects. Several researchers [49, 50] applied this model with some success. To date the Shan and Chen model remains the most popular approach to multiphase flows with LBM due to its simplicity. However, there are problems associated with original Shan and Chen model such as lack of thermodynamic consistency, additional spurious currents around the droplet which eventually destroy the stability, low density ratio of liquid to vapor and dependence of the equation of state on the parameters introduced by model. An improvement to Shan and Chen model was presented by Sbragaglia et al. [51]. In this, so-called multirange pseudo-potential method, the interaction is not limited to the nearest neighbors but also interactions with the next nearest neighbors are considered. The introduction of multirange interactions gives the possibility of choosing the surface tension independently from the equation of state, in a contrast to the original Shan-Chen model. Furthermore, Yuan and Schaefer [52] and Quin [53] proposed modified interparticle-potentials to obtain a suitable equation of state and subsequently achieved larger density ratios. Although the Shan and Chen model and its improvements [51, 52] have been successfully applied to study multiphase problems, they still suffer from thermodynamic inconsistency as explained by He and Doolen [54].

1.3.3 Free-Energy model

The model proposed by Swift et al. [23], so called *free-energy* model, ensures thermodynamic consistency by introducing a pressure tensor derived from minimizing the free energy function. Free energy approaches introduce the non-ideal interaction into LB either through a pressure term [23] or a forcing term [55]. Both approaches are equivalent as far as the recovery of the hydrodynamic equations is concerned. They give very similar simulation results but show a difference in the stability of the algorithms. However, the original free-energy model proposed by Swift et al. suffers from several drawbacks such as Galilean non-invariance, low liquid to vapor density ratio, numerical instability and thus its applications are limited to model either stationary or quasi-dynamical problems [55]. Based on free-energy model, Inamuro et al. [56] achieved high density ratio by introducing two sets of populations, one for capturing interface and the other for computing the

velocity field. In their approach, a projection method for pressure correction is also required for stable simulations. Zheng et al. [26] have further simplified the Inamuro model but their scheme still requires to capture the liquid-vapor interface using other techniques. Thus the most important advantage of multiphase LB formulation (no need for interface capturing) are sacrificed using these improvements. In this thesis we will pursue this direction for developing an accurate and reliable model for multiphase flows that can be used for simulating droplet dynamics for realistic applications.

1.3.4 Mean-Field theory model

The mean-field theory model proposed by He et al. [25] is valid in the nearly incompressible limits and applies to non ideal gases. In this method, two distribution functions are used. The first distribution function is used to calculate the pressure and velocity fields of an incompressible liquid. The second is an index function that is used to locate the interface. Interfacial dynamics is modeled by introducing molecular interaction forces, which are approximated by the mean-field theory. This model can accurately simulate the Rayleigh-Taylor and Kelvin-Helmholtz instabilities, even with non-ideal and dense fluids [57]. Lee and Lin proposed a model based on the mean field theory model that is stable for high density ratios [58]. However, in general, the mean-field theory model and its improvements are similar to the traditional computational fluid dynamics methods for interface capturing and are the LBM analogy to the level set and volume of fluid methods. Publications that demonstrate quantitative simulations for realistic applications are scarce using this method.

1.4 Scope of research

The current research focuses on the development of a novel thermodynamically consistent model for two-phase flow simulations in the context of lattice Boltzmann method. We aim to resolve the limitations of existing LB two-phase models such that simulation of dynamical two-phase problems at high Weber and Reynolds numbers with larger liquid-vapor density ratios becomes possible. To this end, the recently introduced entropic lattice Boltzmann method is combined with a free-energy based model, together with the optimal choice of the equation of state. The proposed entropic lattice Boltzmann method for two-phase flows is successfully employed to achieve high Reynolds and Weber numbers that are typical for two-phase applications. The validity of this model is tested through a vast number of

comparisons between numerical simulations and experimental and theoretical findings ranging from binary droplet collision to drop impact onto solid surfaces. Using simulations, it is demonstrated that the proposed modifications to the free-energy based lattice Boltzmann models brings about a substantial increase in the operating range of multiphase simulations.

1.5 Outline of the thesis

The rest of the thesis is outlined as follows:

- Chapter 2 is devoted to description of the novel numerical method developed in this work. First the "*Entropic Lattice Boltzmann Method*" for single phase is presented in detail and then it is extended to two-phase flows by introducing a forcing term in the entropic lattice Boltzmann equation. The forcing term is constructed so that it reproduces the Korteweg's stresses for two-phase flows and it also includes the interactions between fluid and solid particles at solid walls. Next, to achieve larger density ratio for simulation of dynamical two-phase problems, we introduce a non-ideal equation of state in the form of a polynomial which is a regularization of the well-know Peng-Robinson equation of state. In following of this chapter we present details on the numerical implementation including the computation of the entropy estimate which is the key to the ELBM as well as the boundary conditions at the walls.
- Chapter 3 presents simulation results for fluid-fluid interface problems as a necessary validation for the method. In the first part, the method is validated using the requisite problems such as coexistence curve, Laplace's law, speed of sound, liquid-vapor density profile as well as Taylor deformation. In the second part, simulation results for droplet collision are presented along with detailed comparison with experiments and the role of hydrodynamics in droplet collision and breakup is discussed.
- Chapter 4 is dedicated to simulation of dynamical fluid-solid interface problems on flat surfaces. In this chapter various applications ranging from capillary filling to drop impact on flat surfaces are investigated. First, the necessary validations such as the Young-Laplace law and capillary motion in a channel with heterogeneous wettability are presented. It is demonstrated that simulations are in excellent agreement with the corresponding analytical results. Next, the present model is applied to the problem of drop impact onto wettable and superhy-

drophobic surfaces and simulation results are compared to existing experimental data from the literature. It is shown that the present model is capable of accurately predicting the experimental results.

- Chapter 5 is devoted to testing the use of the present model for simulation of capillary phenomena. The method is first verified by simulating the capillary rise in cylindrical tubes. Then as a test case for complex capillary systems, transport of liquids through twisted yarns is studied.
- Chapter 6 documents our simulation results together with the experimental observations of our collaborator (LTNT-ETHZ group) for oblique impacts of high viscous drops. It is shown both numerically and experimentally that the high viscous drops impacting on tilted sublimating surfaces, rather than showing the conventional rebound behavior (sliding, spreading and recoiling), exhibit a new drop rebound regime called '*tumbling*'. Using numerical simulations we show that when a viscous drop such as glycerol impacts on a tilted sublimating surface, part of its initial linear momentum is converted into angular momentum which is sufficient to allow the drop to tumble off the surface, a phenomenon which causes the drop to rebound faster than low viscosity drops.
- Chapter 7 presents a comprehensive study for drops impacting on superhydrophobic flat surfaces patterned with lattice of submillimeter-scale posts. It had been shown experimentally in Ref. [13] that impacting drops on such a surface, exhibits a distinctively different behavior which was termed '*pancake bouncing*'. In this chapter, we first present the simulation setup for this experiment and then the results obtained by numerical simulations are given in which first the reliability of methodology is established by comparing numerical simulations with experimental observations of Ref. [11–14] and then new finding regarding the dynamics of the pancake bouncing are presented.
- Chapter 8 documents our investigations for discovering new superhydrophobic macrot textured surfaces that are capable of reducing the droplet contact time. Our first design is textured with an '*egg-carton*' pattern with conical posts and holes. It is first shown numerically that the geometrical properties of this surface enable the impacting drop to jump off the surface in a pancake shape with a contact time of factor four smaller than that on a flat surface. After numerical study of this surface, we present the experimental results produced by LTNT-ETHZ group. It is shown that the pancake bouncing occurs in

the experimental setup also. With our second innovative design, it is demonstrated both numerically and experimentally (the experimental results were provided by group of Prof. Quéré, Interfaces & co., ES-PCI) that by adding a finite macroscopic object (spherical defect) on a flat surface where drops land, a new rebound regime '*ring bouncing*' occurs. Using both experiments and simulations, it is demonstrated that due to occurrence of the ring bouncing, the droplet contact time is reduced by factor two compared with flat surface.

- Chapter 9 gives a summary of the dissertation together with recommendations for future research.

Chapter 2

Entropic Lattice Boltzmann method for multiphase flows

The lattice Boltzmann method is gaining traction as an important tool in the computational approach from incompressible to compressible flows [59]. Applications of LBM ranging from hydrodynamics at large Reynolds numbers [60–62] to flows at a micron scale, porous media, and multiphase flows [39]. The LBM solves a fully discrete kinetic equation for populations $f_i(\mathbf{x}, t)$. Populations correspond to discrete velocities $\mathbf{c}_i, i = 1, \dots, N$, which fit into a regular spatial lattice with the nodes \mathbf{x} . This enables a simple and highly efficient "stream along links and equilibrate at nodes" realization of the LBM algorithm. However, one of the limitations of the standard LBM is the inability to attain low viscosity because of numerical instabilities. Hence, large Reynolds numbers in the standard LBM simulation can be achieved only by extensive grid refinement. Recent theoretical development of the entropic lattice Boltzmann method [40–43] alleviates this obstacle by restoring the second law of thermodynamics (Boltzmann's H theorem). This entropy requirement renders the method nonlinearly stable numerically and extends the range of applicability of LBM into new fields which could not be targeted due to stability issues of the standard lattice Boltzmann method.

2.1 Boltzmann equation

The Boltzmann equation has its foundations in gas dynamics and is a well-accepted mathematical model of a fluid at the microscopic level. It provides detailed microscopic information, which is critical for the modeling of the

underlying physics behind complex fluid behavior. It is more fundamental than the Navier-Stokes equations. However, due to the high dimensions of the distribution and the complexity in the collision integral, direct solution of the full Boltzmann equation is a formidable task for both analytical and numerical techniques [63].

The continuum Boltzmann equation describes the evolution of the single-particle distribution function $f(\mathbf{x}, \mathbf{c}, t)$ in the phase space:

$$\partial_t f + \mathbf{c} \cdot \nabla_{\mathbf{x}} f + \mathbf{a} \cdot \nabla_{\mathbf{c}} f = Q(f, f), \quad (2.1)$$

where \mathbf{x} and \mathbf{c} denote the position and microscopic velocity of a particle, \mathbf{a} represents the acceleration due to force action on each particle, and the collision integral $Q(f, f)$ is

$$Q(f, f) = \int d^3 \mathbf{c}_1 \int d\Omega \Theta(\Omega) |\mathbf{c} - \mathbf{c}_1| [f(\mathbf{c}') f(\mathbf{c}'_1) - f(\mathbf{c}) f(\mathbf{c}_1)] \quad (2.2)$$

with $\Theta(\Omega)$ as the differential collision cross section for the binary collision a pair of particles which transforms the velocities from \mathbf{c}, \mathbf{c}_1 into $\mathbf{c}', \mathbf{c}'_1$. $f(\mathbf{x}, \mathbf{c}, t) d^3 \mathbf{x} d^3 \mathbf{c}$ represents the probability of finding a particle in the volume $d^3 \mathbf{x}$ around \mathbf{x} and with velocity between \mathbf{c} and $\mathbf{c} + d\mathbf{c}$.

The collision term Q in (2.2) describes the effect of the binary collisions between particles on the single particle distribution function. The hydrodynamic fields are the first few moments of the distribution function $f(\mathbf{x}, \mathbf{c}, t)$. In particular, the mass, momentum and the energy are first few moments of the distribution function which for a fluid in D dimensions are given by [64, 65]:

$$\int d\mathbf{c} \{1, \mathbf{c}, \mathbf{c}^2\} f(\mathbf{x}, \mathbf{c}, t) = \{\rho, \rho \mathbf{u}, \rho(u^2 + D\kappa_B T/m)\}. \quad (2.3)$$

where the macroscopic quantities of fluid are given by ρ (fluid density), u (fluid velocity) and T (temperature). In (2.3) m is the particle mass and κ_B is the Boltzmann constant.

One of the major difficulties in dealing with the Boltzmann equation is the complicated nature of the collision integral. Therefore, an important simplification of collision term was proposed by Bhatnagar, Gross and Krook [66] which is known as the BGK approximation. The BGK collision operator is given by [66]:

$$Q_{\text{BGK}} = -\frac{1}{\tau} (f - f^{\text{M}}(\mathbf{c}, \rho, u, T)). \quad (2.4)$$

where f^M is known as equilibrium Maxwellian-Boltzmann distribution function and parametrized by values of locally conserved variable, density $\rho(f(\mathbf{x}, t))$, velocity $\mathbf{u}(f(\mathbf{x}, t))$ and temperature $T(f(\mathbf{x}, t))$ as

$$f^M(\mathbf{c}, \rho, \mathbf{u}, T) = n \left(\frac{2\pi\kappa_B T}{m} \right)^{-D/2} \exp \left(-\frac{m(\mathbf{c} - \mathbf{u})^2}{2\kappa_B T} \right) \quad (2.5)$$

where $n = \rho/m$ is the number density.

The time parameter $\tau > 0$ in Eq. (2.4) is interpreted as a characteristic relaxation time to the local Maxwellian [67].

2.2 Lattice Boltzmann equation

In order to solve the distribution function $f(\mathbf{x}, \mathbf{c}, t)$ numerically, the Eq. (2.1) is first discretized in the momentum space using a finite set of velocities (\mathbf{c}_i) without violating the conservation laws. The discrete Boltzmann equation for a single-component fluid with BGK collision operator reads [66]

$$\partial_t f_i + \mathbf{c}_i \cdot \nabla_{\mathbf{x}} f_i = -\frac{1}{\tau} (f_i - f_i^{\text{eq}}) \quad (2.6)$$

where $f_i(\mathbf{x}, t) \equiv f_i(\mathbf{x}, \mathbf{c}_i, t)$ and $f_i^{\text{eq}}(\rho, \mathbf{u}) \equiv f_i^M(\mathbf{c}_i, \rho, \mathbf{u}, T)$ are the distribution function and the equilibrium distribution function of the i th discrete velocity \mathbf{c}_i , respectively.

In the Eq. (2.6), the non-polynomial equilibria of the lattice gas were replaced by low-order polynomial approximations. These polynomials were tailored to get the desired dynamics of N-S equations [39]. (for the case of isothermal flows under consideration in this work, the equilibrium populations, f_i^{eq} , are just function of ρ and \mathbf{u}).

Equation (2.6) can be further discretized in physical space, \mathbf{x} , and time, t . Therefore the discrete lattice Boltzmann equation with the BGK approximation known as the LBGK model, can be set up as:

$$f_i(\mathbf{x} + \mathbf{c}_i, t + 1) - f_i(\mathbf{x}, t) = -\frac{1}{\tau} (f_i(\mathbf{x}, t) - f_i^{\text{eq}}(\rho, \mathbf{u})), \quad (2.7)$$

where τ is related to the kinematic viscosity (ν) of the fluid as $\nu = (\tau - \frac{1}{2})c_s^2\delta t$. The c_s is speed of sound for the model and δt is the lattice time step. The

algorithm to solve Eq. (2.7) numerically is split into the following two steps:

$$\begin{aligned} \text{Collision step: } f_i^t(\mathbf{x}, t + \delta t) &= f_i(\mathbf{x}, t) + \frac{1}{\tau}(f_i^{eq}(\rho, \mathbf{u}) - f_i(\mathbf{x}, t)) \\ \text{Streaming step: } f_i(\mathbf{x} + \mathbf{c}_i\delta t, t + \delta t) &= f_i^t(\mathbf{x}, t + \delta t) \end{aligned} \quad (2.8)$$

where f_i and f_i^t denote the pre- and post-collision state of the distribution function, respectively. From Eq. (2.8), one can see two primary advantages for LBGK equation. The first advantage is the possibility of exact discretization of the streaming step of the populations; this can be achieved by choosing a uniform grid spacing of $\delta x = c_i\delta t$ thus replacing the advection step with a simply copy paste operation. The second advantage is the collision step which is purely local. Therefore, the Eq. (2.8) is explicit, easy to implement, and straightforward for parallel computation.

2.3 Entropic Lattice Boltzmann equation

The most restrictive drawback of original LBGK model is numerical instability. This problem was reduced by restoring the second law of thermodynamics (Boltzmann's H theorem) using the recent theoretical development of the entropic lattice Boltzmann method [40–43]. Since the principles of construction of the entropic scheme were discussed in detail in the Ref. [68], we here present only the resulting scheme.

In the entropic construction, the equilibrium populations, f_i^{eq} , are constructed by minimizing the entropy function H ,

$$H = \sum_i f_i \ln \left(\frac{f_i}{W_i} \right), \quad (2.9)$$

with appropriately chosen weights $W_i > 0$, under the following constraints of local conservation laws of mass and momentum for isothermal flows.

$$\begin{aligned} \sum_i^N f_i^{eq} &= \rho, \\ \sum_i^N \mathbf{c}_i f_i^{eq} &= \rho \mathbf{u}. \end{aligned} \quad (2.10)$$

Where N stands for the number of lattice velocities. Once the equilibrium distributions are known, a LBGK scheme (Eq. (2.7)) can be set up. This simple construction ensures thermodynamic consistency and stability. Fur-

ther enhancement of stability can be achieved by employing the entropic time-stepping instead of the standard LB time steps [40–43].

The solution to this minimization problem can be written in the following product form:

$$f_i^{eq} = W_i \lambda \xi_x^{c_{ix}} \xi_y^{c_{iy}} \xi_z^{c_{iz}} \quad (2.11)$$

where Lagrange multipliers corresponding to mass $\lambda(\rho, u)$ and momentum $\xi_\alpha(\rho, u)$ are found upon substituting Eq. (2.11) into the conserved mass and momentum constraints. (for a detailed discussion on the derivation of weights and Lagrange multipliers reader is directed to [43, 61]).

For the 27-velocity lattice used for the three-dimensional simulations in this work, the result reads,

$$W_i = \begin{cases} 8/27 & i = 0; \\ 2/27 & i = 1, 2, \dots, 6; \\ 1/54 & i = 7, 8, \dots, 18; \\ 1/216 & i = 19, 20, \dots, 26. \end{cases} \quad (2.12)$$

$$c_i = \begin{cases} (0, 0, 0) & i = 0; \\ (\pm 1, 0, 0), (0, \pm 1, 0), (0, 0, \pm 1) & i = 1, 2, \dots, 6; \\ (\pm 1, \pm 1, 0), (\pm 1, 0, \pm 1), (0, \pm 1, \pm 1) & i = 7, 8, \dots, 18; \\ (\pm 1, \pm 1, \pm 1) & i = 19, 20, \dots, 26. \end{cases} \quad (2.13)$$

and the equilibrium populations f_i^{eq} are evaluated to order u^3 as an approximation to the entropy solution (2.11), written here in the standard form as:

$$f_i^{eq} = \rho W_i \left(1 + \frac{c_{i\alpha} u_\alpha}{c_s^2} + \frac{u_\alpha u_\beta}{2c_s^4} (c_{i\alpha} c_{i\beta} - c_s^2 \delta_{\alpha\beta}) + \frac{u_\alpha u_\beta u_\gamma}{6c_s^6} c_{i\gamma} (c_{i\alpha} c_{i\beta} - 3c_s^2 \delta_{\alpha\beta}) \right), \quad (2.14)$$

where $c_s^2 = 1/3$ is the speed of sound for this lattice. Once the equilibrium is know, the entropic Lattice Boltzmann scheme is written for discrete populations, $f_i(\mathbf{x}, t)$, as [68]:

$$f_i(\mathbf{x} + \mathbf{c}_i, t + 1) - f_i(\mathbf{x}, t) = \alpha\beta (f_i^{eq}(\rho, \mathbf{u}) - f_i(\mathbf{x}, t)), \quad (2.15)$$

where parameter $0 < \beta < 1$ is fixed by the kinematic viscosity through $\beta = \frac{\delta t}{2\nu/c_s^2 + \delta t}$ and α is a scalar function of the population vector. Function α ensures the discrete-time H-theorem, and is the nontrivial root of the nonlinear equation,

$$H(f + \alpha(f^{\text{eq}} - f)) = H(f). \quad (2.16)$$

It is evident from Eq. (2.16) that the entropy in the so-called mirror state, $f + \alpha(f^{\text{eq}} - f)$, is equal to the entropy in the initial state, f . Thus, α determines the maximally possible change of populations in the relaxation step with $\beta > 0$ being responsible for the production of entropy. The combination $\alpha\beta$ is the effective relaxation parameter in the fully discrete kinetic picture.

Since the total entropy, $H_{\text{tot}} = \sum_x H(x)$, is a non-increasing function due to Eq. (2.15), the entropy estimate (2.16) ensures the nonlinear stability of the scheme (2.15). When the populations tend to the local equilibrium (resolved simulations), then the solution of (2.16) converges to equilibrium value $\alpha^{\text{eq}} = 2$. If the value $\alpha = \alpha^{\text{eq}}$ is used in (2.15), then the standard LBM (Eq. (2.7)) is recovered. Therefore Eq. (2.16) is required in order to stabilize the scheme (2.15) if the relaxation parameters β is close to 1 (that is for small values of the kinematic viscosity).

2.4 Two-phase fluids

In this section we intend to give a concise introduction into area of fluids undergoing phase transitions which is the subject of this research. Here, we aim to derive the pressure tensor for a liquid-vapor system using fundamental thermodynamics.

2.4.1 Thermodynamics

2.4.1.1 Equilibrium in the multi-component and multi-phase system

We start with thermodynamics of multi-component multi-phase systems. Components: chemically specified pure substances such as pure water H_2O . Phases: Physically different aggregated states, typically gas, liquid or solid. Let us first consider thermodynamic coexistence of different phases of a generic multi-component system without taking into account the physics of the interface which may arise between them.

2.4.1.2 Gibbs free energy

The general condition of equilibrium was formulated by Gibbs on the basis of the Gibbs free energy potential,

$$G(T, p, N_i) = \mathcal{H} - TS, \quad (2.17)$$

Here $\mathcal{H} = U + pV$ (U , p and V denote internal energy, pressure and volume of the system, respectively) is the enthalpy. The differential of G reads

$$dG = -SdT + Vdp + \sum_i \mu_i dN_i, \quad (2.18)$$

where summation is over all components and phases in the system. In (2.18) $\mu_i = (\partial G / \partial N_i)_{T,p,\hat{N}_i}$ is the chemical potential of the i th phase/component, and notation \hat{N}_i means "all of them except for the i th". Note that in this formulation one does not make a distinction between the components and phases.

Gibbs potential depends only on the extensive variables N_i which is the number of moles in each phase of each component. This is the main advantage of using the Gibbs potential for studying the equilibrium in complex systems. This means G is a homogeneous order one function of N_i :

$$G(T, p, qN_1, qN_2, \dots) = qG(T, p, N_1, N_2, \dots), \quad (2.19)$$

upon differentiation in q and setting $q = 1$, we get

$$\sum_i N_i \left(\frac{\partial G}{\partial N_i} \right)_{T,p,\hat{N}_i} = G. \quad (2.20)$$

hence, $G = \sum_i N_i \mu_i(T, p)$. Combining this with Eq. (2.18), we arrive to *Gibbs-Duhem equation*:

$$SdT - Vdp + \sum_i N_i d\mu_i = 0. \quad (2.21)$$

Equation (2.21) implies the following equilibrium condition:

- *Temperature* is homogeneous through all phases and all components.
- *Pressure* is homogeneous through all phases and all components.
- *Chemical potential* is homogeneous through all phases and all components.

In following, using the above equilibrium conditions and by help of a given Gibbs' free energy function, the pressure tensor for a system of liquid and vapour will be derived.

2.4.2 Equilibrium in the presence of the interface

The thermodynamic potential (Gibbs' free energy) of the liquid-vapour system was suggested by van der Waals in the following form [69, 70]:

$$\mathcal{F} = \int_V \left[\Psi(\rho, T) + \frac{\kappa}{2} \nabla \rho \cdot \nabla \rho \right] dV, \quad (2.22)$$

where the bulk free energy density is given by the local function Ψ and the non-local part $\sim |\nabla \rho|^2$, represents the energy stored in the interface. Parameter κ is the surface tension coefficient. The suggestion of adding the interface energy in this way is certainly the simplest assumption of a dependence on the gradient of density.

The equilibrium now is defined as the minimum of free energy subject to a fixed mass in the system:

$$M = \int_V \rho d\mathbf{x}, \quad (2.23)$$

Now, in order to minimize (2.22) under the constraint (2.23), we have:

$$\delta \int_V \left[\Psi(\rho, T) + \frac{\kappa}{2} \nabla \rho \cdot \nabla \rho - \mu \rho \right] dV = 0, \quad (2.24)$$

where μ is the Lagrange multiplier, corresponding to the mass conservation condition (it is denoted by μ since it will turn out to be the chemical potential). Computing the variation term-by-term, we need to take into account that

$$\delta \int_V \nabla \rho \cdot \nabla \rho = -2 \int_V \delta \rho \nabla \cdot \nabla \rho dV + \text{surface term} \quad (2.25)$$

where the surface term $\int_{\partial V} \delta \rho (\nabla \rho \cdot \mathbf{n}) d\mathbf{n}$ vanishes since the variation of the density $\delta \rho$ vanishes at the boundary ∂V . With this, the variational principle reads:

$$\int_V \delta \rho \left[\frac{\partial \Psi}{\partial \rho} - \kappa \nabla \cdot \nabla \rho - \mu \right] dV = 0, \quad (2.26)$$

Since this is to hold for any variation $\delta \rho$, we get the equilibrium condition as follows:

$$\frac{\partial \Psi}{\partial \rho} - \kappa \nabla \cdot \nabla \rho - \mu = 0. \quad (2.27)$$

This the general condition for the equilibrium for a two-phase fluid in the presence of an interface. It is valid for any interface. Let us consider specific cases (flat interface) to get a feeling about it.

2.4.2.1 Gibbs equilibrium conditions for the flat interface

Assuming the density depends only on spacial dimension z , $\rho = \rho(z)$, and that the liquid/vapor phases densities $\rho = \rho_{l,v}$ are attained smoothly at $z \rightarrow \pm\infty$, using the general equilibrium condition (2.27), the equilibrium in the presence of a flat interface is defined by:

$$\frac{\partial\Psi}{\partial\rho} - \kappa \frac{d^2\rho}{dz^2} = \mu, \quad (2.28)$$

As the gradient of density vanishes at infinity for both phases ($\rho(-\infty) = \rho_v, \rho(+\infty) = \rho_l$), we have:

$$\left[\frac{\partial\Psi}{\partial\rho} \right]_{\rho_l} = \left[\frac{\partial\Psi}{\partial\rho} \right]_{\rho_v} (= \mu) \quad (2.29)$$

Thus, we derived one of the Gibbs equilibrium conditions: The chemical potentials, of both phases are equal:

$$\mu_l = \left[\frac{\partial\Psi}{\partial\rho} \right]_{\rho_l} = \left[\frac{\partial\Psi}{\partial\rho} \right]_{\rho_v} = \mu_v \quad (2.30)$$

By multiplying Eq. (2.28) with $d\rho/dz$, we get:

$$\frac{d}{dz} \left[\Psi - \mu\rho - \frac{\kappa}{2} \left(\frac{d\rho}{dz} \right)^2 \right] = 0, \quad (2.31)$$

Or

$$P = -\Psi + \mu\rho + \frac{\kappa}{2} \left(\frac{d\rho}{dz} \right)^2 = \text{constant} \quad (2.32)$$

Considering this expression at $\pm\infty$ and taking into account that the density gradient vanishes as $z \rightarrow \pm\infty$, we get with the help of chemical potential equality (2.28):

$$\left[\rho \frac{\partial\Psi}{\partial\rho} - \Psi \right]_{\rho_l} = \left[\rho \frac{\partial\Psi}{\partial\rho} - \Psi \right]_{\rho_v}, \quad (2.33)$$

This enables us to identify the pressure p (or *equation of state (EoS)*),

$$p = \rho \frac{\partial\Psi}{\partial\rho} - \Psi, \quad (2.34)$$

and the result (2.33) is nothing more than the Gibbs equilibrium condition for the pressure,

$$p_l = p_v, \quad (2.35)$$

Bear in mind, to derive the equilibrium conditions 2.30 and 2.33, the energy function (2.22) was minimized by assuming that the temperature is constant which is the remaining Gibbs equilibrium condition.

2.4.3 Korteweg's stress

With the equations derived above, now we are in a position to derive the Korteweg's stress or pressure tensor for a liquid-vapor system.

Combining (2.32) with (2.28) and (2.34) we get a closed-form equation for the stress (or total pressure, since it includes both the thermodynamic pressure and the effect of the flat interface):

$$P = P_{zz} = p - \kappa\rho\frac{d^2\rho}{dz^2} + \frac{\kappa}{2}\left(\frac{d\rho}{dz}\right)^2 \quad (2.36)$$

This is the zz component of *Korteweg's stress*.

Generalization to three dimensions of the pressure tensor \mathbf{P} for a liquid-vapor system was found by Korteweg known as *Korteweg's stress* which is defined by [70, 71]:

$$\mathbf{P} = \left(p - \kappa\rho\nabla^2\rho - \frac{\kappa}{2}|\nabla\rho|^2\right)\mathbf{I} + \kappa(\nabla\rho) \otimes (\nabla\rho), \quad (2.37)$$

where p is the equation of state (Eq. (2.34)).

2.5 ELBM for non-ideal fluids

So far, we studied the entropic lattice Boltzmann equations for single phase, Eq. (2.15), and we also derived the Korteweg's stress, Eq. (2.37), required for two-phase fluids. Now, in this section, we shall introduce the way to incorporate the Korteweg's stress into lattice Boltzmann equation. Since the Korteweg's stress was derived from free energy function, incorporating the Korteweg's stress into LB is termed free-energy approach.

In general, free energy approaches introduces the non-ideal interactions into LB either through a pressure term [23] (pressure approach) or a forcing term [55] (forcing approach). In the pressure approach proposed by Swift et al. [23], the equilibrium distributions f_i^{eq} are constructed based on three constraints. The first two, are the local mass and momentum conservation,

$\{\rho, \rho \mathbf{u}\} = \sum_i^N \{1, \mathbf{c}_i\} \{f_i^{\text{eq}}\}$, and the third one is the pressure tensor as the second momentum of the equilibrium populations, must be satisfied as follows:

$$\sum_i^N \mathbf{c}_i \mathbf{c}_i f_i^{\text{eq}} = \mathbf{P} + \rho \mathbf{u} \mathbf{u}. \quad (2.38)$$

where \mathbf{P} is the Korteweg's stress defined in Eq. (2.37). (see [23] and [72] for more details on derivation of the equilibrium populations for this approach). Although the original free energy model proposed by Swift et al. was thermodynamically consistent, the model severely suffered from problem of Galilean non-invariance and more importantly it could not be used for simulation of dynamical effects of two-phase problems with large liquid-vapor density ratio due to numerical instability. Therefore, as a first contribution of this research, we aim to propose a free-energy based model that is capable of modeling realistic dynamical problems with relatively large density and viscosity ratio between phases. To this end, we apply the entropic scheme for both pressure and forcing free-energy approaches. We will show that the forcing approach augmented by entropic technique allows us to simulate both stationary and non-stationary problems at simultaneously large liquid-vapor density ratio and low kinematic viscosity while the pressure approaches still can not be usable for simulating dynamical two-phase problems with relatively large density ratio.

2.5.1 An entropic pressure free energy approach

So far we learned that the implementation of the free energy model in the LB equation needs to satisfy the pressure tensor (2.38). The entropy function (2.9) proposed by Karlin et al. [73] was derived for a single phase system where the pressure tensor is defined by $\sum_i^N \mathbf{c}_i \mathbf{c}_i f_i^{\text{eq}} = \rho c_s^2 \mathbf{I} + \rho \mathbf{u} \mathbf{u}$. Therefore, due to difference of pressure tensor between single and two-phase flows, one should begin to construct an appropriate entropy function for a system of liquid and vapor. In [73], due to simplicity of the pressure tensor for a single phase system, the construction of the entropy function H was relatively straightforward. In following we will show that for a two phase fluid, to find the entropy function, some assumptions have to be taken to make the form of the pressure tensor simpler. Now with the help of [73], we begin with derivation of the entropy function for two-phase fluid.

As it was already mentioned, in the entropic scheme, the equilibrium populations are defined based on minimizing a entropy function H under local

mass and momentum conservations. Therefore it reads:

$$H \rightarrow \min, \quad \sum_i^N f_i = \rho, \quad \sum_i^N \mathbf{c}_i f_i = \rho \mathbf{u}. \quad (2.39)$$

where the entropy function H for one dimension with three velocities $\{-c, 0, c\}$ ($c = \delta x / \delta t = 1$), is defined by $H = h_0(f_0) + h_1(f_-) + h_1(f_+)$.

By minimizing H under constraints in (2.39), we have:

$$\begin{aligned} \frac{dh_0}{dz} \Big|_{f_0^{eq}} &= \chi, \\ \frac{dh_0}{dz} \Big|_{f_-^{eq}} &= \chi - \lambda c, \\ \frac{dh_0}{dz} \Big|_{f_+^{eq}} &= \chi + \lambda c, \end{aligned} \quad (2.40)$$

where χ and λ are the Lagrange multipliers corresponding to the density and the momentum constraints, respectively. If we define $\mu_0(z)$ and $\mu_1(z)$ as the inverse of the derivatives ($\mu_0(z) = [dh_0/dz]^{-1}$ and $\mu_1(z) = [dh_1/dz]^{-1}$), we obtain:

$$\begin{aligned} f_0^{eq} &= \mu_0(\chi), \\ f_-^{eq} &= \mu_1(\chi - \lambda c), \\ f_+^{eq} &= \mu_1(\chi + \lambda c), \end{aligned} \quad (2.41)$$

The Lagrange multipliers χ and λ are related to ρ and u upon substitution of the equilibria (2.41) into the constraints in (2.39). This gives:

$$\begin{aligned} \mu_0(\chi) + \mu_1(\chi + \lambda c) + \mu_1(\chi - \lambda c) &= \rho, \\ c\mu_1(\chi + \lambda c) - c\mu_1(\chi - \lambda c) &= \rho u. \end{aligned} \quad (2.42)$$

then the condition for the pressure at the equilibrium (2.38) reads:

$$c^2 \mu_1(\chi + \lambda c) + c^2 \mu_1(\chi - \lambda c) - (\rho u^2 + P(\rho)) = 0. \quad (2.43)$$

Since we are deriving the entropy function in one dimension the $P(\rho)$ in (2.43) is defined by (2.36) as the zz component of the Korteweg's stress.

Equation (2.43) is the central part in the construction of the entropy function. However, by looking at the equation for $P(\rho) = p - \kappa \rho d^2 \rho / dz^2 + \kappa (d\rho/dz)^2 / 2$ in (2.36), it seems to be extremely difficult to continue the solution for finding μ_0 and μ_1 due to the highly non-linear nature of the equation of state used (compared to the second order non-linearity intro-

duced by u^2 term for the ideal gas). Therefore, to make the equation (2.43) solvable, an assumption is made. To this end, we first write the pressure in a way that it is neatly separated into two parts, the ideal gas contribution and the non-ideal contribution:

$$P_{\alpha\beta} = \rho c_s^2 \delta_{\alpha\beta} + K_{\alpha\beta}. \quad (2.44)$$

where $K_{\alpha\beta}$ is the non-ideal part of the Kortewg's pressure tensor (2.37). Therefore we substitute the $P(\rho)$ in (2.43) by $\rho c_s^2 + K_{zz}$ where $K_{zz} = p - \rho c_s^2 - \kappa \rho d^2 \rho / dz^2 + \kappa (d\rho/dz)^2 / 2$. Then we assume that the K_{zz} or the non-ideal part of the pressure behaves as a constant parameter during the solution of (2.43), although it is function of density. This assumption is however mathematically untrue but serves as an approximation and allows us to proceed with the solution to find an entropy function.

We shall now solve Eq. (2.43) by substituting ρ and u in terms of (2.42) together with using a Taylor series expansion to order λ^2 around $\lambda = 0$ (see Ref. [73] for more details on derivation of μ_0 and μ_1 for single phase flows). After some algebra and considering that $c_s = c/\sqrt{3}$ we have:

$$\begin{aligned} \mu_1(\chi) &= e^{\chi-1} + K_{zz}/2, \\ \mu_0(\chi) &= 4e^{\chi-1} - K_{zz}. \end{aligned} \quad (2.45)$$

By inverting and then integrating from the equations for μ_0 and μ_1 , one can find the function h_0 and h_1 as below:

$$\begin{aligned} h_1(\chi) &= (\chi - K_{zz}/2) \ln(\chi - K_{zz}/2), \\ h_0(\chi) &= (\chi + K_{zz}) \ln\left(\frac{\chi + K_{zz}}{4}\right), \end{aligned} \quad (2.46)$$

Now, the entropy function for two-phase flows in one dimension can be written as:

$$\begin{aligned} H &= (f_0 + K_{zz}) \ln\left(\frac{f_0 + K_{zz}}{4}\right) + \\ & (f_+ - K_{zz}/2) \ln(f_+ - K_{zz}/2) + (f_- - K_{zz}/2) \ln(f_- - K_{zz}/2), \end{aligned} \quad (2.47)$$

Finally the equilibrium populations corresponding the entropy function (2.47) can be easily found by expanding the Lagrange multipliers χ and λ into a series in the power of u (see Ref. [73] for more details). The result

of this expansion up to u^2 reads as following:

$$\begin{aligned}
 f_0^{eq} &= \frac{2\rho}{3} \left(1 - \frac{u^2}{2c_s^2} \right) - K_{zz}, \\
 f_-^{eq} &= \frac{\rho}{6} \left(1 + \frac{u^2}{c_s^2} - \frac{uc}{c_s^2} \right) + \frac{K_{zz}}{2}, \\
 f_+^{eq} &= \frac{\rho}{6} \left(1 + \frac{u^2}{c_s^2} + \frac{uc}{c_s^2} \right) + \frac{K_{zz}}{2}.
 \end{aligned} \tag{2.48}$$

Using the equilibrium derived in (2.48), the zeroth, first and second moments are:

$$\begin{aligned}
 \sum_i^3 f_i^{eq} &= \rho, \\
 \sum_i^3 c_i f_i^{eq} &= \rho u, \\
 \sum_i^3 c_i c_i f_i^{eq} &= p - \kappa \rho \frac{d^2 \rho}{dz^2} + \frac{\kappa}{2} \left(\frac{d\rho}{dz} \right)^2 + \rho u^2.
 \end{aligned} \tag{2.49}$$

By looking at the result in (2.48), we recognize that we can write the equilibrium in a general way that neatly separates the ideal-gas contribution from the non-ideal contributions. Therefore, the application of the presented approach can be easily extended to two and three dimensions. From simulations, we observed that by introducing the entropic function (2.47) in the pressure based free energy model, lower kinematic viscosities ($\nu \sim 10^{-6}$) than those reported by Swift et al. [23] ($\nu \sim 10^{-2}$) can be achieved. However, the applicability of this approach was still limited to simulation of stationary or quasi-dynamical problems with low density ratio. We speculated that one possible way to improve this approach might be the use of multi-speed lattices proposed in [74].

It was shown by Ref. [74] that lattices with larger number of velocities than the standard lattices (the three-velocity lattice and its counterparts in higher dimensions) can overcome the problem of Galilean non-invariance of standard lattices and improve the numerical stability of the method. Hence, to enhance the numerical stability, we implemented the pressure approach on the higher order lattices. We used 5 velocity lattices $\{-3c, -c, 0, c, 3c\}$ in one dimension and 25 velocity lattices in two spatial dimensions (see [74] for detailed discussion on how to construct stable lattices in lattice Boltzmann method). Our simulations showed that using higher order lattices, we

can achieve a maximum liquid-vapor density ratio around 50 which is much larger than what was obtained by Swift et al. ($\rho_l/\rho_v \sim 4$). However, due to numerical instabilities, we could not still use this approach to simulate dynamic problems such as collision of liquid drops or drops impinging on solid substrates. Therefore, we shall continue to develop and test another free-energy model in following.

In the next section, we will develop a free-energy approach by introducing a forcing term in the entropic lattice Boltzmann equation which corresponds to the Korteweg's stress. Since it was shown in [55] that the problem of Galilean non-invariance of the original free energy model for standard lattices can be overcome by introducing forcing terms into the kinetic equation, thus we will use the standard lattices for the following forcing scheme. We will demonstrate that the forcing approach augmented with the entropic scheme remarkably improves the performance of the free-energy model and hence can be considered as a promising tool for simulation of both stationary and non-stationary two-phase flow problems with large liquid-vapor density ratio and low kinematic viscosity. The reliability and applicability of this approach will be shown by simulating a large number of experimental and theoretical findings.

2.5.2 An entropic forcing free energy approach

The entropic lattice Boltzmann equation, augmented with a forcing term [75, 76], can be written

$$f_i(\mathbf{x} + \mathbf{c}_i, t + 1) = f_i(\mathbf{x}, t) + \alpha\beta [f_i^{\text{eq}}(\rho, \mathbf{u}) - f_i(\mathbf{x}, t)] + [f_i^{\text{eq}}(\rho, \mathbf{u} + \delta\mathbf{u}) - f_i^{\text{eq}}(\rho, \mathbf{u})], \quad (2.50)$$

where the equilibrium populations f_i^{eq} are given by (2.14). The last term on the right hand side of Eq. (2.50) is a specific realization of the forcing, the so-called exact difference method [77]. It maintains that, the local flow velocity is altered by an amount,

$$\delta\mathbf{u} = \left(\frac{\mathbf{F}}{\rho} \right) \delta t, \quad (2.51)$$

where $\delta t = 1$ is the lattice time step, and \mathbf{F} is the force. The force used in the present model is composed of three contributions,

$$\mathbf{F} = \mathbf{F}_f + \mathbf{F}_s + \mathbf{F}_g, \quad (2.52)$$

which correspond to the implementation of Korteweg's stresses for a two-phase fluid, the fluid-solid interaction and gravity, respectively.

The force \mathbf{F}_f , related to Korteweg's stress is defined in [55] as:

$$\mathbf{F}_f = \nabla \cdot (\rho c_s^2 \mathbf{I} - \mathbf{P}). \quad (2.53)$$

where \mathbf{P} is the pressure tensor given by Eq. (2.37). To complete the computations for fluid-fluid forces, we shall specify the EoS p in (2.37) in the next section. The fluid-solid forces as well as the application of forcing for computing the over relaxation parameter α in Eq. (2.16) will be described in sec. 2.5.2.2 and sec. 2.5.2.3, respectively. The derivation of Navier-Stokes equations for two-phase flows using Chapman-Enskog expansion of the LBM is also given in Appendix A.

2.5.2.1 Equation of state

As always, a concrete realization of the general thermodynamic rules requires an input for a thermodynamic potential dependence on temperature, pressure and composition. Often this is done in a form of an equation of state which describes a dependence of pressure on temperature and density. The familiar ideal gas equation of state, $p = \rho RT$, prohibits any phase change. The first equation of state which was able to describe the coexistence of phases was given by van der Waals (vdW) [69]. But, the vdW EoS is not suitable for a vapor-liquid system with temperatures much lower than the critical one or higher density ratio of liquid to vapor [78]. However, by replacing the vdW EoS with a more realistic modified forms such as the Peng-Robinson (P-R) EoS [78], one can get a much better performance in terms of a wider temperature range or higher density ratios.

Here in this dissertation, we use a polynomial equation of state so chosen as to match the P-R equation of state [78]. Polynomial equation of states have long been used in the literature as an alternative to the realistic equation of states which are a fit of the experimental data in different regimes. We begin with the P-R EoS, as given by Yuan and Schaefer [78]:

$$p_{\text{PR}}(\rho, T) = \frac{\rho R_G T}{1 - b_{\text{PR}} \rho} - \frac{a_{\text{PR}} \Lambda(T) \rho^2}{1 + 2b_{\text{PR}} \rho - b_{\text{PR}}^2 \rho^2}, \quad (2.54)$$

$$\Lambda = \left[1 + (0.37464 + 1.54226\omega - 0.26992\omega^2) \left(1 - \sqrt{\frac{T}{T_c}} \right) \right]^2,$$

with $a_{\text{PR}} = 2/49$, $b_{\text{PR}} = 2/21$, $R_G = 1$, and with the acentric factor $\omega = 0.344$ corresponding to water (see [78]). The choice of the parame-

ters corresponds to the critical temperature $T_c = 0.0729$.

Next, a different EoS is constructed as a polynomial in both density and temperature, in a form

$$p(\rho, T) = \rho R_G T (1 + b\rho\lambda(\rho, T)) - a\rho^2, \quad (2.55)$$

with $a = 9/49$, $b = 2/21$ (the van der Waals parametrization [78]) and $R_G = 1$. Furthermore, function λ can be interpreted as a collision probability [54] considered here as a polynomial in density,

$$\lambda = \sum_{k=0}^4 A_k(T) \rho^k, \quad (2.56)$$

and where, in turn, functions A_k are polynomials of the temperature,

$$A_k(T) = \sum_{n=0}^m a_{kn} T^n. \quad (2.57)$$

The $5 \times (m+1)$ numerical coefficients a_{kn} in (2.57) are defined from matching the values of the function (2.55) with the original Peng-Robinson equation of state (2.54),

$$p(\rho_r, T_s) = p_{\text{PR}}(\rho_r, T_s), \quad r = 0, \dots, 4, \quad s = 0, \dots, m; \quad (2.58)$$

where the density and the temperature values are chosen as follows:

- (i) For each selected T_s , the fourth-order polynomial $p(\rho, T_s)$ matches the isotherm $p_{\text{PR}}(\rho, T_s)$ at the minimum, at the maximum, at the saturated vapor, at the saturated liquid and at the intercept (the latter three points are the Maxwell equal area rule);
- (ii) The $(m+1)$ values of the temperature for this matching procedure (in other words, $(m+1)$ Peng-Robinson isotherms) are selected uniformly in the sub-critical regime, between the lowest value $T_0 = 0.04486$ and the highest value $T_m = 0.07042$.

It was found that with $m = 6$, the polynomial equation of state reproduces well the non-polynomial Peng-Robinson EoS in the domain of interest. Numerical values of the coefficients in these polynomials are given in table 2.1.

A comment on the above construction of the EoS (2.55) is in order. The polynomial approximation just described can be developed, in principle, for any equation of state available. We choose the Peng-Robinson EoS as

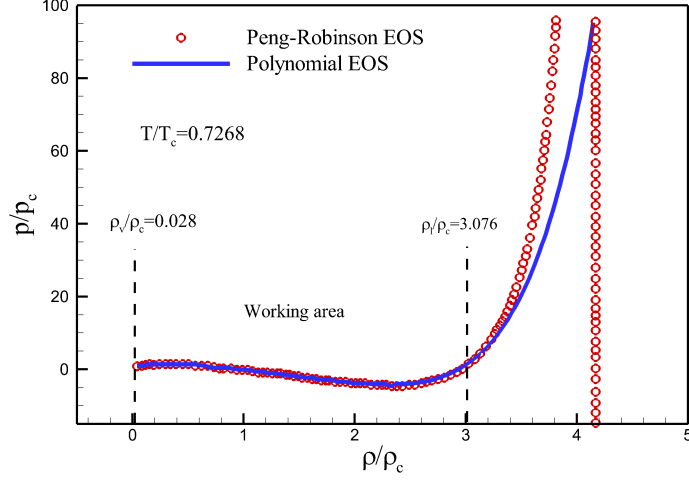


Figure 2.1: The Polynomial (2.55) together with P-R (2.54) equation of state at $T/T_c = 0.7268$.

the input based on its known behavior for static cases [78]. However, the use of the polynomial approximation (2.55) instead of the original Peng-Robinson EoS is motivated by the absence of the singularity in the former. Figure 2.1 shows the polynomial together with P-R equations of state at $T/T_c = 0.7268$. It is seen from Fig. 2.1 that the polynomial and P-R EoS quite match in the range of ρ_v to ρ_l where ρ_v and ρ_l denote the equilibrium densities for liquid and vapor at $T/T_c = 0.7268$, respectively. However, for $\rho > \rho_l$ one can observe the advantage of using a polynomial rather than P-R EoS where the singularity of P-R EoS is eliminated using a polynomial regularization (The pressure remains finite and bounded even beyond the expected operating range).

From simulation of dynamic problems we observed that at some grid nodes it might happen that the computed liquid density approaches to value of singularity for P-R EoS. This occurs due the large values of velocity used which in turn reduced the time available for local pressure disturbances to dissipate. Therefore, by using the polynomial approximation (2.55), we resolved the singularity effects and hence the performance of free energy model in the ELBM setting was improved.

Table 2.1: The coefficients of the polynomial equation of state (2.55).

	A_0	A_1	A_2	A_3	A_4
a_{k0}	120811.58062178911000	-41348.92106377667400	103.6421707699377800	1825.2900101023780000	-180.9789337103330200
a_{k1}	-1.28983504111013340e7	4.42028277123704500e6	-14852.94006017658600	-193820.0904693506300	19226.34150787452700
a_{k2}	5.711912437199099000e8	-1.95947497644443870e8	867999.9204358715000	8.52192304466139500e6	-846003.380887427000
a_{k3}	-1.3426306780291710e10	4.611426936652080250e9	-2.6333326170904934e7	-1.98617881076862930e8	1.9738934450242322e7
a_{k4}	1.76685641376518950e11	-6.0767263570484184e10	4.3726724839498100e8	2.58831868909180600e9	-2.5758986251227623e8
a_{k5}	-1.2343025552457056e12	4.25210519822928300e11	-3.7727025328579288e9	-1.7884218754949093e10	1.7828758087451546e9
a_{k6}	3.57632483911973800e12	-1.2343626081442510e12	1.3234354794274744e10	5.1195639567034300e10	-5.1139394135857930e9

2.5.2.2 Fluid-solid adhesion

Interaction between the fluid and the solid surface is introduced into the present model following [79, 80], with the help of a force \mathbf{F}_s :

$$\mathbf{F}_s(\mathbf{x}, t) = \kappa_w \rho(\mathbf{x}, t) \sum_i w_i s(\mathbf{x} + \mathbf{c}_i \delta t) \mathbf{c}_i, \quad (2.59)$$

where the coefficient κ_w reflects the intensity of the fluid-solid interaction. By adjusting κ_w from negative to positive values, the solid surfaces with different wettability can be modeled from non-wetting to wetting, respectively. In Eq. (2.59), $s(\mathbf{x} + \mathbf{c}_i \delta t)$ is an indicator function that is equal to one for the solid domain nodes, and is equal to zero otherwise. The weights w_i are chosen according to the second-order central difference scheme in three dimensions as proposed by Yuan and Schaefer [78],

$$w_i = \begin{cases} 1/6 & |x_f - x_s| = 1, \\ 1/12 & |x_f - x_s| = \sqrt{2}, \\ 0 & \text{otherwise.} \end{cases} \quad (2.60)$$

Finally, constant body forces such as gravity can be expressed as:

$$\mathbf{F}_g = \rho \mathbf{g}, \quad (2.61)$$

where \mathbf{g} is acceleration due to the body force. In order to compute fluid-solid and fluid-fluid forces, the evaluation of the gradient terms is required. The second-order central difference scheme [78] is used for this purpose (see Appendix B).

2.5.2.3 Application of forcing and computation of the entropy estimate

With all the aforementioned forces specified in the total force (2.52), the lattice Boltzmann model is fully defined. The force terms in (2.50) is first applied after the propagation step, and then the entropic overrelaxation is performed to complete the collision process (2.50). The latter operation amounts to finding the nontrivial root of (2.16).

The non-trivial root of (2.16) is computed at each lattice site at every time step. In the presence of forces, the entropy estimate is done after the force is applied. In order to stress this fact, we rewrite Eq. (2.16) in expanded notation,

$$H(f' + \alpha(f^{\text{eq}}(\rho, \mathbf{u} + \delta \mathbf{u}) - f')) = H(f'), \quad (2.62)$$

where populations f' are collected after the force application,

$$f'_i = f_i + [f_i^{\text{eq}}(\rho, \mathbf{u} + \delta\mathbf{u}) - f_i^{\text{eq}}(\rho, \mathbf{u})]. \quad (2.63)$$

The entropy function H in (2.62) is given by (2.9). In the simulation, we apply the Newton-Raphson method for the evaluation of the root of the equation (2.16) with a convergence criterion of $\approx 10^{-4} - 10^{-5}$. Alternatively one can also use the Boost library TEL8080 as a root solver without computing derivatives. It is important to note that one cannot guarantee the equation (2.16) always has a root since initial and boundary conditions severely affect the populations. Also, it might happen that the maximal allowable α for which the populations remain positive, α_{max} is too small to allow a viable solution to the equation (2.16). In such situations, when $\alpha_{\text{max}} < 2.0$ we are bounded by the positivity constraint and use the solution $0.9\alpha_{\text{max}}$ instead of solving the entropy estimate (2.16). Also, when a viable solution to evaluation of α is not possible with the Newton-Raphson method (due to large local gradients in the solution etc.) we use the LBGK solution, $\alpha = 2$. However, for all the simulations presented here, such situations when the root for equation (2.16) cannot be computed, occurs less than 0.3% of the simulation time (typically, during the transient dynamics at the beginning of the simulation).

Finally, the fluid velocity \mathbf{U} is evaluated by averaging the momentum before and after the collision [55],

$$\mathbf{U} = \mathbf{u} + \frac{\mathbf{F}}{2\rho}\delta t. \quad (2.64)$$

2.6 Wall boundary conditions

In the presence of walls, the distribution functions $f_i(\mathbf{x}, t)$ for $i \in \Omega$, where Ω is the subset of the discrete velocities pointing from the solid into fluid domain, are unknown and must be specified in order to complete the propagation step. To specify these missing populations, the approach of Ref. [81] was adopted. In the first step, the missing populations are replaced by active ones using bounce-back (BB) scheme,

$$f_i^{\text{bb}} = f_{\bar{i}} \quad (2.65)$$

where $\mathbf{c}_{\bar{i}} = -\mathbf{c}_i$. Equation (2.65) guarantees no mass penetration through the wall, and also enables us to find a target value for density and velocity

on the wall boundary nodes,

$$\{\rho_{\text{tgt}}, \rho_{\text{tgt}} \mathbf{u}_{\text{tgt}}\} = \sum_{i \in \Omega} \{1, \mathbf{c}_i\} f_i^{\text{bb}} + \sum_{i \notin \Omega} \{1, \mathbf{c}_i\} f_i. \quad (2.66)$$

It should be noted that in the case of curved and complex wall boundaries, the target velocity \mathbf{u}_{tgt} at the boundary nodes is evaluated by an interpolation scheme involving the wall velocity (zero value) and the velocities at the adjacent fluid nodes [81].

The proper populations which can substitute the missing ones to complete propagation step are written as,

$$f_i \longleftarrow f_i + f_i^{\text{eq}}(\rho_{\text{tgt}}, \mathbf{u}_{\text{tgt}}) - f_i^{\text{eq}}(\rho_{\text{loc}}, \mathbf{u}_{\text{loc}}). \quad (2.67)$$

Here the instantaneous density and velocity, ρ_{loc} and \mathbf{u}_{loc} , are defined by mass and momentum conservation:

$$\{\rho_{\text{loc}}, \rho_{\text{loc}} \mathbf{u}_{\text{loc}}\} = \sum_{i \in \Omega} \{1, \mathbf{c}_i\} f_i^{\text{eq}}(\rho_{\text{tgt}}, \mathbf{u}_{\text{tgt}}) + \sum_{i \notin \Omega} \{1, \mathbf{c}_i\} f_i. \quad (2.68)$$

2.7 Summary and Conclusions

In this chapter, the numerical method used in this work was discussed in details. We proposed novel thermodynamically consistent lattice Boltzmann models augmented by nonlinearly stable entropic scheme for two-phase flow simulations. The first model was constructed by introducing the non-ideal interactions through a pressure term (pressure approach) while the second approach was based on adding a forcing term to the entropic lattice Boltzmann equation. In the forcing scheme, the inter-particle fluid-fluid force was built upon the Korteweg's stress. As it will be shown in next chapters, the combination of the forcing free-energy approach and the entropic lattice Boltzmann method together with the optimal choice of the equation of state, drastically enhances the performance of the free-energy models. The proposed forcing scheme is free of limitations such as thermodynamic consistency, kinematic viscosity, interface thickness, the density ratio and in particular can be used for simulation of wide range of two-phase applications from droplet collision to drop impacting on solid surfaces at simultaneously high Weber number and Reynolds number and liquid-vapor density ratio.

Chapter 3

Binary droplet collisions

In this chapter the dynamic behavior of the collision of two equal-size droplets is investigated. Extensive numerical investigations show that ELBM is capable of accurately capturing the dynamics and complexity of droplet collision. Different types of the collision outcome such as coalescence, reflexive separation and stretching separation are identified. Partition of the parameter plane is compared to the experiments and excellent agreement is observed. Moreover, the evolution of the shape of a stable lamella film is quantitatively compared with experimental results. The end pinching and the capillary-wave instability are shown to be the main mechanisms behind formation of satellite droplets for near head-on and off-center collisions with high impact parameter, respectively. It is shown that the number of satellite drops increases with increasing Weber number, as predicted by experiments. Also, it is demonstrated that the rotational motion due to angular momentum and elongation of the merged droplet play essential roles in formation of satellite droplets in off-center collisions with an intermediate impact parameter.

3.1 Introduction

The dynamics of binary droplet collision has received considerable attention across different fields, from cloud formation in climate theory to engineering applications such as turbine blade cooling, ink-jet printing, spray coating, and spray combustion in diesel internal combustion engines [20, 82]. The droplet collision process is one of the most challenging topics in fluid dynamics because of the complexity of the phenomena involved [83]. Hence, it remains the focus of a number of experimental [1, 2, 82], analytical [84]

and numerical studies [85,86]. However, because of the difficulty to capture small scale configurations of the interface by conventional fluid dynamics means, the study of this type of two phase problems has been mostly limited to either experiments or analytical approaches. Nevertheless numerical simulations provide a great degree of freedom in the choice of initial, boundary conditions as well as provide substantial information on the flow field, stress and fluxes of both the fluid phases. Hence significant attention was given to numerical simulations and understanding of droplet dynamics [85–87]. Here in this chapter, the dynamics of head-on and off-center droplet collisions is investigated in detail using the forcing free-energy model proposed in chapter 2 [88,89]. It is demonstrated that this new entropic LBM model can be applied to simulation of binary droplet collision at large Reynolds and Weber numbers while simultaneously maintaining a large enough liquid-vapor density ratio of over 100. The difficulty in the handling large density ratios is resolved by using the polynomial equation of state (2.55) and adherence to lattice entropy resolves the limitation on attainable grid viscosity in simulations. The advantages on the present scheme over existing simulations of droplet collisions [26, 56, 90, 91] including low grid requirements, computational efficiency, accuracy and thermodynamic consistency are demonstrated in this chapter.

Remarkably, the present model captures the formation of stable lamella film which is just three to four grid spacings thick. Conventional methods for multiphase flows face severe numerical constraints in simulating such problems due to large grid requirements needed to resolve the thin film formed. Also, inaccuracies in the grid refinement can lead to oscillations in the flow field that rupture the lamella film [86,92].

3.1.1 Validation of the model

First, thermodynamic consistency of the present model is verified by simulating coexistence curve as depicted in Fig. 3.1. It is clear from Fig. 3.1 that the predicted values by Maxwell’s equal area construction are captured well by simulation results. The maximal density ratio of liquid and vapor phases achieved in these simulations was over 800.

Also, it is verified that a stationary droplet at equilibrium complies with Laplace’s law. According to Laplace’s law in two dimensions, we have

$$\Delta p = \frac{\sigma}{R} \tag{3.1}$$

where Δp is the pressure difference between the inner and outer regions of the droplet, σ is the surface tension and R stands for the droplet radius.

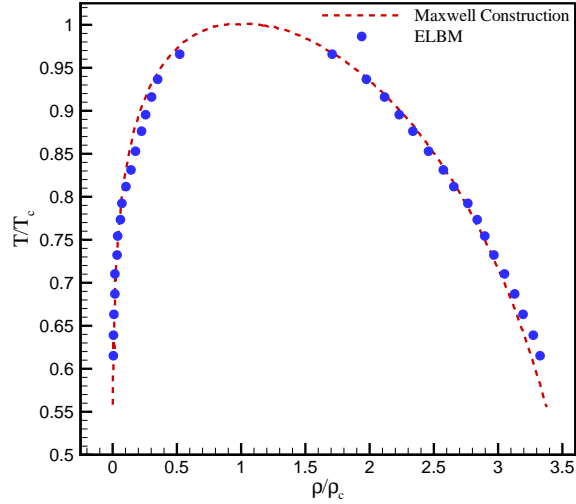


Figure 3.1: Coexistence curve for the proposed equation of state. Symbol: ELBM simulation; Line: Maxwell's equal area rule

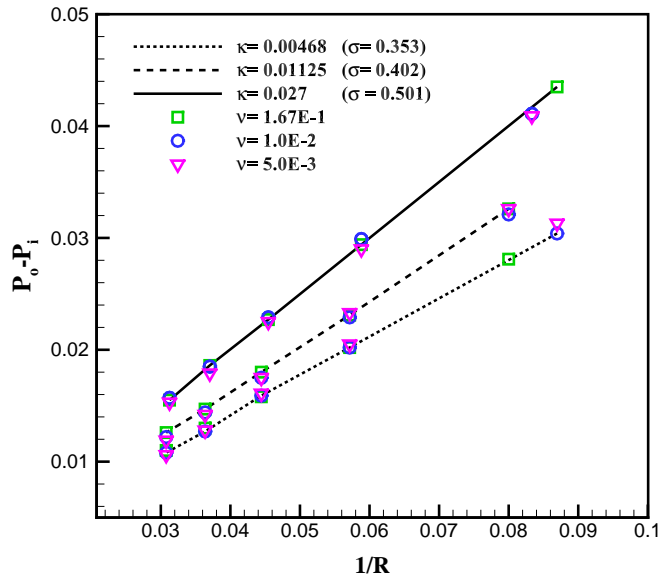


Figure 3.2: Laplace law for various values of kinematic viscosity (ν) and surface tension coefficient κ in two dimensions. With the increasing κ , the surface tension σ increases independent of the viscosity. The liquid and vapor densities are $\rho_l = 7.82$, $\rho_v = 0.071$, respectively.

3. BINARY DROPLET COLLISIONS

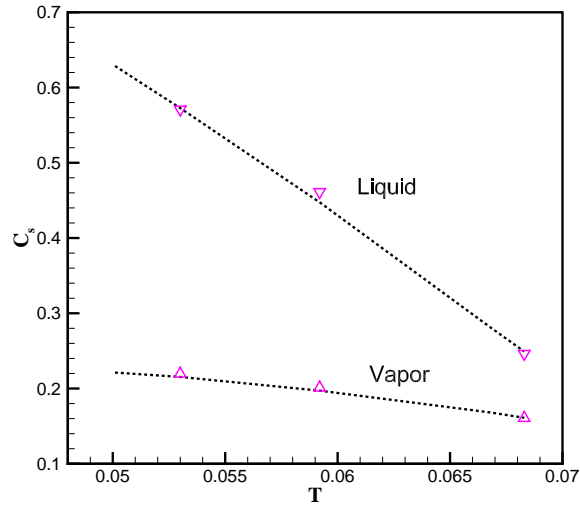


Figure 3.3: Speed of sound as implied by the equation of state (line) and observed in the present simulation (symbol).

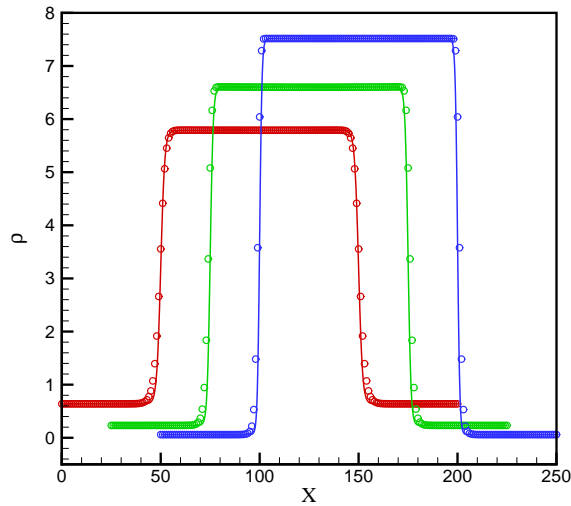


Figure 3.4: Liquid-Vapor density profile for a flat interface obtained by the free energy function (line) and simulation (symbol) for three different density ratios (10, 25 and 125).

The pressure and droplet radius are determined once the droplet reaches the

equilibrium state. It is demonstrated in Fig. 3.2 that the pressure difference between liquid and vapor phases is inversely proportional to the radius of the droplet. Moreover, from Fig. 3.2 it is evident that surface tension can be easily obtained by changing the surface tension coefficient κ in (2.37) independent of the kinematic viscosity.

Further numerical validation of thermodynamic quantities such as speed of sound and interface profile are possible. In Fig. 3.3 we compare the observed speed of sound in the liquid and vapor phases with the analytical estimate obtained from the equation of state for three different liquid-vapor density ratios. Also, the liquid-vapor density profile for a flat interface implied by the free energy function is compared to the simulations for three density ratios in Fig. 3.4. The solid lines in Fig. 3.4 are computed by numerically solving the equation (2.28) for different temperatures corresponding different density ratios. In Eq. (2.28), if the equation of state is known, Ψ can be readily derived from (2.34).

To validate the presented model for a dynamic problem, we performed three-dimensional simulations of a liquid droplet suspended in another fluid under shear flow (Taylor deformation problem [93, 94]). Taylor found that the deformation of the droplet D can be determined by the capillary number $Ca = R\rho_m\nu_m\dot{\gamma}/\sigma$ and the viscosity ratio $\lambda = \rho_d\nu_d/\rho_m\nu_m$. Here, R is droplet radius, $\dot{\gamma}$ is the shear rate, σ is the surface tension, ρ_d, ρ_m are the droplet and medium density and ν_d, ν_m are the kinematic viscosities of the droplet and the surrounding, respectively. For a small deformation, the result reads [93, 94]:

$$D = (L - B)/(L + B) = \frac{19\lambda + 16}{16\lambda + 16}Ca \quad (3.2)$$

where L and B are the largest and smallest distances of the drop surface from its center (the major and minor axes).

Spherical droplet was placed between two parallel plates with a distance H apart. The system experiences shear flow by imposing a velocity u_w on each plate in opposite directions so that the shear rate is $\dot{\gamma} = 2u_w/H$. In our simulations, we fix the densities $\rho_d = 6.65, \rho_m = 0.264$ and the kinematic viscosities $\nu_d = 0.0397, \nu_m = 1$ so as to set the viscosity ratio $\lambda = 1$. Corresponding to chosen densities and $\kappa = 0.00268$ the surface tension measured from Laplace law is 0.168. The droplet radius, R , and distance between two plates, H , are set to 16 and 70 lattice units, respectively. Simulation results for the deformation for different Ca are shown in Fig. 3.5. Excellent agreement between theoretical, Eq. (3.2), and simulation is clearly visible.

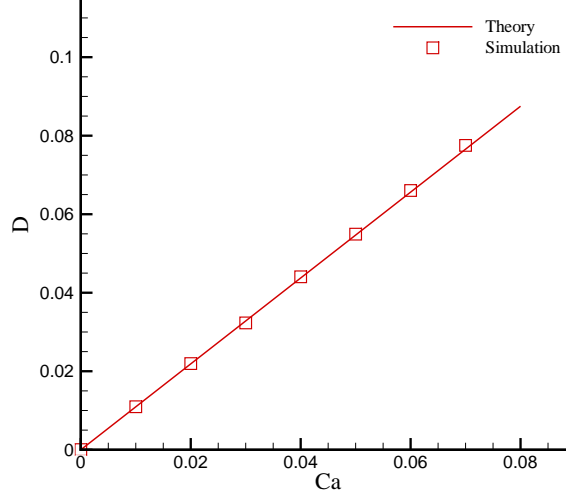


Figure 3.5: Simulation results (symbol) for deformation of a droplet in simple shear flow together with theoretical results of Taylor Eq. (3.2) (line).

3.2 Results and Discussions

3.2.1 Simulation setup for droplet collision

For all simulations reported here, we use $T/T_c = 0.7268$, which gives a density ratio of ≈ 110 , the density of the liquid and vapor now become $\rho_l = 7.82$ and $\rho_v = 0.071$, respectively. The corresponding equation of state for $T/T_c = 0.7268$ can be written explicitly as $p = \sum_{n=1}^6 b_n \rho^n$ where the b_n are given in table 3.1. We set the surface tension $\sigma = 0.353$ corresponding to $\kappa = 0.00468$ in all cases. Also the kinematic viscosity of the liquid and vapor phases is kept the same. This ensures a dynamic viscosity that is proportional to the density ratio of the two phases.

The setup is initialized with two liquid droplets of diameter D_0 , which are placed in their surrounding vapor and a separation between the centers of $1.5D_0$ and with an offset between the centers B (Fig. 3.6). The droplets approach each other with a velocity $U_0/2$ while the vapor is at rest velocity. Periodic boundary condition is applied on all domain boundaries. The computational domain is determined according to size of the droplets. All simulations, unless otherwise stated, were performed on a $8D_0 \times 4D_0 \times 4D_0$ grid (after performing grid independence study).

Table 3.1: The coefficients of the polynomial equation of state (2.55) at $T/T_c = 0.7268$.

b_1	0.05300000000000000000
b_2	-0.03818183621928911000
b_3	0.004139745482116095000
b_4	0.000374848409521031700
b_5	-0.00014552652965531227
b_6	0.000012746947442749278

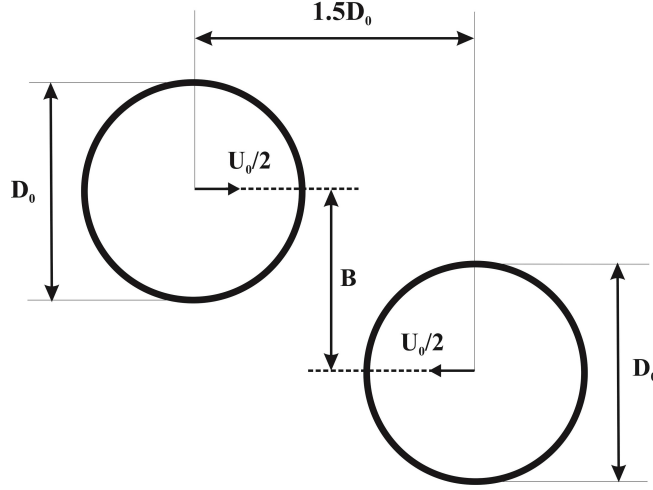


Figure 3.6: Schematic representation of the binary droplet collision.

In general, the outcome of the collision can be different depending on the sizes of the drops, their kinetic energy, the vertical center to center distance between droplets, B , (see Fig. 3.6) and the properties of the fluid. All these factors can be parameterized in terms of a group of dimensionless numbers: The Weber number We (the ratio of the inertial to the surface tension forces), the Reynolds number Re (a measure of the ratio of inertial to viscosity forces) and the impact parameter (χ):

$$Re = \frac{U_0 D_0}{\nu_1}, \quad We = \frac{\rho_1 U_0^2 D_0}{\sigma}, \quad \chi = \frac{B}{D_0}, \quad (3.3)$$

where σ is surface tension and ρ_1 and ν_1 are density and viscosity of the liquid phase, respectively.

In this chapter all the parameters and variables are given in the dimension-

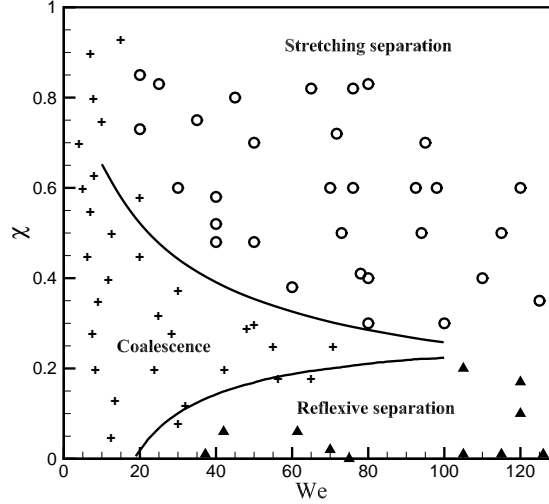


Figure 3.7: Numerical simulations of three types of droplet collisional regimes (Coalescence +, Reflexive separation ▲, Stretching separation ○) together with theoretical prediction (solid line) [1]

less form using the relative velocity U_0 as the reference velocity scale, the drop initial diameter D_0 as the length scale, and the value of D_0/U_0 as the time scale.

3.2.2 Various regimes of droplet collision

Generally, if the Reynolds number is high enough, it does not play a significant role on the outcome of the collision. Therefore, the control parameters on collision outcomes are Weber number and impact parameter [1]. Depending on these parameters, the following collision regimes were identified: coalescence and bouncing at low and moderate Weber numbers, reflexive separation for high Weber numbers and low impact parameters, and stretching separation for both high Weber and large impact parameters [1, 2]. Firstly, we compare the simulation results of binary droplet collisions with experimental observations [1–4].

Different types of collision regimes for two equal-size droplets in the Weber number range of $5 \leq We \leq 130$ and impact parameter, $0 \leq \chi \leq 0.95$, are shown in Fig. 3.7, where the solid lines as predicted by Ashgriz and Poo [1] are marked to separate various regimes of the droplet collision. They had established the boundaries between different regimes of collision outcomes

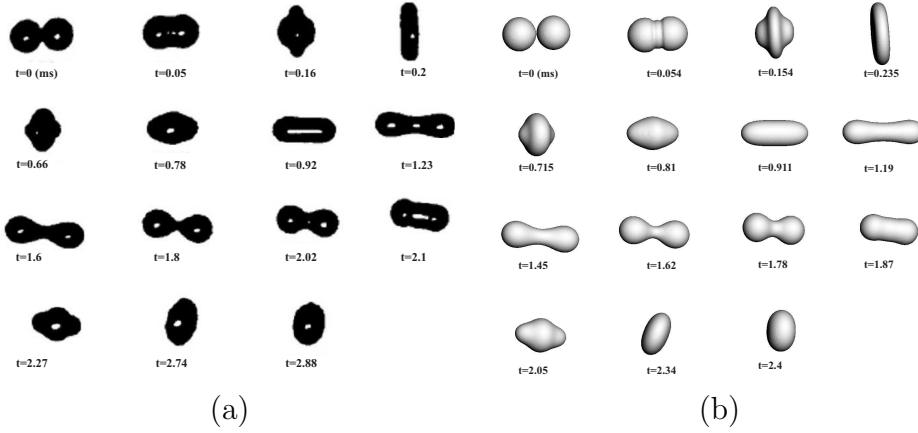


Figure 3.8: Sequence of coalescence observed for binary collision of equal sized droplet at $We = 32.8$, $Re = 210.8$ and $\chi = 0.08$. (a) Experiment of Qian and Law [2] and (b) present simulations.

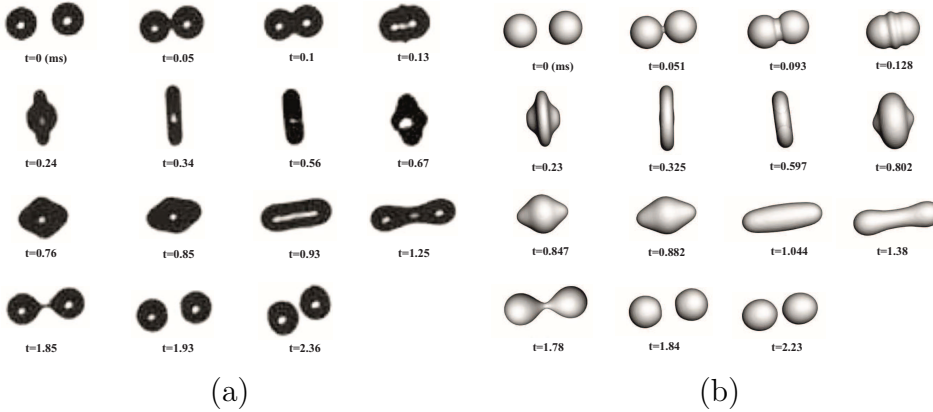


Figure 3.9: Reflexive separation regime as observed during near head on collisions at $We = 37.2$, $Re = 228.8$ and $\chi = 0.01$. (a) Experiment of Qian and Law [2]; (b) Simulation

based on a simple energy balance analysis. Good agreement between the present simulation results and theoretical predictions is evident from Fig. 3.7. The results of a near head-on collision at $We = 32.8$, $Re = 210.8$ and $\chi = 0.08$ shown in Fig. 3.8 is compared with one of the experiments by Qian and Law [2]. It is evident from Fig. 3.8 that the process of the collision is well captured by the simulation. Grid size for this simulation was $150 \times 150 \times 150$, with $D_0 = 30$ lattice units. Figure 3.8 shows that after impact, a disk-like droplet is formed at $t = 0.23$ ms. Due to the pres-

sure difference between inner and outer regions of this liquid sheet caused by surface tension, it contracts radially inwards between $t = 0.715 \text{ ms}$ and $t = 0.911 \text{ ms}$ and then pushes the liquid outwards to form a liquid cylinder at $t = 1.45 \text{ ms}$. After forming rounded ends at $t = 1.62 \text{ ms}$, the liquid cylinder oscillates to finally become a spherical droplet. This is the typical coalescence collision.

In Fig. 3.9, another experiment of Qian and Law [2] is reproduced by the present model and the results are in excellent agreement. Similar to Fig. 3.8, the initial outward spreading disk is observed, which contracts because of the surface tension and after that creates a liquid cylinder. The latter stretches out along the initial coalescence axis until two ending drops are connected by a ligament ($t = 1.78 \text{ ms}$). At $t = 1.84 \text{ ms}$, the inertia overcomes the surface tension and the ligament breaks away from the end droplets. This type of collision falls into reflexive separation category. Grid size for this simulation was $150 \times 150 \times 150$ with $D_0 = 30$ lattice units.

The influence of the viscosity on dynamic behavior of droplet collision was studied experimentally by Gotaas et al [3]. They observed that the border between the coalescence and stretching separation shifts toward high Weber numbers as the viscosity is increased. For high Weber number and large viscosity, the collision regime of stretching separation in which two end spherical drops are formed after the collision is simulated and compared directly with the experiment of Gotaas et al [3]. Figure 3.10 demonstrates that the complete process of the collision of two highly viscous liquid droplets is fully reproduced by the simulation. One can see in Fig. 3.10 that strong rotational motion is generated during the collision process due to a large impact parameter. Owing to this rotation, as well as large viscosity, a slender liquid cylinder is generated in between the end drops. Also, a large impact parameter implies that only a small fraction of the droplet meets its colliding partner while the rest of the droplet continues its inertial motion. Thus, a long liquid filament is generated which breaks up into two large drops as well as a liquid thread in between. For another case for larger viscous drops in Fig. 3.11, it is evident that the generated time-resolved images from the simulation are in good visual agreement with the experiment [3].

3.2.3 Lamella stabilization

Simulation of head-on droplet collision for large enough We and Re numbers produces a very thin film, known as lamella film, during the deformation process, and was also observed experimentally by Willis and Orme [4]. The lamella is bounded by a rim formed by capillary forces. Depending on the

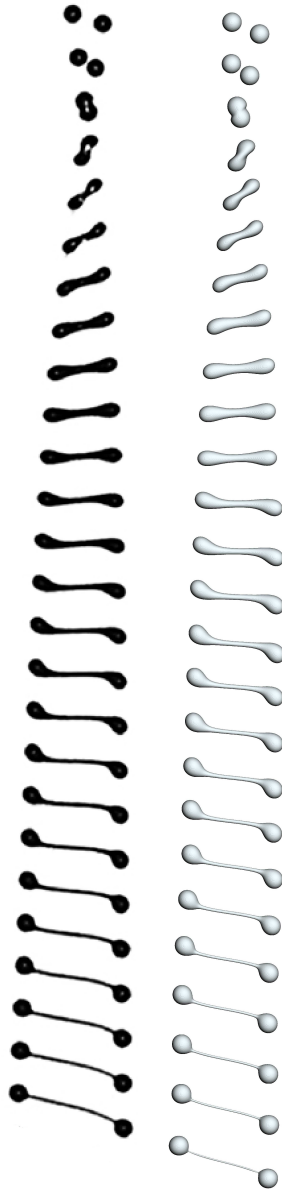


Figure 3.10: Snapshots of the collisional outcome of two highly viscous drops for experiment (left) [3] and present simulations (right) at $We = 92.5$, $Re = 35.65$ and $\chi = 0.6$.

Weber number, the lamella can either remain attached to the rim or it can rupture and detach from the rim.

Numerical simulation of the lamella structure during the extension and contraction can be quite challenging for conventional methods employed for

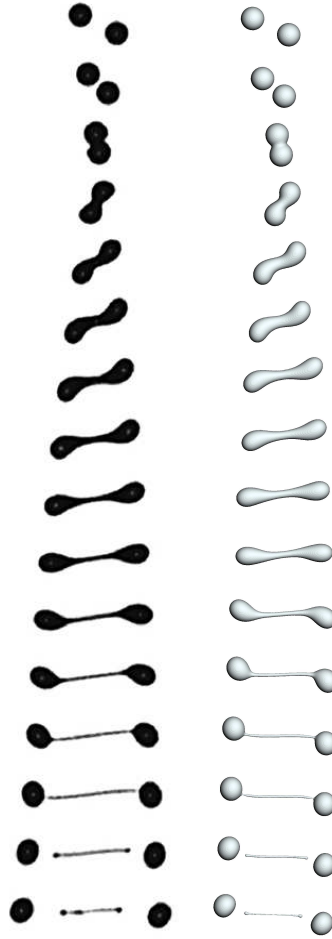


Figure 3.11: Simulation of stretching separation regime (right) compared to experiments (left) [3] at $We = 45.0$, $Re = 43.6$ and $\chi = 0.8$.

multiphase flows. In these methods, insufficient resolution can lead to artificial rupture of the lamella during the collision [86] thus demanding a large grid resolution and added simulation costs. Moreover, inaccuracies in the mesh refinement can lead to oscillation in the flow field that rupture the lamella film artificially. Although theoretically predicted, no experiments could capture the rupture of lamella; hence numerical studies to provide further insights into the collision process are highly sought after.

To validate the lamella stabilization using the present model, the time evolution of the diameter of the merged droplet is compared with experiments in Fig. 3.12. The head-on collision of two equal size droplets is simulated at $We = 269$, $Re = 154$ and $We = 357$, $Re = 178$, and compared with experiment of Willis and Orme [4]. These simulations are performed with a grid

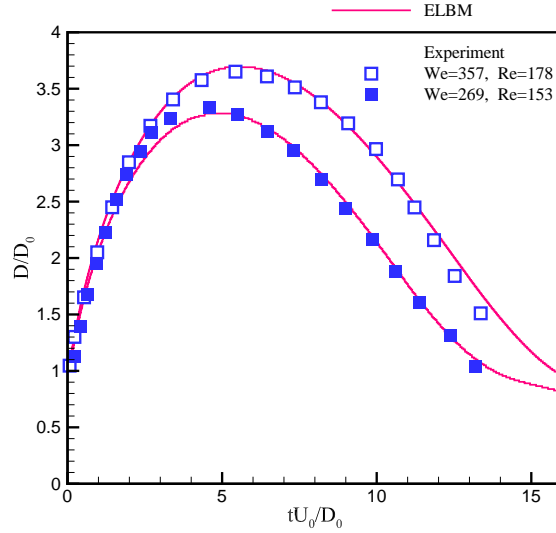


Figure 3.12: Time evolution of maximum radial expansion of a merged droplet as measured by present ELBM simulations (solid line) together with experiments (square) [4] at $We = 269$, $Re = 154$ and $We = 357$, $Re = 178$.

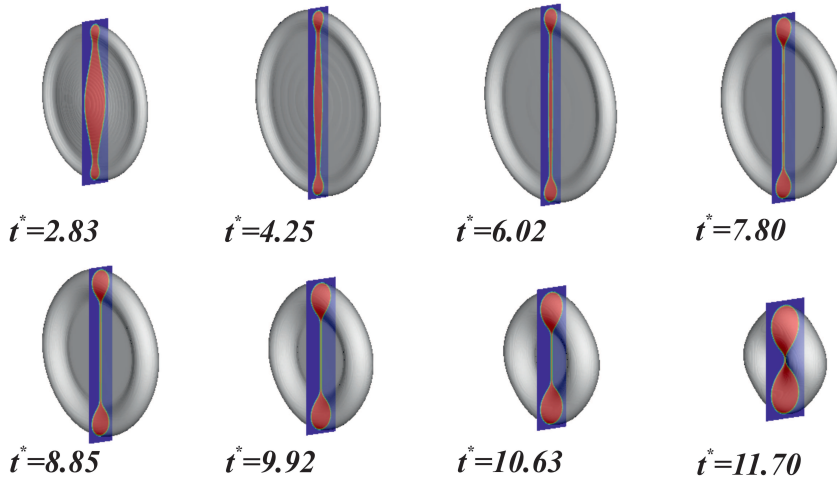


Figure 3.13: Simulation of lamella stabilization at different stages ($We = 269$ and $Re = 154$). The lamella film expands from $t^* = 2.83$ to $t^* = 6.02$ before contracting from $t^* = 7.8$ to $t^* = 11.7$.

size of $8D_0 \times 5D_0 \times 5D_0$ where $D_0 = 150$ lattice units is the droplet initial diameter. Remarkably, the present model captures the thin lamella which is only three to four grids spacing thick. Excellent comparison between the

3. BINARY DROPLET COLLISIONS

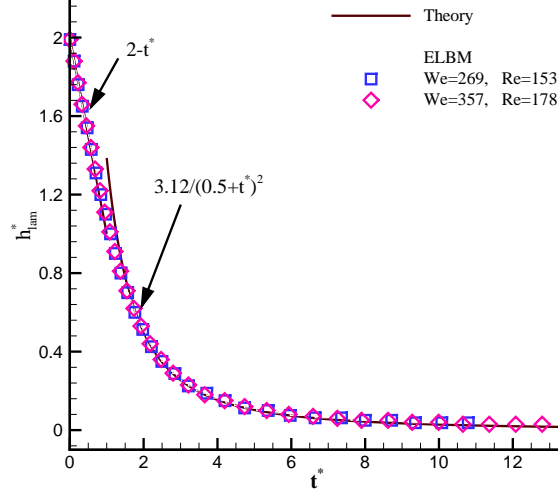


Figure 3.14: Dimensionless thickness of the lamella at the symmetry center, $h_{lam}^* = h/D_0$, versus the non-dimensional time, $t^* = tU_0/D_0$. Open symbol: ELBM simulations for two different impact conditions, $We = 269$, $Re = 154$ and $We = 357$, $Re = 178$; Line: Analytical estimate of Ref. [5] (Eq. 3.4).

simulation result and the experiment is evident from Fig. 3.12.

Fig. 3.13 shows snapshots of simulation of stable lamella at various dimensionless times t^* ($t^* = tU_0/D_0$). The result shows that the lamella starts at $t^* = 4.25$ and disappears at $t^* = 11.70$. It is interesting to note that the minimum thickness of the lamella film does not occur during the radial expansion process but it occurs during the retreat of the capillary rim towards the center of mass as observed by simulations of Focke et al. [92] also.

Roisman et al. Ref. [5] studied the flow in the lamella which is generated by head-on collision of two equal size droplets or drop impact onto a dry flat substrate. They demonstrated that the flow in the lamella is universal and the evolution of lamella thickness (h) depends neither on the impact Weber nor Reynolds number when both We and Re are much larger than unity. The evolution of the non-dimensional thickness of the lamella, $h_{lam}^* = h/D_0$, at the symmetry center was estimated in [5, 92] as:

$$h_{lm}^* = \begin{cases} 2 - t^* & \text{for } t^* < 0.8, \\ 3.12/(0.5 + t^*)^2 & \text{for } 1.4 < t^* < t_{visc}^*, \end{cases} \quad (3.4)$$

where the non-dimensional time $t^* = tU_0/D_0$ is built on the time for which the lamella exists. Figure 3.14 shows the theoretical estimation together with the simulation results for the evolution of the non-dimensional thickness of the lamella at the symmetry plane for head-on collision of two equal size droplets at $We = 269$, $Re = 154$ and $We = 357$, $Re = 178$. It is evident from Fig. 3.14, the theoretical approximations of [5, 92] are well captured by numerical simulations for different drop impact conditions.

3.2.4 Energy dissipation at maximum radial deformation

The total energy of equally sized droplets before the collision (at time $t = t_0$) is the sum of the kinetic energies of the two droplets and their surface energy [4]:

$$E(t_0) = 2 \left[\left(\frac{1}{6} \pi D_0^3 \right) \left(\frac{1}{2} \rho U_d^2 \right) + \sigma (\pi D_0^2) \right], \quad (3.5)$$

where the $U_d = U_0/2$ is the velocity of each droplet. Now considering the viscous dissipation, Φ , in the interior of the droplet, we can write the total energy of the system as a function of time as:

$$E(t) = E_k(t) + E_s(t) + \int_{t_0}^t \Phi dt, \quad (3.6)$$

where $E_k(t)$ and $E_s(t)$ are the kinetic and surface energies of the merged droplet, respectively. By equating Eq. (3.5) and (3.6) at the instant when the coalesced droplet reaches the maximum deformation ($E_k = 0$) the following relation for surface energy and viscous dissipation can be derived [4]:

$$S^* = 1 + We^*(1 - \Phi^*). \quad (3.7)$$

Where S^* is the non-dimensional surface area of the flattened droplet normalized by the the total surface area of the drops before collision, $2\pi D_0^2$, We^* is modified We number equal to $We/48$ and the Φ^* is the dimensionless energy dissipation normalized by $\frac{1}{6}\pi D_0^3 \rho U_d^2$. Now for a given state of simulation, we numerically compute the surface area of the droplet S^* and then compute the predicted value of viscous dissipation, Φ_{theory}^* , according to (3.7). It is now possible to verify the viscous dissipation observed in the simulations, $\Phi_{simulation}^*$, by computing its value from the velocity field \mathbf{u} as [95] :

$$\Phi = \frac{\nu_l \rho_l}{2} \int_{\Omega} \left(\frac{\partial u_i}{\partial x_j} + \frac{\partial u_j}{\partial x_i} \right)^2 dV \quad (3.8)$$

where Ω denotes the interior volume of the drop. Table 3.2 shows the comparison of Φ^* with the theoretical prediction for the simulation of head on droplet collision at two different values of kinematic viscosities. Table 3.2 was obtained for various We numbers in the range of 50 to 750 and for two grid kinematic viscosities of 0.23 and 0.46. Also from table 3.2 we see the linear dependence of S^* with We^* , this also compatible with the experimental observations of [4].

3.2.5 Satellite droplets and instabilities

Various simulations of the two equal-size droplets colliding with each other are shown in Fig. 3.15. The collision regime of coalescence is shown in Fig. 3.15(a) while Figures 3.15(b) and 3.15(c) show the process of stretching separation with one and three satellite droplets, respectively. Simulations in this regime show that the droplets are initially flattened in their contact region and later go on to merge or split up into further droplets depending on the We number. Depending on Weber number, viscosity effect as well as the impact parameter, the merged droplet continues to deform and generates a doughnut shape at $We = 76$, $Re = 262$ and $\chi = 0.2$ (Fig. 3.15(a), $t^* = 3.8$). The disk generated in the interior of the doughnut is connected to the boundary ring through a neck. Owing to the large curvature at the circumference of disk, a pressure difference between the inner and the outer regions of the disk is created by surface tension. Hence, as seen in Fig. 3.15(a) at $t^* = 3.8$, large flow velocities are developed which in turn results in pinch-off of the inner thin liquid disk from the boundary ring (Fig. 3.15(a), $t^* = 4.2$). The inner liquid layer is completely detached from the boundary ring and becomes a ligament (Fig. 3.15(a), $t^* = 5.2$). The flow field reveals that the velocity in the boundary ring increases during $t^* = 4.2$ to $t^* = 5.2$. This results in the increase of the elongation of the liquid torus tending to prevent the merged droplets from coalescence. However, maximum velocity occurs in the ligament at $t^* = 5.2$; therefore, low pressure is created in the ligament region leading to high surface curvature in the ligament. As a result, due to the surface tension, the ligament pulls back toward its center and then elongates in the perpendicular direction. In the last stage, the ligament bridges with the internal edges of the torus (Fig. 3.15(a), $t^* = 6.1$) and then forms a single merged mass at $t^* = 7.5$. The merged droplet continues to rotate around the Y -axis during $t^* = 7.5$ to $t^* = 17.9$. It is eventually deformed into an elliptic shape at time $t^* = 17.9$. Next situation in Fig. 3.15(b) describes the situation with a higher Weber number but the same impact parameter. Two droplets coalesce after their initial collision and then continue to deform and create an egg-shaped

Table 3.2: Comparison of energy dissipation of a droplet at maximum radial deformation for two different kinematic viscosities.

$\nu = 0.23$									
We^*	S^*	Φ_{theory}^*	$\Phi_{simulation}^*$	$\% Error $	We^*	S^*	Φ_{theory}^*	$\Phi_{simulation}^*$	$\% Error $
1.042	1.354	0.66023	0.65086	1.42	1.042	1.216	0.79266	0.81131	2.35
3.125	2.065	0.65914	0.64648	1.92	3.125	1.658	0.78960	0.76768	2.77
5.208	2.774	0.65949	0.64199	2.65	5.208	2.090	0.79080	0.79121	0.05
7.292	3.490	0.65865	0.64317	2.35	7.292	2.527	0.79055	0.78409	0.82
9.271	4.148	0.66041	0.66119	0.12	9.271	2.932	0.79159	0.81070	2.41
11.46	4.899	0.65976	0.66278	0.46	11.46	3.390	0.79138	0.78197	1.19
13.54	5.602	0.66015	0.66841	1.25	13.54	3.868	0.78822	0.76651	2.75
15.63	6.310	0.66016	0.64632	2.09	15.63	4.266	0.79095	0.77052	2.58

 $\nu = 0.46$

3. BINARY DROPLET COLLISIONS

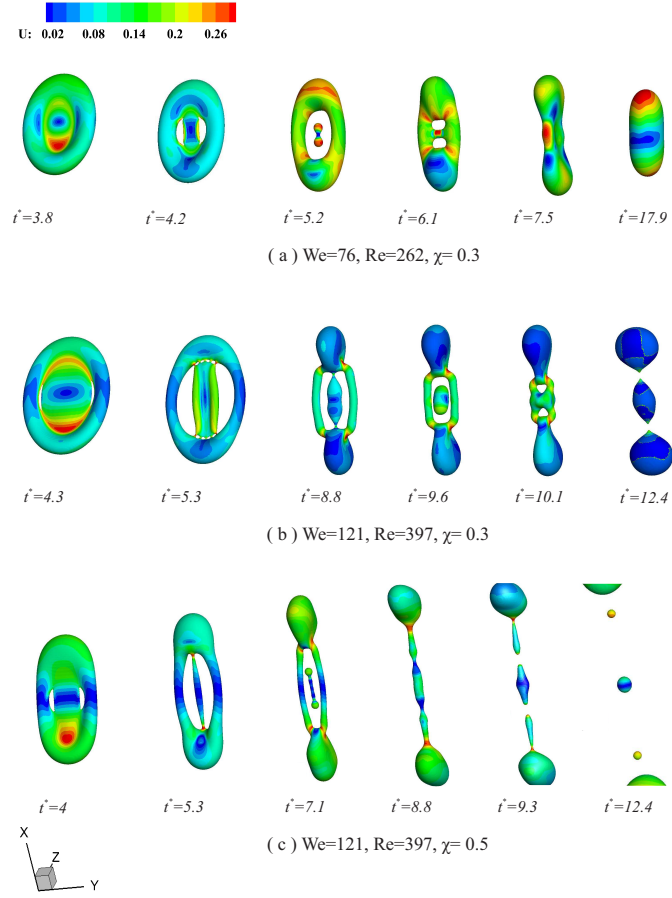


Figure 3.15: Snapshots of the two colliding droplets for various Weber numbers and impact parameters together with velocity magnitude (color).

droplet in Fig. 3.15(b) ($t^* = 4.3$). A thin liquid layer bounded by a rim is formed due to capillary forces. Due to high liquid velocities developed in the thin layer caused by high pressure difference between inner and outer regions of the disk, the detachment of the film from the external ring starts at $t^* = 4.3$ and continues to create holes at the base of the rim (Fig. 3.15(b), $t^* = 5.3$). The wide liquid bridge as well as the boundary ring at $t^* = 5.3$ is transformed in the collision stage at $t^* = 8.8$ including a thick ligament in between as well as two liquid side arms connected by end masses. The end masses are pinched off from the liquid ligament with a central liquid cylinder in between (Fig. 3.15(b), $t^* = 9.6$). One can see that the maximum velocity is observed in the junction of the side arms with accumulated masses at the end. Therefore, low pressure region is formed in this area thus creating a liquid flow from the center of the side arms towards the edges of

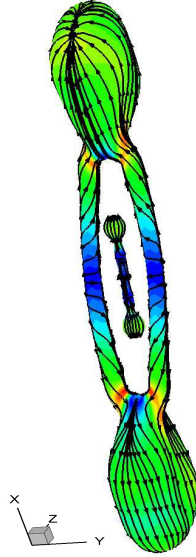


Figure 3.16: Stream lines and velocity magnitude for the state corresponding to time $t^* = 7.1$ of the figure 3.15(c) show the presence of strong rotational motion in the side arms.

end masses. As a result, the volume of the accumulated liquid increases in two end masses. This and surface tension effects cause to bridge the liquid cylinder with the side arms at time $t^* = 10.1$. At time $t^* = 10.1$ and later, a neck is formed at the junction of the emerged liquid in between and the two lobed-shaped end drops. The velocity near the neck becomes large resulting in a low pressure region and finally the end masses are pinched off from the thick ligament in between (Fig. 3.15(b), $t^* = 12.4$).

In the collision regime of the stretching separation, one can observe one or more satellite drops generated in the collision depending of the Weber number as well as the impact parameter. It is believed that the end pinching and capillary-wave instability are the main mechanisms for breakup of the ligament and formation of satellite droplets. This is now confirmed by current simulations which offer a detailed insight into the flow velocities and pressure distributions during droplet collision. The case in Fig. 3.15(c) belongs to the stretching regime with three satellite drops formed at the end. In Fig. 3.15(c), the Weber and the Reynolds numbers are chosen the same as the previous case but the impact parameter is increased. After coalescence of two droplets, the merged mass deforms to generate an elliptical shape at time $t^* = 4$. Due to the aforementioned reasons in the previous cases, the thin liquid layer bounded by the boundary ring is disconnected from the edges of the rim and then transformed into a liquid thread at time

3. BINARY DROPLET COLLISIONS

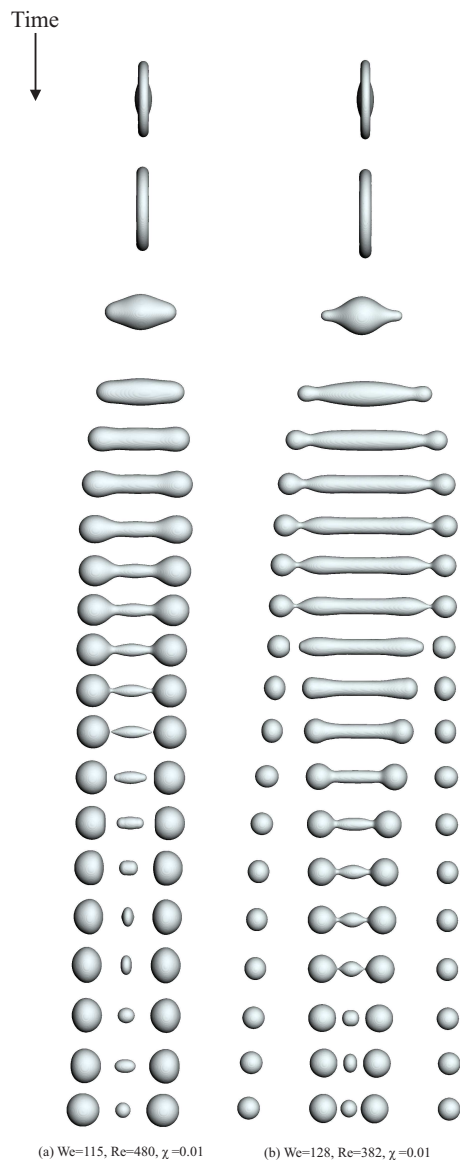


Figure 3.17: “End-pinching” mechanism observed during near head on collisions. This leads to formation of an odd number of satellite droplets.

$t^* = 5.3$. The velocity at the edges of the ligament reaches to a maximum value, leading to low pressure at this region ($t^* = 5.3$). This results in pinch-off of the ligament from the external ring due to high surface curvature at $t^* = 7.1$. At this moment, the velocity at both end edges of the two-sided liquid columns reaches large values and creates a low pressure in those regions. While, the minimum liquid velocity happens at the center of

the side arms which results in generating high pressure in this area. Each of the liquid columns can be considered as a channel with varying pressure along the length of the channel. Therefore, mass flux is generated from a high pressure region to low pressure region thus elongating the side arms with a tendency to prevent the two droplets from coalescing (Fig. 3.15(c), $t^* = 8.8$). Moreover, In the process of stretching separation of this collision, the rotational motion caused by angular momentum plays important role. In order to visualize the rotational motion in the side arms at time $t^* = 7.1$, the stream lines are sketched in Fig. 3.16. It is seen from Fig. 3.16 that the two liquid column have strong rotational motion around X -axis and thus leading to stretching of the merged droplet and then creating an elongated ligament type shape (Fig. 3.15(c), $t^* = 8.8$). At time $t^* = 9.3$ a liquid ligament is formed in between and then disintegrates into a number of liquid threads. One can clearly observe the capillary wave formed in the long ligament at time $t^* = 8.8$. This effect combined with large elongation of the ligament leads to formation of three satellite drops at the end of the collision process (Fig. 3.15(c), $t^* = 12.4$).

Near head-on collision resulting in the reflexive separation with one and three satellite droplets are shown in Fig. 3.17. It is clearly seen that the end-pinching mechanism is dominant in the breakup of the central liquid thread followed by formation of the satellite drops. For both cases in Fig. 3.17, the merged mass continues to deform in such a way as to form a disk-like shape bounded by a rim. Due to surface tension effects, the disk radially contracts inward and pushes the liquid outwards along the impact direction. Accordingly, a dumbbell shape including a long liquid cylinder with rounded ends is generated. It is seen that in both cases in Fig. 3.17, before detaching central cylinder from ending masses, a neck is formed at the edges of the liquid cylinder. Therefore, low pressure is formed in the neck region leading to high surface curvature and finally the rounded ends are pinched off from the liquid cylinder. Figure 3.17(a) shows that due to surface tension, the central liquid thread contracts and then oscillates until a spherical drop is formed. In this case, short length of the ligament as well as low momentum to surface tension ratio are the main reasons for the collision process to be completed with one satellite droplet. On the other side, one can clearly observe from Fig. 3.17(b) that the second end pinching process begins on the central liquid cylinder after it is detached from rounded ends. In this case due to higher Weber number, the central thread is longer and, in particular, the momentum prevails upon surface tension effects. Consequently, the pinch-off of the central ligament is completed by three satellite drops. The obtained results in Fig. 3.17(b) are in a good qualitative agreement on the number and size of satellite drops with

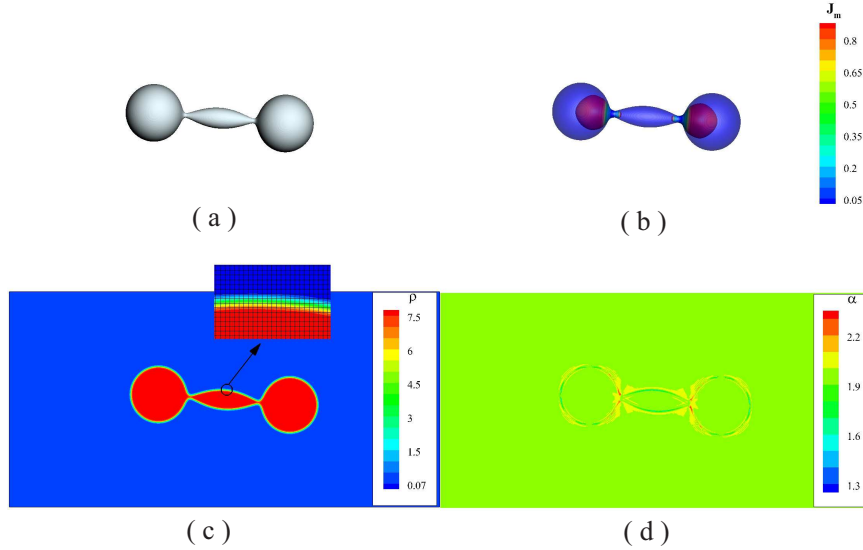


Figure 3.18: The distribution of local density, relaxation parameter α as well as mass flux observed inside a merged droplet for one of the snapshots in Fig. 3.17(a) (just before the ligament disconnects). See text for further discussion.

one of the experiments of Ashgriz and Poo [1] (See Fig. 7 of their paper) and also with one of the presented numerical simulations in paper of Pan and Suga [85]. Figure 3.17 implies that the number and size of satellite drops is dependent on the size of central liquid thread between two rounded ends and especially on the Weber number. It should be stressed that in the case of three satellite drops, Fig 3.17(b), the Weber number is higher than the one-satellite drop case, Fig. 3.17(a), which corresponds with experimental observations of Ashgriz and Poo [1]. Their experimental results showed that the number of satellite drops increase as the Weber number increases. Moreover, theoretical predictions of Benn et. al [96] demonstrated that the number of satellite drops resulting in both reflexive separation and stretching separation is an odd number.

3.2.6 Flow visualization and entropy estimate

In order to elucidate the distribution of the density, relaxation parameter (α) and the magnitude of the mass flux (J_m) inside the merged droplet in our simulations, we choose one of the snapshots in Fig. 3.17(a) (just before the ligament detaches from rounded ends). Figure 3.18(a) shows the density iso-surface while the magnitude of the mass flux inside the merged

droplet is shown in Fig. 3.18(b). One can clearly observe the liquid jet generated inside the rounded ends. As demonstrated before, these liquid jets play a significant role for the pinching-off the ending drops from the liquid cylinder. Figure 3.18(c) shows the density contour on the mid-section of the simulation in Fig. 3.18(a). It is seen that the interface constructed by present model is finite but thin (just three to four grid spacings wide).

Finally, in order to illustrate significance of the ELBM formulation (Eq. (2.50)), the computed relaxation parameter α by Eq. (2.62) is shown in Fig. 3.18(d) for the mid-section in the simulation. As expected, significant deviation of α from $\alpha = 2$ is observed at the interface. This provides evidence that the ELBM performs effective control on the spurious gradients at the interface, thus stabilizing the simulations. It must be noted that such simulations were not possible before due to the lack of entropy considerations in earlier multiphase LB models.

The computational cost associated with evaluation of α is comparable to the standard LBM scheme or equivalently, the simulation time for ELBM increases by a factor of 2 compared to LBM ($\alpha = 2$) (table 3.3). These costs are more than recovered due to the small grid sizes used for ELBM simulations. For example, as it is shown in table 3.4, a simulation of droplet collision with $\chi = 0.35$, $We = 45.5$ and $Re=368$ in the case of an ELBM simulation on grid $480 \times 240 \times 240$ takes 580 sec on 2304 CPUs, while LBM requires a minimum grid size of $960 \times 480 \times 480$ nodes and a computational time of 3688 sec on the same number of CPUs.

3.3 Summary and Conclusions

In this chapter we presented the simulation of binary droplet collisions at various Weber numbers and impact parameters in three dimensions. Accurate prediction of thermodynamic quantities such as co-existence relation, speed of sound, interface profile etc established the reliability and accuracy of the proposed entropic multiphase model [88]. Using simulations, it was shown that the operating range of free energy models can be significantly increased by considering an entropic collision model and a polynomial equation of state. Although the density ratio of the liquid and vapor phases in the simulations was not as high as in experiments (typically of the order 1000) it was clear that the vapor phase had minimal influence on the liquid phase (due to density ratio of around 100) and hence the density ratio used in simulations was sufficient for us to recover all the theoretical predictions and experimental results. Using our simulations we showed that the present model fills the gap in the literature where most of the droplet

3. BINARY DROPLET COLLISIONS

Table 3.3: Computational cost for simulation of binary droplet collision at $Re = 75$, on 2304 CPUs.

LBM ($\alpha = 2$)		ELBM			
Resolution	Time (D_0/U_0)	Wall-clock time	Resolution	Time (D_0/U_0)	Wall-clock time
$480 \times 240 \times 240$	100	282.4 Sec	$480 \times 240 \times 240$	100	543.05 Sec

Table 3.4: Computational cost for simulation of binary droplet collision at $Re = 368$, on 2304 CPUs.

LBM ($\alpha = 2$)		ELBM			
Resolution	Time (D_0/U_0)	Wall-clock time	Resolution	Time (D_0/U_0)	Wall-clock time
$480 \times 240 \times 240$	-	Unstable	$480 \times 240 \times 240$	100	579.39 Sec
$840 \times 420 \times 420$	-	Unstable			
$960 \times 480 \times 480$	100	3687.8 Sec			

3. BINARY DROPLET COLLISIONS

dynamics simulations were performed using the Shan-Chen model because of the aforementioned drawbacks of the original free energy model.

Three major regimes of collisional outcomes namely, coalescence, reflexive separation and stretching separation were clearly observed. Excellent agreement with experimental predictions was obtained by numerical results. Numerous simulations have been performed to determine the influence of Weber number and impact parameter and different configurations of droplet collision regimes have been analyzed. Quantitative prediction of the lamella thickness and viscous dissipation were also provided.

Regarding the collision consequences, it was demonstrated that for collisions at high Weber number and large impact parameter the capillary-wave instability is dominant feature responsible for production of satellite droplets. While, for near head-on collisions with high Weber number, end pinching mechanism plays essential role in formation of satellite drops. For other collisions with an intermediate impact parameter and high Weber number, the influences of rotational motion due to angular momentum combined with elongation of merged droplet due to the inertia of colliding drops are the significant causes for formation of satellite drops.

Chapter 4

Fluid-solid interface problems on flat surfaces

Here in this chapter the proposed entropic lattice Boltzmann model for multiphase flows is extended to the simulation of dynamic fluid-solid interface problems on flat surfaces. Wide range of applications, from capillary filling to liquid drop impact onto flat surfaces with different wettability are investigated. The static interface behavior is tested by means of the liquid column in a channel to verify the Young-Laplace law. The numerical results of a capillary filling problem in a channel with wettability gradient show excellent match with the existing analytical solution. Simulations of drop impact onto both wettable and non-wettable flat surfaces show that the ELBM model reproduces the experimentally observed drop behavior in a quantitative manner.

4.1 Introduction

Wetting and spreading of fluids on solid substrates are important to many natural and industrial processes such as coating, ink-jet printing and oil recovery [97]. Consequently, the contact line motion has been the subject of numerous studies [98, 99].

Recently, the lattice Boltzmann method has attracted attention as an alternative to the complex hydrodynamic phenomena, and in particular, to multiphase flows. In some way, the lattice Boltzmann method is a restatement of the hydrodynamical models of fluids undergoing phase transition, pioneered by van der Waals [69] and Korteweg [71]. Because of specific features of LBM (ease of implementing the effect of molecular forces on the

macroscopic level, ease of imposing boundary conditions and amenability to efficient numerical procedures), it witnessed burgeoning growth in applications, including investigation of the dynamics of binary droplet collision and in particular, the complex behavior of fluid-solid interfaces. For example, based on the free-energy method [23], Inamuro et al. [100] and Zheng et al. [26] proposed a model for multiphase flows with large density ratio. Inamuro et al. [100] investigated the dynamics of binary droplet collision for relatively large Reynolds and Weber numbers with high density ratio and Zheng et al. [26] studied the flow pattern of a bubble rising under buoyancy with density ratio 1000. Gu et al. [101] also conducted the simulation of binary droplet collision as well as the study of impacting liquid drop on a solid substrate, using Inamuro et al. [100] model with density ratio of liquid phase to gas phase fixed at 50. Briant et al [102] investigated the applicability of lattice Boltzmann simulations to the problem of contact line motion in one and two component two phase flows using the free-energy-based lattice Boltzmann model [23]. Using color-gradient-based LBM, Latva-Kokko and Rothman [103] derived an estimate of the contact angle as a function of a wetting tendency of the wall. Based on a mean-field free-energy lattice Boltzmann method, the moving contact line problem of liquid-vapor interfaces was studied by Zhang and Kwok [79]. Furthermore, the multi-component multiphase LBM proposed by Shan and Chen [104] was used in many studies of the contact line problems [80, 105–107].

Although the LBM has been successfully employed in the interface studies, the existing LB methods still suffer from substantial drawbacks such as restriction on thermodynamic consistency [104], kinematic viscosity [79, 102–104], density ratio between liquid and vapor phases [79, 101, 102], interface thickness [79, 102, 103] and, in particular, low impact velocity for the drop impinging on a solid surface [79, 102–104, 108]. Consequentially, the existing LB formulation for multiphase or multiphase multicomponent flows are unable to address complex dynamics for wetting and spreading phenomena in a quantitative fashion and hence, their applications are mainly restricted to simulation of droplets sitting on a surface or displacement of droplets subject to external forces [80, 102, 107, 109].

Aforementioned problems in the lattice Boltzmann methods is essentially overcome by using the entropic lattice Boltzmann method [88]. The proposed forcing free-energy based model in chapter 2 builds upon thermodynamically consistent free-energy lattice Boltzmann approach pioneered by Swift, Osborn and Yeomans [23] and improved by Wagner and Li [55]. However, unlike the previous suggestions, it is based on the nonlinearly stable entropic lattice Boltzmann model [41, 43] rather than on the conventional LBM. As a result, essential dynamical effects, typical of multiphase flows

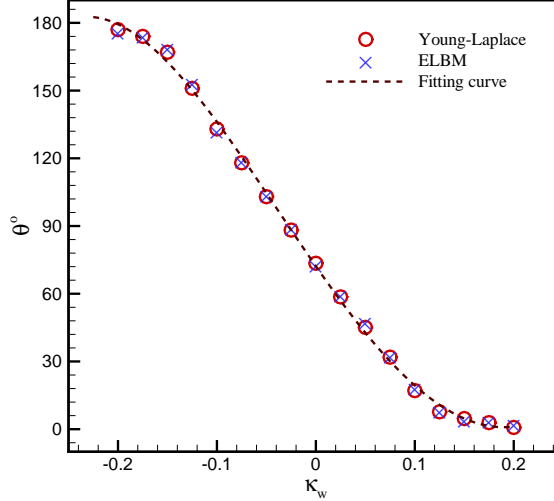


Figure 4.1: Equilibrium contact angle for a liquid drop confined inside the channel as function of the adhesion parameter κ_w (2.59). A comparison between the contact angles derived from Eq. (4.1) (circle) and the simulation results (cross). Line: A fit of numerical results. The surface tension is $\sigma = 0.353$, the liquid density is $\rho_l = 7.82$ and the vapor density is $\rho_v = 0.071$. The channel dimension is 300×70 lattice nodes.

at large Weber and Reynolds numbers for sufficiently high density ratios became achievable.

In this chapter, the previously introduced ELBM for two-phase flows is extended to the study of dynamical effect such as impinging liquid drop onto both wetting and non-wetting flat surfaces. It is confirmed that the ELBM can be applied to simulations of impacting drop on the solid substrates at large Reynolds and Weber numbers and at a substantial density ratio simultaneously. Simulations are compared with the existing analytical and experimental results, and overall excellent agreement is found.

4.2 Validation of the model

4.2.1 Young-Laplace equation

In all simulations reported in this chapter, unless otherwise stated, we set $T = 0.053$ ($T/T_c = 0.7268$) giving a vapour-liquid density ratio approximately 110 ($\rho_l = 7.82$, $\rho_v = 0.071$) The surface tension coefficient is also

considered $\kappa = 0.00468$ corresponding to the surface tension $\sigma = 0.353$. Computation of the equilibrium contact angle is the primary test of validity of fluid-solid interface model. To that end, it is verified that a stationary liquid column in channel complies with the Young-Laplace law. In two dimensions, we have

$$\Delta p = \frac{2\sigma \cos \theta}{H}, \quad (4.1)$$

where the Δp is the pressure difference between inner and outer region of the liquid confined inside the channel, σ is the surface tension, θ is the equilibrium contact angle and H stands for width of the channel.

Initially, a liquid column is considered in a two-dimensional channel. The pressure difference is determined once the droplet reaches the equilibrium state. In Fig. 4.1 the calculated equilibrium contact angle from simulation results are compared with that computed from the Young-Laplace equation. Fig. 4.1 shows that results obtained from the simulations are in excellent agreement with the Young-Laplace equation. Calibration of the adhesion parameter κ_w with the help of data of Fig. 4.1 is used in all our simulations for setting the equilibrium contact angle.

4.2.2 Motion of liquid column in a channel due to wettability gradient

The capillary filling research originates with pioneering works by Washburn [110] and Lucas [111]. Capillary filling is a typical contact line problem where the contact line between liquid, gas and solid is able to move, pulled by capillary forces at the liquid-gas interface and opposed by viscous forces. It is well known that if a drop is placed on a surface with different wettability on two sides, a net surface force is created that drives the drop [112].

Simulation setup is shown in Fig. 4.2. A channel with the width H and length L is considered. Initially, a liquid column is placed in the middle of the channel and the fluid-solid adhesion coefficient $\kappa_w = 0.005$ was initialized uniformly on the top and the bottom walls. After $t = 5000$ time steps, when the liquid column reaches the equilibrium state, κ_w is changed to $\kappa_w^- = 0.02$ for $x > 6H$ while the κ_w remains unchanged for the region with $x < 6H$ ($\kappa_w^+ = 0.005$). This imposes a wettability step through the mid-section and thus triggers a continuous motion of the liquid column along the channel in the x direction. After some time, the liquid column reaches a steady state which indicates a balance between the interface tension and viscosity forces. At this moment, we measure the dynamic contact angles θ^\pm from the density contour. The measured values are $\theta^+ = 69.2^\circ$ and

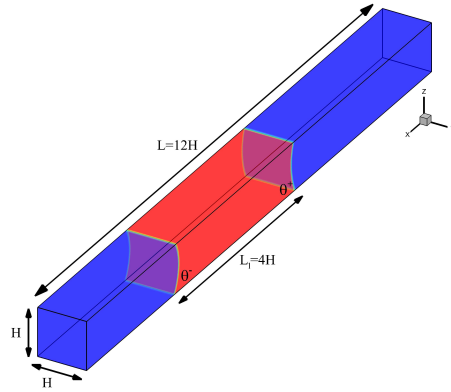


Figure 4.2: Schematic representation of the confined liquid column (red) in a rectangular channel. Liquid column of length L_1 moves along the channel under a wettability step imposed on the bottom ($z = 0$) and on the top ($z = H$) walls. The dynamic contact angles are θ^+ and θ^- .

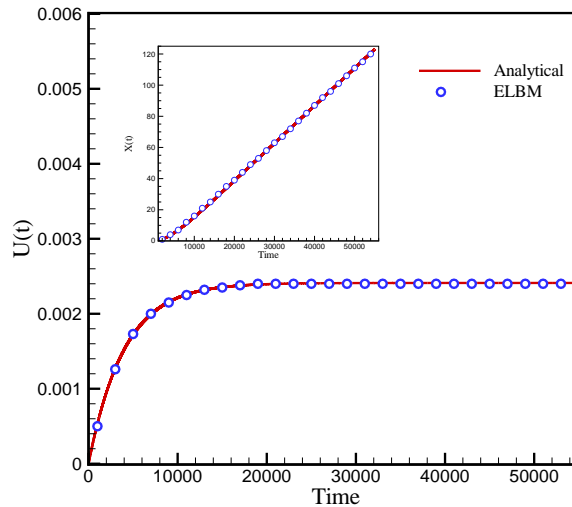


Figure 4.3: History of the centroid velocity U of the liquid column; Line: Analytical (4.3); Symbol: Simulation. Inset: Center-of-mass position X ; Line: Analytical (4.2); Symbol: Simulation. The height of the channel $H = 60$ and the dynamic contact angles are $\theta^+ = 69.2^\circ$ and $\theta^- = 63.15^\circ$. Time and space are given in lattice units.

$\theta^- = 63.15^\circ$. For this problem, an approximate analytical solution for the

center-of-mass position X and the centroid velocity U of the liquid column was found by Esmaili et al [113]:

$$X(t) = \tau U_\infty \left(e^{-\frac{t}{\tau}} + \frac{t}{\tau} - 1 \right), \quad (4.2)$$

$$U(t) = U_\infty \left(1 - e^{-\frac{t}{\tau}} \right), \quad (4.3)$$

where U_∞ is the saturated centroid velocity,

$$U_\infty = \frac{\sigma H (\cos \theta^- - \cos \theta^+)}{6[\rho_l \nu_l L_1 + \rho_g \nu_g (L - L_1)]},$$

with ρ_l and ρ_g are density of the liquid and of the vapor, respectively, and where the transition time τ is

$$\tau = \frac{H^2([\rho_l L_1 + \rho_g (L - L_1)])}{12[\rho_l \nu_l L_1 + \rho_g \nu_g (L - L_1)]}.$$

Fig. 4.3 shows the numerical results and the analytical solution (4.2) and (4.3)) for the displacement and the centroid velocity of the liquid column. Excellent agreement between the simulation and the analytical solution is evident in Fig. 4.3. The liquid and vapor kinematic viscosity in this simulation are $\nu_l = \nu_g = 0.075$ in lattice units.

4.3 Drop impact on a flat surface

Liquid drop impact on solid surfaces plays a significant role in many applications. In spite of its seeming simplicity, this is one of the fundamental problems in micro-fluidics [99, 114–117]. Before addressing various aspects of this problem, we remind that the relevant dimensionless numbers for the dynamics of a drop spreading on a dry wall are the impact Weber number (the ratio of the inertia over the surface tension),

$$We = \frac{\rho_l U_0^2 D_0}{\sigma}, \quad (4.4)$$

and the Reynolds number (the ratio of the inertia over the viscous force),

$$Re = \frac{U_0 D_0}{\nu_l}. \quad (4.5)$$

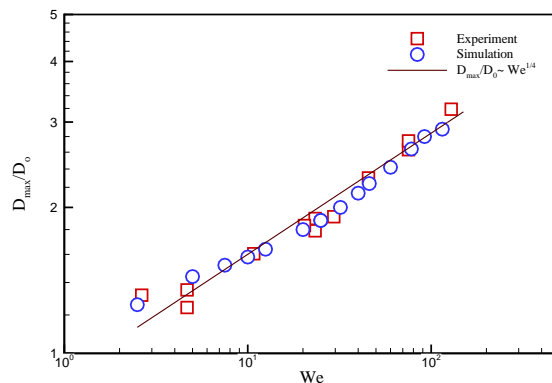


Figure 4.4: The reduced maximum diameter of the spreading drop as a function of the Weber number. Circle: ELBM simulation; Square: Experimental data [6]. Solid line corresponds to the scaling law (4.6).

Here D_0 is the initial drop diameter, U_0 is the impact velocity, ρ_l , σ , and ν_l are the liquid density, surface tension, and liquid kinematic viscosity, respectively. In this chapter, all the parameters and variables are given in non-dimensional form using U_0 as the velocity scale, D_0 as the length scale, and the ratio D_0/U_0 as the time scale. In all simulations, unless otherwise stated, we fix the initial droplet diameter $D_0 = 100$ lattice units.

4.3.1 Drop impact on a flat superhydrophobic surface

4.3.1.1 Maximum deformation of the drop

We first consider the impact of a drop of a low viscosity liquid on a superhydrophobic surface. In the classical experiment of Clanet et al [6] a scaling law of the form,

$$D_{\max}/D_0 \sim We^{1/4}, \quad (4.6)$$

was reported for maximum deformation of the drop. In Fig. 4.4, the results of the simulations of the present model are reported and compared with the experiment [6] for a range of Weber numbers. One can clearly see that all simulations provide excellent agreement with experimental data. To the best of our knowledge, such a wide, experimentally relevant range of Weber numbers could not be addressed by lattice Boltzmann simulation for fluid-solid interface problems before. Simulations in Fig. 4.4 were performed on a $400 \times 400 \times 250$ grid.

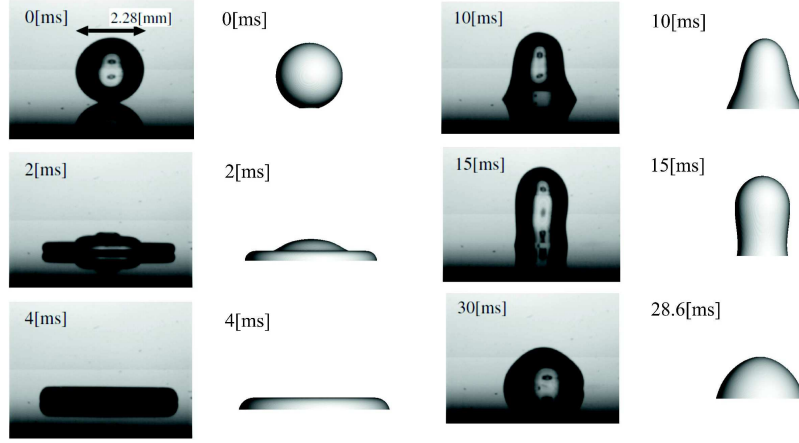


Figure 4.5: Snapshots of a drop impacting on a wettable surface; Left: Experiment [7]; Right: Simulation. $Re = 764$ and $We = 31.5$.

4.3.2 Drop impact on a flat wettable surface

Figure 4.5 shows snapshots of liquid drop impact onto a partially wet surface obtained by numerical simulations and the experiment of Ref. [7]. The grid size for the simulations was $320 \times 320 \times 200$ and the main parameters are as follows: initial droplet size $D_0 = 85$, initial impact velocity $U_0 = 0.115$, equilibrium contact angle $\theta = 90^\circ$, surface tension $\sigma = 0.278$, kinematic viscosity of the liquid $\nu_l = 0.0128$, corresponding to $Re = 764$ and $We = 31.5$. It is seen from Fig. 4.5 that ELBM reproduces well the shape of the liquid drop reported by experiment in the entire regime of spreading and recoiling phases.

The time evolution of the contact patch diameter for Fig. 4.5 is shown in Fig. 4.6. It is observed from Fig. 4.6 that the liquid drop behavior in both spreading and retracting phases reported by experiment can be repeated by numerical simulation until $t^* = tU_0/D_0 \approx 9.5$. This means that the dynamic advancing and receding contact angles are correctly estimated by the model during this time. Nevertheless, one can see that when the drop experiences the spreading phase for the second time ($t^* > 8$), the numerical results deviate from experimental prediction, that is, the dynamic advancing contact angle is underestimated during the second spreading phase (i.e., the dissipation effects are underestimated). This happens because in the present model, the evolution of the dynamic contact angle is not controlled during the simulation.

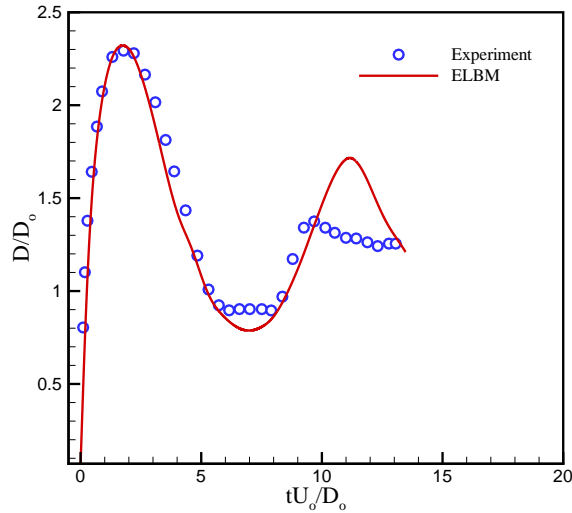


Figure 4.6: Evolution of droplet diameter on a hydrophilic surface. Line: ELBM simulation; Symbol: Experiment [7].

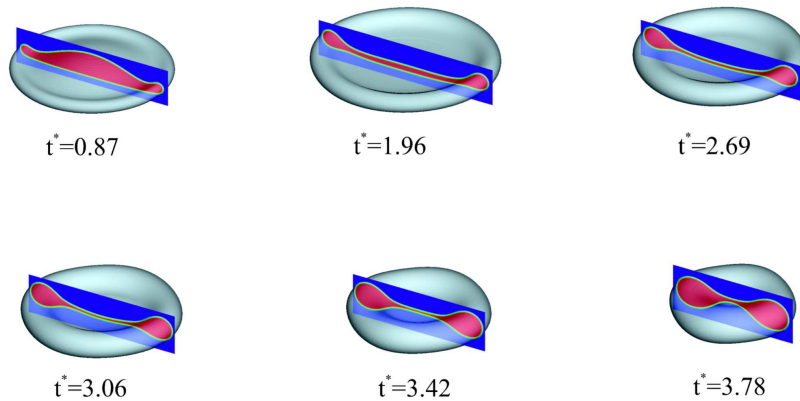


Figure 4.7: Snapshots of lamella stabilization simulation on a superhydrophobic surface at $We = 85$ and $Re = 60$.

4.3.3 Universal flow in the lamella

When a drop impacts a dry flat surface at sufficiently high Weber and Reynolds numbers, a thin liquid film (lamella) is formed during the spreading and recoiling phases. Experimental measurement of the thickness of the lamella is often difficult since the camera view is obscured by the rim. Simulation can be considered to estimate the real geometry of the spread-

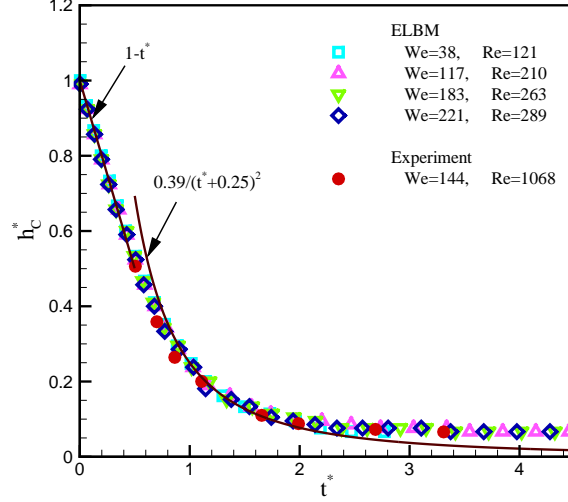


Figure 4.8: Drop impact on a hydrophilic surface. Non-dimensional thickness of the lamella at the symmetry center, $h_c^* = h_c/D_0$, versus the non-dimensional time, $t^* = tU_0/D_0$ is shown. Open symbol: ELBM simulation at various impact conditions; Full circle: Experiment [8]; Line: Analytical estimate of Ref. [5], Eq. (4.7).

ing liquid drop on the surfaces [118]. Simulation of the lamella formed by collision of binary droplets was reported in chapter 3.

We first present a simulation of drop impact onto a superhydrophobic flat surface. Our simulations show that at high Weber and Reynolds numbers the lamella gets out of contact with the solid surface soon after the drop impacts the surface. We also observed that, depending on the impact conditions the lamella can either remain attached to the rim (stable lamella) or can rupture and detach from it (unstable lamella).

Snapshots of the stable lamella on a superhydrophobic surface are shown in Fig. 4.7 at various dimensionless times $t^* = tU_0/D_0$ for $We = 85$ and $Re = 60$. In this case, the lamella starts at $t^* = 1.96$ and disappears at $t^* = 3.78$. It is visible in Fig. 4.7 that the minimum thickness of the lamella occurs during retraction phase.

Recent experimental, theoretical and numerical works [5, 8, 118] suggested that the flow in the lamella is universal, and does not depend on either the impact conditions or on the wetting properties of the flat surface. In particular, the following estimate was proposed in [5] for the evolution of the non-dimensional height $h_c^* = h_c/D_0$ of the lamella at the symmetry center

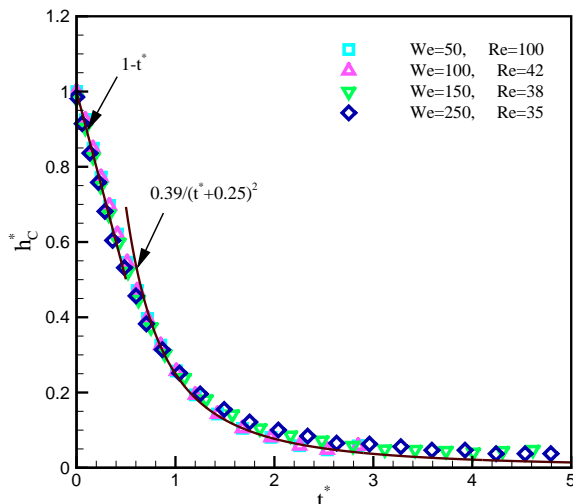


Figure 4.9: Drop impact on a superhydrophobic surface. Non-dimensional thickness of the lamella at the symmetry center, $h_c^* = h_c/D_0$, versus the non-dimensional time, $t^* = tU_0/D_0$ is shown. Open symbol: ELBM simulation at various impact conditions; Line: Analytical estimate of Ref. [5], Eq. (4.7).

versus the non-dimensional time $t^* = tU_0/D_0$:

$$h_c^* = \begin{cases} 1 - t^* & \text{for } t^* < 0.4, \\ 0.39/(0.25 + t^*)^2 & \text{for } 0.7 < t^* < t_{visc}^*, \end{cases} \quad (4.7)$$

where $t_{visc}^* \gg 0.7$ is the time when the advancing lamella attains its minimal thickness determined by the boundary layer [118]. In Fig. 4.8, we show the thickness of the lamella h_c^* at the symmetry center for various impact conditions on the hydrophilic surface. Results are compared with the experiment of Bakshi et al. [8] where a drop striking onto a spherical target was investigated. Note that, according to [8], the spherical target rather than a flat surface was used in the experiment solely for the purpose of visualizing the lamella, and the results of this experiment were used in [5] to validate the flat surface theoretical results. It is clear from Fig. 4.8 that the simulation results are in excellent agreement with the experiment. Also, one can see that the theoretical approximation for the height of the lamella at the symmetry axis (4.7) is well captured by numerical simulations for various drop impact conditions.

Similar results but for the superhydrophobic wall are shown in Fig. 4.9. It is clearly visible that simulation results are in close agreement with the uni-

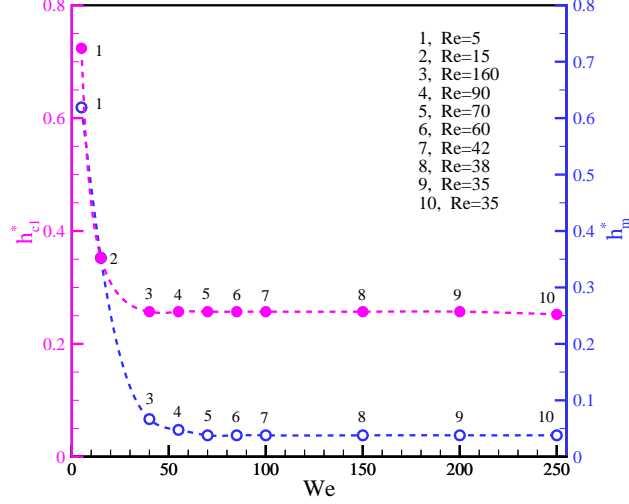


Figure 4.10: Drop impact onto a superhydrophobic surface. Thickness of the lamella as a function of the impact Weber number. Full circl: ELBM simulation result for the thickness of the lamella at the symmetry axis, at the time instant $t^* = 1$: $h_{c1}^* = h_c^*(1)$; Dashed lines: Fitting curve of the numerical results to guide the eye. Asymptotic values for h_{c1}^* for $We > 40$: $h_{c1}^* = 0.2571$ (ELBM); $h_{c1}^* = 0.2496$ (Ref. [5])). Open circle: ELBM simulation result for the minimal thickness of the lamella h_m^* .

versal lamella flow estimates (4.7) also in this case. This confirms that the flow in the lamella is essentially independent of the wettability properties of the substrate. It was demonstrated in [5] that at a typical time instant $t^* = 1$, the range of impact conditions corresponding to the universal flow in lamella requires $Re \gg 17$ and $We \gg 2.5$. In order to evaluate the corresponding range of impact conditions in our simulations, we used the case of the superhydrophobic surface to obtain the thickness of the lammela h_{c1}^* at the symmetry center, at the time instant $t^* = 1$ for various drop impact conditions. Simulation results for the thickness h_{c1}^* are shown in Fig. 4.10 for various Reynolds and Weber numbers. The reported data in Fig. 4.10 confirms that the characteristic thickness at $t^* = 1$ reaches the constant value $h_{c1}^* \approx 0.2571$ for $We > 40$, which is remarkably close to the value predicted by Eq. (4.7) ($h_{c1}^* \approx 0.2496$). Thus, the universality range for the flow in the lamella in our simulations is $We > 40$. Finally, the minimal lamella thickness h_m^* is also shown in Fig. 4.10. One can observe from Fig. 4.10 that h_m^* is constant in the same range of Weber numbers.

4.4 Summary and Conclusions

In this chapter we extended the proposed entropic lattice Boltzmann model for two-phase flows [88] to the simulation of wetting and spreading phenomena involving interface and contact line dynamics on the flat substrates. The relevant numerical simulations demonstrate that the model proposed here brings about a substantial increase in the operating range of the lattice Boltzmann simulations for multiphase flows. It should be stressed that such this simulations were not possible due to lack of entropy consideration in prior multiphase LB models . Simulation of the drop impact onto a flat substrate at both large Weber and Reynolds numbers was achievable due to use of entropic approach to stabilize numerical method together with polynomial equation of state to attain large density ratio. ELBM was applied to a range fluid-solid interface problems, from the validation tests to complex phenomena of drop impacts of substrates with different wettability properties. The results of simulations were found overall to be in excellent quantitative agreement with experiments and theoretical estimates. This suggest that the present ELBM is a valuable alternative for simulation of the fluid-solid interfaces.

Chapter 5

Capillary driven flows

In this chapter, the capillary-driven flow of a wetting liquid inside circular cylinders as well as the vertical wicking through twisted yarns are simulated. By comparing simulation results with theoretical predictions for the evolution of the meniscus height in a capillary tube, we demonstrate that the present approach can be used to model the hydrodynamic behavior inside capillary tubes. It is shown that in the case of zero gravity, the liquid column inside the tube rises faster by increasing the tube radius, as expected. We also present the simulation results for the evolution of wicking in twisted yarns.

5.1 Introduction

The coexistence of gaseous, liquid and solid phases in solid pores gives rise to wide range of interfacial phenomena that, for example, lead to spreading of liquid drops on solid surfaces, liquid rising in narrow tubes, wicking in textiles and penetrating liquid into porous media. These phenomena are partially attributed to capillarity which determines retention and movement of water through solids. Hence, they are of great importance in a variety of environmental and engineering problems [119].

The liquid rising in capillary tubes is the most simplest capillary phenomenon, but it plays an important role for understanding of complex behavior of fluids penetrated into porous media. Thus many attempts have been dedicated to analyze the rise of fluids in capillary tubes. The pioneer workers, Bell and Cameron [120] studied the flow driven by capillarity and resisted only by viscous losses in a tube at zero gravity condition. They showed that the position of the imbibition front advances in time according

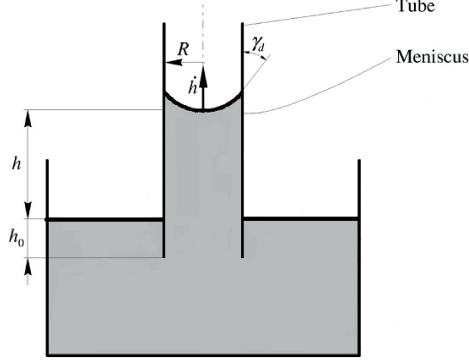


Figure 5.1: Schematic representation of the geometry used in simulation of capillary rise in a tube. The h_0 is the length of the part of the capillary tube dipped into liquid, h is the meniscus height and \dot{h} implies the meniscus velocity. The R and γ_d are the tube radius and the dynamic contact angle, respectively.

to $h \sim t^{1/2}$. A few years later Washburn [110] computed the proportional constant for the case of a tube with a circular cross-section, and found that it depends on the radius of the tube and the properties of the liquid: viscosity, surface tension, and advancing contact angle.

In the classical analysis by Washburn, the flow field inside the tube is assumed to be fully developed (Poiseuille flow). By equating the viscous damping force to the net driving force due to surface tension and gravity, and including inertia and entrance effects, the evolution of the meniscus rise can be computed by solving of the following second order nonlinear differential equation [110, 121]:

$$\rho_l h \frac{d^2 h}{dt^2} + \frac{8\mu_l(h + h_0)}{R^2} \frac{dh}{dt} + \frac{1}{4}\rho_l \left(\frac{dh}{dt}\right)^2 + \rho_l g h = \frac{2\sigma \cos \gamma_d}{R}, \quad (5.1)$$

where R is the tube radius, h_0 stands for the tube's immersion depth into the liquid, $h(t)$ is the position of the meniscus center point and the dh/dt and d^2h/dt^2 imply the velocity and the acceleration of the meniscus rise, respectively. In Eq. (5.1) the μ_l , ρ_l and σ are the liquid dynamic viscosity, liquid density and the surface tension, respectively. It was shown in [122, 123] that the contact angle γ_d rather than being a constant value is dependent on the velocity of meniscus which leads to concept of the dynamic contact angle. To measure the dynamic contact angle during the rise of the meniscus along the tube, number of empirical correlations have been studied in

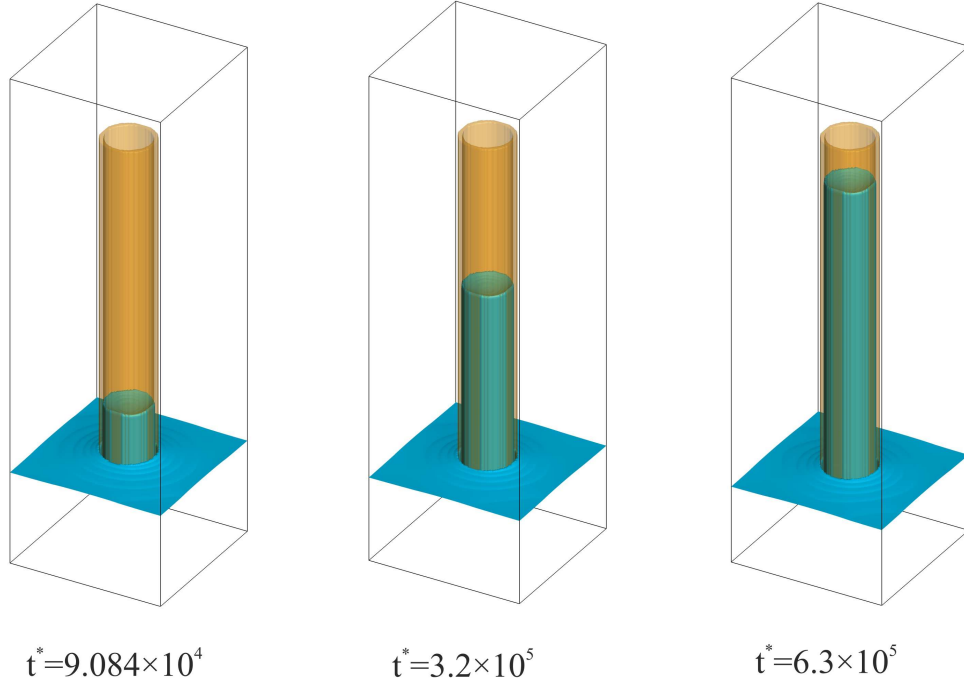


Figure 5.2: Different snapshots of three dimensional simulation of capillary rise with no gravity ($g^* = 0$). The tube radius and static contact angle are $R^* = R/h^+ = 670$ and $\gamma_s = 36^\circ$, respectively.

literature. In this study, the commonly accepted correlation proposed by Jiang et al. [123] which is based on experimental data by Hoffman [122] is used to compute the dynamic contact angle γ_d . For given liquid static contact angle γ_s this correlation reads:

$$\cos\gamma_d = \cos\gamma_s - (1 + \cos\gamma_s)\tanh(4.96\text{Ca}^{0.702}). \quad (5.2)$$

where the capillary number $\text{Ca} = \mu_l \dot{h} / \sigma$ is the ratio of viscous forces to interfacial forces at the liquid-vapor interface.

Numerical solution of Eq. (5.1) for meniscus height $h(t)$, provides a useful benchmark test for methods used for simulation of capillarity. Here in this chapter, first the capillary driven flow inside the circular cylinders is simulated and then the corresponding results are compared with those computed by means of Eq. (5.1). After validation of the present ELBM model, in the second part of this chapter, the transport of liquids through twisted yarns is simulated. We model a simple stack of twisted cylinders to mimic a single twisted yarn structure.

5.2 Results and discussion

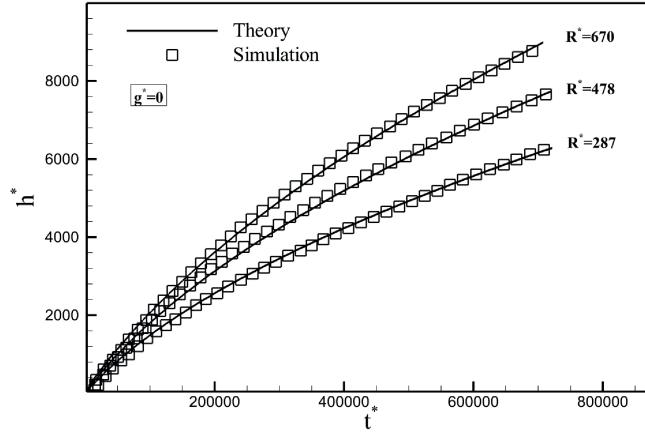
5.2.1 Capillary rise in circular cylinders

When a capillary tube of small diameter is dipped into free water, a meniscus forms in the tube due to the contact angle between liquid and the tube walls, and minimum surface energy requirements. The smaller the tube radius, the larger the degree of curvature and the pressure difference across the liquid-vapor interface. This pressure difference causes liquid to rise into the capillary until the upward capillary force is balanced by the weight of the liquid column. So, the fluid properties, contact angle, gravity and tube radius are the parameters whose play a significant role in liquid rising in tubes. Thus, using numerical simulations, we first measure the location of the liquid column for tubes with different radii at zero gravity and then we investigate the influence of gravity on the capillary rise for a capillary tube with fixed radius.

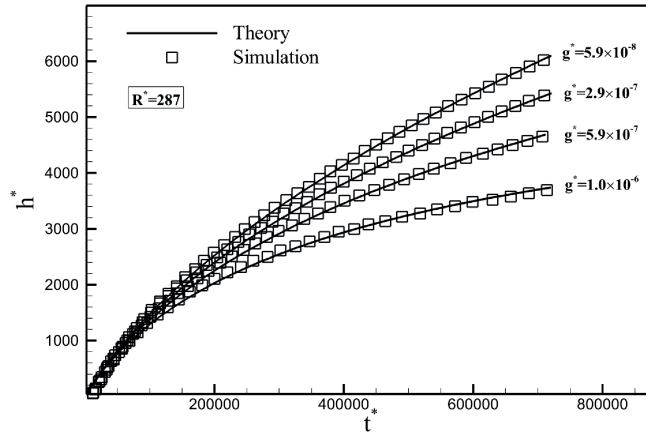
For the present work we have performed the simulation of liquid rising in tubes as seen in Fig. 5.2. We have applied the periodic boundary conditions for all domain boundaries excepted the top and bottom. A solid boundary condition is employed for the top and bottom of the computational domain. All simulations, unless otherwise stated, were performed on a $240 \times 240 \times 672$ grid nodes. Parameters of the simulated fluid presented in this section are: $\rho_l = 7.82$ (liquid density), $\rho_v = 0.071$ (vapor density), $\mu_l = 0.375$, (liquid dynamic viscosity), $\sigma = 0.353$ (surface tension) and $h_0 = 50$ (tube's immersion depth); all in lattice units. The static contact angle between liquid and solid wall is kept constant to $\gamma_s = 36^\circ$ for all simulations done for capillary rise in tube.

To present our simulation results in dimensionless form, we define the non-dimensional parameters $t^* = t/t^+$ (non-dimensional time), $h^* = h/h^+$ (non-dimensional height) and g^* where the characteristic time t^+ and length scale h^+ are given by $t^+ = \mu_l^3/(\rho_l\sigma^2)$ and $h^+ = \mu_l^2/(\rho_l\sigma)$, respectively. The dimensionless number $g^* = \mu_l^4 g/(\rho_l\sigma^3)$ is also defined for gravity.

Figure 5.3 shows our simulation results for the height of the liquid column as function of time. In Fig. 5.3 the effect of the tube radius and the gravity on the rise of liquid in a capillary tube are investigated. It is seen from Fig. 5.3 that the results obtained from numerical simulation (square symbols) are in an excellent agreement with numerical solution of Eq. (5.1) (solid line). Capillary simulations for different tube radii at zero gravity (Fig. 5.3(a)) demonstrate that the fluid rises faster along the tube by increasing the tube radius as predicted by Washburn equation (5.1). We also plot the evolution of the meniscus rise by changing the gravity for a tube of constant



(a)



(b)

Figure 5.3: Comparison of results obtained from simulations (square symbol) with those predicted by Eq. (5.1) (solid line). (a) Evolution of the meniscus height for tubes with different radii at zero gravity ($g^* = 0$). (b) The height of liquid column as a function of time for different gravitational forces in a tube with radius $R^* = R/h^+ = 287$.

radius. It is evident from Fig. 5.3(b) that by increasing the gravity, since the amount of the gravitational resistive force becomes larger, the fluid column rises slower.

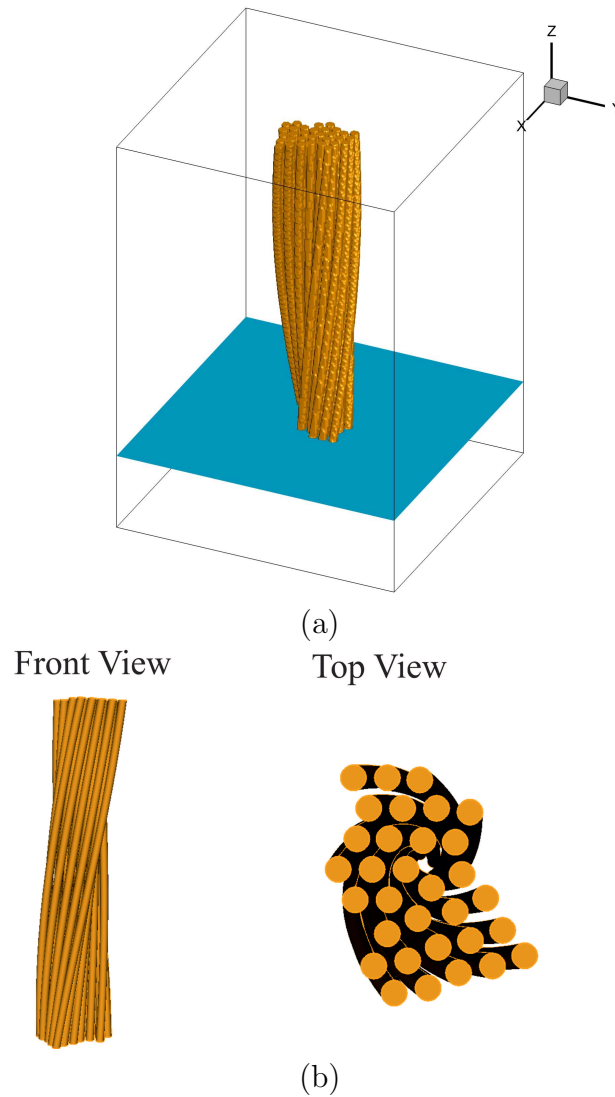


Figure 5.4: (a) The setup used for simulation of wicking in a twisted yarn. (b) The front view as well as the cross-sectional view of the yarn containing 32 twisted fibers.

5.2.2 Wicking in twisted yarns

A textile is an assembly of yarns containing fibers. Yarns can include between 1 and around 100 fibers of a few microns to one millimeter diameter each. Transport of water through textile play a very important role in deciding comfort, dyeing of textile fabrics, liquid filtration and so on [124]. The spontaneous flow of water or wicking occurs due to a pressure differential or capillary action. The complex contours formed by the fibers in the yarn

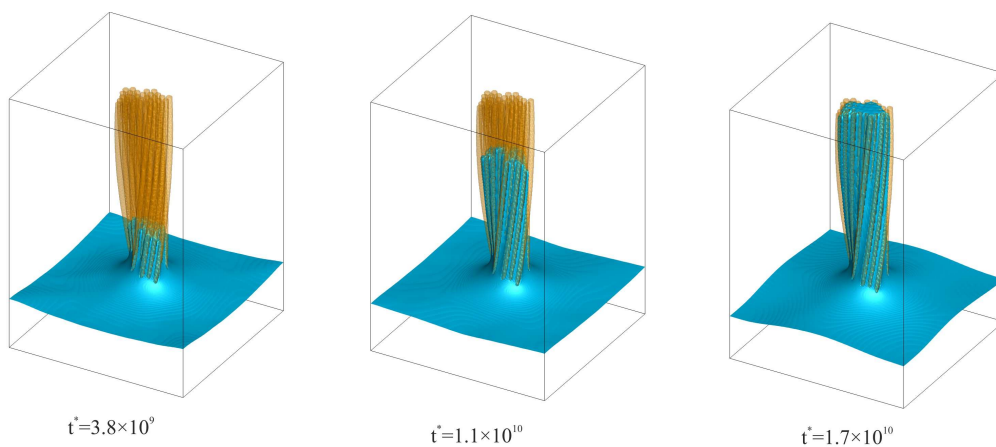


Figure 5.5: Selected snapshots from simulations showing the transport of liquid through a twisted yarn. The static contact angle is $\gamma_s = 5^\circ$. To visualize the water through the fibers, we made the yarn structure transparent.

and the yarns in the fabric constitute the boundaries of channel along the water flows. Therefore, the rate of travel of liquid water is governed by the fiber arrangements in yarns which control capillary size and shape. In general, wicking can only occur when a liquid wets the fibers assembled with capillary space between them. The resulting capillary forces that arise from wetting of the fabric surface due to pressure difference created by surface tension across the curved liquid-vapor interface derive the liquid into the capillary spaces. Capillary forces are governed by the liquid properties, the liquid-solid surface interactions and the geometric configurations of the pore structure in the medium. Since the capillary forces are caused by wetting, wicking is a consequence of spontaneous wetting in a capillary system [124]. Here in this section, we aim to simulate the wicking in a twisted yarn to test the capability of the present ELBM model for simulation of complex capillary systems. To mimic a single twisted yarn structure, we consider a stack of twisted cylinders as fibers assembled with the capillary space varying from 3 to 25 grid points.

Figure 5.4 shows simulation setup together with the geometrical configuration of yarn structure. The twisted yarn in Fig. 5.4(b) contains 32 fibers of 625 grid points height and 15 grid points diameter each. Parameters used for wicking simulations are: $\rho_l = 7.82$, $\rho_v = 0.071$, $\mu_l = 0.012$ and $\sigma = 0.353$; all in lattice units.

Figure 5.5 shows different snapshots for simulation of wicking in a twisted yarn. From Fig. 5.5 one can observe that how the water climbs up between

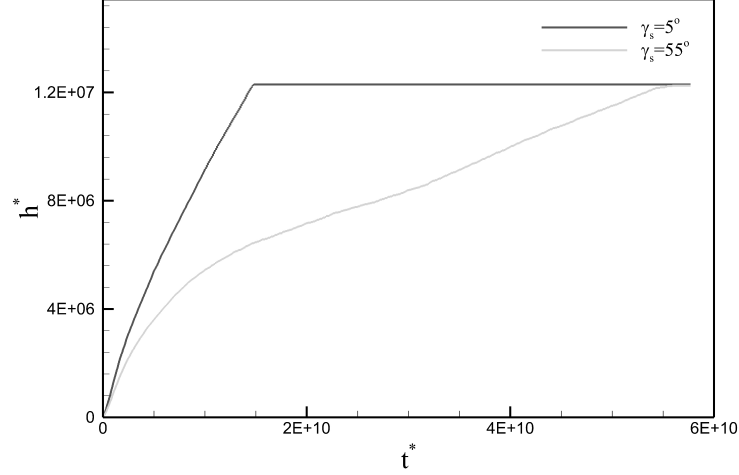


Figure 5.6: Simulation results for the evolution of wicking through the twisted yarn given in Fig. 5.4 for two different wettabilities. The h^* is determined as the maximum location of the wicking height through the fibers in each time step.

the twisted fibers. The sequential images in Fig. 5.5 show that due to geometric configurations of the yarn structure (the fiber arrangements), the liquid rises faster in the middle of the yarn structure than the sides.

Next, we explore the wettability effect on the evolution of wicking height in a twisted yarn. In Fig. 5.6, we plot the wicking height as a function of time for two different equilibrium contact angles. In Fig. 5.6 the h^* is defined as the maximum height of wicking through the fibers at each time step. It is evident from Fig. 5.6 that in the case in which fibers are fully wetted by liquid ($\gamma_s = 5^\circ$), the liquid rises through the yarn faster than that with static contact angle of $\gamma_s = 55^\circ$ as expected, and hence the meniscus arrives to top of the yarn structure very earlier.

5.3 Summary and Conclusions

In this chapter we have tested the use of our ELBM model in the study of capillary phenomena. To this end, the method was validated by comparing the simulation results with the existing macroscopic theory of capillary rise in cylindrical tubes proposed by Washburn. We first simulated the evolution of meniscus rise in tubes of different radii at zero gravity and then compared the numerical simulations with those predicted by Wash-

burn equation. Furthermore, for a tube with fixed radius, the effect of gravity on meniscus height was investigated by comparing our results with theoretical predictions. The results were promising in both cases. Next, as a more complex capillary system, we simulated the transport of liquid through twisted yarns and investigated the effect of wettability properties of fabric surfaces on the evolution of the wicking height. One motivation for simulation of wicking in the twisted yarn was to investigate the possibility to use our method to model wicking in textiles and in particular imbibition of fluid in complex porous media. However, further work to investigate the effect of wall boundary conditions on the dynamic behavior of wicking would allow further insight into different aspects of wicking phenomena and should be the subject of future work.

Chapter 6

Tumbling rebound of high viscous drops from sublimating slopes

In this chapter using experimental observations of our collaborator (LTNT-ETHZ group) together with numerical simulations, we have uncovered a drop rebound regime, characteristic of highly viscous liquids impacting tilted sublimating surfaces. Here the drops, rather than showing a slide, spread, recoil, and rebound behavior, exhibit a prompt tumbling rebound. As a result, glycerol surprisingly rebounds faster than three orders of magnitude less viscous water. When a viscous drop impacts a sublimating surface, part of its initial linear momentum is converted into angular momentum: ELBM simulations confirmed that tumbling owes its appearance to the rapid transition of the internal angular velocity prior to rebound to a constant value, as in a tumbling solid body.

6.1 Introduction

Despite its illusory simplicity, the interaction between a liquid drop and a solid surface during impact is a fascinating fluidics problem, combining a variety of phenomena at multiple temporal and spatial scales [99, 125, 126]. These include splash [127, 128], phase-change-induced surface levitation [129–131], skating on a film of trapped air [132, 133], and rebounding [11, 13, 14]. Recently [129], it was demonstrated that drops can rebound after impact on an extremely cold solid carbon dioxide surface (at -79°C , well below the limit of even homogeneous nucleation of water), because of the formation of a sublimated vapor layer acting both as impact cushion and thermal insulator, enabling drops to hover and rebound without

freezing. A sublimating surface is different from aerodynamically assisted surface levitation [134] and from the Leidenfrost effect [130, 131, 135, 136], in the sense that it is independent from liquid properties, such as boiling temperature, and there is no loss of drop mass due to its own boiling (as in the Leidenfrost phenomenon). Of course, in both cases an intervening layer is generated between the drop and the substrate. Sublimating surfaces can thus be used to study the contactless interaction of virtually any liquid, such as the highly viscous liquids used here. Also, they enable the study of phenomena expected from a superhydrophobic surface with extreme performance [137] (very high contact angles and very low hysteresis), providing further motivation for the fabrication and subsequent study of such surfaces. In the present chapter, we demonstrate and explain the existence of a prompt tumbling rebound mechanism, in which a small conversion of translational to rotational kinetic energy, at nonaxisymmetric impact conditions, promotes fast drop rebound despite high viscosities.

By focusing on nonaxisymmetric impact conditions at increasing viscosity, we observe a transition from an expected slide, spread, recoil, and rebound mechanism (see Figs 6.1(a) and 6.1(b)) to a tumbling behavior, enabling the prompt rebound of highly viscous liquids such as glycerol (Fig. 6.1(c)). Here, after an initial viscosity-limited and impact-driven deformation phase, the drops simply tumble off the surface, rebounding faster than three orders of magnitude less viscous (water) drops. Three-dimensional ELBM simulations confirmed the tumbling rebound of a high viscous drop ($Oh = 3.2$) on tilted surfaces also. The behavior at high viscosities is aided by the contactless nature of the impact and was not observed on classical superhydrophobic surfaces, where an increase of viscosity can protract the rebound time [138] or even prevent rebound.

A representative schematic of a plausible scenario of contactless drop impact on a tilted sublimating surface is shown in Fig. 6.1(a): After impact, the drop simultaneously spreads. The presence of the vapor layer due to substrate sublimation slides down the slope and significantly reduces friction between the drop and the solid substrate, playing a role similar to that of the lubricating melted liquid water layer in ice skating [139]. The drop subsequently bounces off the surface after a certain rebound time t_{reb} , defined as the time lag between the impact and the lift-off. The corresponding downhill distance traveled by the drop L_{slide} was measured from the impact point to the lift-off point [see Fig. 6.1(b)].

To provide insight into the appearance of tumbling, the forcing free-energy based model presented in chapter 2 is used. The impacting liquid was modeled as a drop on a superhydrophobic surface [79] with the contact angle $\theta = 180^\circ$ and partial slip at the wall (see section 2.6 for details on ap-

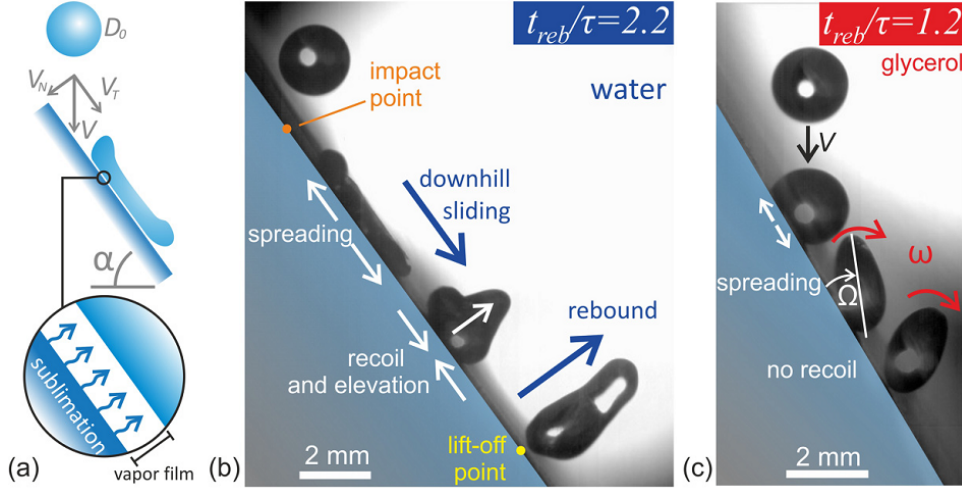


Figure 6.1: Experimental observations for drop impact onto a tilted carbon dioxide sublimating surface [9]: (a) schematic and image sequence of (b) water and (c) glycerol drop impacts. The impact conditions are $\alpha = 55^\circ$, $We = \rho V^2 D_0 / \sigma = 86$ and $Oh = \mu / \sqrt{\rho \sigma D_0} = 2.7 \times 10^{-3}$ for water and $\alpha = 60^\circ$, $We = 121$ and $Oh = 3.2$ for glycerol. The nondimensional rebound time is $t_{reb}/\tau = 2.2$ for water and $t_{reb}/\tau = 1.2$ for glycerol. Also indicated are the normal V_N and tangential V_T components of impact velocity as well as the substrate tilt angle α .

plication of boundary conditions for the lattice Boltzmann populations at the wall). Partial slip at the wall was imposed using the slip coefficient k obtained from the experimental measurements, presented below. The tangential velocity at the wall nodes was made equal to $k\hat{V}_t$, where \hat{V}_t is the tangential velocity at the neighboring node within the fluid, in the direction perpendicular to wall, thus locally enforcing the partial slip observed in the experiments. This procedure helps us circumvent explicit modeling of the submicron gas layer trapped between the drop and the substrate. The validity of the numerical simulations is confirmed *a posteriori* from the good prediction of the rebound time, angular velocity, and drop shape, in comparison to the experiments.

6. TUMBLING REBOUND OF HIGH VISCOUS DROPS FROM SUBLIMATING SLOPES

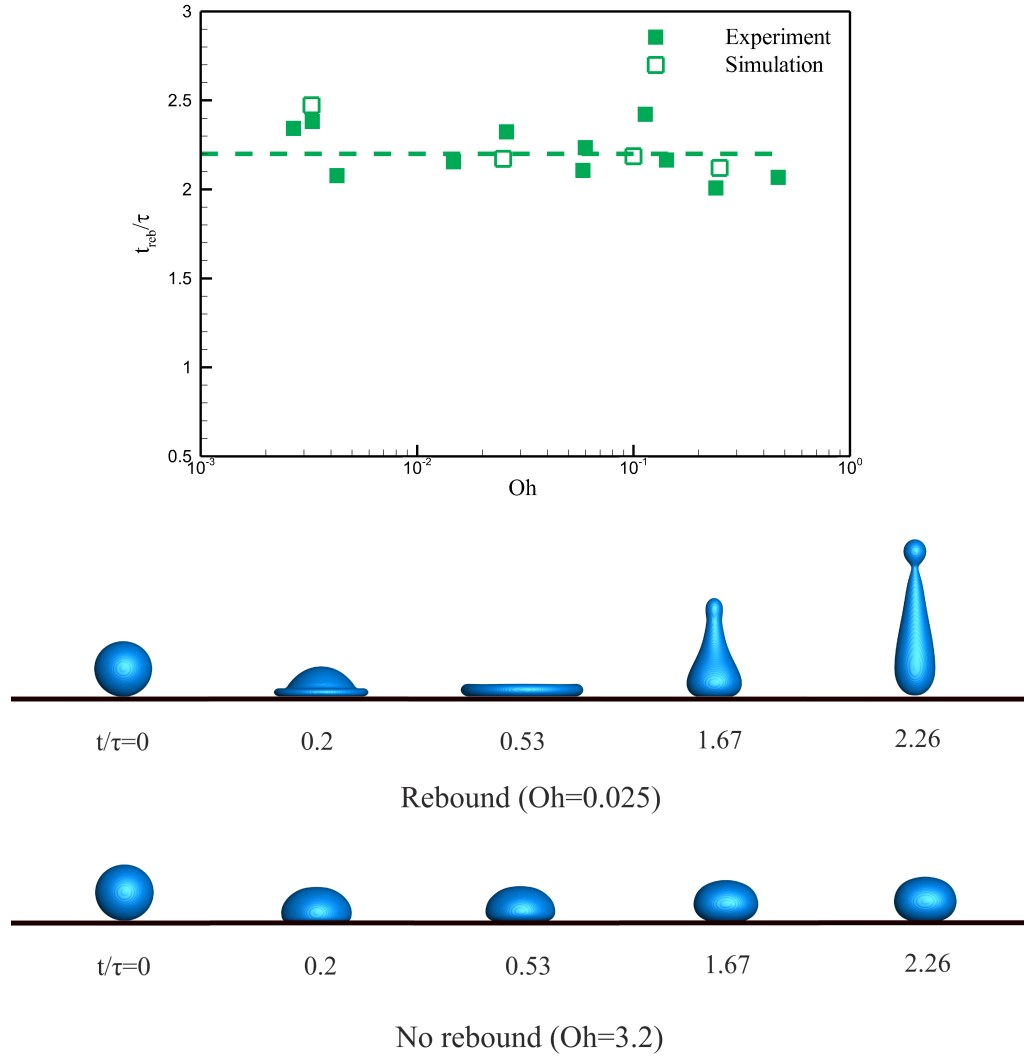


Figure 6.2: Nondimensional rebound time t_{reb}/τ as a function of the Ohnesorge number Oh for simulations (open symbols) and experiments [9] (solid symbols). Selected snapshots show the results for simulation of low viscous ($Oh = 0.025$) and high viscous drops ($Oh = 3.2$) impacting on a horizontal surface.

6.2 Results and discussion

6.2.1 Normal axisymmetric impacts

The identification of a transition in the drop dynamics at high viscosity, i.e., high Oh , can be understood by first looking at the behavior of drops during normal impact on horizontal surfaces (Fig. 6.2) and then oblique impact on tilted surfaces (Figs. 6.3 and 6.4). From Fig. 6.2, it is found that a transition from rebound to no-rebound occurs at $Oh \approx 1$, with low-viscosity drops always rebounding for $Oh < 0.6$ and high-viscosity drops unable to lift off for $Oh > 1.2$. In the in-between transition regime, either outcome is possible. The transition regime at $Oh \approx 1$ can be explained by the fact that in this range the viscous effects become of the same order as the surface energy effects and cause a rapid dissipation of the initial kinetic energy of the impacting drop: Viscous effects thus inhibit the conversion of kinetic energy into surface potential energy and back to kinetic energy, as typically occurs for relatively-low-viscosity liquids, such as water, and prohibit rebound. As shown in the inset in Fig. 6.2, at high Oh the highly viscous drops bead up to a quasispherical shape at rest and eventually roll away at the slightest perturbation, because of the absence of wetting and lateral adhesion forces due to the sublimating substrate. In the rebound regime, the rebound time follows the conventional scaling $t_{reb}/\tau = a = Const$, where $\tau = \sqrt{\rho D_0^3/8\sigma}$ and $a = 2.2 \pm 0.2$ [11, 14], with a being constant and independent of the Ohnesorge number.

6.2.2 Oblique nonaxisymmetric impacts

For nonaxisymmetric impacts on tilted sublimating surface, however, experiments together with simulations reveal a qualitative change of the rebound pattern, showing that highly viscous glycerol drops can also rebound and do this even faster than water drops. Experimental data for the characteristic sliding velocity of the drop V_{slide} , computed as the ratio L_{slide}/t_{reb} , to the tangential component of the impact velocity V_T , are plotted in Fig. 6.3 as a function of Oh . In the ideal inviscid case, assuming zero lateral adhesion forces [140] to cause drop deceleration and negligible acceleration due to gravity, the drop will continue to travel on the substrate at $V_{slide} \approx V_T$. A linear scaling $V_{slide} = kV_T$ holds for all tested liquids, with k depending on the Ohnesorge number (Fig. 6.3). For a millimetric water drop ($Oh = 2.7 \times 10^{-3}$), $k = 0.9$, remarkably close to the ideal inviscid case $k = 1$ and threefold higher than for water drops impacting on a superhydrophobic surface ($k = 0.3$, as reported previously [10]). The enhanced

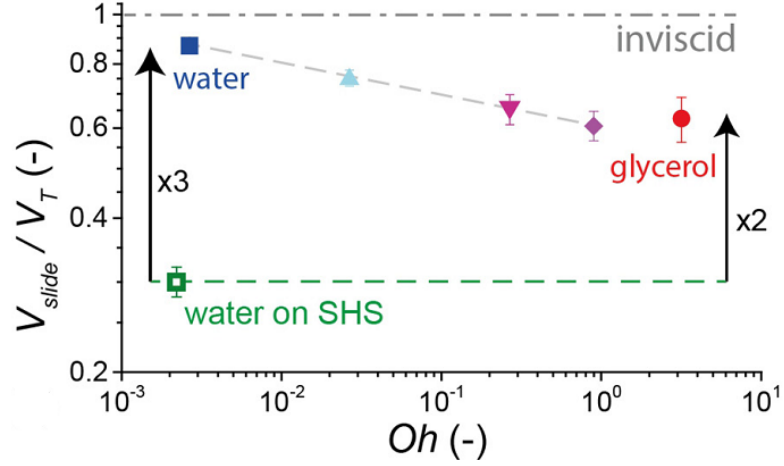


Figure 6.3: Ratio $k = V_{slide}/V_T$ as a function of Oh . The symbols denote the experimental data [9] for impacts on the sublimating substrate: Solid square, water; Upward triangle, water-glycerol mixture 40:60; Downward triangle, water-glycerol mixture 15:85; Diamond, water-glycerol mixture 7:93; Solid circle, glycerol; and Open square, water drop impact on a superhydrophobic surface (SHS) (data from [10]).

sliding on a sublimating surface, even with respect to a superhydrophobic surface, is a consequence of the contactless regime, in which lateral adhesion forces are absent. The value of k decreases with increasing Ohnesorge number (see Fig. 6.3) and subsequently plateaus, remaining approximately constant at the value of $k \approx 0.6$ for $Oh > 1$. Values of $k < 1$ denote that frictional losses in the vapor layer trapped between the drop and the substrate, despite being smaller than on superhydrophobic surfaces, are not negligible. As confirmed by numerical simulations, viscous losses occur mainly in the first (spreading) phase of the impact, over a time scale t_{fr} , as a result of the drop rapid deformation and wall friction. Thus, the friction force can be estimated as $F_{fr} \approx m(V_T - V_{Slide})/t_{fr} = mV_T(1 - k)/t_{fr}$, which we will use below to estimate the drop angular velocity during tumbling.

Figure 6.4(a) shows the variation of the rebound time as a function of the tangential velocity for water and glycerol. Unsurprisingly, for water, the rebound time remains constant for a wide range of tangential impact velocity, up to $V_T \approx 2m/s$, and $t_{reb}/\tau = 2.2$ still holds, meaning that the spreading and recoiling process of the drop is not affected by the simultaneous downward sliding. In other words, the usual picture of the inertia-capillarity interplay during the conventional rebound still holds and the viscosity (if low) does not play a prominent role. Only for $V_T > 2m/s$, the impact devi-

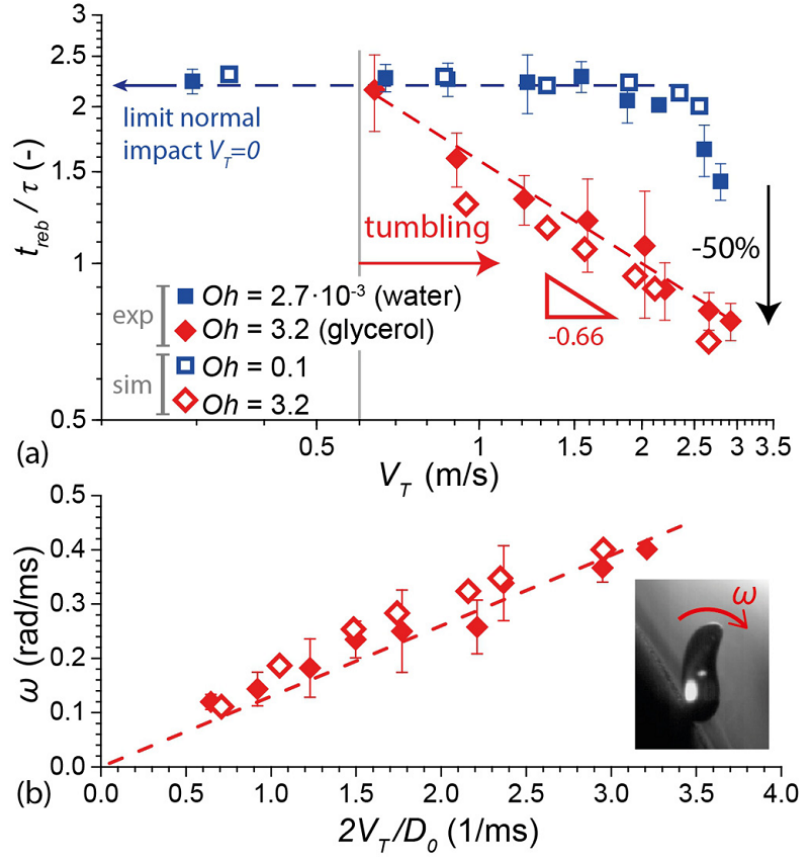


Figure 6.4: (a) Nondimensional rebound time t_{reb}/τ as a function of the tangential velocity V_T : both experimental data [9] and numerical results for water and glycerol are included. The legend reports values of Oh . (b) Angular velocity ω of highly viscous glycerol drop scales linearly with $2V_T/D_0$. Closed symbols show the results of experiments [9] and open symbols simulations. The fitting line is $\omega = 0.13(2V_T/D_0)$.

ates from the classical axisymmetric behavior: As demonstrated recently by Bird et al. [14] in the context of engineered superhydrophobic surfaces, the nonaxisymmetric spreading and recoiling can lead to a reduction of drop rebound time down to $t_{reb}/\tau \approx 1.5$ for the maximum tested tangential velocity ($V_T \approx 3m/s$).

However, for highly viscous glycerol drops ($Oh = 3.2$) a fundamentally different rebound mechanism is identified, as highlighted previously in Fig. 6.1(c). The drop rebound starts at $V_T \approx 0.6m/s$ with a rebound time of $t_{reb}/\tau \approx 2.2$ (see Fig. 6.4(a)), similar to that of water at the same V_T , and is significantly reduces down to a minimum of $t_{reb}/\tau \approx 0.7$ at the highest

tested tangential velocity $V_T = 3m/s$. The glycerol rebound time is thus half that of water above $V_T = 3m/s$, despite the fact that glycerol drops do not rebound for $V_T < 0.6m/s$ and even with the three orders of magnitude higher viscosity of glycerol compared to water (Fig. 6.4(a)).

The reason for faster rebound at high viscosity is that, after some spreading and limited sliding, the drop tumbles off without recoiling. The drop rapidly detaches from the surface by rotating almost as a rigid body. The transition to a different rebound regime at high viscosities can be understood by comparing the drop relaxation time $t_{rel} \propto \mu D_0 / 2\sigma$ [141] to the characteristic oscillation time τ , whose ratio is proportional to Oh . Indeed, at high viscosities, when $t_{rel}/\tau \sim Oh > 1$, the longer t_{rel} delays drop recoiling and leads to sustaining the drop rotational energy during tumbling. Also, the distance traveled by the drop through sliding $L_{slide} = V_{slide} t_{reb}$ is significantly reduced for high Oh , since both V_{slide} and t_{reb} are reduced with increasing Oh , as shown in Figs. 6.3 and 6.4, respectively. Figure 6.4(b) shows that the average drop angular (spinning) velocity ω scales linearly with the ratio $2V_T/D_0$. The average angular velocity ω was defined and measured as the ratio of the angle formed by the major axis of the flattened drop and the substrate at the moment of drop lift-off (Ω_{reb}), and the rebound time t_{reb} . Indeed, since the balance of the drop angular momentum gives $F_{fr} D_0 / 2 \approx I\omega / t_{fr}$, on the basis of the above estimation for F_{fr} we obtain $\omega \approx (1 - k)(2V_T/D_0)$, confirming the linear correlation. Figure 6.5 shows the value of Ω_{reb} as a function of the impact tangential velocity V_T ; Ω_{reb} is practically constant in the range $\sim 60^\circ - 70^\circ$ for $V_T > 1.3m/s$. As such, an increase of angular velocity ω , corresponding to a faster spinning, is responsible for a significant reduction of the rebound time t_{reb} for very viscous liquids with $Oh > 1$ (glycerol, $Oh = 3.2$) compared to the three orders of magnitude less viscous water.

A comparison of the drop shape evolution resulting from ELBM simulations between the low viscosity regime $Oh = 0.1$ (see Fig. 6.6(a)) and the high-viscosity regime $Oh = 3.2$ (see Fig. 6.6(b)) highlights the same trend observed by experiments, confirming the limited role of viscosity on drop dynamics in the regime $Oh < 1$ and the occurrence of tumbling rebound for $Oh > 1$.

The occurrence of tumbling can be better understood within the framework of vorticity generation from a boundary (shear) layer. Injection of vorticity through a shear layer was studied, in particular by [142], in a direct numerical simulation of a drop normal impact onto a flat surface. Transition to tumbling under shear is a common scenario also away from boundaries [143]. In the present study, the tilted slope provides an off-center impact condition and thus can cause generation of the angular momentum. Hence, when a

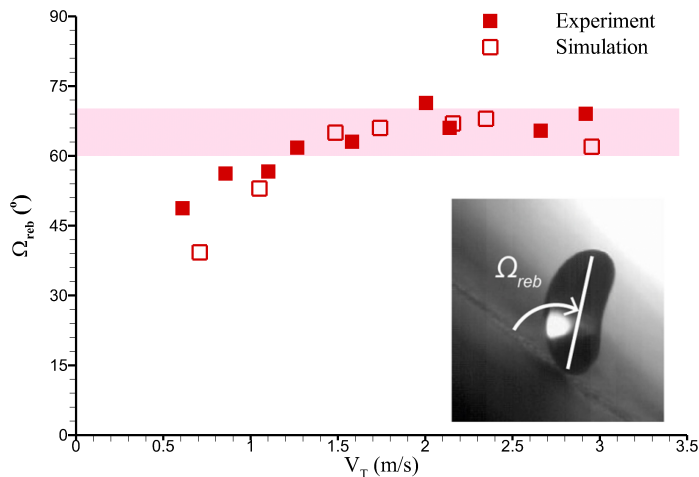


Figure 6.5: Values of the drop tilting angle at the moment of rebound Ω_{reb} as a function of the tangential component of velocity V_T for a highly viscous glycerol drop ($Oh = 3.2$). Open symbols: Simulation, closed symbols: Experiment [9].

viscous drop impacts the sublimating surface, the linear momentum of the drop is partially converted into angular momentum, providing the drop with a spin that facilitates take-off causing tumbling. Note that the energy associated with the rotation $E_r \sim mD_0^2\omega^2/8$ is small compared to the tangential component of translational kinetic energy $E_k \sim mV_T^2/2$. Since $\omega = 0.13(2V_T/D_0)$ (Fig. 6.4(b)), then $E_r/E_k \sim 10^{-2}$; that is, only about 1% of the drop initial kinetic energy is converted into rotational energy.

6.2.3 Vorticity generation and evolution

To better identify the origin of the tumbling effect, the local angular velocity was calculated from the numerical simulations as $\vec{\omega}_{loc} = |\vec{r} \times \vec{v}|/r^2$ where r is the position vector relative to the center-of-mass of the drop and \vec{v} is the relative fluid velocity at that location. The component of the vector $\vec{\omega}_{loc}$ orthogonal to the plane of symmetry of the impacting drop, is overwhelmingly dominant, i.e., two orders of magnitude larger than the other two orthogonal components, since the rotation axis is essentially perpendicular to the plane of symmetry. From this dominant component, the average instantaneous angular velocity over the drop volume $\omega(t)$ was computed: Its evolution is illustrated in Fig. 6.7 together with the characteristic snapshots of the

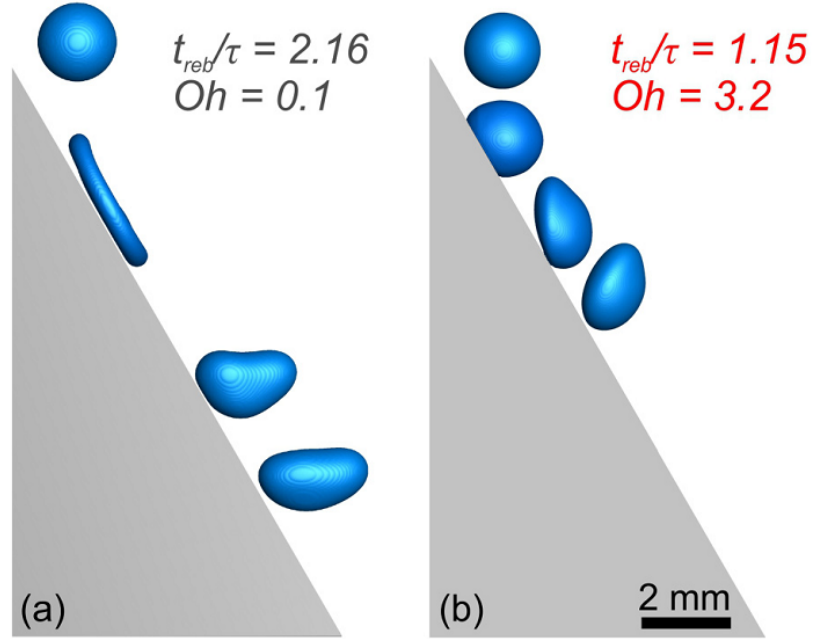


Figure 6.6: Evolution of simulated drop impacting on a sublimating slope: (a) a drop in the low-viscosity regime ($Oh = 0.1$, $We = 121$, and $\alpha = 60^\circ$) and (b) a drop in the high-viscosity regime ($Oh = 3.2$, $We = 121$, and $\alpha = 60^\circ$). The rebound time in the simulation was identified through matching the experimentally observed orientation of the drop at the rebound with the corresponding simulated image.

local angular velocity spatial distribution on the symmetry plane; ω rapidly reaches a maximum value well before rebounding, with the rotational motion initiated near the impact zone and then becoming uniform. Thereafter, ω remains practically constant through the liquid, with the drop exhibiting the behavior of a solid ready to tumble. Put differently, the oblique impact breaks the axisymmetry of the drop at the beginning of the sliding and the gain in angular momentum is thus initiated by the off-center flow reversal. If the relaxation time is large enough ($Oh > 1$), the angular momentum diffuses through the entire drop before it can recoil and the tumbling takes place.

For comparison, Fig. 6.8 shows the history of the averaged angular velocity ω in the low-viscosity regime ($Oh = 0.1$) together with the characteristic snapshots of the distribution of the local angular velocity during impact. Unlike in the case of high viscosity, the angular velocity gained initially in the impact (phases a–c in Fig. 6.8) is not sustained at a constant value

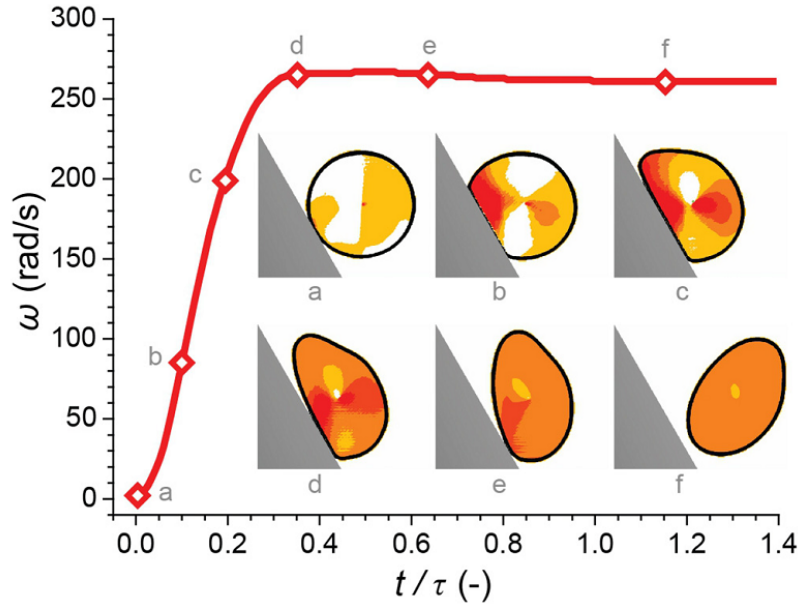


Figure 6.7: History of the average angular velocity ω of highly viscous liquid drop with $Oh = 3.2$, $We = 121$, and $\alpha = 60^\circ$ during tumbling (simulation). Propagation of the dominant angular velocity component of $\vec{\omega}_{loc}$ inside the drop is shown in the insets (a–f), at different stages of tumbling: stages a–c show the initial rise of the angular velocity shortly after the impact and stages d–f show rotation of the drop acting essentially as a solid. The drop rebounds (stage f) at $t/\tau = 1.15$. A shading or color increase corresponds to the increase of the clockwise rotation.

during the extension and sliding (phases c and d) and no solidlike tumbling is observed. At the final stage close to the rebound (phase f), a small gain of the average angular velocity is due to the merging of the dumbbell-like shape of the drop at the intermediate stage, with non-axisymmetric collapse of the rim from phase d to e. In other words, in the low-viscosity regime the fluid slips away and the rotation is not sustained.

6.3 Summary and Conclusions

Taken together, our results demonstrate and explain the existence of a prompt tumbling rebound regime for non-axisymmetric drop impact on surfaces under slip conditions, here readily realized with the help of a sublimating slope. To this end, sublimating surfaces present themselves as an interesting, easy to use platform for the study of unexplored, liquid-surface

6. TUMBLING REBOUND OF HIGH VISCOUS DROPS FROM SUBLIMATING SLOPES

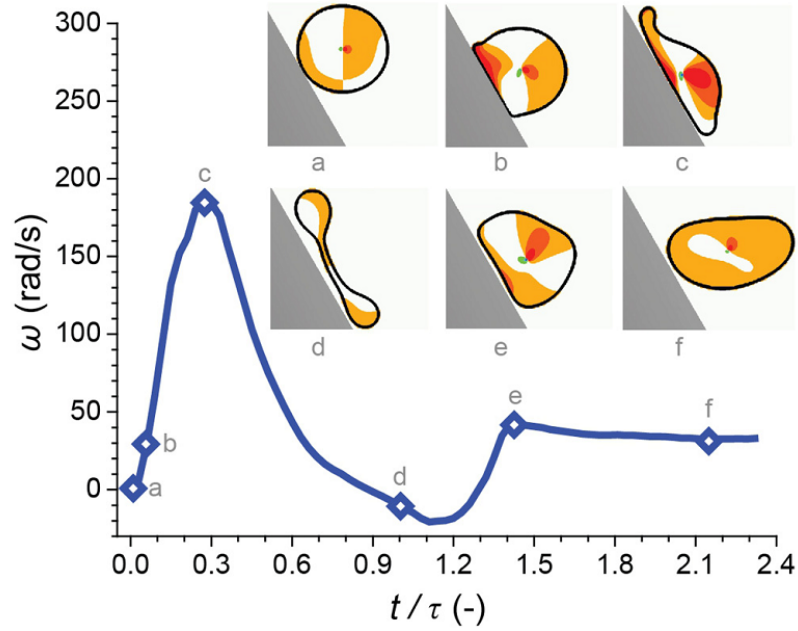


Figure 6.8: History of the average angular velocity ω of a low-viscosity liquid drop with $Oh = 0.1, We = 121$, and slope $\alpha = 60^\circ$ (simulation). Propagation of the dominant angular velocity component of $\vec{\omega}_{loc}$ inside the drop is shown in the insets (a–f), at different stages of drop impact. The drop rebounds (stage f) at $t/\tau = 2.1$. A shading or color increase corresponds to the increase of the clockwise rotation.

interactions, especially in the limit of small friction, brought about by the absence of direct contact between the liquid and the solid surface. Similar effects could be possible also on superhydrophobic surfaces, if they are fabricated to reach extreme performance. Preliminary simulations for contact angles $170^\circ < \theta < 180^\circ$ indicate that tumbling rebound could take place, opening an interesting direction for future work.

Chapter 7

Drops bouncing off macrotextures: pancake bouncing

Recent surge of interest in textured super-hydrophobic surfaces that are capable of reducing the contact time of an impinging droplet has been immense [*Bird et al., Nature 2013, Liu et al., Nature Physics 2014, Gauthier et al., Nature communications 2015*]. However, all the investigations to date have been predominantly experimental in nature. This is partly due to the lack to reliable numerical techniques that can qualitatively and quantitatively capture the physics of droplet wall interactions especially for complex walls. These surfaces have many relevant applications such as self-drying, self-cleaning, anti-icing etc.

In this chapter, a comprehensive simulation technique, the entropic lattice Boltzmann method, is shown to be capable of accurately capturing the physics of droplet wall interactions especially for the complex macrotextured surfaces. Further, we introduce new energy analysis techniques that can play a crucial role in revealing the physics of these flows and can thus lead to new rebound regimes and also discovery of new surfaces. Due the flexible nature of the simulations, we study further the surface introduced by *Liu et al., Nature 2014* in various configurations and establish the limits and advantages of this surface.

For the first time, three-dimensional simulations involving realistic complex texture are performed. The study focuses also on analyzing the flow situations beyond current experiments. We show that the experimentally observed reduction of contact time extends to higher Weber numbers, and analyze the role played by the texture density. We report a non-linear behavior of the contact time with the increase of the Weber number for imperfectly coated textures. The novel energy analysis technique presented

here discusses the interplay between the kinetic and surface energy, and the role played by the dissipation for various Weber numbers.

7.1 Introduction

Understanding of fundamental physics of interaction between the liquid, gas and solid has been at the forefront of contemporary studies. Interaction between liquid drops and solid surface during impact is one of the most beautiful and fascinating fluidics problems in physics, whose complexity derives from the possible co-existence of combinations of a variety of phenomena, occurring at multiple temporal and spatial event scales [99, 125, 144]. These include but are not limited to splash [145–149], phase-change induced surface levitation [150–154], skating [155, 156], rebounding [11, 13, 14, 157], prompt tumbling-rebound [158] and trampoline effect [159].

Surfaces with special wetting properties have profound implications in many engineering applications including power generation, transportation, water desalination, oil and gas production, and microelectronics thermal management. Particularly interesting are surfaces with extreme wetting properties, which are efficient at either repelling (hydrophobic) or attracting liquids (hydrophilic) such as water and oils but can also prevent formation of biofilms or ice [160]. The degree of surface wetting, typically measured by a drop's equilibrium contact angle, depends on the balance of the products of corresponding interfacial surface areas and surface energies. From a theoretical perspective, the contact angle of a liquid interacting with a flat solid is predicted using Young's equation. However, to achieve extreme wetting properties, the interface between the droplet and the substrate must be structured and often contains an additional gas or liquid phase [160]. For example, nano- and/or microscale roughening of a flat hydrophobic substrate yields a super-hydrophobic surface (contact angle above $\theta = 150^\circ$ and negligible contact angle hysteresis) through trapping gas. Drop repellence from hydrophobic and super-hydrophobic surfaces is an area of active research from both a fundamental perspective as well as a source of novel engineering ideas for various applications such as self-cleaning, water resistance and anti-icing [17, 99, 161–164]. Recent interest in the wetting properties of super-hydrophobic surfaces has been intense [11–14, 159, 165]. The time during which the drop stays in a contact with the solid after impact is termed contact time (or rebound time). Minimization of contact time is a central point in a rational design of hierarchically structured surfaces for anti-icing, self-cleaning and other applications [166, 167]. Reduction of contact time has been focus of recent studies [11–14, 159,

165]. Richard, Clanet, and Qu  r   [11] found that the conventional mechanism of rebound on macroscopically flat superhydrophobic surfaces (impact-spread-recoil-rebound, [11, 164, 168, 169]) scales universally with the inertia-capillarity time,

$$\tau = \sqrt{\frac{\rho_l R_0^3}{\sigma}}, \quad (7.1)$$

with ρ_l , R_0 , and σ the liquid density, drop radius, and surface tension, respectively. This scaling, $t_{\text{contact}}/\tau \approx 2.2$, is notably independent on the drop kinetic energy, and holds in a range of Weber numbers [11],

$$\text{We} = \frac{\rho_l R_0 U_0^2}{\sigma}, \quad (7.2)$$

where U_0 is the impact velocity. However, Bird et al [14] demonstrated that by adding a macro-texture (few hundred micrometers) as a ridge on the flat surface, the contact time reduces by about 37%. Recently, Liu et al [13] demonstrated that impact on a flat surface decorated with a lattice of sufficiently tall (almost a millimeter) tapered posts with a nanoscale superhydrophobic coating results in an unconventional rebound before the retraction. While the pattern of the rebounding flattened droplet gave the name of pancake bouncing to this effect, a spectacular reduction by factor four was reported for the contact time. Further experimental studies of similar macro-textures can be found in [12, 165].

Although, pancake bouncing was shown to reduce the contact time significantly, questions remain for understanding the physics behind such complex droplet-wall interactions. A parametric study (dependence on the texture geometry, quality of coating, velocity of the drop etc) can help understanding the limits and optimization of the macro-texture in [13]. Such detailed analysis and information regarding the complex droplet shape and its deformation can be made possible through simulations since it is difficult to probe in full the droplet interior with experiments. To that end, simulations of Ref. [170] were able to capture pancake bouncing in a qualitative manner. However, due to limitations of the lattice Boltzmann model used in [170], a quantitative comparison was quite restrictive. First, only a quasi-three-dimensional simulation was performed (cylindrical droplet instead of spherical) and only square posts rather than the tapered posts were considered. Another limitation was due to the high relative density of the gas phase which precluded the study of a closed bottom setup [170].

In this chapter, we report a comprehensive simulation study of the pancake bouncing effect and outline a new energy analysis techniques that could reveal the interplay between kinetic, surface and viscous forces that influence

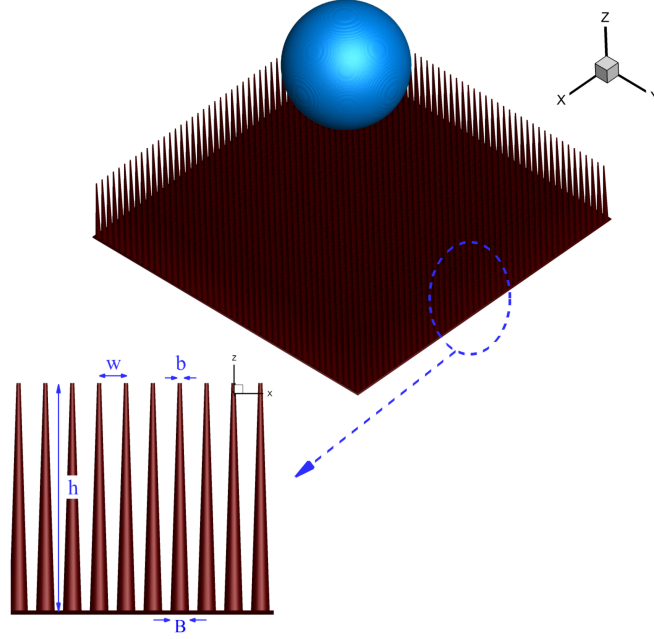


Figure 7.1: Simulation setup. The texture is represented a surface decorated with a lattice of tapered posts. The posts are represented by right conical frustums with the base diameters b and B ; w is the center-to-center spacing and h is the height of the posts.

droplet wall interactions. Our ELBM model for two-phase flows [88, 89, 171] is free of the aforementioned limitations and enables us to consider complex texture with the realistic geometry. We use the proposed forcing free-energy based model (chapter 2) for our numerical simulations [88, 89, 171]. First, the validity and the accuracy of the numerical simulations is established by comparing the simulation results with those recently observed by experiments for pancake bouncing on superhydrophobic surfaces in Ref [13]. Then a detailed parametric study is conducted by varying the geometry of the surface and also the contact angle of the substrate. Interesting analysis of various forces and energies acting during the collision process is also provided. It is important to note that the model used here is free of an tuning parameters and case based modeling. The simulation code including the fluid fluid interactions and the fluid-solid interactions remain the same for collision of two droplets and also collision of droplet with a flat or complex wall in chapters 3 and 4, respectively.

7.2 Results and discussion

7.2.1 Geometry and simulation parameters

The setup of three-dimensional simulations is sketched in Fig. 7.1. A droplet of radius R_0 is placed above the surface in equilibrium with the vapor. A uniform downward velocity is imposed on the drop while surrounding vapor is initialized with zero velocity. Initially the drop is sufficiently elevated to allow the liquid-vapor interface to equilibrate before the impact. No gravity is considered in the simulation. All simulations, unless otherwise stated, were run on computational domain of $6R_0 \times 6R_0 \times 6R_0$. Parameters of the simulated fluid are: $\rho_l = 7.82$ (liquid density), $\rho_v = 0.071$ (vapor density), $\sigma = 0.353$ (surface tension, corresponding to $\kappa = 0.00468$ in Eq. (2.37)) and $\mu_v = 0.01$ (vapor dynamic viscosity); all are in lattice units (see below the match to physical units). The impact velocity was computed in accord with the Weber number $We = \rho_l R_0 U_0^2 / \sigma$, and the range $6 \leq We \leq 150$ was studied. The dynamic viscosity of the droplet was fixed at $\mu_l = 0.415$ corresponding to Ohnesorge number $Oh = 0.025$ ($Oh = \mu_l / \sqrt{\rho_l \sigma R_0}$). This corresponds to a range of Reynolds number $Re = \sqrt{We} / Oh$ as $98 \leq Re \leq 490$. A comment on the parameters of the simulated liquid and those of the used in the experiment [13] (water) is in order. The density contrast $\rho_l / \rho_v \approx 110$ and the Ohnesorge number $Oh = 0.025$ used in the ELBM simulations were shown in previous chapters to be sufficient to recover the pertinent flow dynamics of colliding free droplets and impacts of flat surfaces. The density contrast for water is an order of magnitude higher, whereas the Ohnesorge number is an order of magnitude lower than those of the simulation ($Oh \approx 0.003$ for water). Nevertheless, same as in the previously chapters, we expect that the essential dynamics is captured correctly also in the present simulations with complex textures.

The structure of the substrate is a square lattice of tapered posts placed uniformly with the center-to-center spacing w on a flat plate. Each post is modeled as a right conical frustum of the height h , with the smaller and larger base diameters b and B , respectively (Fig. 7.1). The droplet radius R_0 is the input of the simulations while the rest of the geometry matches the experiment [13]: $R_0/h = 1.8$ (droplet radius to post height), $b/B \approx 0.28$, and $b = B - 2h \tan \varphi$ ($\varphi = 2.6^\circ$ is the apex angle [13]). We introduce the density of the texture (DoT) $\Lambda = R_0/w$ (parameter Λ reflects the relative number of posts seen by the droplet on impact). The spacing between the posts was chosen to reproduce $\Lambda_{\text{exp}} \approx 7.25$ [13] in the simulations of sec. 7.2.2 below. Both the surface of the conical frustum and the supporting flat plate are considered superhydrophobic surface (SHS) with a contact angle

$\theta = 165^\circ$.

Finally, in order to convert lattice time t_{LB} into seconds, we first compute the inertia-capillary time $\tau_{\text{LB}} = \sqrt{\rho_l R_0^3 / \sigma}$ using the density, droplet radius and surface tension in lattice units. Next, τ is extracted from the experimental data. After that, the reduced time for both the experiment and the simulation are matched, $t_{\text{LB}} / \tau_{\text{LB}} = t / \tau$. Thus, knowing t_{LB} (the number of time steps), we uniquely obtain the corresponding physical time $t = (\tau_{\text{LB}} / \tau) t_{\text{LB}}$. It should be noted that the simulations used no parameters other than already specified. If not otherwise stated, the droplet radius $R_0 = 100$ lattice units was used. All simulations were checked for grid convergence using $R_0 = 100$ and lower; only highest resolution results are reported.

7.2.2 Comparison with experiment

In this section we validate the simulations for drop impinging on superhydrophobic surfaces with respect to known data from experiments [11, 13].

Flat surface [11]: Flat SHS is considered first. It was shown in Ref. [11] that the contact time t_{contact} is independent of Weber number in a wide range and can be scaled with the inertial-capillary timescale: $t_{\text{contact}}^* = t_{\text{contact}} / \tau \approx 2.2$. Figure 7.2 reports the variation of contact time on the flat SHS for a range of Weber numbers. From Fig. 7.2 the results obtained from simulations (open symbols) agree well with those observed by experiment (solid symbol) in [12]. We note that the flat SHS test validates the use of the Ohnesorge number $\text{Oh} = 0.025$ for the ELBM fluid in the present context. Indeed, as it was shown in the Fig. 6.2 of chapter 6, the Ohnesorge number takes effect on the contact time at much higher values, $\text{Oh} \approx 1$ (i. e. for highly viscous liquids such as glycerol ($\text{Oh} \approx 3$) or silicon oil). For $\text{Oh} < 0.1$, there is no effect of the viscosity on the impact on flat surfaces, and thus it is not surprising that the present simulation agrees well with the experiments which use water. We refer to chapter 4 for other comparisons of ELBM with experiments on flat surfaces.

Surface with macro scale posts [13]: Now we proceed with the superhydrophobic surfaces patterned with lattices of submilliliter scale posts. Following Ref. [13], we introduce characteristic time instances ($t = 0$ corresponds to the time of first contact): t_\uparrow is the time at which the texture is fully emptied; at t_{max} the drop reaches its maximal lateral extension; t_{contact} is the time at which the drop loses contact with the solid. Snapshots of

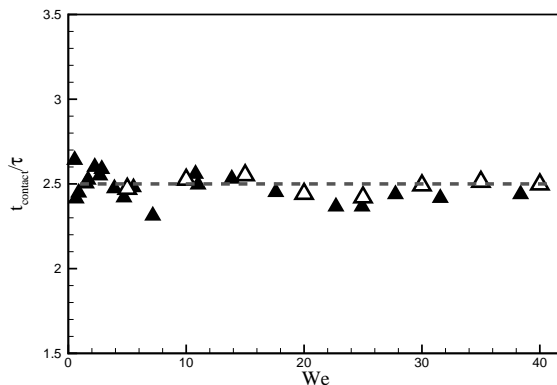


Figure 7.2: Contact time on a flat super-hydrophobic surface with the contact angle of 161° as a function of Weber number. Dashed line: $t_{\text{contact}}^* = 2.5$, Ref. [11]; Open symbols: ELBM simulations, solid symbols: Experiment [12].

a drop impinging on a texture of tapered posts at $We = 14.1$ are shown in Fig. 7.3(a) in parallel with the images from the experiment [13]. Pancake formation and rebound is clearly seen in the simulation. Simulation results for both the shape of the drop and the characteristic times are in excellent agreement with experimental observations.

Along with the tapered posts texture of Fig. 5.1, we simulated a simpler case of rectangular prism posts which was also considered in the experiment of Ref. [13]. The droplet radius for this simulation was $R_0 = 34$ lattice units. The height of posts h , the posts center-to-center spacing, w and the side of the square cross-section b were computed in accord with the aspect ratios R_0/h , R_0/w and b/h in the experiment of Ref. [13]. Results are presented in Fig. 7.3(b) for $We = 7.9$. Also in this case excellent agreement between simulation and experiment is observed.

For a validation, simulations were performed within the experimentally accessed range of Weber numbers $6 < We < 25$. Dependence of characteristic times t_\uparrow , t_{max} , and t_{contact} on Weber number is compared with the experiment in Fig. 7.4(a) (tapered posts) and Fig. 7.4(b) (square posts). Also the so-called pancake quality $Q = d_{\text{jump}}/d_{\text{max}}$ is compared to the experiment, where d_{jump} and d_{max} are the lateral diameters of the drop at t_{contact} and t_{max} , respectively.

Simulations in Fig. 7.4(a) show that for $We < 12$ the contact time is $t_{\text{contact}} \simeq 16[\text{ms}]$ which is in good agreement with the conventional complete rebound [11]. The onset of the pancake bouncing regime at critical

7. DROPS BOUNCING OFF MACROTEXTURES: PANCAKE BOUNCING

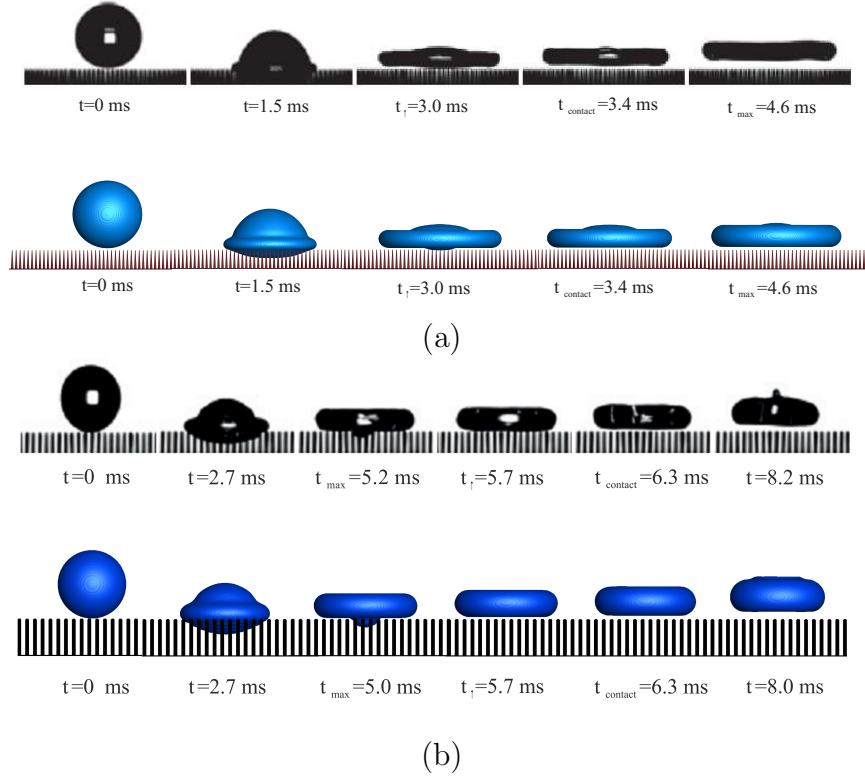
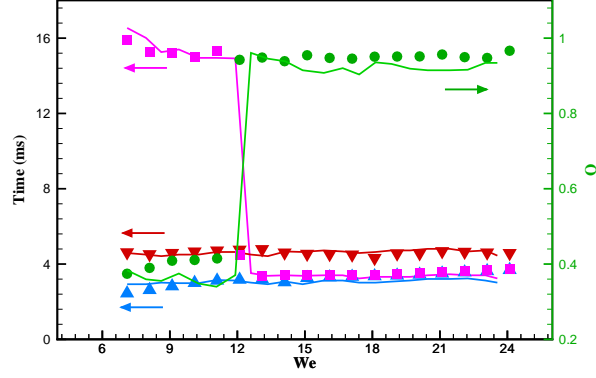


Figure 7.3: Comparison of simulation (bottom) and experiment [13] (top) for the pancake bouncing of a drop impinging on, (a) the tapered posts at $We = 14.1$, (b) the straight square posts at $We = 7.9$.

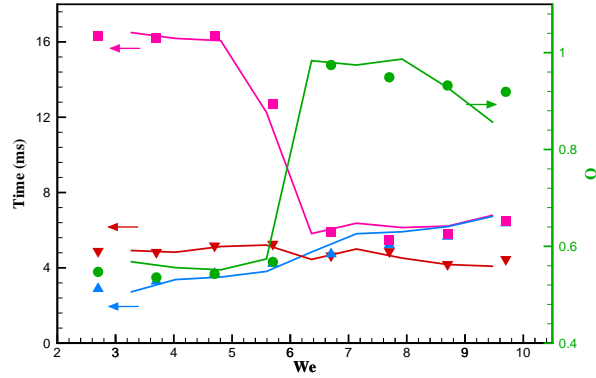
Weber number, $We^* \approx 12$ agrees well with experiment [13]. Reduction in contact time by a factor four is observed. We repeated the measurements of the characteristic time scales for the drop impinging on the straight square posts. Simulation results compare well with the experiment in Fig. 7.4(b). Summarizing, ELBM simulation demonstrates excellent agreement with the existing experimental data. In the remainder of this chapter, we shall address regimes which were so far not studied experimentally in order to gain a more comprehensive picture of bouncing off macro-textured surfaces.

7.2.3 Textures with perfect coating

Ref. [13] reported experiments in a narrow range of Weber numbers ($We < 25$). When the Weber number is increased, penetration depth into the texture increases and the deforming drop will eventually reach the base of the substrate. It is difficult to access the liquid inside the texture in the exper-



(a)



(b)

Figure 7.4: Comparison of simulation (symbol) and experiment [13] (line) of characteristic times t_{\uparrow} , t_{\max} , t_{contact} , and pancake quality, $Q = d_{\text{jump}}/d_{\text{max}}$, with We for a drop impinging on, (a) tapered posts, (b) square posts. The blue, red, pink and green colors show the t_{\uparrow} , t_{\max} , t_{contact} and Q , respectively

iment.

Here we extend the ELBM simulations to higher Weber numbers, $6 < We < 150$. We first consider the same geometry as in the previous section, and assume perfect coating, that is, both the posts and the base are SHS with contact angle $\theta = 165^\circ$. Fig. 7.5 shows snapshots of the impact on the perfectly coated texture at various Weber numbers. For $We > 40$, the penetrated liquid interacts with the base plate at the time t_{mpl} (maximal penetration of the drop). Simulations show that pancake bouncing is still observed for a much wider range of Weber numbers, $12 < We < 150$. Fig.

7. DROPS BOUNCING OFF MACROTEXTURES: PANCAKE BOUNCING

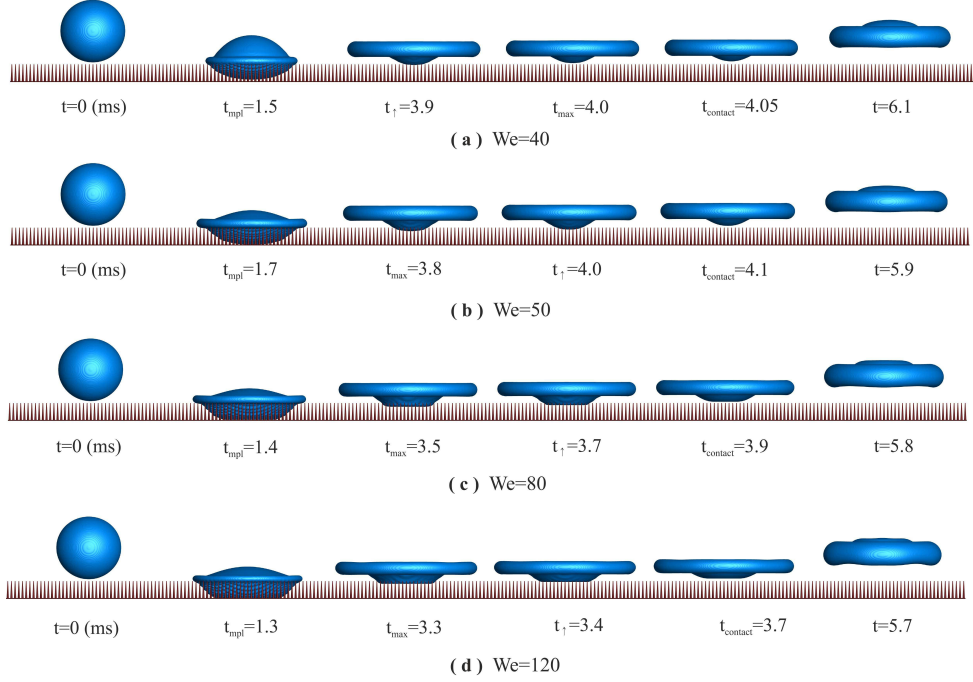


Figure 7.5: Snapshots of the rebound from tapered posts at (a) $We = 40$, (b) $We = 50$, (c) $We = 80$, (d) $We = 120$. Density of the texture $\Lambda_{\text{exp}} = 7.25$. Invading liquid hits the base of the texture at $We \geq 50$. Perfect coating is assumed for both the posts and the base plate (contact angle is set to $\theta = 165^\circ$). After hitting the base, penetrated liquid experiences a quick lateral extension, detaches from the base, returns to the top of the posts and demonstrates pancake rebound.

7.6 shows that both the reduction of the contact time and the pancake quality remain unaffected until at least $We \approx 150$. This can be attributed to the fact that the base plate of the texture is also considered SHS with a uniform contact angle (see sec. 7.2.4). To that end, the density of the texture $\Lambda \approx 7.25$ corresponds to the experiment [13].

In the next simulation series we probe the effect of lower and higher lateral density of the texture by varying the center-to-center spacing. Contact time for various R_0/w is shown in Fig. 7.7 for a selected Weber number $We = 30$. For a denser texture ($R_0/w \approx 10$), since the drop requires larger kinetic energy to start penetrating into the posts, a small portion of the liquid drop penetrates into posts and thus adequate capillary energy required for pancake bouncing is not stored by the penetrated liquid. Therefore, the drop impinging on such a dense texture follows a conventional complete rebound. On the other hand, when the tapered posts are distributed sparsely

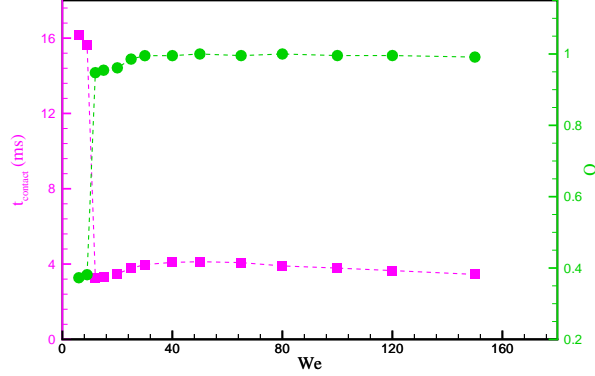


Figure 7.6: Contact time t_{contact} (squares) and pancake quality Q (circles) of a drop impinging on perfectly coated tapered posts with the density of texture $\Lambda_{\text{exp}} = 7.25$, for a range $6 \leq We \leq 150$.

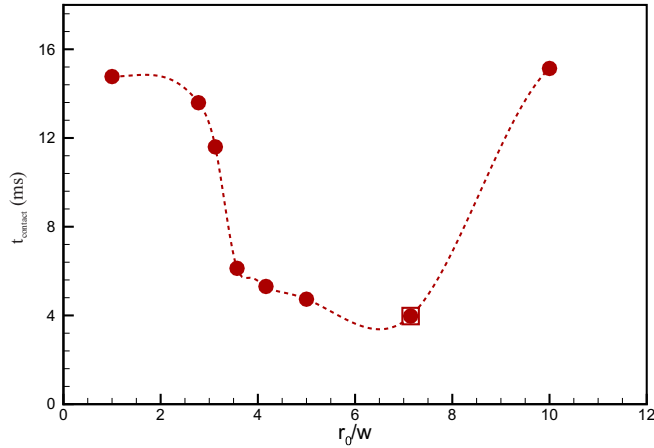


Figure 7.7: Dependence of the contact time on the density of the texture $\Lambda = R_0/w$ at $We = 30$. DoT of the experiment [13] is marked with a square, $\Lambda_{\text{exp}} = 7.25$.

($R_0/w < 7.25$), the drop can penetrate the texture at a lower critical Weber number. However, in this case the total interface area and hence surface energy stored for a given droplet penetration is lower due to a less proliferated interface. When a drop of a given radius meets the texture with sparsely distributed posts, lesser number of penetration valleys (undulated regions) are produced. This results in lower surface energy and lower capillary forces during the emptying process; thus the contact time increases.

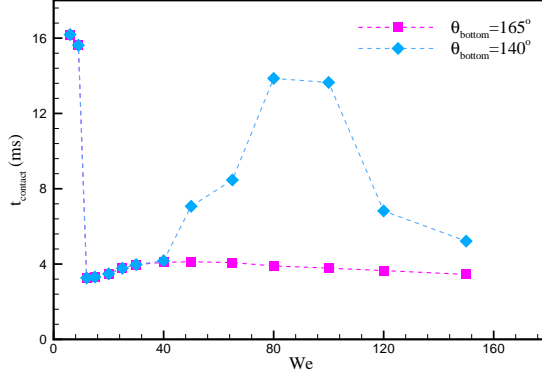


Figure 7.8: Contact time for a perfectly (squares) and imperfectly (diamonds) coated texture as a function of Weber number.

Hence, during a design process, one needs to consider the trade-off between contact time reduction and critical Weber number at which the process of pancake bouncing sets on.

Summarizing, under the assumption of perfect SHS coating, we found that the pancake bouncing extends to much higher Weber numbers whereas the density of the texture strongly affects the critical Weber number. In the next section we shall investigate a more realistic scenario of imperfect coating.

7.2.4 Imperfect coating

In the simulations so far, we assumed that the SHS quality is uniform through the texture and the base plate. However, this is unlikely to hold when, for example, the SHS coating is produced by spraying a polymer solution on the texture. According to Ref. [13], controlling the quality and uniformity of coating throughout the the posts and especially the valleys between them is a difficult task. Hence it is reasonable to assume that the contact angle at the base plate is lower than that on the upper part of the posts. Now, given that the drop interacts with the base plate at $We \geq 50$ (see Fig. 7.5), we probe the effect of imperfect coating by assigning a smaller contact angle $\theta_{\text{bottom}} = 140^\circ$ to the base plate and the bottom part of the posts (10% of the height). Since superhydrophobic surfaces are created by coating hydrophobic surfaces with a nano-scale coating, this assumption of $\theta_{\text{bottom}} = 140$ is reasonable. The rest of the texture is maintained at the contact angle $\theta = 165^\circ$. The contact time with the perfectly and the

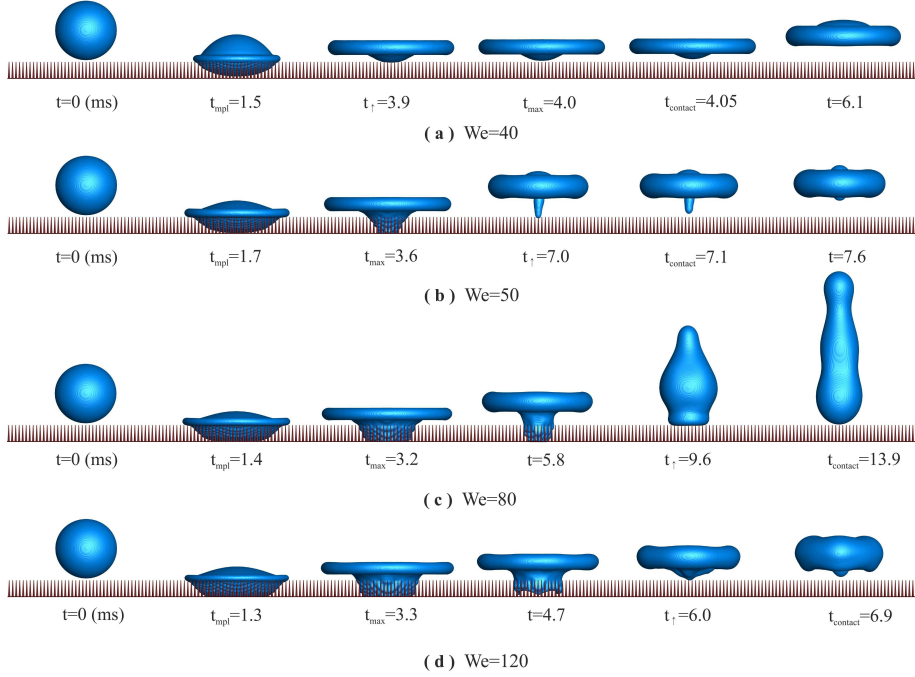


Figure 7.9: Snapshots of impact on imperfectly coated texture at (a) $We = 40$, (b) $We = 50$, (c) $We = 80$, (d) $We = 120$. Contact angle at the base plate and 10% above it set to $\theta_{\text{bottom}} = 140^\circ$, and for the rest of the texture the contact angle is $\theta = 165^\circ$. For $We \geq 50$, the penetrated liquid reaches the base at t_{mpl} .

imperfectly coated textures is shown in Fig. 7.8. For $We \leq 40$, the contact time is the same for both textures. In fact, for $We \leq 40$, since the liquid penetrates the texture without touching the base, the quality of coating does not affect the contact time. However, for $We > 40$, the liquid reaches the substrate base, and the degraded coating alters significantly the contact time and the pancake quality.

To elucidate this, we present snapshots of the impact on the imperfect texture for different Weber numbers in Fig. 7.9. For $We = 50, 80$ and 120 , the drop contacts with the substrate base at t_{mpl} . Due to lack of superhydrophobicity at the bottom, the penetrated liquid sticks to the texture base and after that it is pulled out by the rest of drop moving upward. In Fig. 7.9(b) ($We = 50$), although the penetrated liquid sticks to the substrate base, it returns to the top of the texture quickly thus enabling pancake bouncing but with the almost twice higher contact time, $t_{\text{contact}} \approx 7$ [ms]. At a higher Weber number $We = 80$, Fig. 7.9(c), due to a larger contact area between the liquid and the texture base, the penetrated liquid returns to

the top of the posts with a delay. Consequently, the drop has enough time to retract and the overall picture is resembling the conventional bouncing rather than a pancake rebound. The contact time $t_{\text{contact}} \approx 14 [m.s]$ becomes close to the conventional bouncing value.

Interestingly however, as the Weber number is further increased (see Fig. 7.9(d), $We = 120$), the contact time reduces back to the value $t_{\text{contact}} \approx 7 [m.s]$. While the contact area between the drop and the base becomes even larger, also the number of invaded valleys is larger than at $We = 80$. The force due to surface tension is thus able to overcome the pinning effect of the imperfectly coated base, and the texture is emptied faster. This explains the return of a pancake-like bouncing at $We = 120$, and the contact time becomes smaller than at $We = 80$. These results rely on the condition that $\theta_{\text{bottom}} = 140$, however if the contact angle at the bottom plate is more severely effected then the deterioration in contact time is more pronounced. Due to a lack of experimental access to these bottom regions, one can only perform such inverse analysis to estimate the quality of coating in these hidden regions.

Summarizing, the imperfect coating at the bottom of the texture features a non-linear dependence of the contact time on the Weber number can significantly affect the rebound pattern.

7.2.5 Energy budget

Energy considerations were invoked in Ref. [13] to quantify the mechanism of pancake bouncing. The assumption behind this analysis was that the kinetic energy of the drop is fully converted into the surface energy at the maximal penetration into the texture. However, neglecting energy dissipation is less obvious for the impact on textured surfaces. Indeed, since the shape of the droplet is considerably more distorted as compared to the flat SHS (the flow 'sees more walls'), stresses in the boundary layers contribute more to the dissipation. On the other hand, ELBM has been shown to quantitatively capture the energy budget in binary droplet collisions (chapter 3) [171]. In this section we report and discuss the energy budget of the pancake bouncing regime from the ELBM simulations. For the drop with volume V and surface area A , let us introduce the kinetic energy, $K = \int_V \frac{1}{2} \rho u^2 dV$, the surface energy $S = \sigma A$, and the energy loss due to viscous dissipation Ξ ,

$$\Xi = \int_0^t \Phi dt \quad \text{where} \quad \Phi = \frac{\mu_l}{2} \int_V (\nabla \mathbf{u} + \nabla \mathbf{u}^\dagger)^2 dV. \quad (7.3)$$

Table 7.1: Reduced kinetic and surface energy for the spherical drop

We	$\tilde{K}_0^{\text{exact}}$	\tilde{K}_0^{num}	$\tilde{S}_0^{\text{exact}}$	\tilde{S}_0^{num}
15	0.714	0.712	0.286	0.287
30	0.833	0.835	0.167	0.164
80	0.930	0.926	0.07	0.075

Further introducing normalized energies, $\tilde{K} = K/E_0$, $\tilde{S} = S/E_0$ and $\tilde{\Xi} = \Xi/E_0$, where $E_0 = K_0 + S_0$ is the energy of the drop at $t = 0$, energy balance is written as,

$$\tilde{K} + \tilde{S} + \tilde{\Xi} = 1. \quad (7.4)$$

All the three components of the energy balance equation (7.4) were evaluated individually for the impact on the perfectly coated texture with the texture density $\Lambda_{\text{exp}} = 7.25$ (sec. 7.2.2 and 7.2.3). In Fig. 7.10 we present the time evolution of \tilde{K} , \tilde{S} and $\tilde{\Xi}$. We also show the normalized center-of-mass kinetic energy $\tilde{K}_{\text{cm}} = K_{\text{cm}}/E_0$ where $K_{\text{cm}} = \frac{1}{2}mU_{\text{cm}}^2$ is the kinetic energy of center-of-mass, with m the mass of the liquid and U_{cm} the center-of-mass velocity. Results for three representative Weber numbers are shown: $We = 15$ (shortly after the onset of pancake bouncing at $We^* \approx 12$); $We = 30$ (at the limit of the experimentally accessed Weber numbers; significant intrusion of liquid into the texture) and $We = 80$ (large intrusion).

Before discussing the results, a brief comment on the validation of the numerics is in order. The numerical result at $t = 0$ (spherical unperturbed drop moving with the velocity U_0) satisfies well the exact relations, $\tilde{K}_0 = We/(We + 6)$ and $\tilde{S}_0 = 6/(We + 6)$ (see table 7.1). This validates the choice of the cut-off value $\rho_{\text{int}} = 7$ for the computation of the interface area A in the post-processing of the simulation data. Second, the energy balance (7.4) is satisfied within 2% for all times and Weber numbers which is consistent within the accuracy of evaluation of velocity gradients in the computation of energy dissipation.

The first observation concerns the kinetic energy \tilde{K} and the center-of-mass kinetic energy \tilde{K}_{cm} . While the latter vanishes at the maximal penetration of the drop into the texture, the kinetic energy itself is different from \tilde{K}_{cm} . This difference is attributed to the flow inside the rim of the upper part of the drop remaining above the pillars. The non-negligible amount of kinetic energy carried by the flow of this type was indicated in Ref. [6] for the drop impact on a flat surface. With the increase of Weber number, the greater part of the droplet penetrates the texture, hence the amount of energy in the vortical flow decreases. This is consistent with the result of simulation which shows that the relative difference between \tilde{K} and \tilde{K}_{cm} decreases with

7. DROPS BOUNCING OFF MACROTEXTURES: PANCAKE BOUNCING

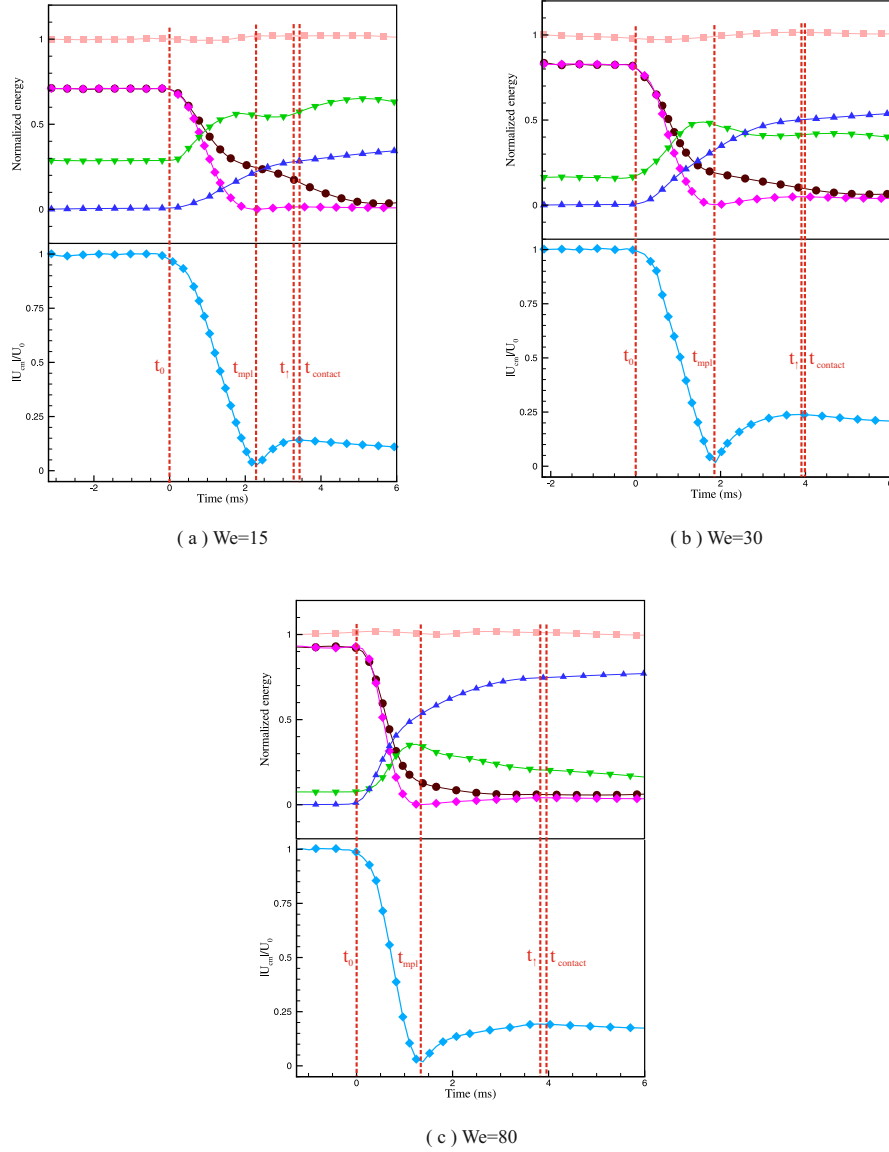


Figure 7.10: Top panel: History of various components of the energy balance. Circle: Normalized kinetic energy \tilde{K} ; Downward triangle: Normalized surface energy \tilde{S} ; Upward triangle: Normalized dissipated energy $\tilde{\Xi}$. Squares: Normalized energy balance $\tilde{K} + \tilde{S} + \tilde{\Xi}$. Diamond: Normalized center-of-mass kinetic energy \tilde{K}_{cm} . Bottom panel: Reduced center-of-mass velocity of the drop U_{cm}/U_0 . Impact on a perfectly coated SHT $\theta = 165^\circ$ for low and high Weber numbers.

the Weber number.

Second, the surface energy \tilde{S} rapidly increases after the impact, as expected. For $We = 15$ we see two maxima of \tilde{S} , a local maximum close to the zero of the center-of-mass velocity (the drop has stopped penetrating into the texture) and then the global maximum at the time of maximum lateral extension. Note that in this case, maximal extension comes after the droplet bounces off the texture. However, with the increase of the Weber number, the second maximum tends to disappear, and is not present at $We = 80$. This situation can be termed a pseudo-pancake rebound in order to distinguish it from the “true” one at $We = 15$: The maximal stretching synchronizes with the maximum penetration time. Note that this does not affect the contact time, as was shown above.

Finally, it is clear from the energy balance at all Weber numbers that the dissipation is not negligible in any of the cases for the simulated Ohnesorge number $Oh = 0.025$. While for the the lower $We = 15$, the surface energy becomes dominant soon after the impact, dissipation is not small even in that case, and levels around 25% at the rebound. It is seen from Fig. 7.10 the fraction of energy loss at higher Weber numbers is even larger and becomes dominant of all at $We = 80$.

Ref. [172] discussed a possibility that macroscopic air pockets get trapped between the droplet and the substrate. Such trapped pockets of air or vapor can undergo compression which could serve as an additional storage of energy to be released into the kinetic energy during the capillary emptying. However, the energy balance evaluation above suggests that such a scenario need not be present.

Summarizing, for the macroscopically flat superhydrophobic surface, the scaling of the contact time, $t_{\text{contact}}/\tau \approx 2.2$ holds whenever the Ohnesorge number is not too large ($Oh < 1$). Similar universality holds also in the case of tapered macro-texture: While the dissipation is not necessarily negligible for $Oh = 0.025$, the contact time of the pancake bouncing scales same way as in the experiment with water droplets. The only important for that mechanism to be realized is the clear dominance of the surface energy over the kinetic energy at the instance of maximal penetration into the texture. Thus, such energy balance analysis could be very handy in estimating the role played by kinetic, surface and viscous forces for a droplet wall interaction. Such analysis is of greater use when the underlying mechanisms of droplet bouncing are not well understood for example complex macro-textured surfaces. Moreover, imbalance in energy analysis could lead to better understanding of the role played by external factors such as trapped air pockets.

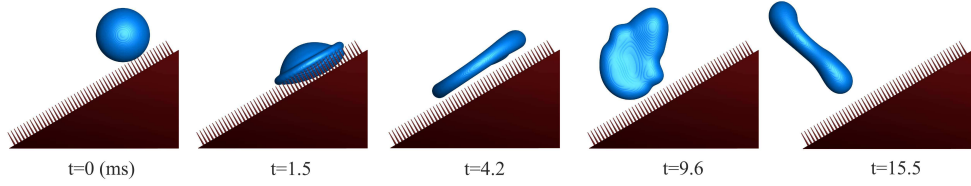


Figure 7.11: Snapshots of an impact on tapered posts tilted at 30° ; $We = 31.2$. The drop rebounds at $t_{\text{contact}} = 3.6 [ms]$ which is in excellent agreement with the experiment [13]. Snapshots correspond to Figure 1d of Ref. [13].

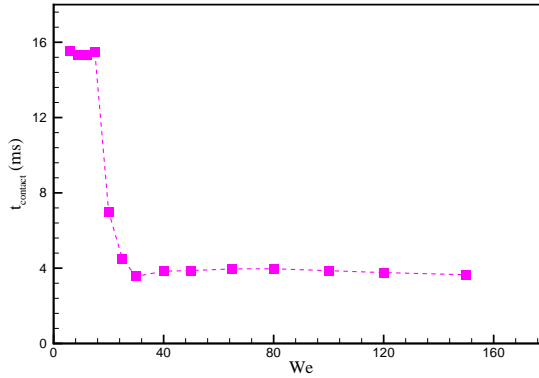


Figure 7.12: Contact time of a liquid drop impinging on tapered surface under a tilt angle of $\theta = 30^\circ$ for a large range of We ($6 \leq We \leq 150$). Our simulations show that significant reduction in contact time occurs for $We \geq 25$.

7.2.6 Impact on a tilted texture

In this section, the simulation results for a drop impacting onto a tapered texture tilted at 30° are presented. Fig. 7.11 demonstrates that pancake bouncing takes place also for tilted surface. The shape as well as the contact time ($t_{\text{contact}} = 3.6 [ms]$) for the droplet shown in Fig. 7.11 are in good agreement with those observed in the experiment [13]. Fig. 7.12 reports the contact time for the tilted surface in a range of Weber numbers from $We = 6$ to $We = 150$. The pancake bouncing sets in at $We \geq 25$, that is, almost at a twice higher Weber number as compared to the normal impact. This happens since the motion along the slope delays the penetration of the liquid into the texture. It is also noted that the transition to the pancake bouncing is more gradual than a sharp transition observed for the horizontally aligned

substrate.

7.3 Summary and Conclusions

The dynamic behavior of a liquid drop impacting a surface with tapered posts was numerically investigated over a wide range of Weber numbers using two-phase entropic lattice Boltzmann method. Superior stability of the ELBM and flexibility of wall boundary conditions allowed us to study, for the first time, the pancake bouncing phenomenon in complete details. Quantitative comparisons of ELBM simulations with previous experiments showed the predictive nature of the multiphase entropic lattice Boltzmann model [88].

Apart from varying the surface parameters such as the spacing between posts and contact angle this simulation technique allowed us to accurately account for the transformation of kinetic energy into surface energy and vice-versa. We presented numerical evidence that reduction in contact time occurs entirely due to increase of droplet surface area which acts as a storage of kinetic energy during the impact process. Such energy balance analysis, for the first time, enabled us to accurately design and optimize surfaces and understand the role played by various physical phenomenon involved in droplet wall interactions. Further more the impact of surface superhydrophobic coating can be quantitatively accessed through numerical simulations.

Drops bouncing off macrotextures: discovery of new surfaces

Here in this chapter, based on ELBM simulations we propose detailed investigation of two new superhydrophobic macrotextured surfaces that show large reduction in droplet contact time while at the same time being robust and effective in a wide range of parameters. The first surface is textured with an egg-carton pattern of macroscopic (few hundred microns) conical posts and holes to maximize the utilization of trapped air pockets and increased surface available to a droplet during impact. ELBM simulations demonstrate that impacting drops on such a surface causes a pancake bouncing behavior with a factor four reduction in the contact time compared to the flat surface. With our second innovative design, we observe numerically a new drop rebound regime, ring bouncing, for a drop impacting on a flat surface decorated with a macroscopic bead. To manipulate the hydrodynamics of the drop center, a macroscopic object is added on the surface at the landing spot. After impacting, the drop spreads on the surface and then, shortly before the maximum lateral extension is reached, the spreading liquid film ruptures at the center due to surface defect and generates an inner rim. Once the droplet has reached the maximum lateral extension, the outer rim starts contracting inwards and collides with the expanding inner rim. This interaction of two liquid jets moving in opposite directions horizontally creates an upward motion of the droplet in the shape of a ring. This process also reduces the contact time by factor two compared to conventional impact on flat surfaces since the rebound happens before the full recoil of the drop.

8.1 Introduction

Hierarchical structures with dimensions of features ranging from the nanoscale to the macroscale are extremely common in nature to provide properties of interest. For instance, Lotus leaves, due to the hierarchical roughness of their leaf surfaces, exhibit extraordinary water repellent behavior. Thus, nowadays, researchers and engineers have focused on designing and fabricating artificial structured surfaces inspired from nature to promote drop mobility by controlling wettability and micro-/macro-scale roughness parameters such as shape, size, spacing and height [13, 14]. The artificial textured surfaces with enhanced drop mobility can be applied for a wide range of applications such as anti-icing and self-cleaning [18, 159].

From the perspective of designing new artificial surfaces, by inspiring clues from various animals and plants in nature, many proposals can come into mind for designing new macro-patterned surfaces. However, the fabrication process for production of the artificial macro-structured surfaces is a challenging issue in terms of the time required for production and fabrication costs and hence can not be applied for any surface before being assured that the surface will provide the properties of interest.

Alternatively, numerical simulations can provide a great degree of freedom in terms of examining various macro-structured surfaces, role of roughness parameters as well as provide substantial information on the flow field, stresses and etc of the liquid drop necessitated for understanding of physical phenomena occurring during drop impact on these surfaces. As a consequence, the knowledge gained by numerical simulations can provide further insights into performance of the new micro/macro patterned surfaces and hence will help in design of these surfaces before production in the laboratory.

Over the past decade researchers and engineers have brought their effort to explore novel strategies for finding new surfaces with exquisite micro/macro structures to break the classical contact time [11–14, 173]. As mentioned in chapter 7, it was shown in Ref. [11] that for a water droplet impinging on a flat super-hydrophobic surface, the amount of time that the drop remains in contact with the substrate is independent of the impact velocity of the drop and can be scaled by the inertia-capillary timescale, $\tau = \sqrt{\rho_l R_0^3 / \sigma}$, ($t_{\text{contact}} / \tau \approx 2.2$) [11]. For a long time, it was assumed that this is the minimum contact time which can be attained by a drop impacting on a superhydrophobic surface. However, after a decade, experimental studies have shattered that long standing notion that the duration of contact between a surface and an impinging drop cannot be reduced [13, 14, 173]. The first idea to reduce the contact time of a bouncing drop was proposed by [14]. It was shown that the overall contact time of drop impacting onto a flat surface

designed by adding a macrotecture, in the range of few hundred microns, is reduced by 37% to conventional rebound from a flat surface. Since the dynamic behavior of drop impacting on flat substrates is nearly axisymmetric. Therefore, after spreading, a drop edge retracts axis-symmetrically towards the center of the drop while the center remains stationary. To perturb the center of the drop, a macrotecture was added on the flat surface where the drop impacts thus creating a non-uniform velocity in the retracting film and there by reducing the contact time [14]. Recently, the experimental study of Ref. [13] proposed an brilliant idea for reducing the contact time. In this study, it was demonstrated that if the flat surface is decorated with a lattice of square posts which are several hundred micrometer tall, after impacting a drop, it can completely bounce off the surface in the shape of a pancake even before the retraction process begins which results a reduction in the contact time by factor four [13] (a detailed discussion on pancake bouncing was presented in chapter 7). Very recently, It was shown that after impacting the drop on a curved macrotectures surface with the curvature of radius comparable to the drop size, the drop spreads larger in the azimuthal direction than in the axial direction, and leaves the surface with an elongated shape along the azimuthal direction. As a result of the asymmetric momentum and mass distribution, there is a preferential fluid flows around the drop rim which results a contact time reduction by about 40% [173].

In this chapter, using our numerical simulations, we discovered two new macrotectured superhydrophobic surfaces that are capable of reducing the contact time of the impinging droplet. The first surface was designed based on a "**egg carton**" pattern including macroscopic conical posts and holes. Numerical simulation showed that when the drop impacts on this surface, the drop spreads out to a maximum expansion and then it jumps off the surface in a pancake shape without experiencing retraction on the surface resulting in prompt bouncing with a factor four reduction in the contact time compared to the flat surface. The reduction in contact time for this surface was the same as the proposed surface in [13]. However, the egg-carton texture is more robust as compared to the sharp elongated texture of Ref. [13]. When the desirable performance of the egg carton surface in terms of reducing the contact time was shown by numerical simulation, the surface was fabricated in cleanroom laboratory by our collaborators in the group of Prof. Poulikakos, LTNT-ETHZ. The experimentally observed results also showed pancake bouncing as predicted by the simulations.

For a second surface we designed, using numerical simulations, we observed a new drop rebound regime "**ring bouncing**" for a drop impacting on a flat surface designed by adding a finite macroscopic hill shape. To manipulate

the hydrodynamics of the drop center, a macroscopic object (conical hill) was added on the flat surface where the drop lands. This phenomenon of ring bouncing was independently and almost simultaneously discovered by the group of Prof. Quéré, and this led to a collaboration with their group as well. Next following the lead of the group of Prof. Quéré we have subsequently modified the shape of our surface defect from a conical hill to a spherical defect, without any significant change in the contact time.

8.2 Results and discussions

In this section we first verify the validity of our simulation results by comparing them with those experimentally observed results for drops impacting on super-hydrophobic macrotextures presented in Ref. [14] and [12]. Then, results for the newly proposed surfaces will be presented.

8.2.1 Validation with experimental data

Macrotextured surface [12,14]: First we compare the simulation results with the experiment of the Ref. [14]. Simulation setup corresponding to this experiment is sketched in Fig. 8.1(a). A drop of diameter 2.66 mm with equilibrium contact angle of 161° is used in both experiments and numerical simulations. The parameter λ in Fig. 8.1(a) stands for the center to center spacing between two macrotextures. Simulation results (open square) together with experimental observations (solid square) for the dimensionless contact time, t_{contact}/τ , against various landing locations along the periodic macrotexture, x/λ , are plotted in Fig. 8.1(b). All results shown in this graph for both experiment and simulation, are at $We = \rho_l R_0 U_0^2 / \sigma = 26.6$. It is clearly seen from Fig. 8.1(b) that the contact time is least when the drop impacts directly on the ridge and it increases as the drop lands further away from the ridge and then it decreases as the drop approaches the next macrotexture. By averaging the contact time obtained by varying the landing location of the drop, the mean contact time is $t_{\text{contact}}/\tau = 1.63$ which is shorter than that on the flat surface. As it seen from Fig. 8.1(b), the simulation results are found to be in an excellent agreement with experimental measurements of Ref. [14].

Next, the simulation results are compared with the recent experimental observations of Ref. [12]. In this reference, the contact time of a drop impacting on a surface with and without macrotexture were measured by varying the impact velocity of the liquid drop. In the simulations, the geometry of the macrotexture is matched with the experiment (a wire of diameter 200

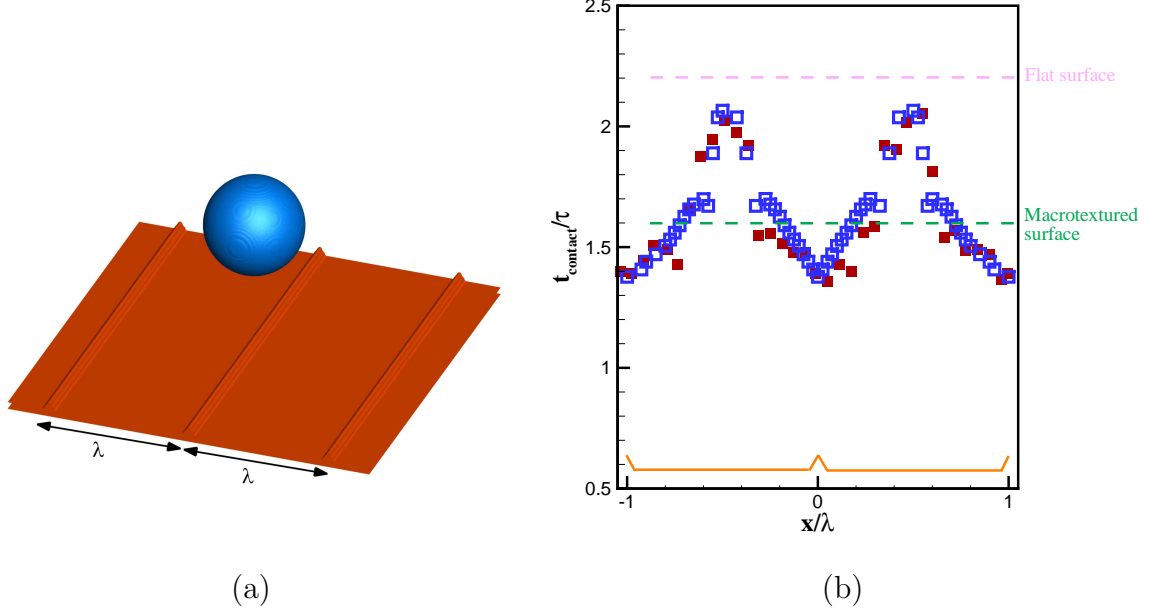


Figure 8.1: Drop impact on super-hydrophobic flat surface designed by adding periodic macrotextures. (a) Simulation setup where parameter λ is the center to center distance between ridges. (b) Comparison between simulations: open square, and experiment of Ref. [14]: solid square. The dimensionless contact time, t_{contact}/τ , is measured by varying the landing location of the drop, x/λ , along the periodic macrotextures. All the experimental and simulations results shown in this plot are for $We = 26.6$.

μm is held along a flat surface where the drop lands) and we use a drop with diameter of 2.6 mm same as that in experiment [12]. Both simulation results (open symbol) and experimental predictions [12] (closed symbol) are plotted in Fig. 8.2. In this graph, circles show the contact times for drops impacting symmetrically on a macrotexture and upward triangles stand for the contact times for flat surface. As it seen from Fig. 8.2, for macrotexture, the contact time adopts discrete values depending on the amount of the impact velocity. This step-like behavior was interpreted in Ref. [12]. As it was shown in Fig. 7.2 of chapter 7 and here in Fig. 8.2 (upward triangles), on superhydrophobic flat surfaces, the contact time t_{flat} is independent of the impact velocity [11]. In fact, due to sprig-like behavior of drops impacting on flat surfaces, the contact time t_{flat} is scaled as $(\rho_l \mathcal{V}/\sigma)^{(1/2)} \sim (\rho_l R_0^3/\sigma)^{(1/2)}$ where \mathcal{V} is the the volume of drop. Now the quantized behavior of the contact time for macrotexture shown in Fig. 8.2

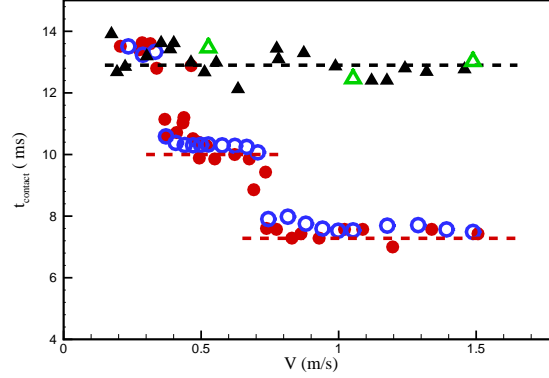


Figure 8.2: Contact time of a drop impacting on a superhydrophobic surface with (circles) and without (upward triangles) macrotexture as a function of impact velocity V . Open symbols are the results obtained from numerical simulations and closed symbols are the experimental observations of Ref. [12].

can be notably simplified. As it is observed from images in Fig. 8.3(a), at larger impacts ($V > 0.7$ m/s), when the liquid drop hits the macrotexture, the drop adopts a butterfly shape before takeoff at $t_c = 7.6$ ms, where we have four subunit liquid drops. Each of subunits with volume of $\mathcal{V}/4$ can be subjected to an individual inertia and capillarity. As a consequence, the contact time is expected to be $t_c \approx t_{\text{flat}}/2 \approx 6.5$ ms, which is very close to the results observed by both experiments [12] and simulations (see Fig. 8.2). In the regime of intermediate impact velocity ($0.4 \text{ m/s} < V < 0.7 \text{ m/s}$), due to smaller kinetic energy, when the drop impacts on the ridge, it spreads less and creates a square-like shape with two subunits of liquid (see Fig. 8.3(b)). By considering the volume of each subunit $\mathcal{V}/2$, it implies that the contact time should be $t_c \approx t_{\text{flat}}/\sqrt{2} \approx 9.2$ ms, which is in good agreement with results predicted by simulations and experiments [12]. Finally at very low impact velocity ($V < 0.4$ m/s), since the thickness of impacting drop is bigger than the ridge, the macrotexture does not influence on the bouncing behavior of the drop and hence the contact time is nearly the same with that on flat surface (see Fig. 8.2).

8.2.2 Egg-carton surface

The first surface proposed here is textured with an "egg-carton" pattern. The egg-carton pattern is constructed by macroscopic conical posts and

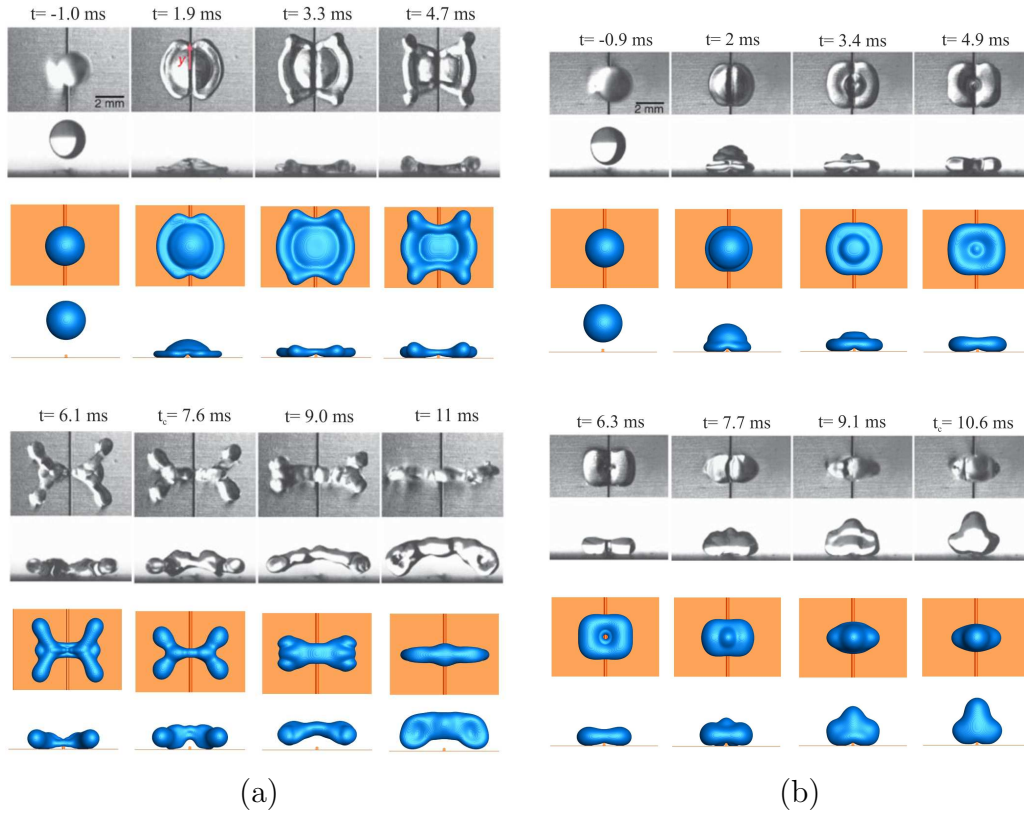


Figure 8.3: The effect of macrotexture on drop impact dynamics and contact time. (a) The drop impacts directly on the ridge with an impact velocity $V = 1$ m/s and then it takes a butterfly shape at $t = 6.1$ ms before taking off at $t_c = 7.6$ ms, a time significantly shorter than that on a surface without macrotexture. (b) A slower impact case with an impact velocity $V = 0.5$ m/s where the drop is deformed less and it first acquires a square-like shape including two subunit of liquid and then it leaves the surface at $t_c = 10.6$ ms. The simulation results (blue images) are compared with those experimentally observed in Ref. [12](black images).

holes. The conical posts together with the conical holes enable us to firstly maximize the utilization of trapped air pockets in the cavities and secondly increase surface area available to a droplet during impact. Using numerical simulations together with experimental observations of our collaborator (LTNT-ETHZ), we show how super-hydrophobic egg-carton surfaces can generate a bouncing regime similar to that observed in Ref. [13]: drops spread on impact and then leave the surface in the shape of pancake before it experiences retraction. However, the egg-carton texture would be physi-

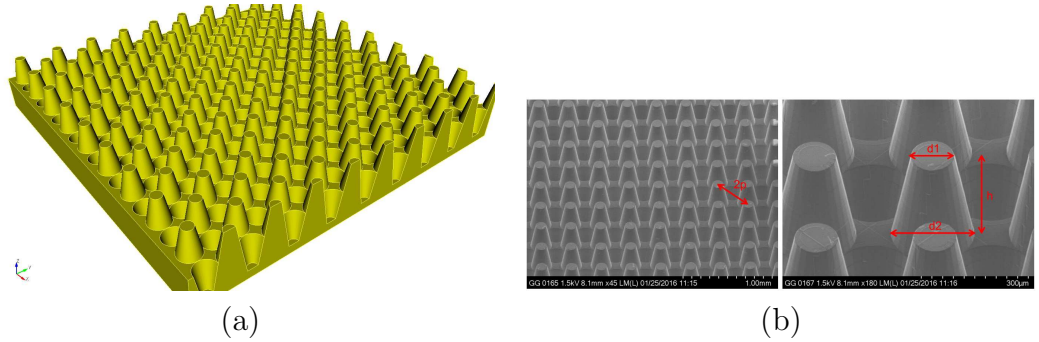


Figure 8.4: Left: Visualization of the egg-carton macro-texture used in the simulation. Right: egg-carton macro-texture created by group of Prof. Poulikakos, LTNT-ETHZ. (no superhydrophobic coating applied). The egg carton surface image in the experiment was provided by Gustav Graeber (LTNT-ETHZ group).

cally more robust as compared to the sharp elongated texture proposed in Ref. [13]. After the egg-carton surface was studied numerically and shown that it delivers promising performance in terms of reducing the contact time, it was fabricated by LTNT-ETHZ group in a cleanroom laboratory using nanoscribe 3D printing and spray coating.

Figure 8.4 shows the egg-carton surface used in the simulations together with that was fabricated by experiment. As it is seen from Fig. 8.4, the conical pillars and holes are in the same size with $d_1 = 134 \mu\text{m}$; smaller diameter of the cone, $d_2 = 258 \mu\text{m}$; larger diameter of the cone, and $h = 335 \mu\text{m}$; height of the cone. In the simulations, the droplet diameter and the equilibrium contact angle are set to 2.6 mm and 161° , respectively.

Figure 8.5 shows selected snapshots of a drop impinging on the egg-carton surface for both lower ($V = 0.52 \text{ m/s}$) and higher ($V = 1.1 \text{ m/s}$) impact velocities. From Fig. 8.5, for the case of lower impact velocity ($V = 0.52 \text{ m/s}$), after impacting, the drop spreads on the surface and then it reaches a maximum lateral extension at 4.2 ms. After that, it retracts while is still in contact with the surface. The drop finally detaches from the surface at 13.56 ms ($\approx 2.4\sqrt{\rho R_0^3/\sigma}$) which is in good agreement with that on a superhydrophobic flat surface [11]. Using our simulations we observed that the liquid invades into holes for $V > 0.7 \text{ m/s}$. Therefore, for lower impact velocities, $V < 0.7 \text{ m/s}$, the holes do not influence on the bouncing behavior of the impacting drop. Moreover, The drop's kinetic energy gained from capillary energy is not sufficient to allow the drop bounces off the surface as a flattened shape and thus, the drop exhibits the conventional complete rebound. Simulations demonstrate that for larger impact velocities ($V > 0.7$

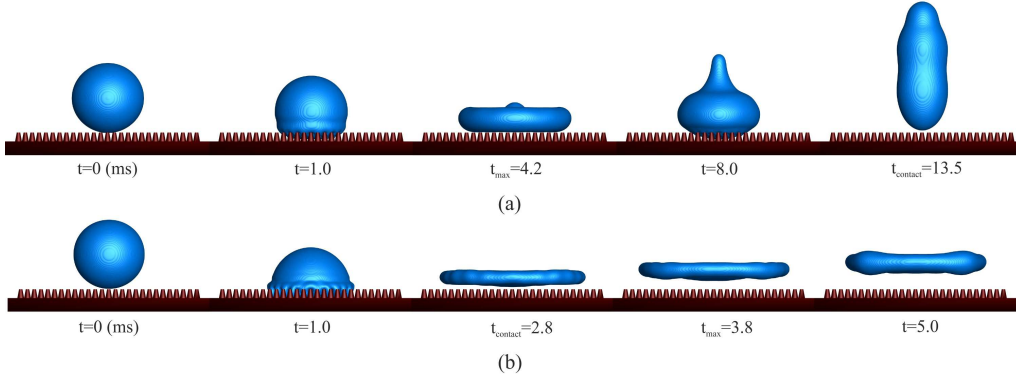


Figure 8.5: Selected snapshots of simulation results for a liquid drop impacting on the egg-carton surface. (a) At lower impact velocity with $V = 0.52$ m/s, the drop exhibits conventional bouncing (spreading, retracting and then leaving substrate). (b) At larger impact velocity with $V = 1.1$ m/s, the drop bounces off the surface as a pancake shape resulting a fourfold reduction in contact time compared with that on a flat surface.

m/s), due to larger kinetic energy, drop penetrates into holes and thus high pressure emerges inside the holes. Due to emergence of high pressures, we observed from simulations that the downward momentum of the invaded liquid in the holes quickly changes to upward direction. This phenomenon together with the effect of the capillary forces exerted by the hydrophobic posts, cause that the penetrated liquid to accelerate upward and accordingly bounce off the substrate in a pancake shape. Figure 8.5(b) shows the appearance of the pancake bouncing on the proposed egg-carton surface at $V = 1.1$ m/s. As it is seen from Fig. 8.5(b), first the drop continues to spread on the surface and simultaneously part of the drop penetrates into the cavities, later the drop detaches from the surface at $2.8 \text{ ms} \approx 0.51 \sqrt{\rho R_0^3 / \sigma}$ which is factor four smaller than that on flat surface. From indications obtained from numerical simulations, occurrence of pancake bouncing on egg-carton surface is consequence of simultaneous effects of the capillary forces caused by non-wetting surfaces and emerging high pressures in the cavities.

Pressure field for different stages of the drop impacting on egg-carton surface is visualized on the middle plane of the computational domain in Fig. 8.6. The drop impact velocity in Fig. 8.6 is $V = 1.1$ m/s. In this graph, in order to visualize the propagation of the pressure inside the valleys, the geometrical structure of the egg-carton surface is made invisible. The red and dark blue colors in Fig. 8.6 are corresponding to regions with high and low pressures, respectively. From Fig. 8.6, before impacting the drop on the substrate ($t = 0$ ms), the pressure in both sides of the liquid drop is

8. DROPS BOUNCING OFF MACROTEXTURES: DISCOVERY OF NEW SURFACES

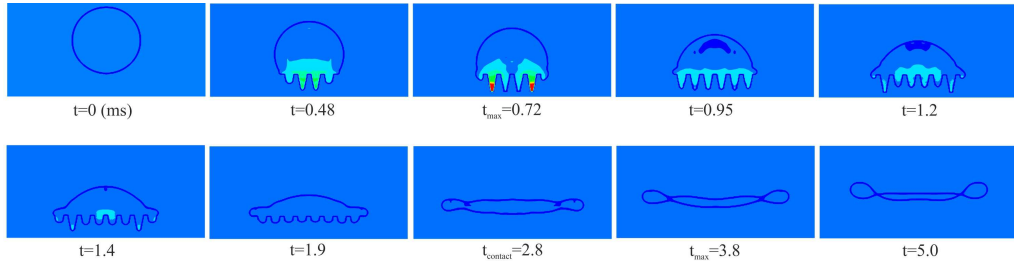


Figure 8.6: Distribution of the pressure inside the drop impacting on egg-carton surface. The impact velocity of the drop is $V = 1.1$ m/s. The red and dark blue colors are corresponding to the zones with very high and low pressures, respectively. The pressure is visualized on the middle plane of the computational domain and to see the pressure field inside the valleys, the egg-carton surface is not shown.

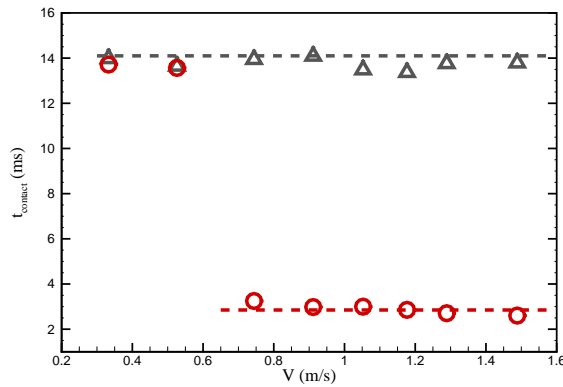


Figure 8.7: Simulation results for the variation of contact time with impact velocity for a drop impacting on a flat (triangle) and the egg-carton surface (circle). For egg-carton surface, at low impact velocities ($V < 0.7$ m/s), the drop exhibits conventional bouncing with the same contact time of flat surfaces. While, at larger impact velocities ($V > 0.7$ m/s), the drop bounces as a pancake resulting a factor four reduction in contact time compared to conventional drop impact on flat surfaces.

uniform, as expected. However, after impacting at $t = 0.48$ ms, one can observe that the pressure is rapidly increased on the impact zone where the liquid penetrates into valleys. An abrupt increase of the pressure is more visible at $t = 0.72$ ms when the vapor is trapped in the bottom of the holes (red spots). Consequently, at this moment, due to occurrence of

high pressures in the cavities placed on impact, the liquid penetrated into valleys accelerates upwards. Therefore, these cavities at the center of the drop impact are first emptied of the intruded liquid (even though the liquid above these holes is still moving downwards exerting small downward force) and this process is gradually extended to the cavities placed far away from impact center (see Fig. 8.6 for the interval between 1.2 ms to 1.9 ms). Eventually, at $t = 2.8$ ms the drop leaves the surface in a flattened pancake shape while a uniform pressure is observed for both sides of the liquid drop.

In Fig. 8.7, we plot our simulation results for the contact time as a function of the impact velocity. In this graph, triangles show the contact times for drops impinging on a flat surface while circles display the results for the egg-carton surface. From Fig. 8.7, for flat surface, as it was already shown in chapter 7, the contact time is independent of the impact velocity. However, for egg-carton surface, a transition occurs at around $V = 0.7$ m/s. Using numerical simulations obtained for the egg-carton surface, we observed that for low impact velocities ($V < 0.7$ m/s), the drop exhibits the conventional complete rebound ($t_{\text{contact}} \approx 13.5$ ms $\approx 2.4\sqrt{\rho R_0^3/\sigma}$), while for higher impact velocities ($V > 0.7$ m/s), the drop jumps off the surface as a pancake shape with a contact time smaller than that on flat surface by factor four ($t_{\text{contact}} \approx 2.8$ ms $\approx 0.51\sqrt{\rho R_0^3/\sigma}$). Figure 8.7 clearly shows that the pancake bouncing occurs for a large range of the impact velocities and more importantly the contact time is almost constant in the pancake bouncing regime.

Finally the performance of the proposed egg-carton surface was tested by experiments in laboratory of Prof. Poulikakos, LTNT-ETHZ. Figure 8.8 shows the preliminary results obtained by experimental observations for drop impact onto both flat and egg-carton surfaces. From Fig. 8.8, it is clearly visible that the pancake bouncing on the egg-carton surface is also observed by experiment for larger impact velocity ($V > 0.7$ m/s) as was already predicted by numerical simulations. However, the contact time measured by experiment in Fig. 8.8, is bigger than that predicted by simulations ($t_{\text{contact}} = 3.4$ ms $\approx 0.79\sqrt{\rho R_0^3/\sigma}$). This difference can be due to the effect of the SHS coating quality of the conical holes. In the experiments, the SHS coating was produced by spraying a polymer solution on the egg-carton surface. We predict that the SHS coating of the holes in the experiments, is not as perfect as that for the conical posts. Therefore, further work to improve the quality of SHS coating in the experiment which consequently would allow further insight into different aspects of the pancake bouncing phenomenon on the egg-carton surface should be the subject of future investigation.

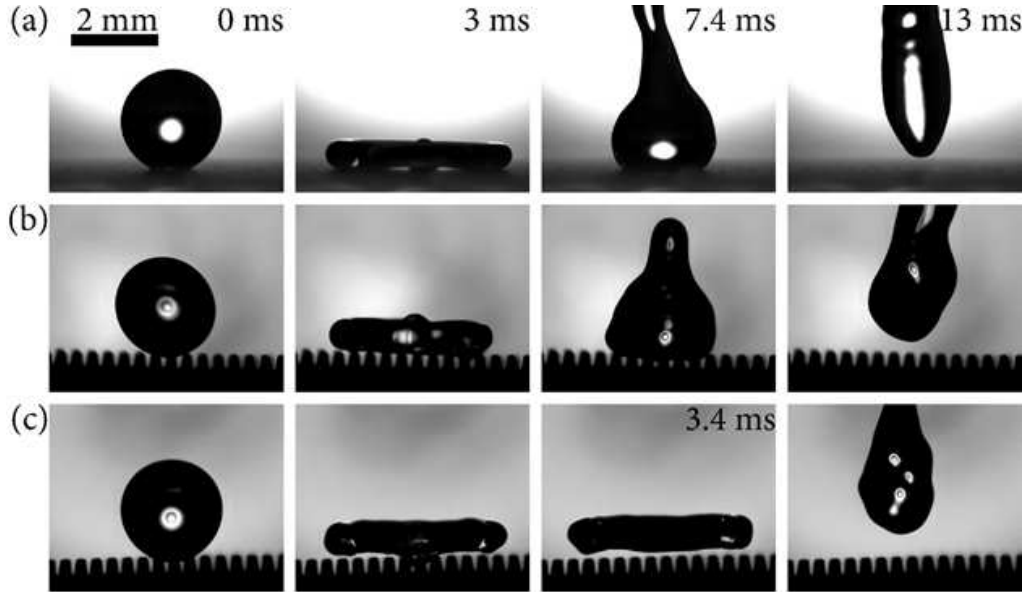


Figure 8.8: Experimental results for impact dynamics of water droplets: (a) Conventional rebound on a flat surface at $V = 0.75$ m/s; (b) Conventional rebound on the egg carton surface at $V = 0.6$ m/s; (c) Pancake rebound at $V = 0.8$ m/s; all images have the same scale bar and are synchronized in time with (a) if not otherwise stated. The drop diameter in experiment was 2.2 mm. The experimental images were provided by Gustav Graeber (group of Prof. Poulikakos, LTNT ETHZ).

8.2.3 Ring bouncing

In the second innovative design, the flat surface was first designed by adding a finite size conical hill on the surface where the drop lands. Then on the suggestion of our collaborators (the group of Prof. Quéré) we switched to spherical defect and it had no impact on contact time (see Fig. 8.9). The idea of adding macrotextures on a flat surface to manipulate the hydrodynamics of the drop center, was first proposed in [12, 14]. There, a very long macroscopic ridge or wire with thickness of a few hundred microns was held along a flat surface at landing location of the liquid drop. However, we propose a flat surface decorated with a finite macroscopic object (spherical defect) at landing spot rather than what was proposed in [12, 14]. Using numerical simulations together with experimental observations of our collaborators in the group of Prof. Quéré (Interfaces & Co., ESPCI Paris), we show that for a drop impacting on such a surface, a new drop rebound regime **”ring bouncing”** occurs.

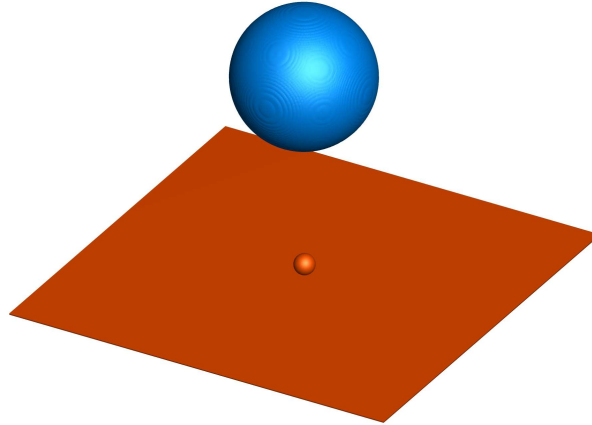


Figure 8.9: Ring bouncing simulation setup. A water drop with diameter of 2.6 mm is impacted on a spherical defect of diameter 0.4 mm.

Drop impact dynamics usually displays two phases: spreading and retraction. The new macrot textured surface shown in Fig. 8.9 exhibits a distinctive dynamic behavior for drop bouncing. For this surface, after impacting, the drop spreads on the surface and then, when it reaches the maximum radial deformation, since the thickness of the spreading liquid film becomes smaller than the defect thickness, the liquid film ruptures at the center and generates an inner rim. At this moment, the outer rim starts contracting inwards while the inner rim begins expanding outwards because of its momentum. Later, when these two opposing fluid motions collide, the horizontal momentum of drop is converted into vertical motion due to the presence of the wall. Finally the drop lifts off the surface in the shape of ring. Since the departure from the surface begins before the completion of the retraction process, the contact time is reduced by factor two compared to conventional impact on flat surfaces. Experimental confirmation of ring bouncing on a geometrically similar surface with simulations was independently demonstrated by Interfaces & Co. group at ESPCI Paris also.

The ring bouncing simulation setup is shown in Fig. 8.9. Unless otherwise stated, for both simulations and experiments, a water drop with diameter of 2.6 mm is impacted on a spherical defect of diameter 0.4 mm (Fig. 8.9). Both flat surface and spherical defect are superhydrophobic with contact angle of 161° .

8. DROPS BOUNCING OFF MACROTEXTURES: DISCOVERY OF NEW SURFACES

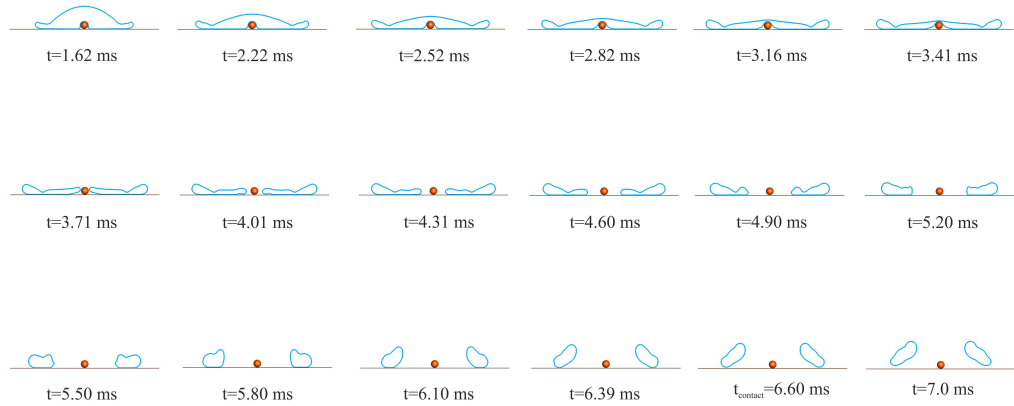


Figure 8.10: Selected snapshots of a drop impinging on a spherical defect. Each image shows the interface profile for middle plane of the computational domain. The drop impact velocity is 1.28 m/s.

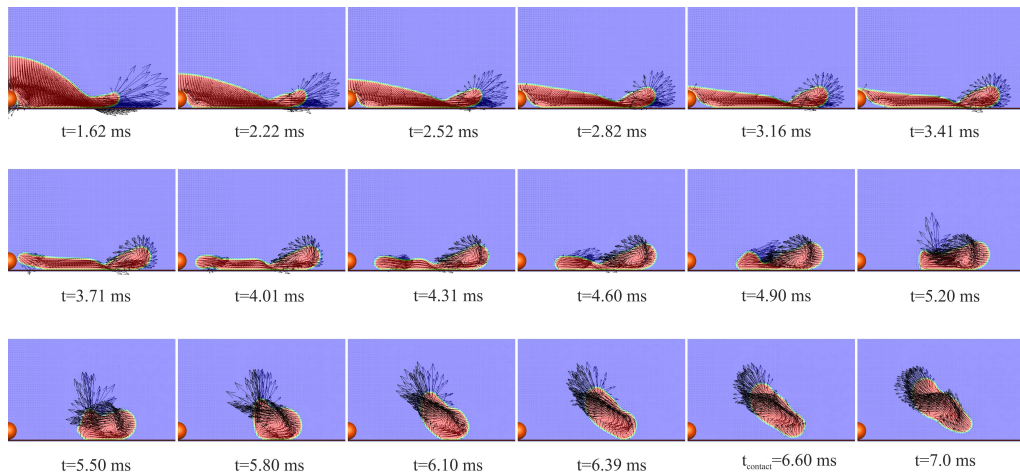


Figure 8.11: Visualization of velocity field inside the drop during impact on the macrotextured spherical defect. The drop impact velocity is 1.28 m/s.

To a better understanding of the physics governing the ring bouncing, using our numerical simulations, we first visualize the liquid-vapor interface profile as well as the velocity field inside the drop, during drop impact on the spherical defect. Figure 8.10 shows different snapshots of the liquid-vapor interface profile during impacting the drop on the surface for symmetry plane. The impact velocity of the drop is 1.28 m/s. As it is clearly visible from Fig. 8.10, after drop impact on the spherical object, the drop starts spreading on the surface till the moment it reaches a maximum radial expansion at

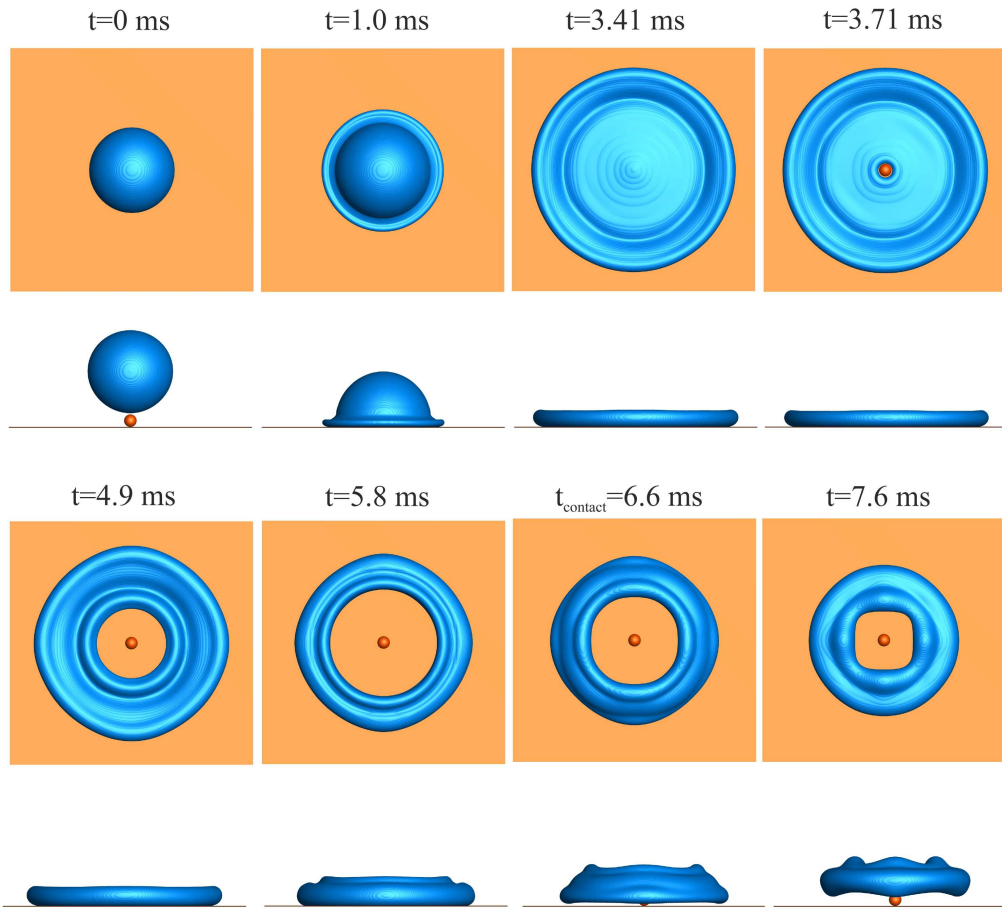


Figure 8.12: Different snapshots obtained by numerical simulations showing front and top view of a liquid drop with diameter of 2.6 mm impacting on a spherical defect of diameter 0.4 mm.

$t = 3.41$ ms. Later at $t = 3.71$ ms, since the spreading film becomes thinner than the defect diameter, the liquid film ruptures from the center and thus an inner rim is generated from the center (see Fig. 8.12 (simulation) and Fig. 8.13 (experiment) for three dimensional view). From this moment, the liquid drop is carried by two liquid jets; the liquid jet activated by generating the inner rim and the liquid jet due to recoiling process of the outer rim (see velocity field shown in Fig. 8.11 for the interval between $t = 3.41$ ms to $t = 4.9$ ms). When two liquid jets moving in opposite directions interact with each other at $t = 5.2$ ms, as it is obvious from the velocity field inside the drop shown in Fig. 8.11, the horizontal momentum of the liquid jets is converted into vertical momentum which results in the drop bouncing off from surface in the shape of ring at $t = 6.6$ ms (see also the the selected

8. DROPS BOUNCING OFF MACROTEXTURES: DISCOVERY OF NEW SURFACES

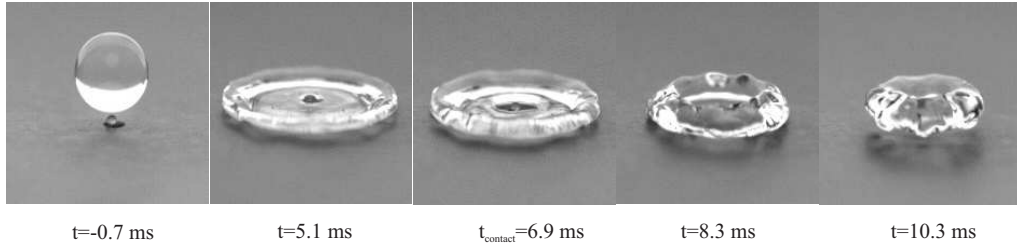


Figure 8.13: Selected snapshots obtained by experiments showing a water drop of diameter 3.2 mm impacting on a superhydrophobic surface textured by a bead of diameter 0.4 mm. The experimental images were prepared by Pierre Chantelot (group of Prof. Qu er , Interfaces & Co., ESPCI).

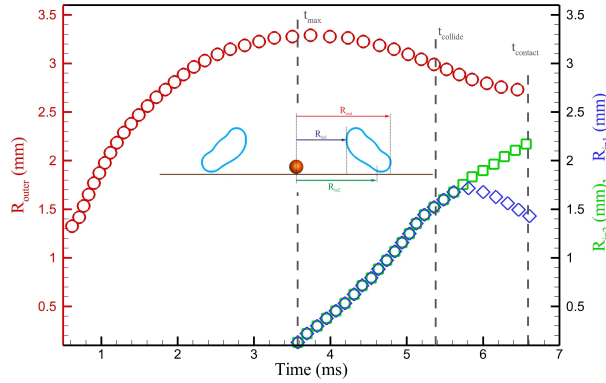


Figure 8.14: Evolution of the radius of the outer and the inner rim during the impact. R_{out} is the maximum radial expansion of the outer rim. The R_{in1} and R_{in2} are measured when the drop breaks from the center and generates an inner rim. The R_{in1} and R_{in2} stand for the minimum and maximum radial expansion of the inner rim. The impact velocity of the drop is 1.28 m/s.

snapshots in Fig. 8.12 (simulation) and Fig. 8.13 (experiment)).

For the simulation shown in Figs. 8.10, 8.11 and 8.12, we measured the temporal variation of the outer and the inner rim radius during the impact. The results are plotted in Fig. 8.14. In this graph, R_{out} is the maximum lateral deformation of the outer rim and R_{in1} and R_{in2} are the minimum and the maximum radius of the inner rim, respectively. Figure 8.14 shows that spreading lasts about half the contact time and the liquid film rupturing is initiated almost at maximum lateral spreading. Moreover and surprisingly, it is seen from Fig. 8.14 that, the inner rim moves towards the spreading

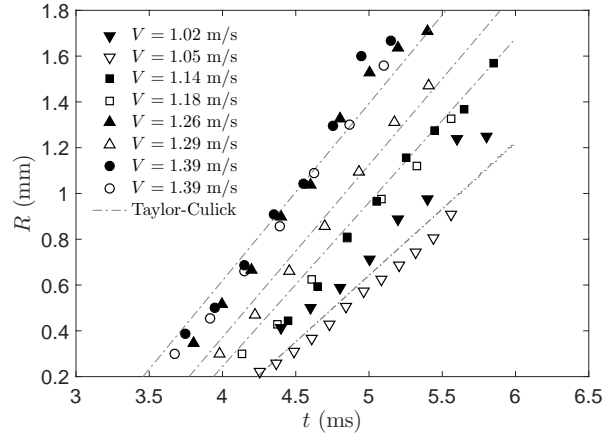


Figure 8.15: The inner rim radius, R , as a function of time for different impact velocities. The R is measured from the moment when the spreading film is ruptured, t_{rupture} , till the moment when it collides with the outer rim. Open symbols are simulations and solid symbols are experiments. The dash lines are computed by Taylor-Culick law ($R = \sqrt{2\sigma/(\rho_l h_l)}(t - t_{\text{rupture}})$). The experimental data were provided by Pierre Chantelot (group of Prof. Quéré, Interfaces & Co., ESPCI).

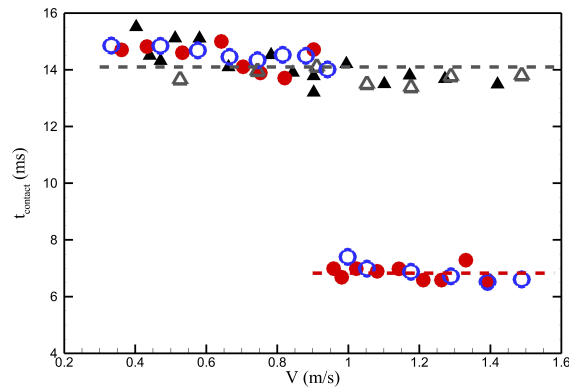


Figure 8.16: Variation of contact time with impact velocity for a drop impacting on a flat surface (triangles) and spherical defect (circles) of diameter 0.4 mm. Open symbol: simulations, Solid symbol: experiments. The experimental data were provided by Pierre Chantelot (group of Prof. Quéré, Interfaces & Co., ESPCI).

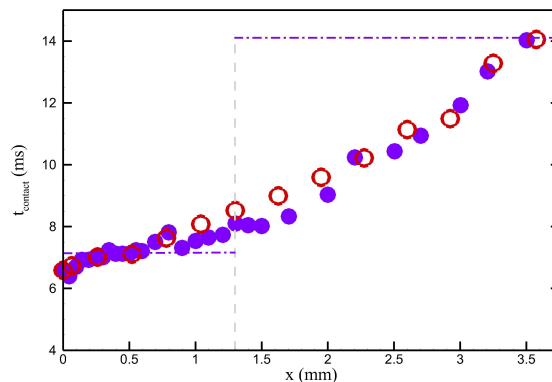


Figure 8.17: Variation of contact time with distance x (the distance between drop center to spherical defect center along the symmetry axis) for water drops impacting on spherical defect. Open symbol: simulations, Solid symbol: experiments. For all measurements, the impact velocity of the drop is fixed to 1.28 m/s. The experimental data were provided by Pierre Chantelot (group of Prof. Quéré, Interfaces & Co., ESPCI).

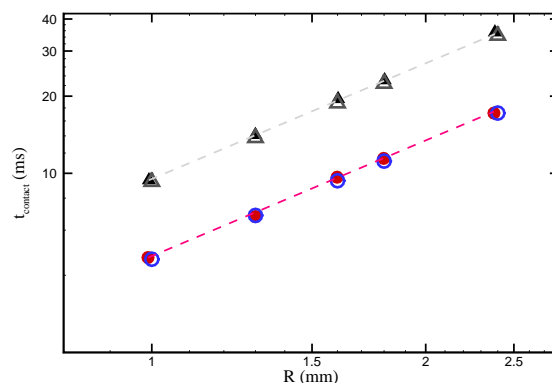


Figure 8.18: Contact time versus drop radius for a flat surface with (circles) and without (triangles) spherical defect. Results for flat surface are fitted by the gray dashed line computed by the equation $t_{\text{contact}} = 2.55\sqrt{\rho R_0^3/\sigma}$ as found in Ref. [11] and data for flat surface with defect fitted by the equation $t_{\text{contact}} = (2.55\sqrt{\rho R_0^3/\sigma})/2$ (red dashed line) as found in this research. Open symbol: simulations, Solid symbol: experiments. The experimental data were provided by Pierre Chantelot (group of Prof. Quéré, Interfaces & Co., ESPCI).

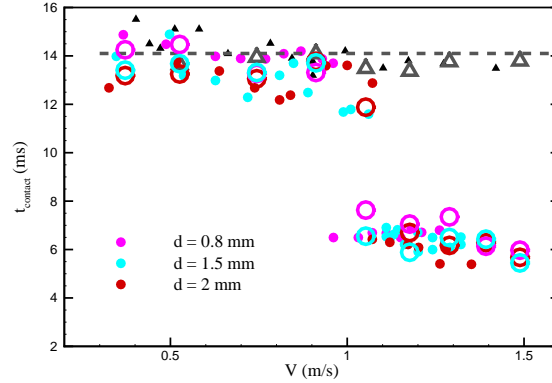


Figure 8.19: Contact time versus impact velocity for a drop impacting a cylindrical defect of different radii. The height of texture is kept constant and equal to diameter of spherical defect (0.4 mm) while the diameter is varied ($d=0.8, 1.5$ and 2 mm). For all simulations and experiments the droplet diameter is fixed to 2.6 mm. Open symbol: simulations, Solid symbol: experiments. The experimental data were provided by Pierre Chantelot (group of Prof. Quéré, Interfaces & Co., ESPCI).

outer rim with a roughly constant speed (linear squared line) and then it collides with the outer rim at time t_{collide} . This collision causes that the drop to lift off the surface later at $t_{\text{contact}} = 6.6$ ms (see Fig. 8.14).

This statement that the speed of the inner rim towards the outer rim is almost constant can be proved by comparing simulation results with the well-known Taylor-Culick law. Taylor [174] and Culick [175] predicted a constant velocity for the rim of an opening hole in a soap film of uniform thickness. They showed that the constant opening velocity V_c results from a balance between the rim inertia and surface tension in the film, and is given by $V_c = \sqrt{2\sigma/(\rho_l h_l)}$, where σ is the surface tension, ρ_l is the liquid density and h_l is the liquid film thickness. Using the equation given by V_c , one can derive the equation for the inner rim radius as a function of time as; $R = \sqrt{2\sigma/(\rho_l h_l)}(t - t_{\text{rupture}})$, where t_{rupture} is the moment when the spreading film is ruptured from the center. In Fig. 8.15, we have plotted the inner rim radius, R , as a function of time for various drop impact velocities. Both simulations and experiments show a close match with theoretical predictions.

Next, we compare our contact time measurements with the experimental observations of our collaborator (Interfaces & Co., ESPCI Paris) in Figs. 8.16 to 8.19. In Fig. 8.16 we plot the variation of the contact time with impact

velocity for a drop impacting on a flat surface with (circles) and without (triangles) spherical defect. In this graph, open symbols are the result obtained from simulations while solid ones are the experimental predictions. An excellent match between simulations and experiments is evident from this plot. As it is seen from Fig. 8.16, for lower impact velocities ($V < 0.9$ m/s), the contact time for both flat and macrot textured surfaces are roughly the same. In fact, for lower impact velocities, due to low kinetic energy of the drop, it spreads less on the surface and thus at maximum deformation the spreading liquid film is thicker than the defect diameter. Therefore, the liquid film does not rupture at all and thus the macroscopic defect does not have significant effects on the rebound. As a results, the drop detaches from the surface at ≈ 14.5 ms ($\approx 2.55\sqrt{\rho R_0^3/\sigma}$) which is in good agreement with previous results for conventional complete rebound [11]. However, for higher impact velocity cases ($V > 0.9$ m/s), the drop exhibits a distinctively different bouncing behavior called 'ring bouncing' which was already shown in Figs. 8.12 (simulation) and 8.13 (experiment). Figure 8.16 shows that in the region of the ring bouncing ($V > 0.9$ m/s), the contact time is roughly half that observed by the flat surface ($t_{\text{contact}} \approx 6.8$ ms $\approx 1.2\sqrt{\rho R_0^3/\sigma}$).

Contact time on the spherical defects as a function of the landing location x (center to center spacing between the drop and spherical defect along the symmetry axis) is reported in Fig. 8.17. For all simulations and experiments in this graph, the drop impact velocity is fixed to 1.28 m/s. The contact time is shortest when the drop impacts directly on the spherical defect and it increases as the drop lands further away from the macroscopic object. It is seen in Fig. 8.17 that at $x = 3.5$ mm the contact time is the same with that on flat surfaces. This is because, the maximum drop spreading according to $R_{\text{max}} \sim R_0 We^{1/4}$ [6] and simulation results, is around 3.2 mm that is smaller than the $x = 3.5$ mm. Thus, for $x > 3.2$ mm, the drop does not meet the spherical defect during impact and it rebounds from the surface as it does on flat surfaces.

Next, to investigate the effect of other parameters such as the drop size and defect width, the contact time is measured by varying the droplet radius (Fig. 8.18) and the width of the defect (Fig. 8.19). For both plots, solid symbols are experiments and open symbols are our simulation results. In Fig. 8.18 we report the contact time as a function of drop radius for a flat surface with (circles) and without spherical defect (triangles). For both surfaces, data are fitted by the equation $t_{\text{contact}} = q\sqrt{\rho R_0^3/\sigma}$ (gray and red dashed lines), where the prefactor q is equal 2.55 for the flat surface (gray dashed line) as was found in Ref. [11] and is equal to 2.55/2 (by factor 2 smaller) for the flat surface with spherical defect (red dashed line) as was shown in this work. It should be noted that circles in Fig. 8.18 are corre-

sponding to ring bouncing regime ($V > 0.9$ m/s).

Finally, To complete our observations, the drop contact time is measured by varying the width of the finite macrotecture placed on flat surface. For the results shown in Fig. 8.19, a cylindrical macrotecture is added on flat surface at landing location of the drop. The hight of texture is kept the same with the diameter of the previously spherical defect (0.4 mm) while the width is varied by three different values ($d=0.8, 1.5$ and 2 mm). From Fig. 8.19, for both lower and larger impact velocities, the contact times do not show significant changes compared with spherical defect by varying the width of the texture. For all results shown in this plot, the droplet diameter was fixed to 2.6 mm. Therefore, as long as the defect width is comparable with drop diameter, we do not expect to see significant effects on the contact time.

8.3 Summary and Conclusions

To reduce the contact time of drops impinging on superhydrophobic surfaces, we proposed two new textured surfaces here. The validity, reliability and applicability of our proposals was first demonstrated by an extensive detailed numerical investigation and then confirmed by experimental observations of our collaborators (the group of Prof. Poulikakos, LTNT-ETHZ, and Prof. Quéré, Interfaces & Co., ESPCI). The first proposed surface was textured with an egg-carton pattern including macroscopic conical posts and holes. Utilizing a combination of posts and cavities in egg-carton surface allowed us firstly to maximize the surface area being available to droplet during impact and secondly and more importantly to utilize from advantage of the air pockets trapped in the cavities. Using numerical simulations we showed that as soon as the impacting drop penetrates into cavities, the pressure inside the cavities rapidly rises and then due to that the direction of drop's momentum changes from downwards to upwards. It was illustrated that this phenomenon together with the effect of the capillary forces exerted by non-wetting surfaces cause the penetrated liquid to return very quickly to top of the posts and then jumps off the surface in a pancake form. From results obtained by numerical simulations, it was shown that the pancake bouncing occurs for a large range of impact velocities ($V > 0.7$ m/s) with a contact time of factor four smaller than that on flat surface. The preliminary experimental results also confirmed the pancake bouncing behavior on the egg-carton surface, as predicted by simulations.

With our second innovative design, we showed that if a finite hill structure

such as a spherical defect with a size of few hundred microns, is placed on a flat surface where the drop lands, a new drop rebound regime "ring bouncing" will be observed. Using our simulations, we demonstrated that, for drops with sufficient kinetic energy ($V > 0.9$ m/s), after impacting, at appropriate time close to maximum deformation, the spreading liquid film is ruptured from the center where the defect is placed. As a consequence, an inner rim is created which owing to its momentum, it moves towards the expanding outer rim which moves inwards due to retraction. It was interpreted that the ring bouncing is consequence of colliding these two opposite motions. For larger impact velocities ($V > 0.9$ m/s), both experiment and simulation showed a factor two reduction in contact time compared with flat surfaces due to occurrence of ring bouncing .

Chapter 9

Conclusions and future work

In this dissertation we propose an advanced approach to simulate the complex dynamic phenomena of two-phase fluids in the framework of the lattice Boltzmann method. In spite of many attempts to develop two-phase flow techniques using LBM, the existing multiphase LB formulations suffered from substantial drawbacks such as restriction on thermodynamic consistency, liquid-vapor interface thickness, low liquid-vapor density ratio and others. Moreover and in particular, these approaches could not be applied for simulation of dynamical applications at sufficiently high Weber and Reynolds numbers with simultaneously large enough liquid-vapor density ratio and hence they were unable to address complex dynamics of two-phase phenomena in a quantitative fashion. These limitations motivated us to introduce a model such that it brings about a substantial increase in the operating range of lattice Boltzmann simulations of multiphase flows for both stationary and particularly non-stationary applications. To this end, the entropic lattice Boltzmann method was studied in details and then combined with a free-energy based multiphase model. We have demonstrated that the forcing free-energy method augmented by the nonlinearly stable entropic scheme together with a polynomial equation of state, resolves the setbacks of those multiphase LB models in literature and allows us to simulate various problems ranging from binary droplet collisions to drop impacting on solid surfaces. The newly proposed model drastically increased the liquid-vapor density ratio and decreased the minimal viscosity in multiphase simulations. The entropic lattice Boltzmann method was successfully employed to achieve large enough Weber and Reynolds numbers that are typical for two-phase applications. Also, for the first time, accurate and reliable results were obtained for non-stationary droplets using the free energy formulation that assures thermodynamic consistency and provides

deep physical insights into the flow field.

The path to a successful model for two-phase dynamics would be to develop a simulation tool which can handle, in the order of increasing complexity, multiple droplet interactions for different system conditions, topological shape changes due to the dynamics of fluid which may result in break-up or coalescence of a fluid phase, interaction of droplets with solid walls having different contact angles and so forth. Once all these scenarios have been independently tested and validated with the available theoretical and experimental predictions, one will have more confidence and of course more understanding of the physics being simulated when simulations are performed for more complicated scenarios. Thus, in this dissertation, a successful attempt has been made to address the above mentioned goals. We have verified and tested the viability of the proposed model for simulation of complex dynamics of two-phase flows by comparing the simulation results with various experimental and theoretical findings. Moreover, since numerical simulations provide substantial information on the flow field, stresses and etc, we also focused on analyzing the flow situations beyond those experiments.

9.1 Summary of results

The contribution of this dissertation can be divided as two parts. One is theoretical, numerical and program development of a new numerical tool based on lattice Boltzmann method to simulate liquid-vapor interfacial flows. The other is the detailed study of the various two-phase problems made possible by this new multiphase model. The conclusion from each of these contributions are now summarized.

- As a first contribution of this dissertation, we proposed a novel thermodynamically consistent lattice Boltzmann model for simulation of complex dynamics of multiphase phenomena. As presented in chapter 2, we first studied the entropic lattice Boltzmann method in detail and then we extended the ELBM to two-phase flows by introducing a forcing term in the entropic lattice Boltzmann equation. The forcing term was derived by incorporating the Korteweg's stress obtained by minimizing the free-energy function of non-ideal fluid for one-component multiphase cases which assures the thermodynamic consistency of the model. Then we demonstrated that a good choice of equation of state to attain larger density ratio for dynamical problems is a polynomial regularization of the well-known Peng-Robinson EoS. Indeed, since the

liquid density computed in simulations might tend to singular point of P-R EoS at some grid points due the large time step used in LB simulations, the polynomial EoS enhanced the performance of our model for simulation of both stationary and non-stationary problems with large density ratio. As a consequence, using the ELBM approach for two-phase flows, we could simulate a wide range of applications ranging from collision of droplets to impacting drops onto solid substrates at large Weber and Reynolds numbers with sufficiently high liquid-vapor density ratio which were not possible before due to lack of entropy considerations and polynomial representation of the equation of state in earlier multiphase LB models.

After development of the ELBM for two-phase flows, the viability and reliability of the model was evaluated by applying the model to a range of fluid-fluid and particularly fluid-solid interface problems. A brief review of the results obtained from simulation of these problems are given below.

- Simulation of the fluid-fluid interface problems were presented in chapter 3. There, first the thermodynamic consistency of the present model was verified by simulating the thermodynamic quantities such as the coexistence curve, Laplace's law, speed of sound and the liquid-vapor density profile. Then, an extensive numerical simulation of the binary droplet collisions was presented. First, different regimes of collisional outcomes namely coalescence, reflexive separation and stretching separation were simulated and an accurate identification of boundaries between these regimes, was observed. Then, detailed comparison with experimental observations together with the roles played by Weber number and impact parameter in droplet collision and breakup, was presented. Moreover and as an asset for present model, quantitative prediction of the evolution of the lamella thickness and viscous dissipation were provided.
- In chapter 4, we extended the application of the present model to simulation of dynamic fluid-interface problems. The accuracy of the method was first verified by comparing the simulation results with the existing analytical solutions for Young-Laplace law and capillary filling in channels. Then, the proposed model was applied to simulation of drops impinging on flat substrates with different wettability. The geometrical properties of the impacting drops such as, maximum radial deformation and thickness of the spreading liquid film (lamella) were compared with those observed by experiments and reported by theory.

- In chapter 5, we tested the capability of our model in study of capillary phenomena. The method first validated by simulating the meniscus rise in capillary tubes. The simulation results were found to be in a good agreement with theoretical predictions proposed by Washburn. Chapter 5 was ended by simulating the rise of liquid through twisted yarns as a test case to investigate the usability of the present method for simulation of capillary systems with more complexities. It was shown that for a given fiber arrangement in yarns, the liquid rises faster through the fibers by increasing the wettability of surfaces. However, to provide further insight into the wicking results presented in chapter 5, further work to examine the numerical effect of the wall boundary conditions on the dynamic behavior of the wicking is needed which it should be considered as a direction for future work.
- In chapter 6, our numerical method was used for detailed investigation of the new experimentally discovered rebound regime called "tumbling". It was first shown by LTNT-ETHZ group in experiment that the high viscous drops such as glycerol drops, after impacting on sublimating slopes, rather than showing the conventional rebound behavior (sliding, spreading and recoiling), exhibit a prompt tumbling rebound faster than the water drops with three order of magnitude less viscous. Using numerical simulations, it was demonstrated that the tumbling rebound is consequence of conversion of part of the initial linear momentum of the drops into angular momentum. ELBM simulations showed that the tumbling appeared due to a rapid transition of the internal angular velocity prior to rebound to drop rotation. It was demonstrated that this amount of the angular velocity is sufficient for drops to tumble off the slopes without experiencing retraction on the surface.
- The dynamic behavior of drop impact onto superhydrophobic surfaces designed with sub-millimeter posts was investigated comprehensively in chapter 7. Superior stability of the ELBM together with the flexibility of the wall boundary conditions allowed us to study, for the first time, the pancake bouncing phenomenon in complete detail. The reliability of the methodology was tested and verified by comparing simulation results with those reported by experiments for pancake bouncing in Ref. [13]. Apart from reproducing those experimental predictions, we also extensively studied the influence of the drop impact velocity and the surface parameters such as the spacing between posts and the coating quality of the surface, on the pancake quality. Furthermore and in particular, we presented an energy balance anal-

ysis, for the first time, which enabled us to understand the physics being behind of the pancake bouncing. This energy analysis allowed us to accurately account for the transformation of kinetic energy into surface energy and vice-versa and the role played by viscous dissipation caused by droplet wall interactions.

- After testing and benchmarking our method with large number of experiments for drop impact on substrates, further investigation was conducted to discover new textured surfaces that minimize the contact time between impacting drops and solid surfaces. Based on ELBM simulations, we proposed detailed investigation of two new textured surfaces in chapter 8. It was first shown numerically that these surfaces are capable of reducing the droplet contact time compared to the flat surfaces. After that, the performance of the proposed surfaces in terms of reducing the contact time, was shown experimentally by our collaborators. Our first design was called "egg-carton". The egg-carton pattern was textured with a combination of conical posts and holes of the same size. Using numerical simulations we showed that the simultaneous effects of the rising pressure inside the cavities and the capillary forces exerted by non-wetting surfaces allow the drop to jump off the surface in a flattened pancake shape. We showed numerically that in the range of pancake bouncing ($V > 0.7$ m/s), the contact time of the drop reduces by factor four compared with that on a flat surface. In our second design, to manipulate the hydrodynamics of the drop center, a macroscopic spherical defect was added on a flat surface where the drop lands. We showed that after impacting drops on such a surface, a new drop rebound regime, which we termed ring bouncing, was observed. By visualizing velocity field inside the impacting drop and the liquid-vapor interface profile, it was shown that after spreading the drop on the surface, an appropriate time close to its maximum radial deformation, the spreading liquid film is ruptured from the center where the defect is placed. Then, the inner rim generated from the center moves with almost constant speed towards the retracting outer rim. Later due to colliding these two motions, the drop jumps off the surface in the shape of ring. Using both experiment and simulation, it was demonstrated that the ring bouncing occurs in the regime of high impact velocities ($V > 0.9$ m/s) and leads to reduce the contact time by factor two compared with conventional bouncing on flat surfaces.

It is hoped that the developments presented in this research will lead to a better understanding of two-phase interactions, formation of various flow

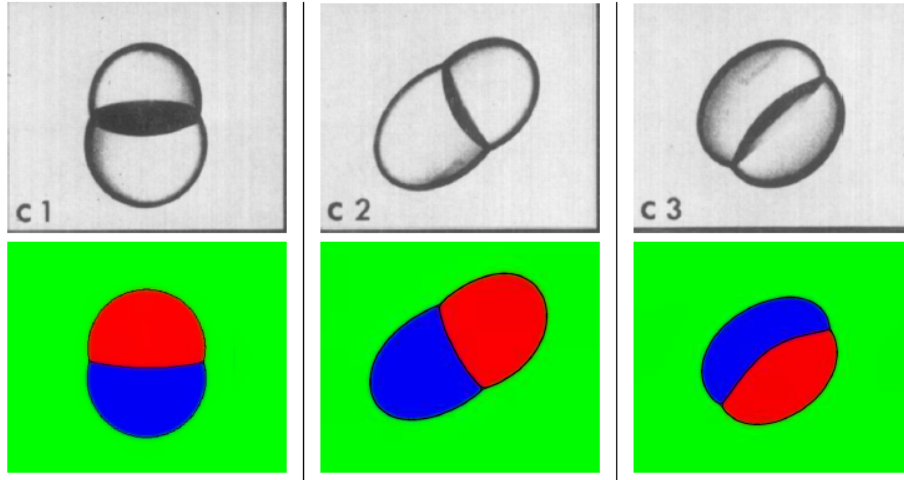


Figure 9.1: Comparison between simulation (bottom) and experiment [15] (top) for a compound droplet in shear flow (Janus droplet) at orientation angle $\varphi = 0^\circ$ (c1), $\varphi = 58^\circ$ (c2) and $\varphi = 145^\circ$ (c3).

patterns and thus will pave the way towards a simulation-based capability to predict the complex dynamics of two-phase flow problems made possible using the proposed approach. However, although the simulation results shown in this dissertation are promising, they only represent a beginning for the ELBM model for multiphase flows. Therefore, next, we suggest possible directions for future work.

9.2 Directions for future work

The field of ELBM fluid simulations is very large and relatively young. As a consequence, there is still room for deep analysis and development. A few of the areas specially related to the work presented here are now listed below for future task. We have conducted preliminary research in some of these areas.

- *ELBM for multiphase multicomponent flows*

The ELBM model presented in this research, was proposed for simulation of two-phase systems with one component. The first direction for future work would be to extend the present approach to simulation of multiphase multicomponent flows. The challenge for LB simulation of a multicomponent system lies in the fact that momentum conservation is only valid for over-all system but not for each component separately, and therefore diffusion

occurs between different components. The existing LB approaches for simulation of the multiphase multicomponent suffer either from thermodynamic inconsistency or numerical instability. Therefore, their applications are limited either to modeling stationary problems or quasi-dynamical simulations with low density ratio between different components [176, 177]. Here, first, we shall proceed by identifying an appropriate free energy functional that is capable of accurately capturing the hydrodynamic behavior of multicomponent systems [177]. Further, we shall introduce the concept of Boltzmann entropy function to enhance the stability regime and flow parameter range. In order to simulate realistic multicomponent problems such as water and air including higher density ratios, (~ 1000), we need to specify a more proper and realistic equation of state for at least one component (particularly in the liquid phase) instead of using the existing ones. The other component (or the phase gas) can be described by the ideal gas law. Very recently, for simulation of multiphase multicomponent systems, a ternary free energy lattice Boltzmann model was proposed by Semperebon et al. [177]. We have implemented this model in the framework of the entropic lattice Boltzmann method. The preliminary results in two dimensions are shown in Fig. 9.1. Figure 9.1 shows simulation snapshots (bottom) together with those images observed experimentally in [15] (top) for a compound droplet (Janus droplet) in shear flow. In the simulations shown in Fig. 9.1, each color is corresponding an individual component and the density and viscosity ratios between different components are matched with experiment [15]. From Fig. 9.1, it can be found that the combination of the entropic stabilizer and the ternary free energy model [177] shows promising results, however, since in the spirit of the model proposed by Semperebon et al., the density ratio between different components is fixed to one, further advancement is still required and it should be considered as a direction for future work.

- *Thermal effects*

The two-phase model presented in this work is an isothermal approach and thus the temperature dynamics and phase change is not considered. In the existing thermal lattice Boltzmann multiphase flow approaches, usually, a passive scalar method is utilized for the solution of the energy equation due to its computational simplicity and clear interpretation. In the passive scalar approach, temperature is passively advected by the fluid flow and can be simulated as an additional component of the fluid system. However, this approach suffers from some drawbacks such as neglecting the effects of the viscous and compressive heating. Therefore, efforts should be made to develop a more accurate thermal model. We think one possible way of achieving an accurate thermal model for multiphase multicomponent flows

would be the use of lattices with a larger number of velocities than the standard lattices used throughout this work. Using the multi-speed lattices, the higher order moments can be calculated directly from the population distribution functions (PDFs). These moments include additional information about the system dynamics, such as the momentum and energy fluxes. Thus, it is possible to determine information about the energy evolution of the domain directly from the information stored in the PDFs. The long standing notion of how to construct lattices with larger velocity sets have been recently solved in [59, 74]. Therefore, we shall introduce the notion of multispeed lattices to extend our current isothermal model to thermal multiphase multicomponent flows. Further thermal effects such as latent heat and phase transition need to be incorporated in line with existing suggestions for free-energy based multiphase lattice Boltzmann models [178].

- *Larger Weber and Reynolds numbers*

The ELBM two-phase model presented in this research was tested and benchmarked against a large number of experiments such as binary droplet collision and drop impact onto solid surfaces. The typical We and Re values for such problems are $We \sim O(10^2)$ and $Re \sim O(10^3)$. However, to simulate applications such as high speed sprays with very higher We and Re , further developments are still required. One way to simulate applications with very large Weber and Reynolds numbers would be the use of the multispeed lattices. It was shown in Ref. [74] that the use of the multispeed lattice will support stable simulations. Moreover, very recently, it was demonstrated in [59] that a version of multispeed lattices (49 velocities in two dimensions (D2Q49)) based on the concept of the entropic lattice Boltzmann method drastically enhances the numerical stability of simulations. Therefore, we have implemented the D2Q49 in the framework of the two-phase flows and our preliminary results show that such large lattices allow us to achieve We and Re with one order of magnitude larger than those were already obtained ($We \sim O(10^3)$ and $Re \sim O(10^4)$). As an example, the two-dimensional simulation for droplet splashing on a thin liquid film at very high We and Re is shown in Fig. 9.2.

- *Grid refinement*

While the above mentioned improvements are necessary for the future of the ELBM for multiphase flows, further development can also be considered. The resolution of interfaces in LB multiphase simulations has always been the topic under discussion. Indeed, since the LB multiphase approaches are based on the diffusive interface method, the fluid-fluid interface is constructed by some grid nodes in simulations. Although it seems so far, im-

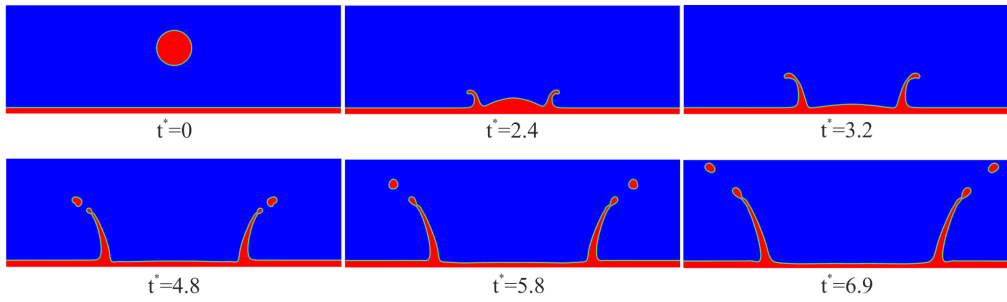


Figure 9.2: Different snapshots for simulation of droplet splashing on a thin liquid film.

Improvements to LB multiphase approaches have reduced the width of the interface, there still exists a limit of a few lattice points. As it was already mentioned in [179], one way to reduce further the fluid-fluid interface width would be to introduce some form of grid refinement around the interface. Therefore, this can be considered as a future task for further investigation.

Appendix A

Chapman-Enskog expansion of the LBM

For the forcing free-energy scheme presented in sec 2.5.2, we aim to derive the Navier-Stokes equations using the Chapman-Enskog method, under local conservation laws in (2.10). Let us write the equation (2.50) in general form as:

$$f_i(\mathbf{x} + \mathbf{c}_i \delta t, t + \delta t) - f_i(\mathbf{x}, t) = \omega (f_i^{\text{eq}}(\rho, \mathbf{u}) - f_i(\mathbf{x}, t)) + F_i, \quad (\text{A.1})$$

where the forcing term $F_i = f_i^{\text{eq}}(\rho, \mathbf{u} + \delta \mathbf{u}) - f_i^{\text{eq}}(\rho, \mathbf{u})$ is defined using the exact difference method (EDM) in [77] and satisfies the following moments,

$$\begin{aligned} \sum_i^N F_i &= 0, \\ \sum_i^N \mathbf{c}_i F_i &= \mathbf{F} \delta t, \\ \sum_i^N \mathbf{c}_i \mathbf{c}_i F_i &= \Psi \end{aligned} \quad (\text{A.2})$$

where the general term Ψ determines the second order moment of F_i . We shall specify the form of Ψ later.

We now start by expanding the shift operator in a Taylor series until second

order,

$$\begin{aligned} & \left[\delta t (\partial_t + \partial_\mu c_{i\mu}) + \frac{\delta t^2}{2} (\partial_t + c_{i\mu} \partial_\mu) (\partial_t + c_{i\nu} \partial_\nu) \right] f_i \\ & = \omega (f_i^{\text{eq}} - f_i) + F_i \end{aligned} \quad (\text{A.3})$$

and by introducing a characteristic time scale of the flows, Θ , and a reduced time $t' = t/\Theta$. We also introduce the reduced velocities $c'_i = c_i/c$, where $c = 1$, and the reduced coordinate $x' = x/(c\Theta)$. Now Eq. (A.3) can be rewritten in terms of the reduced variables, t' , c'_i and x' . After introduction of the smallness parameter $\varepsilon = \delta t/\Theta$, and omitting primes to simplify notation, we have:

$$\begin{aligned} & \left[\varepsilon (\partial_t + \partial_\mu c_{i\mu}) + \frac{\varepsilon^2}{2} (\partial_t + c_{i\mu} \partial_\mu) (\partial_t + c_{i\nu} \partial_\nu) \right] f_i \\ & = \omega (f_i^{\text{eq}} - f_i) + F_i \end{aligned} \quad (\text{A.4})$$

We can now introduce a multiscale expansion of the time derivative operator, the populations and the forcing term to second order as:

$$\varepsilon \partial_t = \varepsilon \partial_t^{(1)} + \varepsilon^2 \partial_t^{(2)} + \dots, \quad (\text{A.5})$$

$$f_i = f_i^{(0)} + \varepsilon f_i^{(1)} + \varepsilon^2 f_i^{(2)} + \dots, \quad (\text{A.6})$$

$$F_i = \varepsilon F_i^{(1)} + \varepsilon^2 F_i^{(2)} + \dots, \quad (\text{A.7})$$

where the moments of the coefficients of the expansion of F_i are given by:

$$\begin{aligned} & \sum_i^N F_i^{(1)} = 0, \\ & \sum_i^N \mathbf{c}_i F_i^{(1)} = \mathbf{F} \delta t, \\ & \sum_i^N \mathbf{c}_i \mathbf{c}_i F_i^{(1)} = \mathbf{\Psi}^{(1)}, \end{aligned} \quad (\text{A.8})$$

and

$$\begin{aligned}
\sum_i^N F_i^{(2)} &= 0, \\
\sum_i^N \mathbf{c}_i F_i^{(2)} &= 0, \\
\sum_i^N \mathbf{c}_i \mathbf{c}_i F_i^{(2)} &= \Psi^{(2)},
\end{aligned} \tag{A.9}$$

By substituting Eqs. (A.5)-(A.7) into (A.4) and equating terms with the same order ($\varepsilon^{(0)}$, $\varepsilon^{(1)}$ and $\varepsilon^{(2)}$), on order $\varepsilon^{(0)}$, we find that the leading term in the expansion (A.6) is the local equilibrium,

$$f_i^{(0)} = f_i^{\text{eq}}, \tag{A.10}$$

Using the implication of the local conservation laws we have:

$$\sum_{i=0}^N \{1, c_{i\alpha}\} f_i = \sum_{i=0}^N \{1, c_{i\alpha}\} f_i^{\text{eq}}, \tag{A.11}$$

By substituting the expansion (A.6) into (A.11) under the preceding equation (A.10), one can find the solvability conditions as:

$$\sum_{i=0}^N \{1, c_{i\alpha}\} f_i^{(1)} = \sum_{i=0}^N \{1, c_{i\alpha}\} f_i^{(2)} = \dots = 0, \tag{A.12}$$

Now in equation (A.4) we collect the terms to the order $\varepsilon^{(1)}$ and $\varepsilon^{(2)}$ and accordingly derive the relations for the first and second order population as:

$$\left(\partial_t^{(1)} + c_{i\mu} \partial_\mu\right) f_i^{(0)} = -\omega f_i^{(1)} + F_i^{(1)}, \tag{A.13}$$

and

$$\begin{aligned}
&\partial^{(2)} f_i^{(0)} + \left(1 - \frac{\omega}{2}\right) \left(\partial_t^{(1)} + c_{i\mu} \partial_\mu\right) f_i^{(1)} + \frac{1}{2} \left(\partial_t^{(1)} + c_{i\mu} \partial_\mu\right) F_i^{(1)} \\
&= -\omega f_i^{(2)} + F_i^{(2)},
\end{aligned} \tag{A.14}$$

The zeroth order velocity moments of Eqs. (A.13) and (A.14) under the solvability conditions (A.12) and the equations in (A.8) and (A.9), are re-

spectively:

$$\partial_t^{(1)}\rho + \nabla \cdot (\rho\mathbf{u}) = 0, \quad (\text{A.15})$$

$$\partial_t^{(2)}\rho + \frac{\delta t}{2}\nabla \cdot \mathbf{F} = 0, \quad (\text{A.16})$$

By combining the Eqs. (A.15) and (A.16), the mass conservation equation is derived as:

$$\partial_t\rho + \nabla \cdot (\rho\mathbf{U}) = 0. \quad (\text{A.17})$$

where the actual fluid velocity \mathbf{U} is defined as:

$$\rho\mathbf{U} = \rho\mathbf{u} + \frac{\mathbf{F}}{2}\delta t, \quad (\text{A.18})$$

Using Eqs. (A.8), (A.9) and (A.12) the first order velocity moments of Eqs. (A.13) and (A.14) are respectively:

$$\partial_t^{(1)}(\rho\mathbf{u}) + \nabla \cdot \mathbf{\Pi}^{(0)} = \mathbf{F}, \quad (\text{A.19})$$

$$\partial_t^{(2)}(\rho\mathbf{u}) + \left(1 - \frac{\omega}{2}\right)\nabla \cdot \mathbf{\Pi}^{(1)} + \frac{1}{2}\partial_t^{(1)}\mathbf{F} + \frac{1}{2}\nabla \cdot \mathbf{\Psi}^{(1)} = 0, \quad (\text{A.20})$$

where $\mathbf{\Pi}^{(0)}$ and $\mathbf{\Pi}^{(1)}$ are the second order moments of $f_i^{(0)}$ and $f_i^{(1)}$, respectively. Since $f_i^{(0)} = f_i^{eq}$ and the equilibrium populations are given by Eq. (2.14), the second order moment of $f_i^{(0)}$ is:

$$\Pi_{\alpha\beta}^{(0)} = \sum_i^N c_{i\alpha}c_{i\beta}f_i^{eq} = \rho c_s^2\delta_{\alpha\beta} + \rho u_\alpha u_\beta, \quad (\text{A.21})$$

By substituting (A.21) into (A.19) we have:

$$\partial_t^{(1)}(\rho\mathbf{u}) + \nabla \cdot (\rho c_s^2\mathbf{I}) + \nabla \cdot (\rho\mathbf{u}\mathbf{u}) = \mathbf{F}, \quad (\text{A.22})$$

The expression for $\mathbf{\Pi}^{(1)}$ in (A.20) can be found from the second moment of Eq. (A.13) as:

$$\partial_t^{(1)}\mathbf{\Pi}^{(0)} + \nabla \cdot \mathbf{Q}^{(0)} = -\omega\mathbf{\Pi}^{(1)} + \mathbf{\Psi}^{(1)} \quad (\text{A.23})$$

where the third order moment $\mathbf{Q}^{(0)}$ of equilibrium populations is:

$$\mathbf{Q}_{\alpha\beta\gamma}^{(0)} = \sum_i^N c_{i\alpha}c_{i\beta}c_{i\gamma}f_i^{eq} = \rho c_s^2 (u_\alpha\delta_{\beta\gamma} + u_\beta\delta_{\alpha\gamma} + u_\gamma\delta_{\alpha\beta}), \quad (\text{A.24})$$

Computing the first order time derivative of the function $\mathbf{\Pi}^{(0)}$ using chain rule and the results of the preceding Eqs. (A.15) and (A.19), for the density and velocity, and neglecting terms of the order of $O(u^3)$ as pertinent to the standard lattices, the expression for $\mathbf{\Pi}^{(1)}$ becomes:

$$\mathbf{\Pi}^{(1)} = -\frac{1}{\omega} (\rho c_s^2 (\nabla \mathbf{u} + (\nabla \mathbf{u})^T) + \delta t (\mathbf{F}\mathbf{u} + \mathbf{u}\mathbf{F}) - \mathbf{\Psi}^{(1)}), \quad (\text{A.25})$$

By combining the equations (A.20), (A.22) and (A.25), the following macroscopic momentum equation can be obtained at the Navier-Stokes level [180, 181]:

$$\partial_t(\rho \mathbf{U}) + \nabla \cdot (\rho \mathbf{U}\mathbf{U}) + \nabla \cdot (\rho c_s^2 \mathbf{I}) = \mathbf{F} - \nabla \cdot \mathbf{P}^{\text{visc}} + \nabla \cdot \mathbf{\epsilon}, \quad (\text{A.26})$$

where the viscous stress tensor \mathbf{P}^{visc} is:

$$\mathbf{P}^{\text{visc}} = -\nu \rho (\nabla \mathbf{U} + (\nabla \mathbf{U})^T), \quad (\text{A.27})$$

The ν in (A.27) is the kinematic viscosity, $\nu = (\frac{1}{\omega} - \frac{1}{2}) c_s^2$.

After replacing the forcing term \mathbf{F} with $\mathbf{F} = \mathbf{F}_f + \mathbf{F}_s + \mathbf{F}_g$, and since the force related Korteweg's stress, \mathbf{F}_f , is given by (2.53), the macroscopic momentum equation becomes:

$$\partial_t(\rho \mathbf{U}) + \nabla \cdot (\rho \mathbf{U}\mathbf{U}) = -\nabla \cdot \mathbf{P} - \nabla \cdot \mathbf{P}^{\text{visc}} + \mathbf{F}_s + \mathbf{F}_g + \nabla \cdot \mathbf{\epsilon}, \quad (\text{A.28})$$

where \mathbf{P} is the Korteweg's stress in (2.37).

The $\mathbf{\epsilon}$ in (A.28) is an error term given by:

$$\mathbf{\epsilon} = \frac{\delta t}{\omega} (\mathbf{F}\mathbf{u} + \mathbf{u}\mathbf{F}) + \frac{\mathbf{F}\mathbf{F}}{4\rho} \delta t^2 - \frac{1}{\omega} \mathbf{\Psi}^{(1)}, \quad (\text{A.29})$$

From Eq. (A.29) it is clear that $\mathbf{\Psi}^{(2)}$ does not appear in the error term. It was shown by Wagner [181] that the usual second order Chapman-Enskog expansion is insufficient to identify the exact form of the error term. Therefore, using higher order expansion, the exact form of the error term in (A.29) was derived in [180, 181] as:

$$\mathbf{\epsilon} = \frac{\delta t}{\omega} (\mathbf{F}\mathbf{u} + \mathbf{u}\mathbf{F}) + \left(\frac{1}{\omega} - \frac{1}{4} \right) \frac{\mathbf{F}\mathbf{F}}{\rho} \delta t^2 - \frac{1}{\omega} \mathbf{\Psi}, \quad (\text{A.30})$$

We shall now derive the second order moment of the forcing term $\mathbf{\Psi}$.

According the equilibrium populations defined in (2.14) and neglecting terms of the order of $O(u^3)$, the forcing term of the EDM can be rewrit-

ten as follows:

$$\begin{aligned}
F_i &= f_i^{\text{eq}}(\rho, \mathbf{u} + \delta\mathbf{u}) - f_i^{\text{eq}}(\rho, \mathbf{u}) \\
&= \rho W_i \left(\frac{c_{i\alpha} \delta u_\alpha}{c_s^2} + \frac{\delta u_\alpha \delta u_\beta + u_\alpha \delta u_\beta + u_\beta \delta u_\alpha}{2c_s^4} (c_{i\alpha} c_{i\beta} - c_s^2 \delta_{\alpha\beta}) \right) \\
&= W_i \delta t \left(\frac{c_{i\alpha} F_\alpha}{c_s^2} + \frac{U_\alpha F_\beta + F_\alpha U_\beta}{2c_s^4} (c_{i\alpha} c_{i\beta} - c_s^2 \delta_{\alpha\beta}) \right) \tag{A.31}
\end{aligned}$$

where \mathbf{U} is defined by Eq. (A.18).

Using Eq. (A.31), we can now derive the expression for Ψ as:

$$\Psi = \sum_i^N \mathbf{c}_i \mathbf{c}_i F_i = \delta t \left(\mathbf{F} \mathbf{u} + \mathbf{u} \mathbf{F} + \frac{\mathbf{F} \mathbf{F}}{\rho} \delta t \right) \tag{A.32}$$

By substituting (A.32) into (A.30) the error term becomes [180, 181]:

$$\boldsymbol{\varepsilon} = -\frac{1}{4} \frac{\mathbf{F} \mathbf{F}}{\rho} \delta t^2. \tag{A.33}$$

Unlike the other forcing schemes in LB proposed by Shan and Chen [24] and He et al. [25], the error term produced by the EDM in (A.33), is no longer dependent on viscosity. Moreover and most importantly, it was shown in Ref. [180] that among various forcing schemes in literature, the EDM gives the lowest error between the measured vapor density and that predicted by Maxwell rule (we also showed in Fig. 3.1 that the vapor branch of the coexistence curve is accurately captured by our simulations). Therefore, for the present work, between different forcing schemes in literature, the EDM was chosen, since, firstly it gives the minimum error in terms of reproducing the vapor branch of the coexistence curve and secondly the error term in macroscopic momentum equation is not dependent on viscosity.

Appendix B

Evaluation of derivatives

As an example, in three dimensions, evaluation of the first and of second derivatives of a function $\varphi(\mathbf{x})$ in the x direction reads:

$$\begin{aligned}\frac{\partial\varphi(i, j, k)}{\partial x} &= \frac{1}{6}[\varphi(i+1, j, k) - \varphi(i-1, j, k)] \\ &+ \frac{1}{12}[\varphi(i+1, j+1, k) - \varphi(i-1, j+1, k)] \\ &+ \frac{1}{12}[\varphi(i+1, j-1, k) - \varphi(i-1, j-1, k)] \\ &+ \frac{1}{12}[\varphi(i+1, j, k+1) - \varphi(i-1, j, k+1)] \\ &+ \frac{1}{12}[\varphi(i+1, j, k-1) - \varphi(i-1, j, k-1)];\end{aligned}\quad (\text{B.1})$$

$$\begin{aligned}\frac{\partial^2\varphi(i, j, k)}{\partial x^2} &= \frac{1}{3}[\varphi(i+1, j, k) - 2\varphi(i, j, k) + \varphi(i-1, j, k)] \\ &+ \frac{1}{6}[\varphi(i+1, j+1, k) - 2\varphi(i, j+1, k) + \varphi(i-1, j+1, k)] \\ &+ \frac{1}{6}[\varphi(i+1, j-1, k) - 2\varphi(i, j-1, k) + \varphi(i-1, j-1, k)] \\ &+ \frac{1}{6}[\varphi(i+1, j, k+1) - 2\varphi(i, j, k+1) + \varphi(i-1, j, k+1)] \\ &+ \frac{1}{6}[\varphi(i+1, j, k-1) - 2\varphi(i, j, k-1) + \varphi(i-1, j, k-1)].\end{aligned}\quad (\text{B.2})$$

Bibliography

- [1] N. Ashgriz and J. Poo, “Coalescence and separation in binary collisions of liquid drops,” *Journal of Fluid Mechanics*, vol. 221, pp. 183–204, 1990.
- [2] J. Qian and C. Law, “Regimes of coalescence and separation in droplet collision,” *Journal of Fluid Mechanics*, vol. 331, pp. 59–80, 1997.
- [3] C. Gotaas, P. Havelka, H. A. Jakobsen, H. F. Svendsen, M. Hase, N. Roth, and B. Weigand, “Effect of viscosity on droplet-droplet collision outcome: Experimental study and numerical comparison,” *Physics of Fluids (1994-present)*, vol. 19, no. 10, p. 102106, 2007.
- [4] K. Willis and M. Orme, “Binary droplet collisions in a vacuum environment: an experimental investigation of the role of viscosity,” *Experiments in fluids*, vol. 34, no. 1, pp. 28–41, 2003.
- [5] I. V. Roisman, E. Berberović, and C. Tropea, “Inertia dominated drop collisions. i. on the universal flow in the lamella,” *Physics of Fluids (1994-present)*, vol. 21, no. 5, p. 052103, 2009.
- [6] C. Clanet, C. Béguin, D. Richard, and D. Quéré, “Maximal deformation of an impacting drop,” *J. of Fluid Mech.*, vol. 517, pp. 199–208, 2004.
- [7] D. Vadillo, *Characterization of hydrodynamics phenomena during drop impact onto different types of substrates*. PhD thesis, University Joseph Fourier, 2006.

- [8] S. Bakshi, I. V. Roisman, and C. Tropea, “Investigations on the impact of a drop onto a small spherical target,” *Physics of Fluids (1994-present)*, vol. 19, no. 3, p. 032102, 2007.
- [9] C. Antonini, S. Jung, A. Wetzel, E. Heer, P. Schoch, A. M. Moqaddam, S. S. Chikatamarla, I. Karlin, M. Marengo, and D. Poulikakos, “Contactless prompt tumbling rebound of drops from a sublimating slope,” *Physical Review Fluids*, vol. 1, no. 1, p. 013903, 2016.
- [10] C. Antonini, F. Villa, and M. Marengo, “Oblique impacts of water drops onto hydrophobic and superhydrophobic surfaces: outcomes, timing, and rebound maps,” *Experiments in Fluids*, vol. 55, no. 4, pp. 1–9, 2014.
- [11] D. Richard, C. Clanet, and D. Quéré, “Surface phenomena: Contact time of a bouncing drop,” *Nature*, vol. 417, no. 6891, pp. 811–811, 2002.
- [12] A. Gauthier, S. Symon, C. Clanet, and D. Quéré, “Water impacting on superhydrophobic macrottextures,” *Nature communications*, vol. 6, 2015.
- [13] Y. Liu, L. Moevius, X. Xu, T. Qian, J. M. Yeomans, and Z. Wang, “Pancake bouncing on superhydrophobic surfaces,” *Nature Physics*, 2014.
- [14] J. C. Bird, R. Dhiman, H.-M. Kwon, and K. K. Varanasi, “Reducing the contact time of a bouncing drop,” *Nature*, vol. 503, no. 7476, pp. 385–388, 2013.
- [15] S. Torza and S. Mason, “Three-phase interactions in shear and electrical fields,” *Journal of Colloid and Interface Science*, vol. 33, no. 1, pp. 67–83, 1970.
- [16] Y. S. Joung and C. R. Buie, “Aerosol generation by raindrop impact on soil,” *Nature communications*, vol. 6, 2015.
- [17] R. Blossey, “Self-cleaning surfaces—virtual realities,” *Nature materials*, vol. 2, no. 5, pp. 301–306, 2003.
- [18] M. J. Kreder, J. Alvarenga, P. Kim, and J. Aizenberg, “Design of anti-icing surfaces: smooth, textured or slippery?,” *Nature Reviews Materials*, vol. 1, p. 15003, 2016.

-
- [19] H. Minemawari, T. Yamada, H. Matsui, J. Tsutsumi, S. Haas, R. Chiba, R. Kumai, and T. Hasegawa, “Inkjet printing of single-crystal films,” *Nature*, vol. 475, no. 7356, pp. 364–367, 2011.
- [20] N. Ashgriz and P. Givi, “Binary collision dynamics of fuel droplets,” *International journal of heat and fluid flow*, vol. 8, no. 3, pp. 205–210, 1987.
- [21] A. Patnaik, R. Rengasamy, V. Kothari, and A. Ghosh, “Wetting and wicking in fibrous materials,” *Textile Progress*, vol. 38, no. 1, pp. 1–105, 2006.
- [22] A. K. Gunstensen, D. H. Rothman, S. Zaleski, and G. Zanetti, “Lattice boltzmann model of immiscible fluids,” *Physical Review A*, vol. 43, no. 8, p. 4320, 1991.
- [23] M. R. Swift, W. Osborn, and J. Yeomans, “Lattice boltzmann simulation of nonideal fluids,” *Physical Review Letters*, vol. 75, no. 5, p. 830, 1995.
- [24] X. Shan and H. Chen, “Lattice boltzmann model for simulating flows with multiple phases and components,” *Physical Review E*, vol. 47, no. 3, p. 1815, 1993.
- [25] X. He, X. Shan, and G. D. Doolen, “Discrete boltzmann equation model for nonideal gases,” *Physical Review E*, vol. 57, no. 1, p. R13, 1998.
- [26] H. Zheng, C. Shu, and Y.-T. Chew, “A lattice boltzmann model for multiphase flows with large density ratio,” *Journal of Computational Physics*, vol. 218, no. 1, pp. 353–371, 2006.
- [27] C. K. Aidun and J. R. Clausen, “Lattice-boltzmann method for complex flows,” *Annual review of fluid mechanics*, vol. 42, pp. 439–472, 2010.
- [28] Q. Li, K. Luo, Q. Kang, Y. He, Q. Chen, and Q. Liu, “Lattice boltzmann methods for multiphase flow and phase-change heat transfer,” *Progress in Energy and Combustion Science*, vol. 52, pp. 62–105, 2016.
- [29] S. O. Unverdi and G. Tryggvason, “A front-tracking method for viscous, incompressible, multi-fluid flows,” *Journal of computational physics*, vol. 100, no. 1, pp. 25–37, 1992.

- [30] G. Tryggvason, B. Bunner, A. Esmaeeli, D. Juric, N. Al-Rawahi, W. Tauber, J. Han, S. Nas, and Y.-J. Jan, “A front-tracking method for the computations of multiphase flow,” *Journal of Computational Physics*, vol. 169, no. 2, pp. 708–759, 2001.
- [31] M. Nobari, Y.-J. Jan, and G. Tryggvason, “Head-on collision of drops—a numerical investigation,” *Physics of Fluids (1994-present)*, vol. 8, no. 1, pp. 29–42, 1996.
- [32] C. W. Hirt and B. D. Nichols, “Volume of fluid (vof) method for the dynamics of free boundaries,” *Journal of computational physics*, vol. 39, no. 1, pp. 201–225, 1981.
- [33] E. Puckett and J. Sethian, “Level set methods: Evolving interfaces in geometry, fluid mechanics, computer vision, and materials science,” 1998.
- [34] W. Aniszewski, T. Ménard, and M. Marek, “Volume of fluid (vof) type advection methods in two-phase flow: a comparative study,” *Computers & Fluids*, vol. 97, pp. 52–73, 2014.
- [35] E. Olsson and G. Kreiss, “A conservative level set method for two phase flow,” *Journal of computational physics*, vol. 210, no. 1, pp. 225–246, 2005.
- [36] J. Sethian and P. Smereka, “Level set methods for fluid interfaces,” *Annual Review of Fluid Mechanics*, vol. 35, no. 1, pp. 341–372, 2003.
- [37] T. L. Hill, *An introduction to statistical thermodynamics*. Courier Corporation, 2012.
- [38] D. Ceperley, “Microscopic simulations in physics,” *Reviews of Modern Physics*, vol. 71, no. 2, p. S438, 1999.
- [39] S. Succi, *The Lattice-Boltzmann Equation*. Oxford university press, Oxford, 2001.
- [40] I. V. Karlin, A. N. Gorban, S. Succi, and V. Boffi, “Maximum entropy principle for lattice kinetic equations,” *Physical Review Letters*, vol. 81, no. 1, p. 6, 1998.
- [41] I. Karlin, A. Ferrante, and H. Öttinger, “Perfect entropy functions of the lattice boltzmann method,” *EPL (Europhysics Letters)*, vol. 47, no. 2, p. 182, 1999.

-
- [42] S. Ansumali and I. V. Karlin, “Stabilization of the lattice boltzmann method by the h theorem: A numerical test,” *Physical Review E*, vol. 62, no. 6, p. 7999, 2000.
- [43] S. Ansumali, I. Karlin, and H. Öttinger, “Minimal entropic kinetic models for hydrodynamics,” *EPL (Europhysics Letters)*, vol. 63, no. 6, p. 798, 2003.
- [44] D. H. Rothman and J. M. Keller, “Immiscible cellular-automaton fluids,” *Journal of Statistical Physics*, vol. 52, no. 3-4, pp. 1119–1127, 1988.
- [45] X. Shan and H. Chen, “Simulation of nonideal gases and liquid-gas phase transitions by the lattice boltzmann equation,” *Physical Review E*, vol. 49, no. 4, p. 2941, 1994.
- [46] D. Kehrwald, “Numerical analysis of immiscible lattice bgk,” *PhD. diss, UNI Kaiserslautern, Germany*, 2002.
- [47] T. Reis and T. N. Phillips, “Lattice boltzmann model for simulating immiscible two-phase flows,” *Journal of Physics A: Mathematical and Theoretical*, vol. 40, no. 14, p. 4033, 2007.
- [48] S. Lishchuk, C. Care, and I. Halliday, “Lattice boltzmann algorithm for surface tension with greatly reduced microcurrents,” *Physical review E*, vol. 67, no. 3, p. 036701, 2003.
- [49] Q. Kang, D. Zhang, and S. Chen, “Displacement of a two-dimensional immiscible droplet in a channel,” *Physics of Fluids (1994-present)*, vol. 14, no. 9, pp. 3203–3214, 2002.
- [50] Q. Kang, D. Zhang, and S. Chen, “Immiscible displacement in a channel: simulations of fingering in two dimensions,” *Advances in water resources*, vol. 27, no. 1, pp. 13–22, 2004.
- [51] M. Sbragaglia, R. Benzi, L. Biferale, S. Succi, K. Sugiyama, and F. Toschi, “Generalized lattice boltzmann method with multirange pseudopotential,” *Physical Review E*, vol. 75, no. 2, p. 026702, 2007.
- [52] P. Yuan and L. Schaefer, “Equations of state in a lattice boltzmann model,” *Physics of Fluids (1994-present)*, vol. 18, no. 4, p. 042101, 2006.

- [53] R. Qin, “Mesoscopic interparticle potentials in the lattice boltzmann equation for multiphase fluids,” *Physical Review E*, vol. 73, no. 6, p. 066703, 2006.
- [54] X. He and G. D. Doolen, “Thermodynamic foundations of kinetic theory and lattice boltzmann models for multiphase flows,” *Journal of Statistical Physics*, vol. 107, no. 1-2, pp. 309–328, 2002.
- [55] A. J. Wagner and Q. Li, “Investigation of galilean invariance of multiphase lattice Boltzmann methods,” *Physica A*, vol. 362, no. 1, pp. 105–110, 2006.
- [56] T. Inamuro, S. Tajima, and F. Ogino, “Lattice boltzmann simulation of droplet collision dynamics,” *International journal of heat and mass transfer*, vol. 47, no. 21, pp. 4649–4657, 2004.
- [57] X. He, S. Chen, and R. Zhang, “A lattice boltzmann scheme for incompressible multiphase flow and its application in simulation of rayleigh–taylor instability,” *Journal of Computational Physics*, vol. 152, no. 2, pp. 642–663, 1999.
- [58] T. Lee and C.-L. Lin, “A stable discretization of the lattice boltzmann equation for simulation of incompressible two-phase flows at high density ratio,” *Journal of Computational Physics*, vol. 206, no. 1, pp. 16–47, 2005.
- [59] N. Frapolli, S. S. Chikatamarla, and I. V. Karlin, “Entropic lattice boltzmann model for compressible flows,” *Phys. Rev. E*, vol. 92, p. 061301, Dec 2015.
- [60] F. Bösch, S. S. Chikatamarla, and I. V. Karlin, “Entropic multirelaxation lattice boltzmann models for turbulent flows,” *Phys. Rev. E*, vol. 92, p. 043309, Oct 2015.
- [61] S. Chikatamarla, S. Ansumali, and I. Karlin, “Entropic lattice boltzmann models for hydrodynamics in three dimensions,” *Physical review letters*, vol. 97, no. 1, p. 010201, 2006.
- [62] S. S. Karlin, I.V. and S. Chikatamarla, “Comment on ”numerics of the lattice boltzmann method: Effects of collision models on the lattice boltzmann simulations”,” *Phys. Rev. E*, vol. 84, p. 068701, 2011.

-
- [63] “Front matter,” in *Statistical Mechanics (Second Edition)* (R. PATHRIA, ed.), pp. iii –, Oxford: Butterworth-Heinemann, second edition ed., 1996.
- [64] H. Grad, “Principles of the kinetic theory of gases,” in *Thermodynamik der Gase/Thermodynamics of Gases*, pp. 205–294, Springer, 1958.
- [65] C. Cercignani, R. Illner, and M. Pulvirenti, *The mathematical theory of dilute gases*, vol. 106. Springer Science & Business Media, 2013.
- [66] P. L. Bhatnagar, E. P. Gross, and M. Krook, “A model for collision processes in gases. i. small amplitude processes in charged and neutral one-component systems,” *Physical review*, vol. 94, no. 3, p. 511, 1954.
- [67] S. Chapman and T. G. Cowling, *The mathematical theory of non-uniform gases: an account of the kinetic theory of viscosity, thermal conduction and diffusion in gases*. Cambridge university press, 1970.
- [68] I. V. Karlin, S. Ansumali, C. E. Frouzakis, and S. S. Chikatamarla, “Elements of the lattice boltzmann method i: Linear advection equation,” *Commun. Comput. Phys*, vol. 1, no. 4, pp. 616–655, 2006.
- [69] J. D. van der Waals, “Thermodynamische theorie der capillariteit in de onderstelling van continue dichtheidsverandering,” *Verhand. Kon. Akad. V Wetensch. Amst. (Sect. 1)*, vol. 1(8), pp. 1–54, 1893.
- [70] M. Slemrod, “Dynamic phase transitions in a van der waals fluid,” *Journal of differential equations*, vol. 52, no. 1, pp. 1–23, 1984.
- [71] D. J. Korteweg, “Sur la forme que prennent les equations du mouvements des fluides si l’on tient compte des forces capillaires causes par des variations de densite,” *Arch. Neerl. Sci. Exactes Nat. Ser. II*, vol. 6, pp. 1–24, 1901.
- [72] M. R. Swift, E. Orlandini, W. Osborn, and J. Yeomans, “Lattice boltzmann simulations of liquid-gas and binary fluid systems,” *Physical Review E*, vol. 54, no. 5, p. 5041, 1996.
- [73] I. V. Karlin, S. S. Chikatamarla, and S. Ansumali, “Elements of the lattice boltzmann method ii: Kinetics and hydrodynamics in one dimension,” *Communications in Computational Physics*, vol. 2, no. 2, pp. 196–238, 2007.

- [74] S. S. Chikatamarla and I. V. Karlin, “Lattices for the lattice boltzmann method,” *Physical Review E*, vol. 79, no. 4, p. 046701, 2009.
- [75] Q. Li, K. Luo, X. Li, *et al.*, “Forcing scheme in pseudopotential lattice boltzmann model for multiphase flows,” *Physical Review E*, vol. 86, no. 1, p. 016709, 2012.
- [76] D. Lycett-Brown and K. H. Luo, “Improved forcing scheme in pseudopotential lattice boltzmann methods for multiphase flow at arbitrarily high density ratios,” *Physical Review E*, vol. 91, no. 2, p. 023305, 2015.
- [77] A. L. Kupershtokh, D. A. Medvedev, and D. I. Karpov, “On equations of state in a lattice Boltzmann method,” *Computers & Mathematics with Applications*, vol. 58, no. 5, pp. 965–974, 2009.
- [78] P. Yuan and L. Schaefer, “Equations of state in a lattice Boltzmann model,” *Phys. Fluids*, vol. 18, no. 4, p. 042101, 2006.
- [79] J. Zhang and D. Y. Kwok, “Lattice boltzmann study on the contact angle and contact line dynamics of liquid-vapor interfaces,” *Langmuir*, vol. 20, no. 19, pp. 8137–8141, 2004.
- [80] H. Huang, D. T. Thorne Jr, M. G. Schaap, and M. C. Sukop, “Proposed approximation for contact angles in shan-and-chen-type multicomponent multiphase lattice boltzmann models,” *Phys. Rev. E*, vol. 76, no. 6, p. 066701, 2007.
- [81] S. Chikatamarla and I. Karlin, “Entropic lattice boltzmann method for turbulent flow simulations: Boundary conditions,” *Physica A*, vol. 392, no. 9, pp. 1925–1930, 2013.
- [82] M. Orme, “Experiments on droplet collisions, bounce, coalescence and disruption,” *Progress in Energy and Combustion Science*, vol. 23, no. 1, pp. 65–79, 1997.
- [83] J. Nijdam, B. Guo, D. Fletcher, and T. Langrish, “Challenges of simulating droplet coalescence within a spray,” *Drying Technology*, vol. 22, no. 6, pp. 1463–1488, 2004.
- [84] I. V. Roisman, “Inertia dominated drop collisions. ii. an analytical solution of the navier–stokes equations for a spreading viscous film,” *Physics of Fluids*, vol. 21, no. 5, pp. –, 2009.

-
- [85] Y. Pan and K. Suga, “Numerical simulation of binary liquid droplet collision,” *Physics of Fluids (1994-present)*, vol. 17, no. 8, p. 082105, 2005.
- [86] S. Tanguy and A. Berlemont, “Application of a level set method for simulation of droplet collisions,” *International journal of multiphase flow*, vol. 31, no. 9, pp. 1015–1035, 2005.
- [87] F. Mashayek, N. Ashgriz, W. Minkowycz, and B. Shotorban, “Coalescence collision of liquid drops,” *International Journal of Heat and Mass Transfer*, vol. 46, no. 1, pp. 77–89, 2003.
- [88] A. Mazloomi M, S. S. Chikatamarla, and I. V. Karlin, “Entropic lattice boltzmann method for multiphase flows,” *Phys. Rev. Lett.*, vol. 114, p. 174502, May 2015.
- [89] A. Mazloomi M., S. S. Chikatamarla, and I. V. Karlin, “Entropic lattice boltzmann method for multiphase flows: Fluid-solid interfaces,” *Phys. Rev. E*, vol. 92, p. 023308, Aug 2015.
- [90] D. Lycett-Brown, K. H. Luo, R. Liu, and P. Lv, “Binary droplet collision simulations by a multiphase cascaded lattice boltzmann method,” *Physics of Fluids (1994-present)*, vol. 26, no. 2, p. 023303, 2014.
- [91] K. Luo, J. Xia, and E. Monaco, “Multiscale modeling of multiphase flow with complex interactions,” *Journal of Multiscale Modelling*, vol. 1, no. 01, pp. 125–156, 2009.
- [92] C. Focke and D. Bothe, “Computational analysis of binary collisions of shear-thinning droplets,” *Journal of Non-Newtonian Fluid Mechanics*, vol. 166, no. 14, pp. 799–810, 2011.
- [93] G. I. Taylor, “The viscosity of a fluid containing small drops of another fluid,” *Proceedings of the Royal Society of London. Series A, Containing Papers of a Mathematical and Physical Character*, pp. 41–48, 1932.
- [94] G. Taylor, “The formation of emulsions in definable fields of flow,” *Proceedings of the Royal Society of London. Series A, Containing Papers of a Mathematical and Physical Character*, pp. 501–523, 1934.
- [95] T. Qian, X.-P. Wang, and P. Sheng, “A variational approach to moving contact line hydrodynamics,” *Journal of Fluid Mechanics*, vol. 564, pp. 333–360, 2006.

- [96] G. Brenn, D. Valkovska, and K. Danov, “The formation of satellite droplets by unstable binary drop collisions,” *Physics of Fluids (1994-present)*, vol. 13, no. 9, pp. 2463–2477, 2001.
- [97] J. De Coninck, M. J. De Ruijter, and M. Voué, “Dynamics of wetting,” *Current opinion in colloid & interface science*, vol. 6, no. 1, pp. 49–53, 2001.
- [98] P.-G. De Gennes, “Wetting: statics and dynamics,” *Rev. Mod. Phys.*, vol. 57, no. 3, p. 827, 1985.
- [99] A. L. Yarin, “Drop impact dynamics: splashing, spreading, receding, bouncing...,” *Annu. Rev. Fluid Mech.*, vol. 38, pp. 159–192, 2006.
- [100] T. Inamuro, T. Ogata, S. Tajima, and N. Konishi, “A lattice boltzmann method for incompressible two-phase flows with large density differences,” *Journal of Computational Physics*, vol. 198, no. 2, pp. 628–644, 2004.
- [101] X. Gu, A. Gupta, and R. Kumar, “Lattice boltzmann simulation of surface impingement at high-density ratio,” *Journal of Thermophysics and Heat Transfer*, vol. 23, no. 4, pp. 773–785, 2009.
- [102] A. J. Briant, A. J. Wagner, and J. M. Yeomans, “Lattice boltzmann simulations of contact line motion. i. liquid-gas systems,” *Phys. Rev. E*, vol. 69, p. 031602, Mar 2004.
- [103] M. Latva-Kokko and D. H. Rothman, “Static contact angle in lattice boltzmann models of immiscible fluids,” *Phys. Rev. E*, vol. 72, p. 046701, Oct 2005.
- [104] X. Shan and H. Chen, “Lattice boltzmann model for simulating flows with multiple phases and components,” *Phys. Rev. E*, vol. 47, pp. 1815–1819, Mar 1993.
- [105] N. S. Martys and H. Chen, “Simulation of multicomponent fluids in complex three-dimensional geometries by the lattice boltzmann method,” *Phys. Rev. E*, vol. 53, pp. 743–750, Jan 1996.
- [106] C. Pan, M. Hilpert, and C. Miller, “Lattice-boltzmann simulation of two-phase flow in porous media,” *Water Resources Research*, vol. 40, no. 1, 2004.

-
- [107] Q. Kang, D. Zhang, and S. Chen, “Displacement of a three-dimensional immiscible droplet in a duct,” *J. Fluid Mech.*, vol. 545, pp. 41–66, 2005.
- [108] G. Falcucci, S. Ubertini, and S. Succi, “Lattice boltzmann simulations of phase-separating flows at large density ratios: the case of doubly-attractive pseudo-potentials,” *Soft Matter*, vol. 6, no. 18, pp. 4357–4365, 2010.
- [109] J. Zhang, B. Li, and D. Y. Kwok, “Mean-field free-energy approach to the lattice boltzmann method for liquid-vapor and solid-fluid interfaces,” *Physical Review E*, vol. 69, no. 3, p. 032602, 2004.
- [110] E. W. Washburn, “The dynamics of capillary flow,” *Phys. Rev.*, vol. 17, no. 3, p. 273, 1921.
- [111] R. Lucas, “Rate of capillary ascension of liquids,” *Kolloid Zeitschrift*, vol. 23, no. 15, pp. 15–22, 1918.
- [112] H. P. Greenspan, “On the motion of a small viscous droplet that wets a surface,” *J. Fluid Mech.*, vol. 84, no. 01, pp. 125–143, 1978.
- [113] E. Esmaili, A. Moosavi, and A. Mazloomi, “The dynamics of wettability driven droplets in smooth and corrugated microchannels,” *J. Stat. Mech.: Theory and Experiment*, vol. 2012, no. 10, p. P10005, 2012.
- [114] Y. Renardy, S. Popinet, L. Duchemin, M. Renardy, S. Zaleski, C. Josserand, M. Drumright-Clarke, D. Richard, C. Clanet, and D. Quéré, “Pyramidal and toroidal water drops after impact on a solid surface,” *J. Fluid Mech.*, vol. 484, pp. 69–83, 2003.
- [115] H. Ding and P. D. Spelt, “Inertial effects in droplet spreading: a comparison between diffuse-interface and level-set simulations,” *J. of Fluid Mech.*, vol. 576, pp. 287–296, 2007.
- [116] J. Fukai, Z. Zhao, D. Poulikakos, C. M. Megaridis, and O. Miyatake, “Modeling of the deformation of a liquid droplet impinging upon a flat surface,” *Physics of Fluids A: Fluid Dynamics (1989-1993)*, vol. 5, no. 11, pp. 2588–2599, 1993.
- [117] M. Bertagnolli, M. Marchese, G. Jacucci, I. St Doltsinis, and S. Noelting, “Thermomechanical simulation of the splashing of ceramic droplets on a rigid substrate,” *J. Comput. Phys.*, vol. 133, no. 2, pp. 205–221, 1997.

- [118] R. D. Schroll, C. Josserand, S. Zaleski, and W. W. Zhang, “Impact of a viscous liquid drop,” *Phys. Rev. Lett.*, vol. 104, p. 034504, 2010.
- [119] J. C. Maxwell, *Capillary action*. Media Galaxy, 2015.
- [120] J. M. Bell and F. Cameron, “The flow of liquids through capillary spaces,” *The Journal of Physical Chemistry*, vol. 10, no. 8, pp. 658–674, 1906.
- [121] E. Schäffer and P.-z. Wong, “Contact line dynamics near the pinning threshold: A capillary rise and fall experiment,” *Physical Review E*, vol. 61, no. 5, p. 5257, 2000.
- [122] R. L. Hoffman, “A study of the advancing interface. i. interface shape in liquid—gas systems,” *Journal of colloid and interface science*, vol. 50, no. 2, pp. 228–241, 1975.
- [123] T.-S. Jiang, O. Soo-Gun, and J. C. Slattery, “Correlation for dynamic contact angle,” *Journal of Colloid and Interface Science*, vol. 69, no. 1, pp. 74–77, 1979.
- [124] E. Kissa, “Wetting and wicking,” *Textile Research Journal*, vol. 66, no. 10, pp. 660–668, 1996.
- [125] I. V. Roisman, E. Berberović, and C. Tropea, “Inertia dominated drop collisions. i. on the universal flow in the lamella,” *Physics of Fluids (1994-present)*, vol. 21, no. 5, p. 052103, 2009.
- [126] D. Bonn, J. Eggers, J. Indekeu, J. Meunier, and E. Rolley, “Wetting and spreading,” *Reviews of modern physics*, vol. 81, no. 2, p. 739, 2009.
- [127] M. Mani, S. Mandre, and M. P. Brenner, “Events before droplet splashing on a solid surface,” *Journal of Fluid Mechanics*, vol. 647, pp. 163–185, 2010.
- [128] G. Riboux and J. M. Gordillo, “Experiments of drops impacting a smooth solid surface: A model of the critical impact speed for drop splashing,” *Physical review letters*, vol. 113, no. 2, p. 024507, 2014.
- [129] C. Antonini, I. Bernagozzi, S. Jung, D. Poulikakos, and M. Marengo, “Water drops dancing on ice: How sublimation leads to drop rebound,” *Physical review letters*, vol. 111, no. 1, p. 014501, 2013.

-
- [130] T. Tran, H. J. Staat, A. Prosperetti, C. Sun, and D. Lohse, “Drop impact on superheated surfaces,” *Physical Review Letters*, vol. 108, no. 3, p. 036101, 2012.
- [131] L. Wachters and N. Westerling, “The heat transfer from a hot wall to impinging water drops in the spheroidal state,” *Chemical Engineering Science*, vol. 21, no. 11, pp. 1047–1056, 1966.
- [132] J. M. Kolinski, L. Mahadevan, and S. M. Rubinstein, “Lift-off instability during the impact of a drop on a solid surface,” *Physical review letters*, vol. 112, no. 13, p. 134501, 2014.
- [133] J. de Ruiter, R. Lagraauw, D. van den Ende, and F. Mugele, “Wettability-independent bouncing on flat surfaces mediated by thin air films,” *Nature physics*, vol. 11, no. 1, pp. 48–53, 2015.
- [134] M. Goldshtik, V. Khanin, and V. Ligai, “A liquid drop on an air cushion as an analogue of leidenfrost boiling,” *Journal of Fluid Mechanics*, vol. 166, pp. 1–20, 1986.
- [135] G. Lagubeau, M. Le Merrer, C. Clanet, and D. Quéré, “Leidenfrost on a ratchet,” *Nature Physics*, vol. 7, no. 5, pp. 395–398, 2011.
- [136] I. U. Vakarelski, N. A. Patankar, J. O. Marston, D. Y. Chan, and S. T. Thoroddsen, “Stabilization of leidenfrost vapour layer by textured superhydrophobic surfaces,” *Nature*, vol. 489, no. 7415, pp. 274–277, 2012.
- [137] H.-J. Butt, C. Semperebon, P. Papadopoulos, D. Vollmer, M. Brinkmann, and M. Ciccotti, “Design principles for superamphiphobic surfaces,” *Soft Matter*, vol. 9, no. 2, pp. 418–428, 2013.
- [138] T. Maitra, C. Antonini, M. K. Tiwari, A. Mularczyk, Z. Imeri, P. Schoch, and D. Poulikakos, “Supercooled water drops impacting superhydrophobic textures,” *Langmuir*, vol. 30, no. 36, pp. 10855–10861, 2014.
- [139] L. F. Loucks, “Subtleties of phenomena involving ice-water equilibria,” *Journal of Chemical Education*, vol. 63, no. 2, p. 115, 1986.
- [140] E. Pierce, F. Carmona, and A. Amirfazli, “Understanding of sliding and contact angle results in tilted plate experiments,” *Colloids and Surfaces A: Physicochemical and Engineering Aspects*, vol. 323, no. 1, pp. 73–82, 2008.

- [141] K. Moran, A. Yeung, and J. Masliyah, “Shape relaxation of an elongated viscous drop,” *Journal of colloid and interface science*, vol. 267, no. 2, pp. 483–493, 2003.
- [142] R. D. Schroll, C. Josserand, S. Zaleski, and W. W. Zhang, “Impact of a viscous liquid drop,” *Physical review letters*, vol. 104, no. 3, p. 034504, 2010.
- [143] J. Skotheim and T. Secomb, “Red blood cells and other nonspherical capsules in shear flow: oscillatory dynamics and the tank-treading-to-tumbling transition,” *Physical review letters*, vol. 98, no. 7, p. 078301, 2007.
- [144] I. V. Roisman, “Inertia dominated drop collisions. ii. an analytical solution of the navier–stokes equations for a spreading viscous film,” *Physics of Fluids (1994-present)*, vol. 21, no. 5, p. 052104, 2009.
- [145] M. Mani, S. Mandre, and M. P. Brenner, “Events before droplet splashing on a solid surface,” *Journal of Fluid Mechanics*, vol. 647, pp. 163–185, 2010.
- [146] S. Mandre and M. P. Brenner, “The mechanism of a splash on a dry solid surface,” *Journal of Fluid Mechanics*, vol. 690, pp. 148–172, 2012.
- [147] G. Riboux and J. M. Gordillo, “Experiments of drops impacting a smooth solid surface: A model of the critical impact speed for drop splashing,” *Physical review letters*, vol. 113, no. 2, p. 024507, 2014.
- [148] L. Xu, W. W. Zhang, and S. R. Nagel, “Drop splashing on a dry smooth surface,” *Physical review letters*, vol. 94, no. 18, p. 184505, 2005.
- [149] L. Xu, “Liquid drop splashing on smooth, rough, and textured surfaces,” *Physical Review E*, vol. 75, no. 5, p. 056316, 2007.
- [150] C. Antonini, I. Bernagozzi, S. Jung, D. Poulikakos, and M. Marengo, “Water drops dancing on ice: How sublimation leads to drop rebound,” *Physical review letters*, vol. 111, no. 1, p. 014501, 2013.
- [151] L. Wachters and N. Westerling, “The heat transfer from a hot wall to impinging water drops in the spheroidal state,” *Chemical Engineering Science*, vol. 21, no. 11, pp. 1047–1056, 1966.

-
- [152] A.-L. Biance, C. Clanet, and D. Quéré, “Leidenfrost drops,” *Physics of Fluids (1994-present)*, vol. 15, no. 6, pp. 1632–1637, 2003.
- [153] T. Tran, H. J. Staat, A. Prosperetti, C. Sun, and D. Lohse, “Drop impact on superheated surfaces,” *Physical Review Letters*, vol. 108, no. 3, p. 036101, 2012.
- [154] T. Tran, H. J. Staat, A. Susarrey-Arce, T. C. Foertsch, A. van Houselt, H. J. Gardeniers, A. Prosperetti, D. Lohse, and C. Sun, “Droplet impact on superheated micro-structured surfaces,” *Soft Matter*, vol. 9, no. 12, pp. 3272–3282, 2013.
- [155] J. M. Kolinski, S. M. Rubinstein, S. Mandre, M. P. Brenner, D. A. Weitz, and L. Mahadevan, “Skating on a film of air: drops impacting on a surface,” *Physical review letters*, vol. 108, no. 7, p. 074503, 2012.
- [156] J. de Ruiter, R. Lagraauw, D. van den Ende, and F. Mugele, “Wettability-independent bouncing on flat surfaces mediated by thin air films,” *Nature physics*, vol. 11, no. 1, pp. 48–53, 2015.
- [157] C. Antonini, F. Villa, I. Bernagozzi, A. Amirfazli, and M. Marengo, “Drop rebound after impact: the role of the receding contact angle,” *Langmuir*, vol. 29, no. 52, pp. 16045–16050, 2013.
- [158] C. Antonini, S. Jung, A. Wetzels, E. Heer, P. Schoch, A. M. Moqaddam, S. S. Chikatamarla, I. Karlin, M. Marengo, and D. Poulikakos, “Contactless prompt tumbling rebound of drops from a sublimating slope,” *Phys. Rev. Fluids*, vol. 1, p. 013903, May 2016.
- [159] T. M. Schutzius, S. Jung, T. Maitra, G. Graeber, M. Köhme, and D. Poulikakos, “Spontaneous droplet trampolining on rigid superhydrophobic surfaces,” *Nature*, vol. 527, no. 7576, pp. 82–85, 2015.
- [160] K. Rykaczewski, T. Landin, M. L. Walker, J. H. J. Scott, and K. K. Varanasi, “Direct imaging of complex nano-to microscale interfaces involving solid, liquid, and gas phases,” *ACS nano*, vol. 6, no. 10, pp. 9326–9334, 2012.
- [161] M. Rein, “Phenomena of liquid drop impact on solid and liquid surfaces,” *Fluid Dynamics Research*, vol. 12, no. 2, p. 61, 1993.
- [162] S. Jung, M. K. Tiwari, N. V. Doan, and D. Poulikakos, “Mechanism of supercooled droplet freezing on surfaces,” *Nature communications*, vol. 3, p. 615, 2012.

- [163] A. Tuteja, W. Choi, M. Ma, J. M. Mabry, S. A. Mazzella, G. C. Rutledge, G. H. McKinley, and R. E. Cohen, “Designing superoleophobic surfaces,” *Science*, vol. 318, no. 5856, pp. 1618–1622, 2007.
- [164] K. Okumura, F. Chevy, D. Richard, D. Quéré, and C. Clanet, “Water spring: A model for bouncing drops,” *Europhys. Lett.*, vol. 62, no. 2, p. 237, 2003.
- [165] Y. Liu, M. Andrew, J. Li, J. M. Yeomans, and Z. Wang, “Symmetry breaking in drop bouncing on curved surfaces,” *Nature communications*, vol. 6, 2015.
- [166] R. B. Bird, “Transport phenomena,” *Applied Mechanics Reviews*, vol. 55, no. 1, pp. R1–R4, 2002.
- [167] T. M. Schutzius, S. Jung, T. Maitra, P. Eberle, C. Antonini, C. Stamatopoulos, and D. Poulikakos, “Physics of icing and rational design of surfaces with extraordinary icephobicity,” *Langmuir*, vol. 31, no. 17, pp. 4807–4821, 2014.
- [168] D. Richard and D. Quéré, “Bouncing water drops,” *Europhys. Lett.*, vol. 50, no. 6, p. 769, 2000.
- [169] Z. Wang, C. Lopez, A. Hirska, and N. Koratkar, “Impact dynamics and rebound of water droplets on superhydrophobic carbon nanotube arrays,” *Applied Physics Letters*, vol. 91, no. 2, p. 023105, 2007.
- [170] L. Moevius, Y. Liu, Z. Wang, and J. M. Yeomans, “Pancake bouncing: simulations and theory and experimental verification,” *Langmuir*, vol. 30, no. 43, pp. 13021–13032, 2014.
- [171] A. Mazloomi M, S. S. Chikatamarla, and I. V. Karlin, “Simulation of binary droplet collisions with the entropic lattice boltzmann method,” *Phys. Fluids*, vol. 28, no. 2, p. 022106, 2016.
- [172] Y. Liu, G. Whyman, E. Bormashenko, C. Hao, and Z. Wang, “Controlling drop bouncing using surfaces with gradient features,” *Applied Physics Letters*, vol. 107, no. 5, p. 051604, 2015.
- [173] Y. Liu, M. Andrew, J. Li, J. M. Yeomans, and Z. Wang, “Symmetry breaking in drop bouncing on curved surfaces,” *Nature communications*, vol. 6, 2015.

- [174] G. Taylor, “The dynamics of thin sheets of fluid. iii. disintegration of fluid sheets,” in *Proceedings of the Royal Society of London A: Mathematical, Physical and Engineering Sciences*, vol. 253, pp. 313–321, The Royal Society, 1959.
- [175] F. Culick, “Comments on a ruptured soap film,” *Journal of applied physics*, vol. 31, no. 6, pp. 1128–1129, 1960.
- [176] J. Bao and L. Schaefer, “Lattice boltzmann equation model for multi-component multi-phase flow with high density ratios,” *Applied Mathematical Modelling*, vol. 37, no. 4, pp. 1860–1871, 2013.
- [177] C. Semperebon, T. Krüger, and H. Kusumaatmaja, “Ternary free-energy lattice boltzmann model with tunable surface tensions and contact angles,” *Physical Review E*, vol. 93, no. 3, p. 033305, 2016.
- [178] R. Zhang and H. Chen, “Lattice boltzmann method for simulations of liquid-vapor thermal flows,” *Physical Review E*, vol. 67, no. 6, p. 066711, 2003.
- [179] J. Tölke, S. Freudiger, and M. Krafczyk, “An adaptive scheme using hierarchical grids for lattice boltzmann multi-phase flow simulations,” *Computers & fluids*, vol. 35, no. 8, pp. 820–830, 2006.
- [180] D. Lycett-Brown and K. H. Luo, “Multiphase cascaded lattice boltzmann method,” *Computers & Mathematics with Applications*, vol. 67, no. 2, pp. 350–362, 2014.
- [181] A. Wagner, “Thermodynamic consistency of liquid-gas lattice boltzmann simulations,” *Physical Review E*, vol. 74, no. 5, p. 056703, 2006.

Curriculum Vitæ

Ali Mazloomi Moqaddam

Address: ETH Zürich,
Institut für Energietechnik,
LEE N205, Leonhardstrasse 21,
8092 Zürich, Switzerland,
Phone: +41 44 632 3412,
Email: alim@lav.mavt.ethz.ch
mazloomi.moqaddam@gmail.com

Gender: Male
Nationality: Iranian
Birthday : 08-07-1988
Place of Birth: Tabas

EDUCATION

- Ph.D. Mechanical Engineering, ETH Zürich, 2016.
- M.S. Mechanical Engineering, Sharif University of Technology, 2012.
- B.S. Mechanical Engineering, Isfahan University of Technology, 2010.

JOURNAL PUBLICATIONS

- Ali Mazloomi M., Shyam S. Chikatamarla, and Ilya V. Karlin. "Simulation of binary droplet collisions with the entropic lattice Boltzmann method." *Physics of Fluids* (1994-present) 28.2 (2016): 022106.
- C. Antonini, S. Jung, A. Wetzel, E. Heer, P. Schoch, A. Mazloomi M., S. S. Chikatamarla, I. V. Karlin, M. Marengo and D. Poulikakos, "Contactless prompt tumbling-rebound of drops from a sublimating slope" *Physical Review Fluids* 1.1 (2016): 013903.
- Ali Mazloomi M., Shyam S. Chikatamarla, and Ilya V. Karlin. "Mechanisms of droplet bouncing from a micro textured surface" *Journal of Fluid Mechanics* (under review) 2016.
- Ali Mazloomi M., Shyam S. Chikatamarla, and Ilya V. Karlin. "Entropic lattice Boltzmann method for multiphase flows." *Physical review letters* 114.17 (2015): 174502.
- Ali Mazloomi M., Shyam S. Chikatamarla, and Ilya V. Karlin. "Entropic lattice Boltzmann method for multiphase flows: Fluid-solid interfaces." *Physical Review E* 92.2 (2015): 023308.
- Ali Mazloomi M., Shyam S. Chikatamarla, and Ilya V. Karlin. "Simulation of Droplets Collisions Using Two-Phase Entropic Lattice Boltzmann Method." *Journal of Statistical Physics* 161.6 (2015): 1420-1433.
- Ali Mazloomi M., and A. Moosavi. "Thin liquid film flow over substrates with two topographical features." *Physical Review E* 87.2 (2013): 022409.
- Ali Mazloomi M., A. Moosavi, and E. Esmaili. "Gravity-driven thin liquid films over topographical substrates." *The European Physical Journal E* 36.6 (2013): 1-13.
- E. Esmaili, Ali Moosavi, and Ali Mazloomi M. "The dynamics of wettability driven droplets in smooth and corrugated microchannels." *Journal of Statistical Mechanics: Theory and Experiment* 2012.10 (2012): P10005.
- Ali Mazloomi M. , F. Sharifi, M. R. Salimpour, and A. Moosavi. "Optimization of highly conductive insert architecture for cooling a rectangular chip." *International Communications in Heat and Mass Transfer* 39, no. 8 (2012): 1265-1271.

CONFERENCE PROCEEDINGS AND WORKSHOPS

- Ali Mazloomi M., Shyam S. Chikatamarla, and Ilya V. Karlin. "Free-energy based entropic lattice Boltzmann method: a new approach for two-phase flow simulations." *Conference on Discrete Simulation of Fluid Dynamics*, Edinburgh, Scotland, 2015.
- Ali Mazloomi M., Shyam S. Chikatamarla, and Ilya V. Karlin. "Reducing the contact time of a drop impacting on tapered surfaces." *Workshop on Flowing Matter Across the Scales*, Rome, Italy, 2015.
- Ali Mazloomi M., Shyam S. Chikatamarla, and Ilya V. Karlin. "Entropic lattice Boltzmann method for multiphase flows." *Conference on Discrete Simulation of Fluid Dynamics*, Paris, France, 2014.